Imperial College London
Department of Materials

Using Advanced Surface Analysis Techniques to Investigate the Solid-Solid Interfaces in Solid State Batteries.

Mohammed Nomaan Nabi

Submitted in part fulfillment of the requirements
for the degree of Doctor of Philosophy at
Imperial College London, May 2023.

I hereby declare that this thesis and the work reported herein was composed by and originated entirely from me. Information derived from the published and unpublished work of others has been acknowledged in the text and references are given in the list of sources.

Mohammed Nomaan Nabi (2023)

The copyright of this thesis rests with the author. Unless otherwise indicated, its contents are licensed under a Creative Commons Attribution-Non Commercial 4.0 International Licence (CC BY-NC). Under this licence, you may copy and redistribute the material in any medium or format. You may also create and distribute modified versions of the work. This is on the condition that: you credit the author and do not use it, or any derivative works, for a commercial purpose. When reusing or sharing this work, ensure you make the licence terms clear to others by naming the licence and linking to the licence text. Where a work has been adapted, you should indicate that the work has been changed and describe those changes. Please seek permission from the copyright holder for uses of this work that are not included in this licence or permitted under UK Copyright Law.

Abstract

Scientific interest is strongly drawn towards all-solid-state lithium batteries, considered the future generation of electrochemical energy storage solutions. Their appeal lies in their enhanced safety characteristics and their capacity to open up fresh avenues in chemistry, thereby improving performance. The features of the solid-state electrolyte play a crucial role in the battery's overall cell competence. So far, the materials showing the most promise are garnet-structured oxides, notably those based on LLZO, which demonstrate high ionic conductivity at room temperature and an extensive electrochemical stability range. However, lithium-stuffed garnets remain hindered from the onset of metallic dendrites that permeate the electrolyte upon cycling.

This research aimed to explore whether elemental segregation and electronic conductivity are key contributors to dendrite-induced garnet failure, utilizing Ga-doped LLZO and Ta-doped LLZO as case studies. The initial sections (Chapters 5 and 6) present a thorough evaluation of each solid electrolyte's properties, including their composition, microstructure, purity, and electrochemical performance, as determined by Electrochemical Impedance Spectroscopy (EIS) and Galvanostatic cycling.

Chapter 5 focuses on Ga-LLZO prepared using alumina, magnesia, or zirconia crucibles in either argon or oxygen atmospheres. EPR spectroscopy was employed to detect free electrons in the garnet, revealing signals for unpaired electrons in Ga-LLZO treated under a reducing atmosphere. However, a conclusive analysis of the nuclear environment around the free electron could not be drawn from the hyperfine splitting data. Chapter 6

mirrors the trajectory of Chapter 5 but centres on Ta-LLZO SE. Chapter 7 delves into the surface chemistry and elemental segregation of both doped LLZO compositions using XPS, ToF-SIMS, and LEIS. The findings showed that Ga tends to segregate towards the LLZO surface and grain boundaries, while Ta behaves similarly to matrix cations in LLZO, residing predominantly in the bulk of the electrolyte. The impact of the crucible was examined, with magnesia serving as a relatively new sample support for LLZO sintering. It was confirmed that MgO^- contamination is prevalent in the LLZO, with ToF-SIMS imaging revealing MgO in the grain boundary of Ga-LLZO, similar to observations with LLZO sintered using alumina crucibles.

Chapter 8 explores oxygen diffusion in LLZO using IEDP on ToF-SIMS to obtain secondary ion images and diffusion profiles of the ^{18}O isotope. Preliminary findings suggested ^{18}O segregation in grain boundaries of Ga-LLZO that underwent chemical diffusion with ^{18}O. Tracer diffusivity was obtained from self-exchanged LLZO with ^{18}O, showing a D* of 10^{-17}-10^{-19} cm^2/s. These results were compared with previous literature values of D* for ^{18}O diffusion in garnets such as YIG and YAG which were lower. Thus indicating a higher degree of disorder due to possible oxygen vacancies in LLZO. The initial attempt at determining the activation energy for oxygen diffusion in LLZO showed an Ea of 1.7 eV, though more data collection is necessary to minimize potential errors. Finally, future work encompasses contributions from *in-operando* SIMS using the bespoke Hi5 instrument, which will facilitate SIMS analysis alongside battery operation. This system has also demonstrated the ability to collect both polarities of SI with a highly focused plasma primary beam, a challenge with previous SIMS-based instruments.

Acknowledgments

I would like to start by expressing my profound gratitude to Allah SWT for providing me with this opportunity, despite the numerous challenges that made it the most strenuous period of my life so far. Throughout the highs and lows, I have endeavoured to keep my faith at the forefront of my consciousness.

I wish to express my deepest gratitude to Dr. Ainara Aguadero, my supervisor during these challenging times. Her patience and countless opportunities offered to me will forever be appreciated. Despite the trials of COVID and our long-distance professional relationship following her tenure in Spain, Ainara consistently made time for me, even on short notice.

During this period, Professor Stephen Skinner provided invaluable advice, continuously encouraging my curiosity and reminding me that incomplete experiments are a fundamental part of the research process. I would like to thank Professor Paul Shearing, who always left me feeling more motivated, thanks to his enthusiastic encouraging nature. My time in his group, including discussions with Dr. Francesco Lacoviello about our XCT experiments, was truly enriching.

The Electroceramics group has seen many changes throughout my PhD journey, but one thing has remained consistent: a welcoming environment that allowed me to be myself. To each member, past and present, I extend my heartfelt thanks for making me feel at home from the very beginning.

I extend my sincerest thanks to Dr. Sarah Fearn, Dr. Richard Chater, and Professor John Kilner. Each of you has greatly contributed to my personal and professional development, whether it was through teaching me new skills, engaging in amusing and stimulating conversations that extended beyond the realm of my research, or providing mentorship that has significantly boosted my confidence. Looking back, I wish I had seized the opportunity to interact with you all at an earlier stage.

I am grateful to the CDT-ACM and UKRI for funding my research and providing me with this invaluable opportunity. To Hafiza Bibi, the former centre manager at Imperial College, your assistance has been invaluable. From facilitating the numerous orders necessary for my work to scheduling all my events, your remarkable efforts have kept me on track and moving forward. Thank you for your outstanding contributions.

Lastly, to my family, words fall short of expressing my gratitude for your unwavering support. I trust that you comprehend the depth of my appreciation, even though it is encapsulated in a simple 'thank you.'

Contents

1 Introduction **28**

1.1 Motivation 29

1.2 Climate Change and the Energy Crisis 30

1.2.1 Energy Storage 31

1.3 Batteries 32

1.3.1 Lithium Ion Batteries (LIBs) 34

1.3.2 All Solid-State Batteries (ASSBs) 36

1.4 Thesis Aim 38

2 Theory and Background Understanding **39**

2.1 Battery Electrochemistry 40

2.1.1 Fundamentals of Battery Electrochemistry 42

2.2 Defect Chemistry and Ionic transport 45

2.2.1 Defects in Crystals 45

2.2.2 Kröger-Vink Notation 46

2.3 Ion Transport and Conductivity 49

2.4 Diffusion Fundamentals 52

2.4.1 Fick's Laws 52

2.4.2 Crank's Solution for Semi-Infinite Media 53

2.5 Summary 56

3 Literature Review **57**

3.1 All Solid-State Batteries (ASSBs) 58

3.1.1 Solid Electrolytes 60
3.1.2 Oxides 61
3.2 Lithium-Rich Garnets 64
3.2.1 Structure 65
3.2.2 Ionic Transport 66
3.2.3 Doping Strategies 68
3.2.4 Surface Degradation 70
3.3 Dendrites in LLZO 73
3.3.1 Interface with Lithium Metal 74
3.3.2 Electronic conductivity in LLZO 77
3.4 Summary and Objectives 82

4 Experimental and Instrumentation 83

4.1 Sample Processing Methods 84
4.1.1 Thermal Treatments 84
4.1.2 Grinding and Polishing 87
4.1.3 Density Determination 88
4.1.4 Vickers Hardness 89
4.2 X-ray Diffraction 90
4.2.1 X-ray Diffraction Theory 90
4.2.2 X-ray Diffraction Measurements 91
4.2.3 Le Bail Refinement 91
4.3 Microstructure Analysis 94
4.3.1 Optical microscopy-based measurements 94
4.3.2 Scanning Electron Microscopy 96
4.4 Stoichiometry Determination using ICP-OES 101
4.5 Electrochemical Characterisation 102
4.5.1 Cell Assembly 102
4.5.2 Electrochemical Impedance Spectroscopy (EIS) 104

4.5.3 Electronic Conductivity . . . 110
4.5.4 Cell Cycling . . . 111
4.6 Surface Analysis . . . 112
4.6.1 X-ray Photoelectron Spectroscopy . . . 112
4.6.2 Low Energy Ion Scattering . . . 115
4.6.3 Secondary Ion Mass Spectroscopy . . . 118
4.6.4 Analysers in SIMS . . . 121
4.6.5 SIMS Instruments and Measurement . . . 125
4.7 Isotopic Exchange Depth Profile (IEDP) . . . 130
4.7.1 Isotopic Exchange . . . 130
4.8 Electron Paramagnetic Resonance (EPR) . . . 133
4.8.1 Working Principles of EPR . . . 133
4.8.2 Sample Analysis with EPR . . . 135

5 Sintering Atmosphere and Crucible Choice for Ga-LLZO Preparation 136
5.1 Phase Purity . . . 137
5.1.1 Density and Hardness . . . 141
5.1.2 Elemental Analysis . . . 142
5.2 Microstructure . . . 143
5.3 Electrochemical Measurements . . . 147
5.3.1 Ionic and Electronic Conductivity . . . 148
5.4 EPR Analysis . . . 158
5.5 Summary . . . 162

6 Sintering Atmosphere and Crucible Choice for Ta-LLZO Preparation 163
6.1 Phase Purity . . . 164
6.1.1 Density and Hardness . . . 166
6.1.2 Elemental Analysis . . . 168
6.2 Microstructure . . . 169
6.3 Electrochemical Analysis . . . 172

6.3.1 Conductivity measurements . . . 173
6.3.2 Cell Cycling . . . 177
6.4 EPR analysis . . . 179
6.5 Summary . . . 180

7 Understanding the Effect of Atmosphere and Crucible on the Surface Chemistry of LLZO 181

7.1 Surface Chemistry of Ga-LLZO . . . 183
7.1.1 XPS . . . 183
7.1.2 ToF-SIMS Depth Profile . . . 186
7.1.3 LEIS Depth Profile . . . 189
7.1.4 ToF-SIMS Imaging . . . 192
7.2 Surface Chemistry of Ta-LLZO . . . 196
7.2.1 XPS . . . 196
7.2.2 ToF-SIMS Depth Profile . . . 199
7.2.3 LEIS Depth Profile . . . 201
7.3 Summary . . . 204

8 The Role of Oxygen Vacancies on Dendrite Formation 207

8.1 Isotopic Labelling and Imaging . . . 208
8.2 Oxygen Diffusion . . . 209
8.3 Summary . . . 215

9 Overall Summary and Future Work 216

9.1 Overall Summary . . . 217
9.2 Future Work . . . 221

Bibliography 225

A Supplementary Information for Chapter 6 248

B Supplementary Information for Chapter 7 252

C Supplementary Information for Chapter 8 **255**

D Supplementary Information for Chapter 9 **259**

List of Figures

1.1 (a) Depiction of global surface temperatures from 1884 and 2022, showing the red regions as warmer than normal and the blue as colder than the average (image adapted from [1]), (b) Projection of energy resources with the increase in global renewable energy as predicted by BloombergNEF and the decrease in fossil fuels from 2030 on-wards (image adapted from [2]). (c) Percentage of global primary energy for 2021, showing an even distribution of fossil fuels and minimal renewables. Prediction for 2050 showing a decrease in coal combustion and uptake in nuclear and renewable energy, with oil and gas remaining similar to 2021 primary energy uptake as published by ExxonMobil(image adapted from [3]). 30

1.2 Schematic of the basic battery components, showing the electron and ion flow when the electrodes are connected externally and the dashed line as the separator. 33

1.3 Demand for Li-ion batteries from 2015 to 2030, showing the main sectors with highest demand such as the transport industry (mobility), grid storage, and consumer electronics which is expected to grow by +32% annually, (graph adapted from McKinsey & Company [4]). 34

1.4 Schematic showing the battery architecture used in modern LIBs. The illustration shows the intercalation of Li ions in the graphitic anode and the $LiMO_2$ (M = Co) cathode, figure obtained with permission from [5]. . . 35

2.1 Illustration of energy levels (a) the relative energy of electrodes and electrolyte where E_g is the electrolyte window (or band gap) and μ_A and μ_C are the chemical potentials for the anode and cathode respectively. V_{OC} is the voltage of the cell and Φ_A and Φ_C are the work functions of the electrodes. (b) A schematic of a LiC_6 and Li_xCoO_2 system and the relative density of states, where E_f is the Fermi energy and n is the number of electrons transferred per mole of electrode material [6–8]. 43

2.2 Schematic illustrating point (0D) and line (1D) defects in a crystal. 46

2.3 Schematic illustrating ion hopping using neighbouring vacant sites. The solid line represents the energy profile in the absence of an external electric field, the dotted line if the energy barrier with the applied electric field and ΔH_m is the activation energy. With an applied field, the energy barrier is lowered in one direction by $\frac{1}{2}\alpha qE$ where α is the separation between the start site and the next vacant site and q is the charge on the mobile ion. [9] 51

2.4 Schematic illustrating the gas-solid interface for semi-infinite diffusion with boundary conditions of constant surface (at $x = 0$) concentration (C_s) and constant gas concentration (not shown but it is greater than C_s). 54

3.1 Radar plots representing the various properties sought after from solid electrolytes (a) Oxides comprising mainly of garnets, perovskites, NASICON and LISICON, (b) Sulfides comprising of thio-LISICONs, Argyrodite and LGPS-like, (c) hydrides which are primarily Li-Halide salts, (d) Halides, (e) Thin Films (LiPON) and (f) polymers (PEO), where ASR = area specific resistance or interfacial resistance. Further information on specific compositions is found in [10]. Reprinted with permission from [10]. 61

3.2 Crystal structures of (a) perovskite ABX_3 where A = Li,La,or vacancy, B = Ti, and X = O. Image obtained with permission from [11](b) NASICON-like $LiM_2(PO_4)_3$ where M = Ti or Ge. (c) Conduction pathway in NASICON-like solid electrolytes where T1 and T2 are triangular oxygen bottlenecks. ((b) and (c) extracted with permission from [12]. 63

3.3 Crystal structures of (a) LLZO garnet with inset showing the location of Li ions as Li1 in the tetrahedron and Li2 in the twisted octahedron. (b) the Li-ion pathway in the garnet structure with the yellow dots as Li1 sites and purple dots as the Li2 sites and off-centre octahedral sites used for migration. Image taken with permission from [13, 14]. 65

3.4 (a) Li sites in garnet, showing face-shared octahedral with tetrahedrals, (b) role of lithium concentration on-site occupation and conductivity, (c) schematic representation of two proposed migration routes of lithium either a single-ion migration (high energy) or the concerted multi-ion migration (low energy). All images were obtained with permission from [15]. 67

3.5 Periodic table with the site and oxidation states of dopants studied using density functional theory (DFT) to determine the defect energies for each dopant. The colours represent sight preference (Li = green, La = red, and Zr = blue). The least faint colours have the lowest defect energy, as seen from the comparison B^{3+} and Ga^{3+} for the lithium site, which means Ga doping is favourable. Figure reprinted with permission from [16, 17]. 68

3.6 Proposed mechanisms for dendrite formation and propagation in LLZO. Image obtained with permission from Aguesse *et al.* [18]. 74

4.1 [Left] furnace inside glovebox for heat treatments under argon atmosphere. [Right] Tube furnace with a dry vacuum pump and high-purity oxygen cylinder. 85

4.2 Lithia-Alumina phase diagram showing the liquid phase of lithia-alumina eutectic at 23% Al_2O_3 concentration at 1055°C. Modified Cook and Plante phase diagram of lithia-alumina taken with permission from Kulkarni *et al.* [19] 86
4.3 Schematic representation of Bragg's Law in a Bragg-Brentano geometry. . . 91
4.4 In phase light waves showing constructive interference. [20] 95
4.5 Out-of-phase light waves showing destructive interference. [20] 95
4.6 Interference fringes on Si wafer using NewView 7000. 96
4.7 Schematic of White Light Interferometer 97
4.8 Full topography map of the silicon wafer displayed in 3D view. 98
4.9 Schematic showing the interaction volume of primary electrons towards the samples which generates three main signals picked up by the detectors [21]. 99
4.10 Schematic showing the interaction of primary electrons resulting in characteristic x-rays, which are using SEM-EDX and the generation of Auger electrons. [22] 100
4.11 Steps showing the fabrication of LLZO with gold blocking electrodes in a symmetric configuration. 103
4.12 Assembly of lithium metal on LLZO, (a) image of an LLZO pellet before and after placing the lithium metal electrodes to make a Li|LLZO|Li symmetrical cell used for galvanostatic cycling in a coin cell and (b) schematic of coin cell components used to cycle the cell. 104
4.13 Schematic of Nyquist plot, representing where each impedance signal is generated from using the diagram of a symmetric cell, the Randles circuit shown represents each contribution to the Nyquist plot. 105
4.14 Linkam climate stage used for variable temperature EIS measurements. Image shows the difficulty of conducting measurements below -10°C which results in ice formation. 107
4.15 KK test comparison of residual plots (a) measurement from 32 MHz to 1 Hz, and (b) 13 MHz to 1 Hz. 108

4.16 Diagram showing relative analysis depth of the different surface characterisation techniques used in this work, (not drawn to scale). 112

4.17 Schematic showing micro view (atomistic scale) on the left side and the macro scale on the right side of the interaction of X-ray radiation on core level electron to generate photoelectrons. VL is for the vacuum level and E_F is for Fermi Level. (not drawn to scale). 114

4.18 Schematic showing (a) Primary ion interaction with surface particles and (b) basic working principles of how backscattered ions are detected (image taken with permission from a publication by Cushman *et al.* [23].). 116

4.19 500x500 μm secondary electron images showing the primary ion beams (a) He^+ and (b) Ne^+)alignment on the 50 mesh grid and (c) Ar^+ sputter beam alignment to avoid analysing crater edges, poor definition in the image from the Ar^+ is due to it having a larger spot size, (d) is the camera view of the 50 mesh grid on the sample holder. 118

4.20 Diagram showing key processes that can occur during primary ion bombardment of target materials and these include; (1) recoil implantation, (2) cascade mixing, (3) primary ion reflection and (4) cascade mixing with sputtering. Image adapted from [24] 120

4.21 Three main SIMS analysers used (a) magnetic sector, (b) time of flight, and (c) quadrupole. 122

4.22 500x500 μm images using 1024x1024 pixels, optical image of A-grid (left), SI image using a Bi^+ primary ion beam on the A grid (centre), and an SI image from the Cs^+ sputter beam on the A-grid (right). The alignment of the beams was done to avoid analysing crater edges, the poor definition in the image from the Cs^+ is due to it having a larger spot size. 126

4.23 Image inside the Hi5 main chamber with all components labelled. The sample holder and stage were removed during the time of this picture. electron flood gun and caesium gun are not visible from this angle and are located on the opposite side. 129

4.24 Schematic of dry exchange rig 131

4.25 EPR operation basics. 133

5.1 Le Bail refined XRD pattern for as purchased Ga-LLZO, showing no noticeable reflections from impurities or secondary phases. Reference of Ga-LLZO from ICSD ref. 136577 139

5.2 XRD pattern of all Ga-LLZO samples after processing, (a) all samples sintered under argon with different crucibles, (b) all samples sintered under oxygen with different crucibles. A red asterisk indicates the presence of pyrochlore secondary phase in GZO, and a black cross indicates reflection from an unknown material. 140

5.3 Vicker's Hardness values of all samples, compared with lithium metal. The red dashed line indicates average literature values obtained for LLZO [25, 26]. 142

5.4 Microstructure images before and after polishing and thermal grooving from left to right (a) optical image of GAA, (b) SEM image of GAA, (c) optical image of GAO, and (d) SEM image of GAO 144

5.5 Microstructure images before and after polishing and thermal grooving from left to right (a) optical image of GMA, (b) SEM image of GMA, (c) optical image of GMO, and (d) SEM image of GMO. 145

5.6 Microstructure images before and after polishing and thermal grooving from left to right (a) optical image of GZA, (b) SEM image of GZA, (c) SEM image of GZO. (no optical image of GZO is presented, owing to the difficulty of getting a suitable image showing grain size before polishing and thermal grooving) 146

5.7 Au|LLZO|Au Nyquist and Arrhenius plots for GAA (a) and (b) respectively and for GAO (c) and (d). Inset on the Nyquist plot shows an equivalent circuit used to fit experimental data. Characteristic frequencies for bulk and grain boundaries are shown, calculated from 1/RC. 149

5.8 Au|LLZO|Au Nyquist and Arrhenius plots for GMA (a) and (b) respectively and for GMO (c) and (d). Inset on the Nyquist plot shows an equivalent circuit used to fit experimental data. 151

5.9 Au|LLZO|Au Nyquist and Arrhenius plots for GZA (a) and (b) respectively. Inset on the Nyquist plot shows an equivalent circuit used to fit experimental data. Characteristic frequencies for bulk and grain boundaries are shown. . 152

5.10 Galvanostatic cycling profiles of (a) GAA, (b) GAO, (c), GMA, (d) GMO, and (e) GZA. Cycling was done at room temperature (*approx.* 28°C). Measurement was done using a constant areal capacity of 0.1 mAh/cm^2 and an initial current density of 0.01 mA/cm^2. Inset on spectra show photos of LLZO after cycling 156

5.11 SEM back-scattered image of GAA cross-section post cycling, the red circle shows lithium metal traversing the electrolyte. Inset is an image of a GAA pellet after cycling 157

5.12 EPR response of powder, as-purchased Ga-LLZO (top) and the heat-treated material. Blank corresponds to an empty EPR sample tube, which has a background signal. 160

5.13 EPR response fitting of GMA powder, g = 2.001. 161

6.1 Le Bail refined XRD pattern for as-purchased Ta-LLZO. Reference of Ta-LLZO from ICSD ref. 22958. 165

6.2 XRD pattern of all Ta-LLZO samples after processing, (a) all samples sintered under argon with different crucibles, (b) all samples sintered under oxygen with different crucibles. The red asterisk indicates the presence of pyrochlore secondary phase, the green circle labels reflection for $La(OH)_3$, and the black cross indicates reflection from an unknown material. 166

6.3 Histogram display the Vicker's Harness of Ta-LLZO pellets prepared under various conditions. The red dotted line is the average hardness of LLZO reported in literature [26] 168

6.4 Microstructure of TAA and TAO pellet surface, (a) optical image of TAA after sintering, (b) SEM image of TAA pellet after polishing and thermal grooving, (c) optical image of TAO, and (d) SEM image of TAO pellet after polishing and thermal grooving. 170

6.5 Microstructure of TMA and TMO pellet surface, (a) optical image of TMA after sintering, (b) SEM image of TMA pellet after polishing and thermal grooving, (c) optical image of TMO, and (d) SEM image of TMO pellet after polishing and thermal grooving. 171

6.6 Microstructure of TZA and TZO pellet surface, (a) optical image of TZA after sintering, (b) SEM image of TZA pellet after polishing and thermal grooving, (c) SEM image of TZO pellet after polishing and thermal grooving (no suitable optical image of TZO could be obtained). 172

6.7 EIS data of TAA and TAO. (a) Nyquist plot of TAA, (b) Arrhenius plot of TAA, (c) Nyquist plot of TAO, and (d) Arrhenius plot of TAO. Inset on Nyquist plots show the equivalent circuits used for fitting 174

6.8 EIS data of TMA and TMO. (a) Nyquist plot of TMA, (b) Arrhenius plot of TMA, (c) Nyquist plot of TMO, and (d) Arrhenius plot of TMO. Inset on Nyquist plots show the equivalent circuits used for fitting 175

6.9 Galvanostatic cycling profiles of (a) TAA, (b) TAO, (c) TMA, and (d) TMO. Inset show the Ta-LLZO pellets after cycling. A constant areal capacity of 0.1 mAh/cm^2 and initial current density of 0.01 mA/cm^2 was used 178

6.10 EPR of as-purchased Ta-LLZO and samples from various processing conditions 179

7.1 XPS spectra of key element core levels for Ga-LLZO pellets. The core levels are Li 1s. C 1s, O 1s, Ga 2p, Zr 3d, and La 3d, in order from left to right. The dashed line indicates the characteristic binding energy. 185

7.2 ToF-SIMS depth profile of GAA (left) and GAO (right). Depth profile of negative secondary ions using 2 keV, 150 nA Cs^+ sputter beam and 25 keV, 0.20 pA Bi^+ primary beam, analysis area is 150x150 μm, sputter area is 300x300 μm. The red dashed line indicates (1) the surface corrosion, (2) the LLZO surface, and the remaining is the bulk. 187

7.3 ToF-SIMS depth profile of GMA (left) and GMO (right). Depth profile of negative secondary ions using 2 keV, 150 nA Cs^+ sputter beam and 25 keV, 0.20 pA Bi^+ primary beam, analysis area is 150x150 μm, sputter area is 300x300 μm 188

7.4 ToF-SIMS depth profile of GZA. Depth profile of negative secondary ions using 2 keV, 150 nA Cs^+ sputter beam and 25 keV, 0.20 pA Bi^+ primary beam, analysis area is 150x150 μm, sputter area is 300x300 μm 189

7.5 LEIS spectra of GAA (left) and GAO (right). Two primary ion beams are used to help distinguish between the Zr and La scattering energy using Ne^+ beam. 190

7.6 LEIS depth profile of (a) GAA, (b) GAO, (c) GMA, (d) GMO, and (e) GZA. Measurement using He^+ (solid line) and Ne^+ (scatter plot) primary beams, analysis area is 1x1 mm with a sputter area of 1.5x1.5 mm using Ar sputter beam. 191

7.7 ToF-SIMS total SI maps of GAA showing (a) total SI, (b) Li^+ normalised to total, (c) GaO^- normalised to total, (d) LaO^- normalised to total, (e) ZrO^- normalised to total, and (f) AlO^- normalised to total. Measurement with Cs^+ sputter beam and 25 keV, 0.20 pA Bi^+ primary beam, analysis area is 150x150 μm, sputter area is 350x350 μm, and 512 pixels. 192

7.8 ToF-SIMS maps overlay of GAA showing, AlO^- in red, and ZrO^- in green (left), and GaO^- in red, and ZrO^- in green (right). Measurement with Cs^+ sputter beam and 25 keV, 0.20 pA Bi^+ primary beam, analysis area is 150x150 μm, sputter area is 350x350 μm, and 512 pixels. 193

7.9 ToF-SIMS total SI maps of GMA showing (a) total SI, (b) Li^+ normalised to total, (c) GaO^- normalised to total, (d) LaO^- normalised to total, (e) ZrO^- normalised to total, and (f) MgO^- normalised to total. Measurement with Cs^+ sputter beam and 25 keV, 0.20 pA Bi^+ primary beam, analysis area is 500x500 μm, sputter area is 1000x1000 μm, and 1024 pixels. 194

7.10 ToF-SIMS maps overlay of GMA showing, oxygen-18 in red, GaO^- in green, and LaO in blue. Measurement with Cs^+ sputter beam and 25 keV, 0.20 pA Bi^+ primary beam, analysis area is 500x500 μm, sputter area is 1000x1000 μm, and 1024 pixels. 195

7.11 ToF-SIMS maps of GMA showing, (left) 2D overlay of GMA showing, MgO^- in red and ZrO^- in blue. (right) 3D overlay render of MgO^- in green and ZrO^- in blue (measurement by Dr Sarah Fearn). Measurement with Cs^+ sputter beam and 25 keV, 0.20 pA Bi^+ primary beam, analysis area is 500x500 μm, sputter area is 1000x1000 μm, and 1024 pixels. 196

7.12 ToF-SIMS total SI maps of GZA showing (a) total SI, (b) Li^+ normalised to total, (c) GaO^- normalised to total, (d) LaO^- normalised to total, (e) ZrO^- normalised to total, and (f) GaO^- (green) overlay on $^{18}O^-$ (red). Measurement with Cs^+ sputter beam and 25 keV, 0.20 pA Bi^+ primary beam, analysis area is 150x150 μm, sputter area is 350x350 μm, and 512 pixels. 197

7.13 XPS spectra of key element core levels for Ta-LLZO pellets. The core levels are Li 1s. C 1s, O 1s, Zr 3d, La 3d, and Ta 4f, in order from left to right. The dashed line indicates the characteristic binding energy. 198

7.14 ToF-SIMS depth profile of TAA (left) and TAO (right). Depth profile of negative secondary ions using 2 keV, 150 nA Cs^+ sputter beam and 25 keV, 0.20 pA Bi^+ primary beam, analysis area is 150x150 μm, sputter area is 300x300 μm. The region left to the red dashed line indicates (1) the surface corrosion/ SIMS artefact, (2) the LLZO surface, and the remaining is the bulk. 200

7.15 ToF-SIMS depth profile of TMA (left) and TMO (right). Depth profile of negative secondary ions using 2 keV, 150 nA Cs^+ sputter beam and 25 keV, 0.20 pA Bi^+ primary beam, analysis area is 150x150 μm, sputter area is 300x300 μm. The region left to the red dashed line indicates (1) the surface corrosion/ SIMS artefact, (2) the LLZO surface, and the remaining is the bulk. 202

7.16 LEIS spectra of TAA (left) and TAO (right). Two primary ion beams are used to help distinguish between the Zr and La scattering energy using the Ne^+ beam. 203

7.17 LEIS depth profile of (a) TAA, (b) TAO, (c) TMA, and (d) TMO. Measurement using 3 keV, 4.4 nA He^+ (solid line) or 3 keV, 1 nA Ne^+ (scatter plot) primary beams, analysis area is 1x1 mm with a sputter area of 1.5x1.5 mm using 50 eV, 100 nA Ar sputter beam. 203

8.1 ^{18}O enriched ToF-SIMS maps of GAA (left), GMA (centre), and GZA (right). Beam conditions, Cs^+ sputter beam and 25 keV, 0.20 pA Bi^+ primary beam. Analysis area is 500x500 μm, sputter area is 1000x1000 μm, and 1024 pixels, for GAA and GMA. Analysis area is 150x150 μm, sputter area is 350x350 μm, and 512 pixels, for GZA. 209

8.2 IEDP ^{18}O self-diffusion profiles and corresponding ^{18}O SI maps via ToF-SIMS for (a, b) GAA, (c,d) GMA, and (e, f) GZA (red dotted line showing the elimination of lower ^{18}O fraction at the surface from corrosion layer, when fitting). Beam conditions, Cs^+ sputter beam and 25 keV, 0.20 pA Bi^+ primary beam. Analysis area is 150x150 μm, sputter area is 350x350 μm, and 256 pixels, for GAA. Analysis area is 200x200 μm, sputter area is 400x400 μm, and 256 pixels, for GMA. Analysis area is 100x100 μm, sputter area is 300x300 μm, and 256 pixels, for GZA. Diffusion profiles are fit to Crank's solution for a semi-infinite media. 210

8.3 IEDP ^{18}O self-diffusion profiles and corresponding ^{18}O SI maps via ToF-SIMS for (a, b) TAA, (c,d) TMA, and (e, f) TZA. The red dotted line shows the elimination of the lower ^{18}O fraction at the surface from the corrosion layer when fitting. Beam conditions, Cs^+ sputter beam and 25 keV, 0.20 pA Bi^+ primary beam. Analysis area is 100x100 μm, sputter area is 300x300 μm, and 256 pixels, for TAA, TMA, and TZA was used. Diffusion profiles are fit to Crank's solution for a semi-infinite media. 211

8.4 Arrhenius plot for oxygen diffusion in GAA, and comparison with other garnets including data for YAG [27], YIG [28–30], and YbIG [31]. The plot includes the self-diffusion coefficient for Ga-LLZO [32] with a similar composition to GAA. The magnified region shows a clearer representation of Arrhenius plots at higher temperatures. 212

9.1 Current Hi5 capabilities using a Xe plasma primary ion beam. (a) show the correlation between beam current for a 30 keV Xe beam and sport size, (b) shows an SI image of a TEM grid achieved using Xe beam current at 10 pA. (c) Is the signal intensity from the edge of the TEM grid from Xe (30 keV, 10 pA) giving spot size down to 30 nm. (d) SE image of Ga-LLZO pellet surface viewed using 30 keV, 2 pA Xe beam, with inset showing magnification capability down to a grain boundary. (e) SI image of Ga-LLZO grain, with (f) as the corresponding SIMS images with simultaneous Li^+ and O^- collection 222

9.2 Proposed *in-operando* setups where, (a) shows SI image of grain boundaries island achieved with pattern milling, (b) micro-probes in position for possible electrochemical measurements, and (c) schematic of *in-operando* battery cycling. 224

A.1 Le Bail refined XRD pattern for all samples in chapter 5, used to determine lattice parameters, volume, space group and density. 248

A.2 Ga-LLZO green pellet after sintering process melted into MgO crucible. . . 249

A.3 Grain roughness post sintering of GMA, image from the white light interferometer. 249

A.4 Nyquist plots for Ga-LLZO prepared under various conditions. EIS obtained using Li|Ga-LLZO|Li at 25°C. Nyquist plot of (a) GAA, (b) GAO, (c) GMA, (d) GMO, and (e) GZA. Inset on the Nyquist plot shows the respective R-CPE equivalent circuit used to fit the data. 250

A.5 All time-resolved DC voltage data for electronic conductivity measurements. Au|Ga-LLZO|Au used at RT with a measurement time up to 1 hour. 251

B.1 Le Bail refined XRD pattern for all samples in chapter 5, used to determine lattice parameters, volume, space group and density. 252

B.2 Nyquist plots for Ta-LLZO prepared under various conditions. EIS obtained using Li|Ta-LLZO|Li at 25°C. Nyquist plot of (a) TAA, (b) TAO, (c) TMA, and (d) TMO. Inset on the Nyquist plot show the respective R-CPE equivalent circuit used to fit the data. 253

B.3 All time resolved DC voltage data for electronic conductivity measurements. Au|Ta-LLZO|Au used at RT with a measurement time up to 1 hour.. 254

C.1 XPS survey spectra for each Ga-LLZO composed pellet, with labelled core level peaks of interest 255

C.2 Fitting of XPS core level spectra of key elements in Ga-LLZO. 256

C.3 ToF-SIMS DP of (right) GMA surface not in contact with MgO crucible during sintering and (left) GMA in the surface in contact with MgO crucible. Measurement is done with 25 keV, 0.20pA Bi^+ primary beam and 1 keV, 200 nA O_2^+ sputter beam. The analysis area is 500x500μm analysis area, 1000x1000μm crater area, and 512 pixels. 256

C.4 SEM and EDX map of SIMS crater on GAA, SE image (left), Zr EDX map (middle), and La EDX map (right). 257

C.5 XPS survey spectra for each Ta-LLZO composed pellet, with labelled core level peaks of interest 257

C.6 Fitting of XPS core level spectra of key elements in Ta-LLZO. 258

D.1 Crater depth measurement using Zygo WLI, showing crater on GZA as an example. Depth is used for the diffusion profile. 259

List of Tables

1.1 Electrochemical reaction and half cell reactions in a Sony LIB with LiC_6 (graphite) anode and $LiCoO_2$ cathode, and with the respective potentials vs. the standard hydrogen electrode [33] 35

2.1 Kröger-Vink notation for possible point defects [34] 46

2.2 Possible defect pairs for charge balance 48

3.1 Summary of doping on various LLZO sites and defects generated 70

3.2 Examples of doping on various sites in LLZO, doping resulting in the highest ionic conductivity are shown. 72

4.1 Field of resonance for g = 2 sample at various microwave frequencies [35] . 134

5.1 Sample name for Ga-LLZO SE after processing. 138

5.2 Stoichiometery of samples after processing determined via ICP-OES and oxygen determined using equation 4.6, cell volume obtained from XRD refinement and relative densities. 141

5.3 Ionic conductivity, and capacitance values from EIS measurements at 25°C with Au|LLZO|Au cell, activation energy values from Au|LLZO|Au cell at a temperature range between 0-100°C, R_{int} from Li|LLZO|Li cell at 25°C. Electronic conductivity values form Au|LLZO|Au cell at 25°C 154

6.1 Sample name for Ta-LLZO SE after processing. 164

6.2 Stoichiometery of samples after processing determined via ICP-OES and oxygen determined using equation 4.6, cell volume obtained from XRD refinement and relative densities. 167

6.3 Ionic conductivity, and capacitance values from EIS measurements at 25°C with Au|LLZO|Au cell, activation energy values from Au|LLZO|Au cell at a temperature range between 0-100°C, R_{int} from Li|LLZO|Li cell at 25°C. Electronic conductivity values for Au|LLZO|Au cell at 25°C 176

8.1 Tabulated oxygen diffusion activation energies in garnets along with methods used to measure. 214

Nomenclature and Abbreviations

- B_0 - Magnetic field
- C(x) - Isotopic concentration in various regions
- C - Capacitance
- C' - Isotope concentration in reservoir
- D - Diffusion coefficient
- D* - Tracer diffusivity
- D_i - Self-diffusion coefficient
- E_a - Activation energy
- E_f - Fermi energy
- E_g - Electrolyte window/band gap
- eV - Electron volts
- E^0 - Standard cell potential
- F - Faraday constant = 96485.33 s A/ mol
- λ - Wavelength

- k - Boltzmann constant = 1.38 x 10^{-23} $m^2kgs^{-2}K^{-1}$
- k - Surface exchange coefficient
- M_W - Molecular weight
- μ_e - Chemical potential / mobility
- n - Number of electrons
- ϕ^0 - Half cell potential
- Φ - Work function
- R - Gas constant = 8.314 J/ mol· K
- R_{bulk} - Bulk (grain interior) resistance
- R_{GB} - Grain boundary resistance
- R_{int} - Interfacial resistance
- ρ - Density
- σ - Conductivity
- t - time
- T - Temperature
- τ - Transport number
- V - Voltage
- V_0 - Equilibrium potential
- V_{OC} - Open circuit voltage
- Q - Capacity

- q - Charge

- ASR - Area Specific Resistance
- ASSB - All Solid State Battery
- BAM - Burst Alignment Mode
- C - Capacitor
- CCD - Critical Current Density
- c-LLZO - Cubic LLZO
- CPE - Constant Phase Element
- EDX - Energy Dispersive X-ray Spectroscopy
- EIS - Electrochemical Impedance Spectroscopy
- EPR - Electron Paramagnetic Spectroscopy
- FIB-SIMS - Focused Ion Beam - Secondary Ion Mass Spectroscopy
- Ga-LLZO - $Ga_{0.25}Li_{6.25}La_3Zr_2O_{12}$
- GB - Grain Boundary
- HOMO - Highest Occupied Molecular Orbital
- HV - Vickers Hardness
- ICP-OES - Inductively Coupled Plasma Optical Emission Spectroscopy
- IEDP - Isotopic Exchange Depth Profile
- K-V - Kröger-Vink
- LAGP - $Li_{1.5}Al_{0.5}Ge_{1.5}(PO_4)_3$
- LATP $Li_{1.3}Al_{0.3}Ge_{1.7}(PO_4)_3$

- LE - Liquid Electrolyte
- LEIS - Low Energy Ion Scattering
- LGP - $LiGe_2(PO_4)_3$
- LIB - Lithium Ion Battery
- LiPON - $Li_xPO_yN_z$
- LISICON - $Li_{2+2x}Zn_{1-x}GeO_4$
- LLTO - $Li_{3x}La_{(2/3)-x}TiO_3$
- LLZO - $Li_7La_3Zr_2O_{12}$
- LMIG(S) - Liquid Metal Ion Gun (Source)
- LTP - $LiTe_2(PO_4)_3$
- LUMO - Lowest Unoccupied Molecular Orbital
- NASICON - $LiM_2(XO_4)_3$
- R - Resistor
- SE - Solid Electrolyte
- SEI - Solid Electrolyte Interphase
- SEM - Scanning Electron Microscope
- SIMS - Secondary Ion Mass Spectroscopy
- TEM - Transmission Electron Microscope
- ToF-SIMS - Time of Flight Secondary Ion Mass Spectroscopy
- UHV - Ultra High Vacuum

- WLSI - White Light Scanning Interferometry
- XPS - X-ray Photoelectron Spectroscopy
- XRD - X-ray diffraction

Chapter 1

Introduction

In this chapter, we will delve into the significance of battery research and how the efforts of the research community can help address the energy crisis. We will start by outlining the motivation behind this work and its crucial role in tackling climate change. A brief history of battery technology will follow, leading up to the inception of the lithium-ion battery. We will then discuss the limitations of the current lithium-ion battery and explore the latest research on solid-state batteries. To wrap up, we will outline the purpose of this thesis and how it can contribute to the scientific community.

1.1 Motivation

With the ever-increasing demand for energy and electricity, due to the increasing global population (set to reach 8.5 billion by 2030) [36], and the development of countries occurring at an unprecedented rate, it is clear that finite resources of energy such as fossil fuels are not feasible as a long-term solution. Fossil fuels are not a viable solution to the high energy demand, due to their impact on the environment by greenhouse effects and geopolitical tensions caused by their reliance, making it difficult for nations to have independent energy sources. Renewable energy including; solar, wind, tidal, hydro-power, biomass, and geothermal to name a few are the way forward for many countries, especially developing regions, as nuclear is not an option for many due to the construction and maintenance cost as outlined by the International Atomic Energy Agency (IAEA) [37]. With the uptake of more renewable energy sources, they still possess the inherent disadvantage of being intermittent and hindered by geographical location, for example, countries close to the poles not receiving enough solar radiation for half a year to generate electricity from solar panels. Methods of storing the energy need to be implemented, such as in batteries, for renewable energy not to be as much of a burden. Batteries can play a critical role in solving the energy crisis. However, environmental concerns still remain including where the materials are sourced and currently, there is no suitable method for battery recycling, hence further research efforts are essential.

1.2 Climate Change and the Energy Crisis

Careful consideration is now being taken by global governments on how to prevent a catastrophic energy crisis while simultaneously having no further negative impact on the climate. A study by the Goddard Institute for Space Studies at NASA shows the global surface temperatures increased substantially from 1884 to 2022 [1] as shown in figure 1.1. This rise in temperature has already caused destruction to fragile ecosystems such as marine life by growing heat stress resulting in the bleaching of coral [38] and frequent wildfires [39, 40].

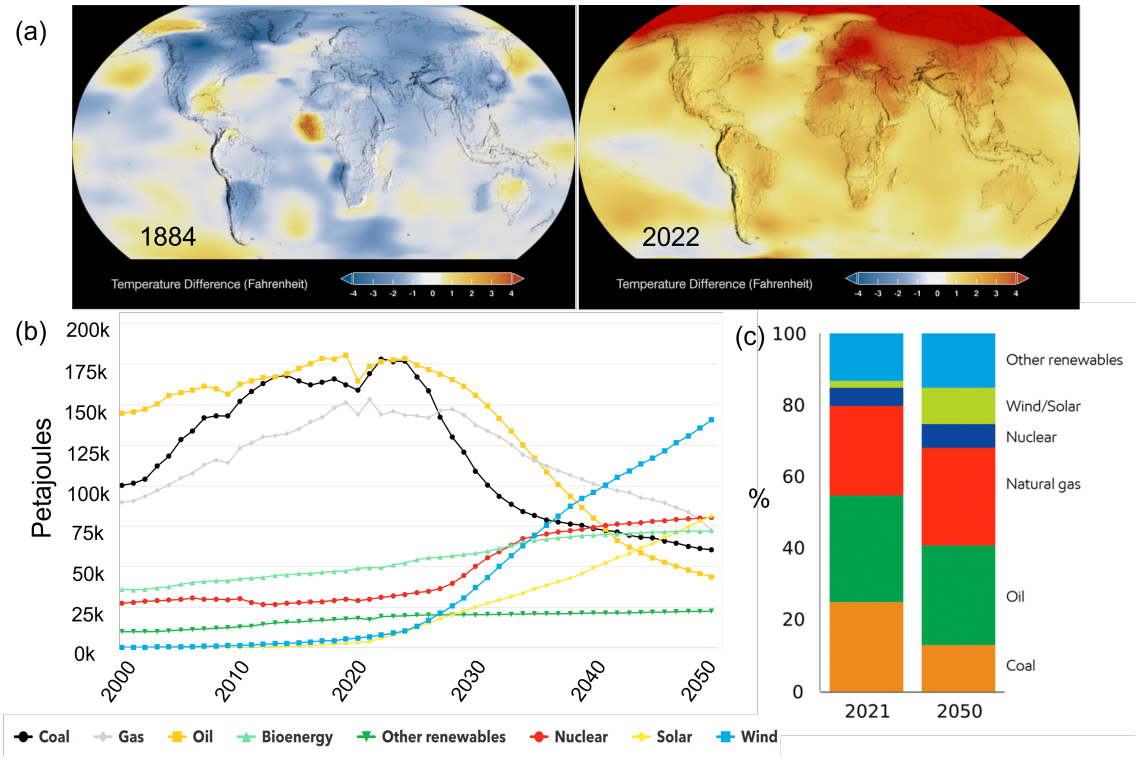


Figure 1.1: (a) Depiction of global surface temperatures from 1884 and 2022, showing the red regions as warmer than normal and the blue as colder than the average (image adapted from [1]), (b) Projection of energy resources with the increase in global renewable energy as predicted by BloombergNEF and the decrease in fossil fuels from 2030 on-wards (image adapted from [2]). (c) Percentage of global primary energy for 2021, showing an even distribution of fossil fuels and minimal renewables. Prediction for 2050 showing a decrease in coal combustion and uptake in nuclear and renewable energy, with oil and gas remaining similar to 2021 primary energy uptake as published by ExxonMobil(image adapted from [3]).

Government regulations are making efforts to mitigate the harmful effects of using CO_x, NO_x, and SO_x emitting fuels. Global projections of energy sources made by BloombergNEF [2] have shown a decrease in the use of coal, gas, and oil by 2030. Furthermore, a report by ExxonMobil [3] shows that coal consumption will reduce in 2050 to half that of 2021, whereas oil and gas production will remain similar in the world's energy mix from 2021 to 2050. This may be due to the ease of oil and gas mining versus that of coal, but coal may still be used in developing parts of the world. Both of these reports' predictions are shown in figures 1.1(a) and (b). The reports show the uptake of renewable energy such as solar and wind, which are much more easily implemented domestically. The cost of solar energy is still a major factor and most domestic panels have a solar energy efficiency of 20% depending on location. Therefore a method of storing this energy is vital to have a smooth transition to sustainable energy.

1.2.1 Energy Storage

There are a vast amount of technologies that are used to store energy, and they are divided into four major groups; electrochemical, electrical, thermal/thermochemical, and mechanical systems [41]. Electrochemical energy storage includes all batteries from lithium-ion (Li-ion), lead acid, and nickel-metal hydride to redox flow batteries, etc. Capacitors and super-capacitors are considered electrical storage, and thermal energy storage would include phase-change materials that can release heat upon a change in the physical state [42]. Mechanical energy storage includes flywheels, compressed air and pumped hydro storage (PHS). The construction of water dams is prevalent in many parts of the world for grid-level energy storage, as it is highly efficient, with long discharge times $>$ 24h [41]. However, when it comes down to energy and power density PHS is the lowest due to their large scale in comparison to electrochemical systems such as batteries. Electrochemical storage devices also provide a sense of independence whereas, PHS is dependent on geographical location and can lead to political tensions as it can restrict water flow to neighbouring countries, as seen for the river Nile in Egypt and Euphrates River in Iraq which are being dammed by Ethiopia and Turkey respectively [43–45].

Batteries have been shown to become more versatile with applications in stationary systems and transport such as electric vehicles, and the drop in production costs from $732 per kWh in 2013 to $151 per kWh in 2022 for a battery pack in electric vehicles. For example, the battery pack for a Tesla Motor Model S or the Chevrolet Bolt with a 60 kWh battery pack will cost approx. $10,000 alone in 2022 [46,47]. Efforts in cutting production costs and research into the development of increased power density Li-ion batteries are being made. Chapter 2 will discuss the fundamental chemistry behind Li-ion batteries and the efforts that can be made to improve their performance.

1.3 Batteries

The three main components of a battery are the electrodes (negative anode and positive cathode) and the electrolyte. The electrodes are described with two different polarities and are dependent on the process being undertaken by the cell. Hence, when a battery is being discharged (which is when the battery is plugged into a device to operate it) one electrode gains electrons which flow through the external circuit (i.e. the device), at this time the electrode is reduced and is called the cathode with a positive polarity. Whereas, the electrode that loses electrons during discharge, is referred to as the anode and is oxidized (negative polarity). The opposite is true when recharging the battery; for simplicity when discussing electrodes it will be based on discharging a battery. The battery operates by having one electrode in a high energy state (i.e. chemical potential), which is the anode, and another in a lower energy state, the cathode. Once electrodes are connected externally as shown in figure 1.2 electrons can flow through a device to power it, whereas ions will flow through the electronically insulating electrolyte to the other electrode.

To prevent self-discharge of the battery a physical separator is inserted in between the electrodes which is semi-permeable to the ions. This is the typical configuration for some of the first batteries discovered [48].

Batteries have come a long way since their inception. The first evidence of a bat-

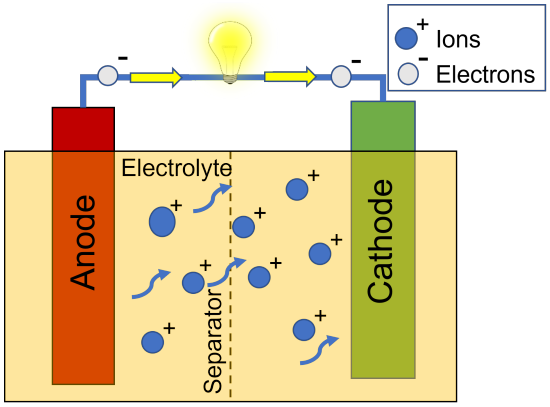


Figure 1.2: Schematic of the basic battery components, showing the electron and ion flow when the electrodes are connected externally and the dashed line as the separator.

tery is said to be more than 2000 years old, which was discovered during an archaeological excavation in Baghdad, Iraq. The item was composed of a ceramic pot casing that had an iron bar and copper cylinder and was named the "Baghdad Battery"; no signs of an electrolyte were present. However, it is believed to have been wine or vinegar [48,49]. The first recorded working battery was by Alessandro Volta in Italy where he used a zinc and copper stack with sulfuric acid or saline (salt) solution as the electrolyte. It was about 50 years after the voltaic cell that the first rechargeable lead acid battery was invented by Gaston Panté in 1859. A further 120 years of intensive research, the modern-day Lithium-ion battery came to fruition thanks to John B. Goodenough, M. Stanley Whittingham, and Akira Yoshino, from their work on the electrodes for which they won the Chemistry Nobel Prize in 2019 [50–52]. Since then the Li-ion battery has played a major role in helping us move away from non-renewable sources of energy and vastly improved the automotive industry and consumer electronics, with demands to only grow further as depicted in figure 1.3, especially in the electric vehicle industry. Therefore, more research efforts need to be made to sustain this growth in battery demand, as it is not proportional to electronics development growth, stated by Moore's Law, *'the number of transistors on a microchip will double every two years'*, hence the improvements in computational power by conventional technologies in coming years will start to plateau [53].

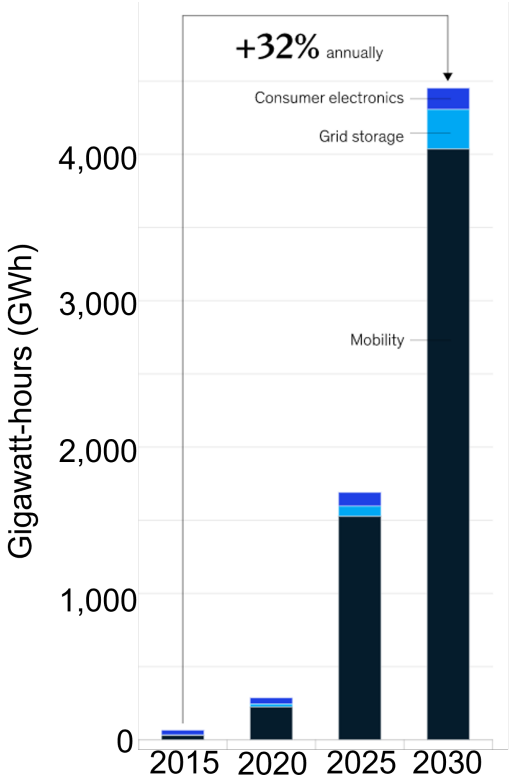


Figure 1.3: Demand for Li-ion batteries from 2015 to 2030, showing the main sectors with highest demand such as the transport industry (mobility), grid storage, and consumer electronics which is expected to grow by +32% annually, (graph adapted from McKinsey & Company [4]).

1.3.1 Lithium Ion Batteries (LIBs)

As lithium-ion batteries (LIBs) have played a critical role in the advancement of human civilization, the basic chemistry behind LIBs will be discussed in this section. The current issues with LIBs will be mentioned and what efforts can be made to resolve these issues.

The first LIB was commercialised by Sony in 1991 [49] which utilized the graphite anode and cobalt-based cathode that benefited from its lithium-ion intercalation chemistry as shown in figure 1.4. Upon discharge of the LIB, the graphitic anode is oxidised (loses electrons), which causes the electrons to flow through the external circuit and the Li-ions travel through the electrolyte and intercalate into the layered crystal structure of the $LiCoO_2$ cathode material. This is made possible as the chemical potential of the anode is greater than the chemical potential of the cathode.

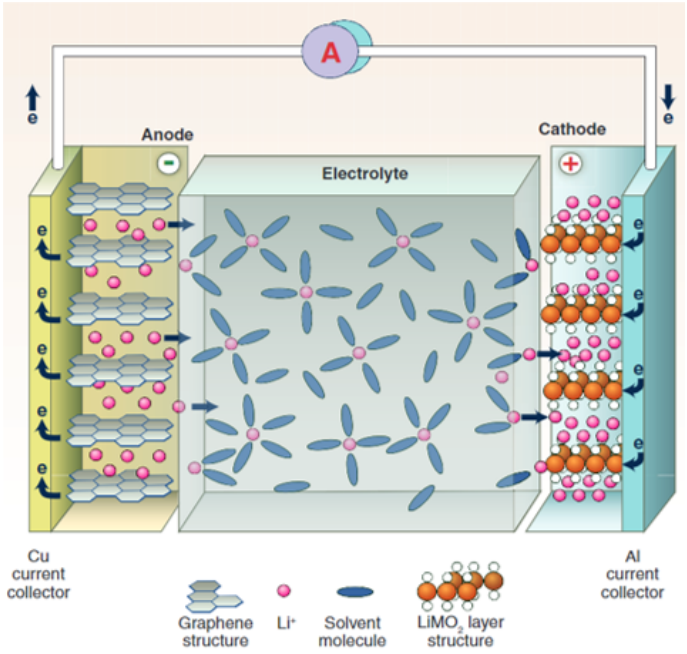


Figure 1.4: Schematic showing the battery architecture used in modern LIBs. The illustration shows the intercalation of Li ions in the graphitic anode and the $LiMO_2$ (M = Co) cathode, figure obtained with permission from [5].

The high energy and power density is what has led to the rapid uptake of this battery technology which is due to the high voltage and capacity of the cell, discussed further in section 2.1. Once the cell has discharged, a potential can then be applied to drive the electrons and Li-ions back to the positive graphitic electrode (reduction). The overall electrochemical reaction and the half-cell reactions for the Sony cell are shown in table 1.1 [33].

Table 1.1: Electrochemical reaction and half cell reactions in a Sony LIB with LiC_6 (graphite) anode and $LiCoO_2$ cathode, and with the respective potentials vs. the standard hydrogen electrode [33]

Anodic reaction:	$Li_xC \rightleftharpoons C + xLi^- + xe^-$	ϕ^0 = -2.90 V
Cathodic reaction:	$Li_{1-x}\ CoO_2 + xLi^- + xe^- \rightleftharpoons LiCoO_2$	ϕ^0 = 1.20 V
Full reaction:	$Li_{1-x}\ CoO_2 + Li_xC \rightleftharpoons C + LiCoO_2$	E^0 = 4.10 V

Even with the high theoretical cell voltage of 4.10 V and hence high energy density, issues still prevail in this configuration. The operating voltage is not always consistent

and decreases from the theoretical value of 4.10 V to approximately 3 V which is a result of the side reactions on the cathode, during delithiation. Oxidation of the cathode can result in oxygen evolution when cobalt goes from Co^{3+} to a Co^{4+} state, causing electron holes to be trapped as peroxides and can combine to form oxygen gas. The oxygen can in turn oxidise the organic electrolyte releasing CO_2 furthering the degradation [54, 55]. The capacity of the Sony LIBs also fades during cycling because not all of the lithium can be de-intercalated, which hinders the practical gravimetric capacity, and lowering it down to 130 mAh g^{-1} [55] compared to the theoretical of 274 mAh g^{-1} [56]. If complete delithiation occurs then this will lead to an irreversible degradation reaction in the battery, via the evolution of oxygen.

In order to increase the energy density of LIBs, electrodes with greater capacity need to be developed and with less host material involved. The ideal case would be a full lithium metal anode as it has a theoretical capacity of 3860 mAh g^{-1}. Lithium metal also has the lowest (negative) electrode potential of -3.04 V which can be paired up with a high voltage (positive) cathode to increase the cell potential, and coupled with the low density of lithium of 0.53 g cm^{-3}, higher gravimetric energy densities can be achieved as less host material is involved [57, 58].

However, lithium metal anodes are not viable in liquid electrolyte-based LIBs as dendrites (i.e. metallic filaments) can propagate and contact the cathode through the electrolyte. The contact results in complete discharge and cell failure. Most LIBs utilise a flammable organic electrolyte that can ignite from a sudden discharge, from dendrites that may release an immense amount of thermal energy. The rise in temperature is enough to surpass the flash point of the organic electrolyte resulting in thermal runaway. It is for this reason that research into solid electrolytes is critical to further battery advancements.

1.3.2 All Solid-State Batteries (ASSBs)

Advancements in electrolytes can help to increase the energy density of batteries. Solid electrolytes with larger band gaps can be paired up with lithium metal anodes and high-

voltage cathodes that dwell within the electrolyte window. One of the current issues with liquid electrolytes is the band gap, which limits the application of high-voltage cathodes and lithium metal anodes. The chemical potential must lie within the electrolyte band gap to prevent side reactions from occurring and recombination of charge carriers which can degrade the electrolyte. To overcome this, solid electrolytes that are stable with new high voltage electrodes [8,59] and having a large electrolyte window is crucial. The theory behind the relative energy levels is discussed in Chapter 2, section 2.1.

Thermal runaways as seen recently with Samsung mobile devices [60] is a major concern for battery manufacturers. The implementation of solid electrolytes with higher operating temperatures is being investigated. Not only can solid electrolytes be safer, but they may also provide longer cycle and shelf life if electrochemical stability is achieved between the electrolyte and potentially high energy electrodes [61,62].

Solid electrolyte development is still in its infancy. Current solid electrolytes need to have high ionic conductivity > 1 mS cm^{-1} at 25°C for Li ions, and be chemically and electrochemically stable with both electrodes. Therefore, it is of utmost importance to study the cause of high resistance within solid electrolytes and at the electrode-electrolyte interface. Solid electrolyte failure via dendrites is still an issue and it is imperative that the route of this be understood and prevented (see Chapter 3).

1.4 Thesis Aim

The work in this thesis aims to investigate the route cause of failure in the ceramic lithium-ion conducting solid electrolyte. The material used throughout is a lithium-stuffed garnet electrolyte, utilising the composition based on $Li_7La_3Zr_2O_{12}$ (LLZO) with supervalent donor doping. Garnet-based solid electrolytes have gained popularity in the battery community, due to their large electrolyte window, stability with lithium metal, and high ionic conductivity.

The layout of the following chapters begins with a theoretical understanding of battery chemistry, crystal defects, and diffusion theory in Chapter 2. Chapter 3 will provide an update on recent studies on solid electrolytes with the main focus on LLZO and an overview of the research done on LLZO|Li metal interface and electronic properties as possible causes for dendrite formation and propagation. Chapter 4 will provide a detailed description of the techniques used in this work, including instrumentation theory and the methods implemented for characterisation. The effect of processing conditions such as atmosphere and crucibles will be discussed in Chapters 5 and 6 on a macroscopic scale and how it affects Ga-LLZO and Ta-LLZO performances respectively. Chapter 7 will discuss the surface chemistry with respect to the aforementioned processing conditions to further understand the interface between LLZO and lithium metal. This will be followed by considering electronic properties and oxygen vacancies as a cause for LLZO failure by lithium-ion reduction within the electrolyte in chapter 8. Finally, constructive future work will be presented in chapter 9 with the application of a novel secondary ion mass spectrometer for *in-operando* analysis of battery materials with contributions already in progress.

Chapter 2

Theory and Background Understanding

This chapter aims to provide a basic background understanding of battery chemistry and ionic transport in solid oxides. The theory and the terminology of batteries will be discussed, followed by the types of defects in solid systems and ionic conductivity via defects. The theory of diffusion will be explained including Fick's Laws and Crank's analytical solutions to the diffusion equations. Oxygen tracer diffusion is mentioned as it is of importance in this work for determining the role of oxygen vacancies and electrolyte failure for garnets.

2.1 Battery Electrochemistry

As mentioned in Chapter 1, advancements in batteries are pivotal to assist in the transition to more renewable, though intermittent, energy sources. The key factors considered for battery development will be mentioned in this section and provide the basic parameters that are typically quoted when considering cell specifications. The key factors that determine a battery configuration's viability are listed below [63]:

- **Safety** - The biggest factor hindering the large-scale implementation of current Li-ion batteries is their flammable constituent which is the organic solvent based electrolyte. The application of solid inorganic electrolytes may be a solution. However, hazards are still of concern upon application of alkali metals, such as Li and Na, as they have low melting points, which can result in cell leakage in hot conditions.

- **Electrochemical Stability** - A large electrochemical band gap between the highest occupied molecular orbital (HOMO) and the lowest unoccupied molecular orbital (LUMO) of the electrolyte is vital. A wide band gap electrolyte can allow the application of higher voltage cathodes, coupled with Li metal anodes. A passivating layer, typically in the form of a solid electrolyte interphase (SEI), is beneficial if electronically insulating between the electrolyte and electrodes as it can prevent lithium metal built up at the interface and maintain the intercalation process during cycling. SEI can also improve the contact between the solid electrolyte and electrodes or increase the interfacial resistance if poor ionic mobility is a result.

- **Power Density** (units Wg^{-1}) - The power density is the amount of power that can be stored per unit weight and is determined by the battery charge-discharge rate (i.e ionic and electronic conductivity of all the components). The power is the product of voltage and current.

- **Theoretical Capacity** (units $mAhg^{-1}$) - The theoretical capacity ($Q_{theoretical}$) can be calculated by $nF/3600M_W$, where n is the number of electrons associated with the ion, F is the Faraday constant, M_W is the molecular weight of the material and the scaling factor of 3600 converts Coulombs (A s) to the conventional unit of A h. The theoretical capacity is limited mainly by the cathode if a lithium metal anode is used.

- **Gravimetric Energy Density** (units Whg^{-1}) - One of the main specifications of a battery considered in the industry is energy density. This is the amount of energy stored per unit weight and is the product of the voltage and capacity (Q) of the reversible process between the electrodes. The voltage is dependent on the chemical potential of the electrodes.

- **Cycle Life** - The cycle life depends on the amount of full discharge-charge cycles a battery can do before dropping below a threshold capacity (e.g. 80% from the initial capacity).

- **Shelf Life** - The shelf life is the ability of the battery to retain its capacity during rest, it can be affected by the cell architecture, atmosphere, or temperature.

- **Sustainability** - Sustainability is important for the commercialisation of batteries as it includes the environmental impact the battery has, its source materials and the cost of production. Cosiderations are also required on processing black mass from failed batteries.

2.1.1 Fundamentals of Battery Electrochemistry

Voltage

The equilibrium potential (V_0), is the difference between the two electrodes' chemical potentials (μ_e). This is calculated using the Nernst equation (eq. 2.1 for a redox couple where the cathode is on the reduced (Red) side (i.e. gaining the charge carriers) during discharge, and the anode is on the oxidised (Ox) side (i.e. losing the charge carriers), during discharge.

$$V_0 = \frac{\mu_{Ox} - \mu_{Red}}{nF} = \Delta\mu_e + \frac{RT}{nF} \times ln\left(\frac{[Ox]}{[Red]}\right) \tag{2.1}$$

Where μ_{Ox} and μ_{Red} is the chemical potential of the oxidised and reduced side respectively, $\Delta\mu_e$ is the difference in the electrode chemical potentials, R is the gas constant, F is the Faraday constant ($1.60 \times 10^{-19} C$) which is the charge on one mole of electrons and T is the absolute temperature. $[Ox]$ and $[Red]$ are the concentration of active charges for either electrode. A representation of the electrode potentials and the electrolyte window (E_g) is shown in figure 2.1(a).

As shown in figure 2.1(a) the chemical potential of the electrodes is within the HOMO-LUMO of the electrolyte, which is vital to the stability of the cell. An anode potential greater than the electrolyte LUMO and a cathode potential lower than the electrolyte HOMO will facilitate the degradation of the battery. An example of this is shown for common battery electrodes such as Li-carbon anode and Li_xCoO_2 cathode shown in figure 2.1(b) [6]. The difference between the Fermi energy of the electrodes determines the cell potential. The Fermi level is used interchangeably for the chemical potential for electrons as $E_f = \mu = \mu_e - q\phi$, where ϕ is the Galvani potential measured with respect to the electrostatic potential, μ is the electrochemical potential, μ_e is the chemical potential for electrons and q is the charge, this relation, is true at T = 0K [6,64]. The voltage limit of the electrode may be determined by the position of the redox couple

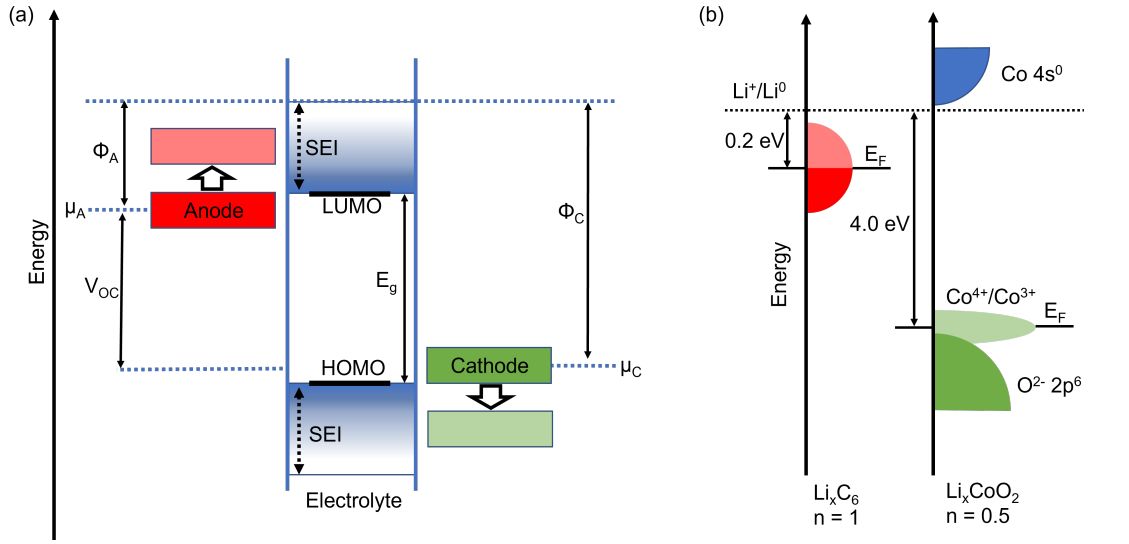


Figure 2.1: Illustration of energy levels (a) the relative energy of electrodes and electrolyte where E_g is the electrolyte window (or band gap) and μ_A and μ_C are the chemical potentials for the anode and cathode respectively. V_{OC} is the voltage of the cell and Φ_A and Φ_C are the work functions of the electrodes. (b) A schematic of a LiC_6 and Li_xCoO_2 system and the relative density of states, where E_f is the Fermi energy and n is the number of electrons transferred per mole of electrode material [6–8].

from either the bottom of the conduction band or the anions p band as can be seen for O 2p level in figure 2.1(b) which limits a higher voltage to be reached by the Co^{4+}/Co^{3+} Fermi energy.

An increase in cell voltage is possible, with suitable solid electrolyte interphase (SEI) formation which can increase the electrolytes band gap, allowing higher voltage cathodes to be employed. The main issue with SEI formation is the requirement for them to be passivating (i.e. does not consume the electrolyte and are electronically insulating). The SEI must have fast cation diffusion, and negligible electron conduction to prevent dendrite formation between the electrodes and electrolyte. Another possibility is the application of solid electrolytes with a larger electrolyte window that is stable with higher voltage electrodes which is a focus for much of battery development [65].

Energy Density

As mentioned previously the gravimmetric energy density is the product of the gravimetric (Q) capacity and the cell potential (V_0) [6]. Therefore this can be increased with larger cell potentials from the application of high voltage electrodes and increased electrode capacity. To increase the capacity it would be a case where more Li^+ ion is transferred per unit of electrode material for example in a Li_xCoO_x cathode 0.5 Li^+ ions are transferred per transition metal, whereas for the anode 1 Li^+ ion is transferred per 6 carbons. In a full cell the energy density decreases with cycle time. The decreasing capacity is due to the electronic current through the external circuit being higher than the current of the Li^+ ion through the electrolyte. The difference in rate prevents the Li^+ ion from intercalating at the electrodes and reaching equilibrium before the reverse process begins. This will result in the build up of 'dead' active material, causing the capacity to fade.

Power Density

The power density is the power supplied per unit weight whereas, the power (W) is the defined as how quickly a battery can discharge its stored energy. The transferred power is affected by the current which is hindered by the internal resistance of the electrode and the electrolyte. Therefore, by decreasing the electrolyte and the electrode-electrolyte interfacial resistance (i.e. increasing the ionic conductivity σ_i), when the external circuit is connected, it will increase the power output.

This is why research into new electrolyte materials is necessary as it benefits the overall advancement for high power batteries. Solid state electrolytes can combat the issue of flammability which is the major flaw of the liquid electrolyte. However, solid electrolytes still suffer from lower Li^+ ion conductivity within the bulk of the material and at electrode-electrolyte interface. Extensive research is being done in lowering the electrolyte and interface resistances either by adding interlayers, applying external pressure, or by altering electrolyte processing conditions [66–68].

2.2 Defect Chemistry and Ionic transport

It is crucial to understand the defect chemistry in solids for lithium batteries, as it can help to understand the conductivity mechanisms and differences in performances. Defect chemistry can also help with the development of new solid electrolytes used in ASSBs. It is typically considered that in lithium solid electrolytes most species are stationary and act as a framework to allow the transport of lithium as it should be the only mobile ion [69]. However, defect studies can show that other species may be mobile or more disorder is present which can result in lithium metal battery failure [32, 70].

2.2.1 Defects in Crystals

The term crystal is used for materials with repeating units with long range order, the opposite is true for amorphous material. As the materials used in this work are crystalline, defects in these systems will be discussed. The third law of thermodynamics states that the "entropy of a perfect crystal is zero at zero kelvin", which implies that as we cannot reach zero kelvin all crystals will have some imperfections. However, it is normally these precise imperfections in crystals that give them functionality resulting in desirable electrical, mechanical, optical, and diffusion characteristics.

Defects are classed by their dimensionality, which includes zero, one, two, and three-dimensional configurations. In zero-dimension defects; vacancies, interstitials, and substitutions are included, and are commonly known as point defects. Line defects (one-dimension) include dislocations within crystals, which are caused by slips in the lattice planes, resulting in holes that are not large enough to be vacancies. Figure 2.2 shows a visual representation of both point defects and a line defect. Two-dimensional defects include grain boundaries which are the interface between two crystals, and three-dimensional defects include pores, cracks, small aggregates of vacancies, or clusters of atoms. Point defects will be discussed further in oxide materials, for further information on higher dimensional defects, refer to [71, 72].

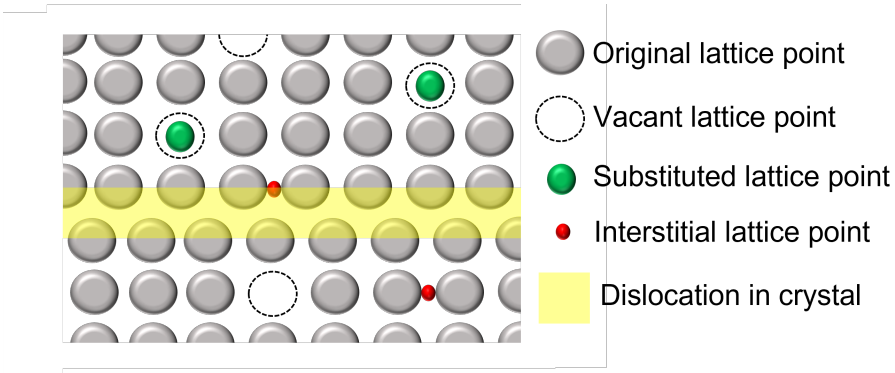


Figure 2.2: Schematic illustrating point (0D) and line (1D) defects in a crystal.

2.2.2 Kröger-Vink Notation

To further understand point defects, a special notation is used in this field, known as the Kröger-Vink (K-V) notation [34, 73]. K-V notation is used to simplify types of point defects, where a general notation such as A_A^x would imply that the original atom or ion (subscript $_A$) is in its own lattice site (A), exhibiting no excess charge (superscript ^{x}). More K-V notations are summarised in table 2.1, where V is for a vacancy, i is for interstitial and F is for foreign atoms or ions. Charges are also represented in the K-V notation using ($^\bullet$) and ($'$) for positive and negative charges respectively, typically in superscript form. To reiterate, superscripts are used to denote the charges present whereas the subscripts are to represent the site being occupied. In solid oxides, two types of point defects can occur including intrinsic and extrinsic both of which are briefly discussed below.

Table 2.1: Kröger-Vink notation for possible point defects [34]

Defect type	Notation
Regular occupied site by original ion or atom	A_A^x, B_B^x
Substitution with other ion or atom from structure	$A_B^x, A_B^\bullet, B_A^x, B_A^{'}$
Substitution with foreign ion or atom	$F_B^x, F_B^\bullet, F_A^x, F_A^{'}$
Vacant lattice sites	$V_A^x, V_A^{'}, V_B^x, V_B^\bullet$
Vacant Interstitial site	V_i^x
Interstitial occupied by other ion or atom from structure	$A_i^x, A_i^\bullet, B_i^x, B_i^{'}$
Interstitial occupied by foreign ion or atom	$F_i^x, F_i^\bullet, F_i^{'}$
Electrons	$e^{'}$
Electron absence (holes)	$h^\bullet$

Intrinsic Defects

Intrinsic defects are those that are always bound to happen as stated by the third law of thermodynamics, that perfect crystal only exists at zero Kelvin and temperatures above this can provide energy to favour entropy in the structure, which can be determined from equation 2.2.

$$\Delta G = \Delta H - T\Delta S \tag{2.2}$$

where, ΔG is the Gibbs free energy, the overall energy change in the system, ΔH is the enthalpy change (heat content) generally defines the change in bond strength and molecular stability and molecular stability, T is the absolute temperature and ΔS is the change in entropy, which is the change in the order of the reaction i.e. disorder is high entropy.

If we take an example of the NaCl structure, there may be some sodium deficient sites which will be denoted as V'_{Na} or chlorine deficient sites ($V^{\bullet}_{Cl}$). However, if there is sufficient charge imbalance the structure can degrade therefore charge compensation is crucial to stabilise the structure. There are three types of point defect pairs to understand the possible charge compensation methods. These include Frenkel, Anti-Frenkel, and Schottky and are shown in table 2.2 for a ZrO_2 fluorite structure where zirconium is Zr^{4+} and oxygen is O^{2-}. A Frenkel defect pair is when a vacant site is balanced with occupancy of an interstitial with the same number of opposite charge generation. Whereas, an Anti-Frenkel defect is a vacancy-interstitial pair caused by the anion in the structure (oxide ion in this example). A Schottky disorder is whereby both the cation and the anion in the structure generate vacancies to charge balance the crystal. The opposite is also possible whereby a pair of cation and anion interstitials are generated, though this is rare and is called an Anti-Schottky pair.

Table 2.2: Possible defect pairs for charge balance

Defect Pair	Notation
Frenkel pair	$\text{null} \rightleftharpoons V_{Zr}^{''''} + Zr_i^{\bullet\bullet\bullet\bullet}$
Anti-Frenkel pair	$\text{null} \rightleftharpoons O_i^{''} + V_O^{\bullet\bullet}$
Schottky pair	$\text{null} \rightleftharpoons V_{Zr}^{''''} + 2V_O^{\bullet\bullet}$
Anti-Schottky pair	$\text{null} \rightleftharpoons Zr_i^{''''} + 2O_i^{\bullet\bullet}$

Extrinsic Defects

Crystals can be engineered by adding more defects to provide functionality to the material. Defects are typically introduced to a crystal structure using non-native species, either as substitution or interstitial defects in order to enhance their performance i.e. doping. The extrinsic defect can also be created by deviating from the crystal normal stoichiometry. This can be shown in the garnet structure with a general formula of $A_3B_2(XO_4)_3$ [74], or for a lithium-containing garnet $Li_3Te_2(LaO_4)_3$ which can be altered by increasing the lithium molar fraction to $Li_7Zr_2(LaO_4)_3$ or more commonly known as $Li_7La_3Zr_2O_{12}$ (LLZO), which was done to increase the ionic conductivity of lithium [75–77]. Different processing conditions can also be used to induce defects for example oxygen partial pressures and temperatures as seen with CeO_2. [78].

Aliovalent substitution is commonly practised in garnet material synthesis for novel electrolyte in batteries. This is done by replacing ions with those of different charges, for example, aluminium (Al^{3+}) which has a greater charge, is (donor) doped into some lithium sites in LLZO. This will result in a net positive charge which is then compensated by lithium vacancies as shown in equation 2.3.

$$Al_2O_3 \xrightarrow{Li_2O} 2Al_{Li}^{\bullet\bullet} + 4V_{Li}^{'} + 3O_O^{x} \tag{2.3}$$

Acceptor-type doping is also possible as shown in $BaTiO_3$ [79] where gallium (Ga^{3+}) is substituted on the Ti^{4+} site. As this substitution results in a net negative

structure. The net negative charge will be compensated by a positively charged defect which can be ionic or electronic in nature and depends on the intrinsic defect of the structure. In this case, the charge compensation may be via oxygen vacancies which leave positive charges.

Dopants are used frequently in LLZO as they have been shown to improve its lithium-ion conductivity, [80–82] more on doping LLZO will be discussed in Chapter 3.

2.3 Ion Transport and Conductivity

The migration of ions and/or electrons can occur through solid oxides when electromotive forces are applied and this is termed conductivity. Electrolytes which are electronic insulators are materials that are developed to solely conduct ions whether they are positively (cations) or negatively (anions) charged. On the other hand, metals are purely electron conductors due to their electron delocalisation (free electron cloud) resulting in a non-existing band gap between the conduction and valence band. Mixed ionic electronic conductors are also possible and used for battery electrodes as they allow electrons to flow through an external circuit and ions to travel between the electrodes (anode and cathode) through the electrolyte. To determine the total conductivity (σ) of a material it is the sum of all the conductive species (2.4), whether it is ionic (σ_i), electrons(σ_e), or holes (σ_h).

$$\sigma = \sum_{species} \sigma_i \sigma_e \sigma_h \tag{2.4}$$

Each partial conductivity is determined using equation 2.5.

$$\sigma_i = n_i q_i \mu_i \tag{2.5}$$

Where q_i is the charge on the species, n_i is the concentration of the charge carrier (derived from the number of charge carriers in a unit cell), and μ_i is the mobility [9]. The

quality of an ionic conductor such as electrolytes can be stated using its transport number (τ_i) which is calculated by $\tau_i = \frac{\sigma_i}{\sigma}$. The transport number is an important parameter for electrolytes to determine what is the dominant contributor to the total conductivity.

The Nernst-Einstein equation (equation 2.6) relates the self-diffusion coefficient with the ionic conductivity under an applied electric field [9, 83]. Where D_i is the self-diffusion coefficient of species i, T is the temperature and k is the Boltzmann constant (1.38 $\times 10^{-23}$ $m^2 kg s^{-2} K^{-1}$). The self-diffusion is the movement of the ions through available nearby vacancies which can move with or without external factors such as temperature or electric fields. The Nernst-Einstein equation is derived by assuming diffusion as a random-hop process, in order to relate diffusional processes to electrical transport.

$$\sigma_i = \frac{n_i q_i^2 D_i}{kT} \tag{2.6}$$

Migration of lithium ions (Li^+) in ionic conductors occurs via the process of ion hopping between different lattice points, which is facilitated by an electric field. An activation barrier exists for Li^+ to travel between lattice sites and can be lowered using thermal energy or applied potential as shown in figure 2.3.

The presence of an external field lowers the activation energy for the ion hop to take place shown with the dotted line in figure 2.3, However, there is a difference in activation energy from the forward and backward migration pathways, whereby the activation energy (E_a) (ΔH_m is lowered by $\frac{1}{2}\alpha qE$ in the forward direction and increased by the same amount in the reverse direction. $\frac{1}{2}\alpha qE$ is the work done by the applied field which moves the charge by half the distance to the next site hence $\alpha/2$.

However, in a real solid, conductivity is more complex as migration of vacancies must be considered similar to that of holes for acceptor-doped silicon semiconductors (i.e. with boron on silicon sites), even if the diffusant is more abundant, To evaluate the activation energy the conductivity at various temperatures are plotted in an Arrhenius

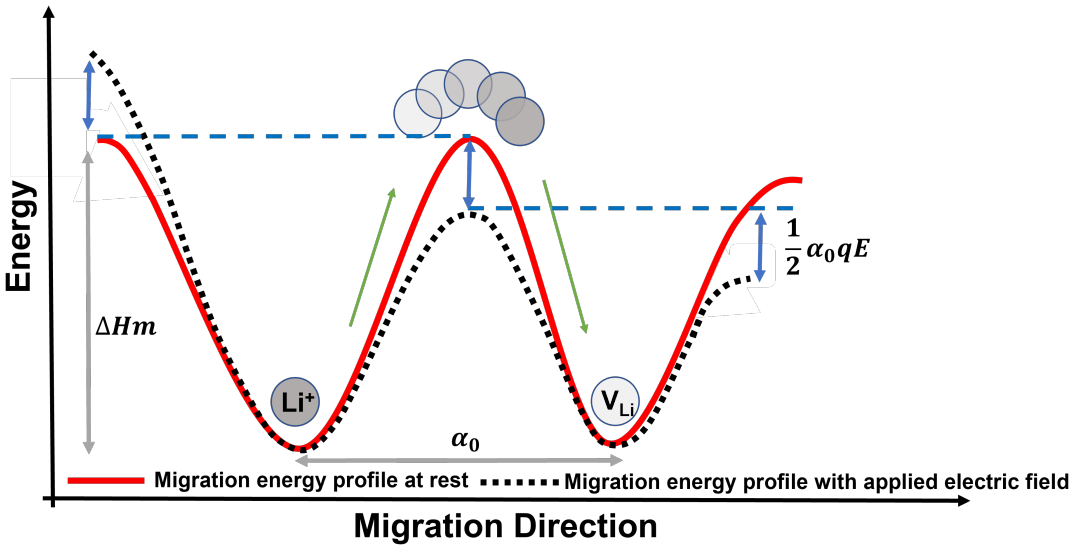


Figure 2.3: Schematic illustrating ion hopping using neighbouring vacant sites. The solid line represents the energy profile in the absence of an external electric field, the dotted line if the energy barrier with the applied electric field and ΔH_m is the activation energy. With an applied field, the energy barrier is lowered in one direction by $\frac{1}{2}\alpha qE$ where α is the separation between the start site and the next vacant site and q is the charge on the mobile ion. [9]

form with $ln(\sigma_i T)$ vs. $1/T$ which will give a gradient of $-E_a/kT$ and simply put for high mobility the activation energy is low. The migration pathway and defects can also be determined with computational efforts using *ab initio* molecular dynamics. which has been applied to LLZO [70, 84, 85].

2.4 Diffusion Fundamentals

In this section, an introduction to diffusion theory will be discussed and how it is applied in this work to determine the ionic transport of oxygen in LLZO. Initially, Fick's Laws [86] will be introduced followed by Crank's solution to the diffusion equation for semi-infinite media [87] which is applied in this work to achieve tracer diffusion coefficients.

2.4.1 Fick's Laws

Adolf Fick first derived the diffusion equations in the 19^{th} century, for quantifying transfer of matter through random motion across a concentration gradient [86]. It states the rate of flow of material i.e. flux (j) is proportional to the difference in concentration with respect to the change in the distance through the medium as shown in equation 2.7, where C is the concentration of the diffusant and x is the distance through the material. The negative sign is due to the decreasing concentration gradient in the material from the source of the diffusing material. D is the diffusion coefficient with units of length^2 per time.

$$j = -D\frac{\partial C}{\partial x} \tag{2.7}$$

As in many real cases, the concentration of the diffusing material and concentration gradient in the medium through which diffusion is occurring changes with time, which the first law did not take into account, therefore a second law was derived. By using equation (2.8) below which states the change in flux at a specific position is proportional to the rate of change (t) at the same position, Fick's second law can be derived.

$$\frac{\partial C}{\partial t} = -\frac{\partial j}{\partial x} \tag{2.8}$$

By substituting j from the first law into equation 2.8, a linear second-order partial differential for concentration or Fick's second law (2.9).

$$\frac{\partial C}{\partial t} = D\frac{\partial^2 C}{\partial x^2} \tag{2.9}$$

The above equation can now be solved analytically with the use of certain boundary conditions as done by John E. Crank [87].

2.4.2 Crank's Solution for Semi-Infinite Media

John Crank developed numerous analytical solutions to Fick's Law [87] which allows the diffusion coefficients to be obtained experimentally using isotopic tracer techniques [88]. The solution discussed here is for a semi-infinite media, which works if the penetration depth of the diffusant is less than the matrix under study. This allows the material to be considered as a semi-infinite solid. The solution also holds true if diffusion is through a homogeneous material with few defects such as grain boundaries and pores [89]. An extensively used method known as isotopic exchange depth profiling (IEDP) is discussed further in Chapter 4, section 4.7. IEDP is applied in the field of oxide ion conductors [88–92] using $^{18}O_2$ as the tracer isotope. IEDP works by annealing the sample in the tracer isotope of known concentration and obtaining the $^{18}O/(^{18}O +^{16} O)$ fraction with respect to the depth from the source using secondary ion mass spectrometry (SIMS) depth profiling. The ^{18}O concentration difference between the sample surface (C_s) and gas (C_g) for a given time is proportional to the flux.

A schematic of a semi-infinite diffusion is shown in figure 3.3 for a gas-solid interface that applies to a set of boundary conditions shown in equations 2.10. 2.11, 2.12.

$$C_{bg} = C(x \geq 0, t = 0) \tag{2.10}$$

$$C_{bg} = C(x = \infty, t > 0) \tag{2.11}$$

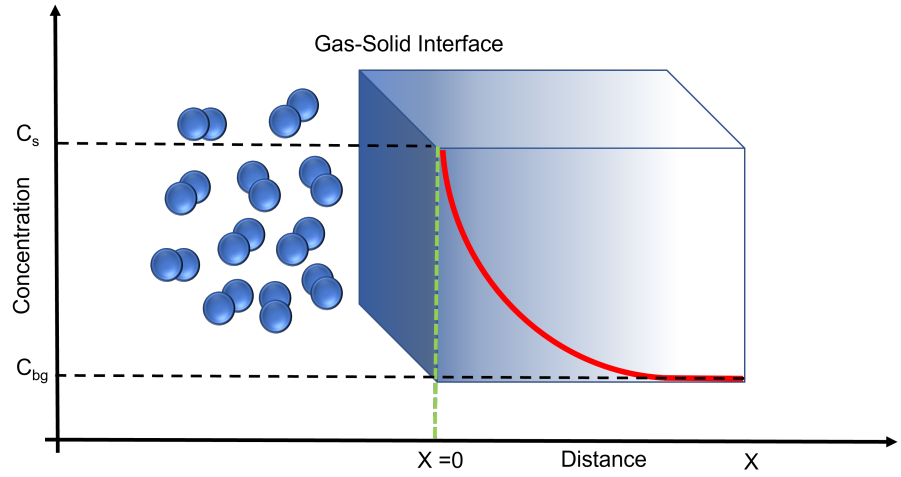


Figure 2.4: Schematic illustrating the gas-solid interface for semi-infinite diffusion with boundary conditions of constant surface (at $x = 0$) concentration (C_s) and constant gas concentration (not shown but it is greater than C_s).

$$-D\left(\frac{\partial C}{\partial t}\right)_{x=0} = k[C_g - C(x=0,t)] \tag{2.12}$$

Where the change between the isotope concentration of the gas and isotope fraction on the sample surface is proportional to the flux of the trace isotope (e.g. ^{18}O). C_{bg} is the background isotopic fraction throughout the sample. k is the proportionality constant, also known as the surface exchange coefficient with units of length per time. k represents the overall surface exchange rate for the trace to cross the gas-solid interface. The isotopic tracer concentration ($C^{'}$) is defined using equation 2.13:

$$C^{'}(x,t) = \frac{C(x,t) - C_{bg}}{C_g - C_{bg}} \tag{2.13}$$

For the gas-solid diffusion system, the semi-infinite solution is given in equation 2.14.

$$C^{'}(x,t) = erfc\left(\frac{x}{2\sqrt{D^{*}t}}\right) - \left[exp\left(\frac{k^{*}x}{D^{*}} + \frac{k^{*2}t}{D^{*}}\right) \times erfc\left(\frac{x}{2\sqrt{D^{*}t}} + k^{'}\sqrt{\frac{t}{D^{*}}}\right)\right] \quad (2.14)$$

Where $erfc$ is defined as the error function given by $\frac{2}{\sqrt{\pi}}\int_{\infty}^{x} e^{-t^2}dt$

The full semi-infinite equation can be simplified down to equation 2.15 by using $x^{'}$ (which is the normalised depth from the exchange surface) and $h^{'}$ (used to describe the influence of the surface exchange and bulk diffusion in an experiment) both are two dimensionless factors shown in equation 2.16 and 2.17 respectively.

$$C^{'}(x^{'},h^{'}) = erfcx^{'} - exp(2x^{'}h^{'} + h^{'2})efrc(x^{'} + h^{'}) \quad (2.15)$$

$$x^{'} = \frac{x}{2\sqrt{D^{*}t}} \quad (2.16)$$

$$h^{'} = k^{*}\sqrt{\frac{t}{D^{*}}} \quad (2.17)$$

The dimensionless factor $x^{'}$ is used to find D from the length x at which the background concentration is reached which is one of the boundary conditions. This is approximated to be $x^{'} \approx 2$ for $x = 4\sqrt{Dt}$ [87].

2.5 Summary

This chapter established the fundamental theoretical framework needed for this study. We first delved into the complexities of battery electrochemistry, exploring the varying components and the ways in which each parameter can affect cell performance. The discussion then transitioned to defects in solid-state materials, particularly in relation to ordered crystal systems. Emphasis was placed on point defects and the methods of their fabrication to achieve specific properties, such as doping. Within this section, we also introduced a rudimentary understanding of ionic conductivity and its operational mechanisms. As a culmination, we presented the basics of diffusion, honing in on Crank's solution to Fick's Law for semi-infinite media, and explaining the methods by which diffusion coefficients can be empirically determined.

Chapter 3

Literature Review

The literature review will serve as the background and update on recent studies done in solid electrolytes, with a focus on garnet-structured lithium ion conductors. This chapter will build upon the theoretical considerations for battery development and the reason for the employment of solid electrolytes, which have already been discussed in Chapters 1 and 2. To begin with, an explanation of why ASSBs and solid electrolytes are being studied, followed by the garnet electrolyte development and timeline. A discussion of the ionic transport through garnets along with the effect of doping and the latest/highest ionic conductivities achieved by different LLZO configurations.

The second half of the literature review will compile the latest research done to understand and mitigate LLZO failure. Dendrites have been at the forefront of garnet failure, with two major hypotheses being put forward. The first is from poor adhesion at the Li|LLZO interface resulting in focused current distribution causing localised stripping and plating of lithium, the second hypothesis is on electronic conductivity resulting in uniform Li ion reduction throughout the electrolyte, and both will be discussed as they play an important role in this work.

3.1 All Solid-State Batteries (ASSBs)

As discussed previously organic liquid electrolytes for lithium-ion batteries (LIBs) need to be replaced to get higher energy density and higher power batteries as they are not compatible with Li metal anodes and high voltage cathodes. It is also predicted that LIBs will also reach their limits based on a 18650 cylindrical cell and to increase performance, cell size will need to be increased [93]. The 18650 cell name represents the dimensions of the cylindrical cell with an 18 mm diameter and 65 mm length, the 0 represents the cylinder. Therefore, all solid-state batteries (ASSBs) using solid electrolytes (SE) are required for high energy and power-dense batteries that are compatible with miniature device designs and bipolar cell stacking architecture [93, 94]. For SEs to be viable in batteries key attributes need to be present, which include:

- **Conductivity** - High total ionic conductivity ($>10^{-3}$ S cm^{-1}) with negligible to no

electronic conductivity ($< 10^{-9}$ Scm^{-1}) and a transference number of 1. Whereas liquid electrolytes (LE) that have a high ionic conductivity up to 10^{-2} S cm^{-1} they have a transfer number for Li-ions less than 0.5. Hence a lower conductivity is sufficient in SE if the transfer number for Li-ions is 1 [95, 96].

- **Wide electrolyte window** (E_g) - As mentioned previously a wide E_g is one the most important properties for a SE as it will indirectly improve the energy and power density by allowing the application of lithium metal and high voltage cathodes.

- **Electro and Chemical Stability** - LEs have been known to form SEI that lowers the E_g making it difficult to use Li metal anodes as it may further degrade the electrolyte from redox reactions. Therefore, SEs with good electrochemical stability with Li metal and cathodes are essential. The chemical stability is crucial to ensure the electrolyte does not degrade easily when exposed to certain environments such as water or air.

- **Mechanical properties** - Mechanical properties including hardness, density and flexibility are desirable. Dense and hard SE can be used to prevent dendrite propagation, which is currently achieved by a separator in LIBs, whereas flexibility is useful for device incorporation.

- **Safety** - LEs used in current LIBs are primarily composed of organic solvents which are highly flammable. Therefore SEs are required to be non-flammable (high thermal stability), low toxicity and environmentally benign.

- **Processability** - From a commercial perspective, manufacturing SEs with relative ease is essential via low-cost manufacturing, energy-inexpensive production, and using low temperatures and abundant material.

- **Sustainability** - Material sourcing with low environmental impact and recyclability of materials is important, though not yet on the mainstream agenda for battery innovations.

Currently, in the battery research community, there has been much development in possible SE contenders for use in ASSBs. These solid electrolytes have been put into groups based on their composition which include; Oxide-based, Sulfide-based, Halide-based, Nitrides and Polymers. However, only a few are practical solutions to alternative electrolytes, based on compiling the above requirements. The next section will discuss the advantages and disadvantages of SEs being researched, before moving on to the top performers, followed by an in-depth discussion on lithium stuffed garnets.

3.1.1 Solid Electrolytes

The highest performing solid electrolytes with respect to ionic conductivity are the sulfides ($Li_{10}GeP_2S_{12}$) with 10^{-2} S cm^{-1} [97] which is as high as liquid electrolytes ionic conductivity. Sulfides also provide good mechanical flexibility and low grain boundary resistance. However, sulfide-based SE are notorious for being unstable with Li-metal and in the ambient atmosphere resulting in degradation and release of H_2S due to its hygroscopic behaviour [10, 94]. Polymer electrolytes have excellent flexibility, and stability with lithium metal and are suitable for large-scale production at low cost, but are limited by a low E_g (<4 V), poor thermal stability and typically used in conjunction with flammable organic solvents. Electrolytes with lower ionic conductivity ranging from 10^{-6} S cm^{-1} are the nitrides which include the thin film LiPON SE known to be stable with both lithium metal and cathode materials but are expensive for large-scale fabrication, thus better suited for miniature devices. A new type of SE receiving more interest is the halides, due to their low grain boundary resistance, mechanical strength, and increasing lithium-ion conductivities up to 10^{-3} S cm^{-1} [98, 99]. However, similar to the sulfides they exhibit poor stability with lithium metal due to the low electrolyte window. Halides also have high sensitivity to moisture.

Oxides are the largest group as they consist of Perovskites, NASICON- and LISICON-type electrolytes as well the most promising SEs the garnet-based electrolytes. Oxides have high ionic conductivities ranging from 10^{-5}-10^{-3} S cm^{-1} but only the garnet

structured SEs have good stability with Li metal anodes due to its large E_g [10]. To summarise the various properties of the common SE groups, figure 3.1 represents the different properties in a radar plot, with a generalised overview for oxides as not all present good chemical/oxidation stability, which is discussed below [10].

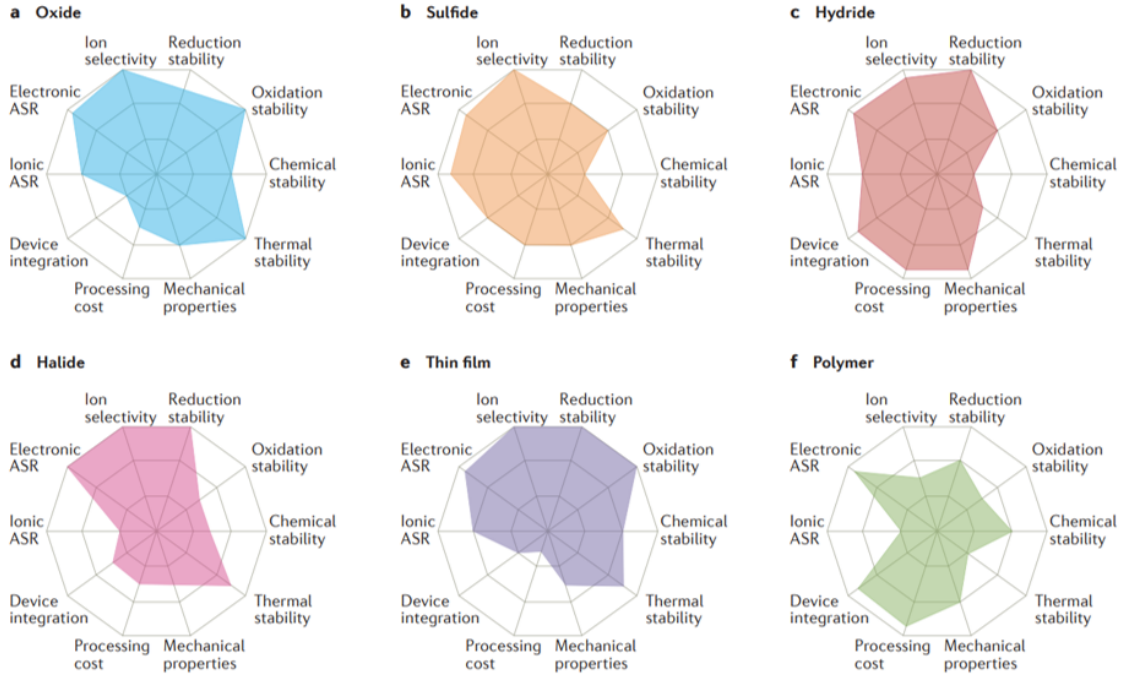


Figure 3.1: Radar plots representing the various properties sought after from solid electrolytes (a) Oxides comprising mainly of garnets, perovskites, NASICON and LISICON, (b) Sulfides comprising of thio-LISICONs, Argyrodite and LGPS-like, (c) hydrides which are primarily Li-Halide salts, (d) Halides, (e) Thin Films (LiPON) and (f) polymers (PEO), where ASR = area specific resistance or interfacial resistance. Further information on specific compositions is found in [10]. Reprinted with permission from [10].

3.1.2 Oxides

Oxide solid electrolytes can be subdivided into three groups with the highest ionic conductivities, including the NASICON-like, Perovskites, and Garnets. LISICON (general formula $Li_{2+2x}Zn_{1-x}GeO_4$ [100]) will not be discussed owing to its poor ionic conductivities ranging from 10^{-8}-10^{-5} S cm^{-1} at room temperature [101,102]; if the reader interested in LISICON electrolytes is directed to the review by Liang *et al.* [103]. Perovskite SE will be discussed first as they present the lowest ionic conductivity of the top three oxides with regards to ionic conductivity, followed by NASICON-type with the intermediate range of

ionic conductivity, and the last will be Garnet structured SEs with a dedicated section.

Perovskite Solid Electrolyte

Perovskites is a name given to a crystal family with a general formula ABX_3, with the first perovskite structure discovered being of a $CaTiO_2$ mineral. It was not until Goldschmidt made the first synthetic perovskite of $BaTiO_3$ that they were considered as functional materials [104], and $BaTiO_3$ is used in high-temperature ferroelectric capacitors. Perovskite structures have found their place in fields such as piezoelectrics, catalysis, photovoltaics etc. The first lithium-ion conducting perovskite was discovered by Inaguma *et al.* for a $Li_{0.34}La_{0.51}TiO_{2.94}$ composition [105]. Figure 3.2a shows the crystal structure of a perovskite with lithium-ion conduction properties. The structure comprises a BX_6 (TiO_6) corner-sharing octahedra framework, with the dodecahedra A sites occupied by Li, La or vacancies. The general formula for lithium lanthanum titanates (LLTO) is $Li_{3x}La_{(2/3)-x}TiO_3$ ($1/25 < x < 1/6$). LLTO has achieved high bulk conductivity of 1.4 x10^{-3} S/cm at 300K by Inaguma *et al.* [106], but grain boundary conductivity has remained low between 10^{-4} to 10^{-5} S/cm, thus increasing the overall resistance [107]. The conduction pathway through the lattice is shown in figure 3.2a where Li ions move via A-site vacancies through the oxygen frame from the corner-sharing octahedra.

The conductivity was improved by Sr doping at the A site which produced σ_{Total} of 1.95 mS/cm [11]. Sr^{2+} substitution assists the migration of Li because of its larger ionic radius in comparison to La^{3+} which enlarges the lattice size, facilitating low energy barriers for the Li to transport and with charge composition from doping, an increase in Li composition is possible.

However, the biggest downfall of LLTO perovskites is the reduction of Ti^{4+} to Ti^{3+} when paired with Li metal. The reduction causes the electrolytes' electronic resistance to drop which hinders the application of LLTO in ASSBs with lithium metal anodes [108].

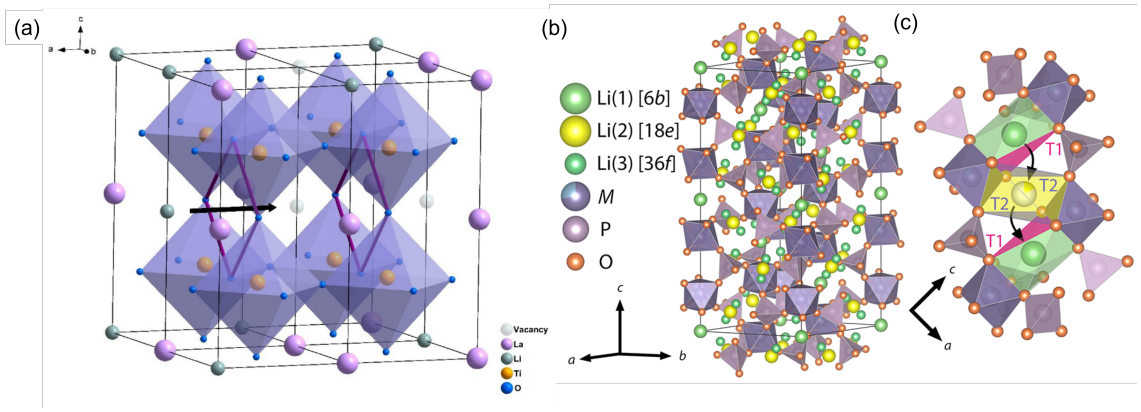


Figure 3.2: Crystal structures of (a) perovskite ABX_3 where A = Li,La,or vacancy, B = Ti, and X = O. Image obtained with permission from [11](b) NASICON-like $LiM_2(PO_4)_3$ where M = Ti or Ge. (c) Conduction pathway in NASICON-like solid electrolytes where T1 and T2 are triangular oxygen bottlenecks. ((b) and (c) extracted with permission from [12].

NASICON-Like Solid Electrolyte

NASICON is an acronym for Sodium (Na) Super Ionic CONductors, but this also represents a general formula on which lithium conducting SEs can be based, $LiM_2(XO_4)_3$, hence "NASICON-like" solid electrolytes. In the general formula $LiM_2(XO_4)_3$, M can be Ti, Ge, Sc, Zr or Hf and X is normally P or Si, the doping is used to increase the Li content [107]. NASICON has a rhombohedral lattice with a space group $R\bar{3}c$ as depicted in figure 3.2b [12].

The structure consists of XO_4 tetrahedra at *18e* sites (Wyckoff notation), which are corner shared with MO_6 octahedra which form the scaffold for lithium to migrate. The Li ions occupy anti-prismatic *6b*, *18e*, and *36f* sites which face share with the octahedra as shown in figure 3.2c [12]. The highest ionic conductivity for the parent structure of $LiTi_2(PO_4)_3$ (LTP) and $LiGe_2(PO_4)_3$ (LGP) were $\sim 10^{-6}$ S/cm. The low conductivity was due to the full occupancy of the Li *6b* sites with the *18e* sites remaining vacant, which had high migration energy barriers. A solution was presented to improve the performance by partial substitution on the M site with Al giving stoichiometries of $Li_{1.3}Al_{0.3}Ti_{1.7}(PO_4)_3$ (LATP) and $Li_{1.5}Al_{0.5}Ge_{1.5}(PO_4)_3$ (LAGP) which yielded significant improvements on the total conductivity as high as 2.7 10^{-3} S/cm and activation energy of 0.31 eV [12,107,109].

The enhanced conduction is due to both 6b and 18e sites being occupied and with Al^{3+} substitution resulting in 36f sites being occupied by Li. With the increasing occupancy of these sites by Li, repulsion occurs between the Li1 and Li3 locations, the repulsion is what pushes the Li1 into an intermediatory Li3* site between Li1 and Li3 which pushes the Li3 into Li3* site [110].

NASICON-like Li-ion conductors are also the few SEs that have both high conductivity and stability in the ambient atmosphere. However, the main drawback comes from the severe degradation of the electrolyte when in contact with lithium metal. As with LLTO, the Ti in LATP and Ge in LAGP are reduced when coupled with lithium metal anodes making them electronically conducting and forming a reactive SEI which consumes the electrolyte [107, 111, 112].

Both perovskites and NASICON-like solid electrolytes for Li metal ASSBs have good σ_i but poor stability with Li metal. There have been concerted efforts for research into garnet SEs. Garnets have shown both good conductivity and stability with Li metal which is discussed in more detail in the section below.

3.2 Lithium-Rich Garnets

Garnets are the most promising contenders as solid electrolytes in ASSBs owing to their high total ionic conductivities of $\sim$ 1 mS/cm, chemical and electrochemical stability with Li metal, wide E_g, high density and mechanical hardness [113–116]. It was the work done by Murugan *et al.* that led to the synthesis of $Li_7La_3Zr_2O_{12}$ (LLZO) in 2007 [77] and nicknamed the "lithium stuffed garnet". Since then multiple efforts have been made to improve the garnet's performance, with intensive research on ion migration in the lattice, defect chemistry studies, the effect of doping on the conductivity, and the electrolyte-electrolyte interface to tackle the ongoing issue of cell failure by short-circuiting dendrites.

This review on LLZO garnets is split into two main sections, the first section will discuss the garnet's structure, Li^+ ion transport mechanism and conductivity, and doping

strategies. The second section will bring to light the recent work done to understand dendrite formation in LLZO when cycled with lithium metal and the main hypothesis being put forward.

3.2.1 Structure

The general formula for garnet is $A_3B_2(XO_4)_3$ where A is coordinated to 8 oxygens (dodecahedra), B is coordinated to 6 oxygens (octahedra), and X is coordinated to 4 oxygen (tetrahedra). Garnets with this formula naturally form a cubic lattice structure with $Ia\bar{3}d$ space group [117]. A lithium-containing garnet was first synthesised by O'Callaghan *et al* in 2006 with the formula $Li_3Ln_3Te_2O_{12}$ (Ln = Y, Pr, Nd, Sm-Lu) [118]. The ionic conductivity of $Li_3Ln_3Te_2O_{12}$ was poor due to all the Li being tightly held in the tetrahedral sites as shown in figure 3.3a.

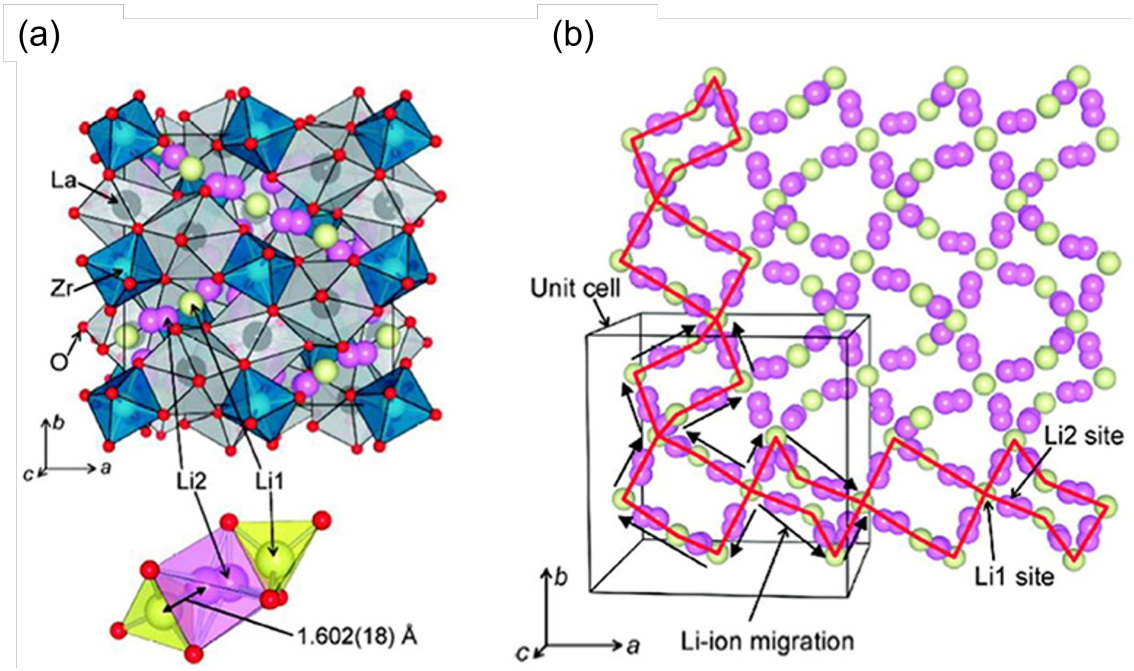


Figure 3.3: Crystal structures of (a) LLZO garnet with inset showing the location of Li ions as Li1 in the tetrahedron and Li2 in the twisted octahedron. (b) the Li-ion pathway in the garnet structure with the yellow dots as Li1 sites and purple dots as the Li2 sites and off-centre octahedral sites used for migration. Image taken with permission from [13, 14].

By further increasing the lithium content in the garnet Murugan *et al.* synthesised the lithium stuffed garnet $Li_7La_3Zr_2O_{12}$ with the highest ionic conductivity of

$3 \times 10^{-4} S/cm$ with activation energy (E_a) of 0.3 eV [77]. The crystal structure of LLZO is illustrated in figure 3.3a. The structure is that of LLZO where the LaO_8 dodecahedron and ZrO_6 octahedron from the framework through which lithium migrates as shown in figure 3.3b. However, LLZO undergoes a phase transition from cubic (c-LLZO) to tetragonal (t-LLZO) at room temperature. The phase change occurs as the occupied sites by Li are different at lower temperatures. In t-LLZO the lithium resides in all the available sites, which include the 8a tetrahedral (Li1), 16f octahedral (Li2) and 32g eccentric octahedral (Li3) sites leaving very few vacant sites for migration [119]. Whereas, the c-LLZO lithium sites occupied are the 24d Li1 and off-centre 96h octahedral sites, and the octahedral 48g sites are absent which allows more space for Li^+ to move, resulting in increased conductivity [113, 119]. Extensive research has been done to understand the mechanism behind the high ionic conductivity in garnets which is discussed below.

3.2.2 Ionic Transport

Techniques such as X-ray and neutron diffraction, NMR spectroscopy and computational simulations have been used to investigate the ion transport mechanism in garnets as it is essential to further the advancement of these electrolytes [17, 81, 120, 121]. In 2010 work by Cussen on cubic garnet (space group $Ia\bar{3}d$) using neutron diffraction showed that lithium was on three sites as shown in figure 3.4a. The three sites with partial occupation included the tetrahedral 24d site, 48g and 96h octahedral and off-centre octahedral sites respectively with not all occupied at once [122]. It was found that the initial garnet with 3Li per formula unit (p.f.u.) had all the Li in tightly held 24d sites giving the poor σ_i. On the other hand increasing the Li content from 5 to 7 moles would lead to a significant increase in the conductivity [117] as seen in figure 3.4b. The improvement in σ_i is due to more octahedral 96h/48g sites being filled and 24d sites becoming vacant, and with the optimal concentration of 6.4 Li p.f.u obtained before the structure collapse into t-LLZO phase [123, 124].

Xu *et al* used *ab initio* molecular dynamics to understand the reason behind

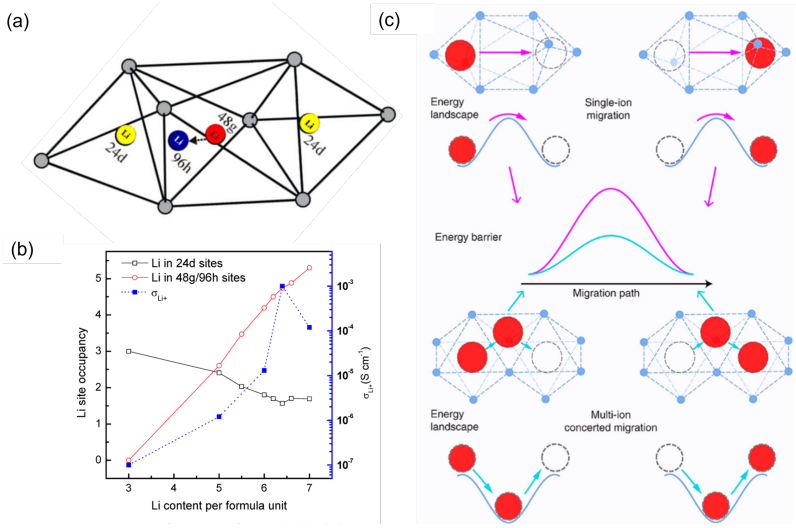


Figure 3.4: (a) Li sites in garnet, showing face-shared octahedral with tetrahedrals, (b) role of lithium concentration on-site occupation and conductivity, (c) schematic representation of two proposed migration routes of lithium either a single-ion migration (high energy) or the concerted multi-ion migration (low energy). All images were obtained with permission from [15].

the difference in conductivity in c-LLZO and t-LLZO. Two migration mechanisms were modelled for LLZO as shown in figure 3.4c [17]. The first model uses a single ion migration method by which the 24d site Li moves to the octahedral through the triangular face shared border. The second model used a concerted multi-ion migration, whereby the Li3 in the octahedron moves via the tetrahedra without residing there and pushing the following Li3 site forwards. The second method produced the lowest energy barrier and is preferred in cubic phase LLZO, whereas, the former is preferred in the t-LLZO. To confirm this finding, Jalem *et al* used molecular dynamics simulations and showed that the concerted migration mechanisms are the cause of superionic conductivity in c-LLZO garnets [125].

Recent practical efforts are being made to improve the σ_i by doping and have proven success over undoped LLZO, the methods for doping are explained in the following section.

3.2.3 Doping Strategies

Nominal un-doped LLZO with a high-temperature cubic structure has attractive properties such as wide E_g, and high mechanical hardness $\sim$ 6.3 GPa [126]. However, elemental substitution has been experimented on LLZO and shown to be beneficial as it can further decrease the garnet impedance and manage to stabilise the cubic lattice structure of LLZO at room temperature. Elemental doping can be done on Li, La or Zr sites as well as co-doping on two sites. Figure 3.5 shows the elements that can be used as dopants on each site; the results in the figure are from a computational study by Miara *et al.* [16]. Examples of doing this on each site will be discussed in the following sub-sections and with some examples summarised in table 3.1. It is worth noting that the predictions for the doping site are not absolute, as Ge doping on Li sites as possible as reported by Brugge *et al.* [127].

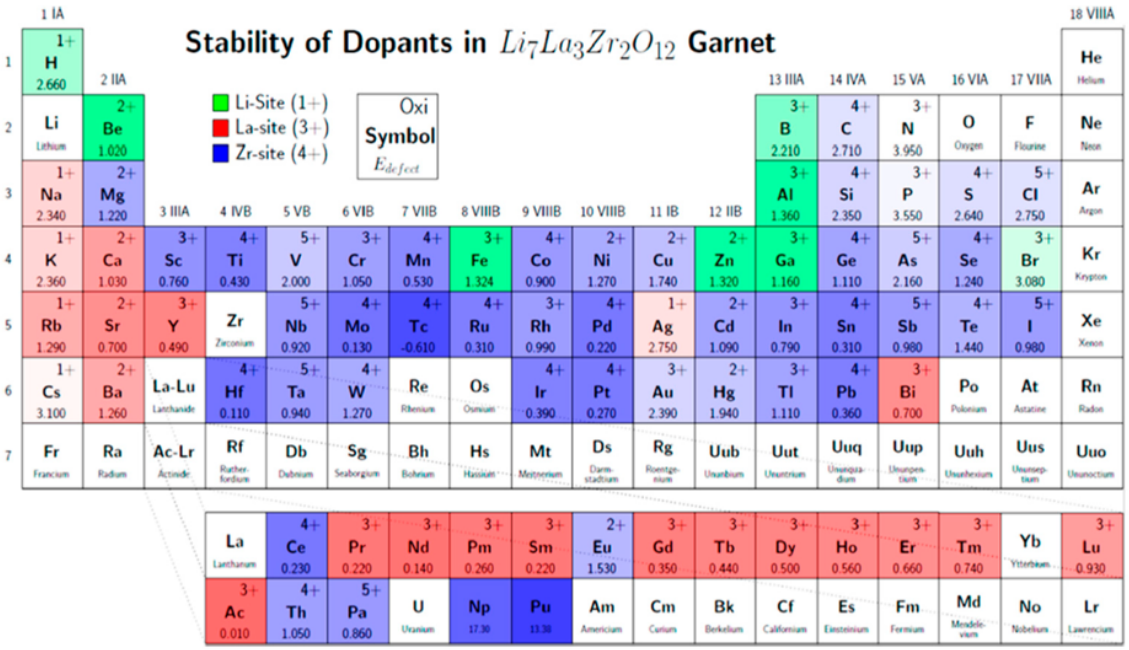


Figure 3.5: Periodic table with the site and oxidation states of dopants studied using density functional theory (DFT) to determine the defect energies for each dopant. The colours represent sight preference (Li = green, La = red, and Zr = blue). The least faint colours have the lowest defect energy, as seen from the comparison B^{3+} and Ga^{3+} for the lithium site, which means Ga doping is favourable. Figure reprinted with permission from [16, 17].

Li site doping

Substitution at the Li sites is one of the most commonly used sites, as it has been able to give some of the highest conductivities above 1 mS/cm. The elements used in practical work include Al, Ga, and Fe which give the most promising results. The general formula when doping at the Li site with e.g. Al is $Al_xLi_{7-3x}La_3Zr_2O_{12}$. Al doping was found to partially occupy the 24d and 48g sites determined by solid-state NMR, and neutron diffraction [128–130]. Al doping has been shown to stabilise the cubic phase at room temperature, as discovered by Rangasamy *et al.* [131]. Al is also thought to improve the density of c-LLZO through liquid phase sintering with alumina crucibles [19]. However, this makes it difficult to control the Al concentration in LLZO and causes Al segregation at the grain boundaries [132].

Some of the highest achieved conductivity comes from Ga-doping of 0.25 and 0.15 moles p.f.u to gain a σ_{total} of 1.46 mS/cm and 1.3 mS/cm respectively [133, 134] and activation energy (E_a) of 0.25 and 0.3eV respectively which is a significant improvement over undoped c-LLZO. Gallium doping also stabilised the cubic phase, but with a different space group ($I\bar{4}3d$) as deduced by Wagner [135]. The change in space group is due to Ga favouring the occupation of the larger and distorted 12a tetrahedral sites because Ga is larger than Al [135, 136]. The different site occupation by Ga was used to explain the increase the conductivity as it does not lead to long-range blocking in the lithium pathway, by occupying the 24d site as in the case for Al doping [135]. Doping induces more Li vacancies when higher valence ions are used, as in the case of LLZO not all the Li ions can participate in the conductivity with an estimation of $\sim 12.3\%$ of the total lithium ions contributing because of the small amount of vacant site [137]. The role of dopants on the defects generated on each site is summarised in table 3.1.

Zr and La site doping

Octahedral Zr^{4+} sites have been doped with Ta, Nb, Te, Gd, W, Ca etc. This site for doping has been shown to be the second most promising site after the Li site. The highest

conductivity of doping on the Zr site was achieved by Ta and Te at 0.6 and 0.25 moles p.f.u respectively to give σ_{total} of ∼1 mS/cm [124, 138]. Zr plays a crucial role in the garnet framework, therefore doping on this site may have an impact on the lattice size which can influence the conductivity by decreasing the bottleneck between Li-ion jumps. Doping on the Zr (16a) sites can improve the conductivity as the substitution is not on the lithium pathway, therefore, no blocked sites. Similar principles are observed when doping on La (24c) sites with elements such as Ce or Y. Cerium can also be doped on Zr sites as reported by Dong *et al.* [139]). However, lower conductivities are observed when La is partially doped as shown in table 3.2.

Table 3.1: Summary of doping on various LLZO sites and defects generated

Doping site	Defect equation
Li site	$Al_2O_3 \rightleftharpoons 2\mathrm{Al}_{Li}^{\bullet\bullet} + 4\mathrm{V}_{Li}^{'} + 3\mathrm{O}_O^X$
Zr site	$Ta_2O_5 \rightleftharpoons 2\mathrm{Ta}_{Zr}^{\bullet} + 2\mathrm{V}_{Zr}^{\bullet} + 4V_{Li}^{'} + 5\mathrm{O}_O^X$
La site	$CeO_2 \rightleftharpoons \mathrm{Ce}_{La}^{\bullet} + V_{La}^{\bullet} + 2\mathrm{V}_{Li}^{'} + 2\mathrm{O}_O^X$

Co-doping

A combination of doping on Li, Zr, and La sites have been explored [140–143]. However, co-doping does not obtain a synergistic advantage, compared to individual doping.

3.2.4 Surface Degradation

Despite the advantageous properties of garnets, the stability of LLZO in ambient conditions has been a subject of ongoing research, with surface degradation due to moisture and carbon dioxide exposure recognized as significant challenges [121,144,145]. In ambient conditions, LLZO's surface reacts with water vapour to form lithium hydroxide (LiOH) via lithium-proton exchange. Likewise, exposure to carbon dioxide (e.g. in the air) results in the formation of lithium carbonate (Li_2CO_3), which can increase the interfacial resistivity between the garnet and lithium metal [68]. Several techniques have been employed to investigate the composition and effect of the corrosion layer on the interfacial resistance

including, EIS, SIMS, XRD, XPS, and NMR [68, 145–149].

The corrosion layer has also been linked to poor interfacial adhesion between the garnet and lithium metal, which in turn can cause poor cyclability and dendrite propagation, discussed further in the section below.

Table 3.2: Examples of doping on various sites in LLZO, doping resulting in the highest ionic conductivity are shown.

Doping site	Composition	σ_{total} (mS/cm)	E_a (eV)	Temperature (°C)	Refs.
Un-doped	t-LLZO	2x10^{-3}	0.49	25	[77]
	c-LLZO	0.77	0.30	25	[128]
Li site	$Ga_{0.25}Li_{6.25}La_3Zr_2O_{12}$	1.46	0.25	25	[133]
	$Al_{0.24}Li_{6.28}La_3Zr_2O_{12}$	0.44	0.37	30	[150]
	$Ga_{0.20}Li_{6.4}La_3Zr_2O_{12}$	1.00	0.30	-	[151]
	$Fe_{0.25}Li_{6.25}La_3Zr_2O_{12}$	1.38	0.28	-	[136]
	$Fe_{0.20}Li_{6.4}La_3Zr_2O_{12}$	1.10	-	RT	[152]
Zr site	$Li_{6.4}La_3Zr_{1.4}Ta_{0.6}O_{12}$	1.00	0.35	25	[124]
	$Li_{6.7}La_3Zr_{1.7}Ta_{0.3}O_{12}$	0.69	0.36	RT	[153]
	$Li_{6.7}La_3Zr_{1.5}Ta_{0.5}O_{12}$	0.90	0.43	-	[154]
	$Li_{6.75}La_3Zr_{1.75}Nb_{0.25}O_{12}$	0.80	0.31	25	[155]
	$Li_{6.75}La_3Zr_{1.5}Te_{0.25}O_{12}$	1.02	0.41	30	[138]
	$Li_{6.3}La_3Zr_{1.75}W_{0.35}O_{12}$	0.66	0.43	25	[156]
	$Li_{7.1}La_3Zr_{1.95}Ca_{0.05}O_{12}$	0.52	0.27	27	[157]
La site	$Li_7La_{2.75}Y_{0.25}Zr_2O_{12}$	0.32	0.31	30	[158]
	$Li_{6.6}La_{2.6}Ce_{0.4}Zr_2O_{12}$	0.14	0.48	-	[159]
Co-doping	$Li_{6.6}La_{2.75}Y_{0.25}Zr_{1.6}Ta_{0.4}O_{12}$	0.47	0.34	27	[140]
	$Li_{6.29}Al_{0.07}La_3Zr_{1.75}Te_{0.25}O_{12}$	0.40	0.33	RT	[141]
	$Li_{6.65}Ga_{0.15}La_3Zr_{1.9}Sc_{0.1}O_{12}$	1.80	0.29	27	[142]
	$Li_{5.9}Al_{0.2}La_3Zr_{1.75}W_{0.25}O_{12}$	0.49	0.35	RT	[143]

3.3 Dendrites in LLZO

Garnet electrolytes have been paired up with Li metal and have shown both high ionic conductivity and interface stability with no SEI layer formation yet discovered [160]. However, upon cycling lithium through the un-doped LLZO, even at low current densities ($10\mu A/cm^2$) failure of the SE is observed, reported by Kotobuki [161]. LLZO fails from the short circuit by dendrites, which connect both electrodes through the electrolyte. Dendrites were thought to not be an issue as LLZO exhibits a wide electrochemical stability window which allows it to be stable against lithium metal and has a significantly greater hardness/yield strength ($\sim$6 GPa) [26] over that of Li metal (0.655 GPa) which was thought to prevent dendrites infiltrating LLZO as it would act as a physical barrier proposed by Monroe and Newman model for polymer electrolytes [162]. However, this has been clearly opposed by recent findings of facile dendrite nucleation and growth through LLZO.

Dendrites are metallic lithium growths inside or through an electrolyte, in LIBs with liquid electrolytes they tend to take two general forms (i) long finger/needle-like projections which grow by building on from the tip and (ii) mossy lithium metal growth which propagate from the base [163, 164]. On the other hand dendrite formation in solid electrolytes, specifically LLZO ceramics is unclear. Work by Porz *et al.* [165] on the study of dendrite propagation showed that Li metal fills defects such as pores before inducing stress which builds up at the tip and forms micro-cracks in the SE through which more lithium plates into, this model was shown to be the case experimentally using *in operando* techniques [25, 166, 167]. However, this does not explain exactly what causes dendrites to nucleate. Aguesse *et al.* [18] has proposed several hypotheses for the cause of dendrites as illustrated in figure 3.6. The potential mechanisms put forward were either; dendrites can be from localised charge carrier distribution on the surface, plating of lithium at cracks and pores leading to lithium metal building up, or residual electronic conductivity in the electrolyte reducing Li^+ or trapped electron from oxygen framework.

The formation of dendrites is LLZO may be separated into two groups, either (i)

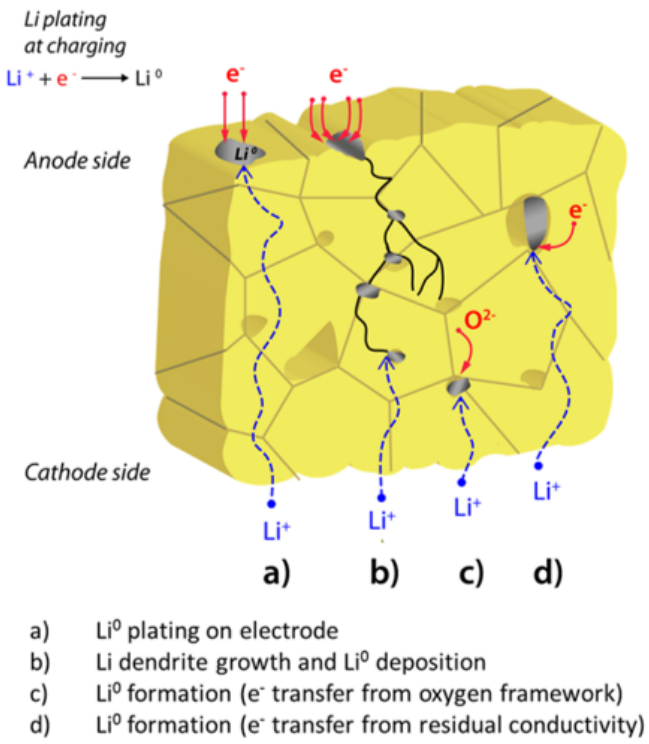


Figure 3.6: Proposed mechanisms for dendrite formation and propagation in LLZO. Image obtained with permission from Aguesse *et al.* [18].

poor Li|LLZO interface adhesion and (ii) electronic defects and local chemistry variation. Recent work on preventing and improving the contact between LLZO and Li metal will be discussed first, which is then followed by research efforts into understanding the local chemistry in LLZO and electronic properties, which has gained popularity in recent years as the culprit behind lithium-ion reduction in LLZO.

3.3.1 Interface with Lithium Metal

The Li|LLZO interface has been studied extensively with different surface modifications and novel inter-layers to improve the wetting and to drop the interface resistance (R_{int}), which is presumed to be the bottleneck for LLZO incorporation in ASSBs and the cause for dendrite formation [168]. To drop the R_{int} a vast amount of methods have been used including; heat, pressure, microstructure, chemical modification, interlayers and composites, some of which are discussed below.

A simple method to improve the wettability of LLZO to Li metal was to polish the surface of LLZO to remove corrosion layers such as carbonates and hydroxides which form on exposure to ambient atmospheres [145, 168]. Sharafi *et al.* followed up on these results by doing a quantitative analysis using contact angle measurements. They carried out a systematic approach by dry polishing, wet polishing and wet polishing with heating to 500°C, with each step improving the wettability of lithium metal on LLZO and achieving the lowest R_{int} of 2 Ω/cm^2 at 500°C, the high temperatures were used to work with molten Li. The low interfacial resistance was said to have been from the removal and combustion of surface contaminants.

External pressure to improve homogeneous Li|LLZO contact was done by Krauskopf *et al.* [67], showing that negligible R_{int} is possible by applying external pressure without the need for any interlayers or chemical modifications. A pressure of 400 MPa was required to reach such low resistive levels. However, this is not possible for commercial integration. The principal put forward was, that with enough pressure lithium void formation would be limited at the interface during cycling. Therefore, uniform stripping/platting of lithium and no localised current flow, as lithium ions would come from the surface of the metal, rather than the bulk.

Grain microstructure on R_{int} was studied by Cheng *et al.* [169]. The results showed that LLZO with smaller grain sizes ranging from 10-40 μm produced lower interfacial resistance and cycled to greater current densities over LLZO with grain sizes from 100-200 μm. In the same work, X-ray Laue micro-diffraction was used to probe the grain orientation and grain boundary misorientation between adjacent grains. The improvement in lowered R_{int} was said to be from more grain boundaries at the surface of LLZO with small grains, as no significant differences were observed via the X-ray technique. A different type of microstructure adaptation was made by Fu *et al.* using a bilayer structure [170]. In this work, Fu *et al.* established a 3D porous interlayer of LLZO prepared on a dense LLZO support, which was able to cycle up to a current density of 1 mA/cm^2 for 230 hours. The high performance of this 3D scaffold was said to be from the high surface

area for lithium to plate onto, the R_{int} was not provided most likely due to the difficulty in determining the contact surface area by Li metal. A similar approach by Zhang *et al.* [171] also showed cyclability up to 0.5 mA/cm^2 with over 160 cycles at an areal capacity of 0.25 mAh/cm^2. Sastre *et al.* [172] devised a 70 nm amorphous LLZO (aLLZO) via magnetron sputtering to form the interlayer and block lithium dendrite growth. The aLLZO allowed for Li|aLLZOcoatedLLZO|Li to be cycled up to 3.2 mA/cm^2 before signs of dendrites were apparent. The interfacial resistance achieved was down to 3.5 Ω/cm^2 which is similar to results observed when an Al_2O_3 layer was used by Han *et al.* [173] with cycling up to 0.2 mA/cm^2 and an extrapolated interfacial resistance of 1 Ωcm^2 at RT on a Ca and Nb co-doped LLZO. An amorphous Si interlayer also showed cyclability to 0.2 mA/cm^2 however, a greater R_{int} was observed at 127Ω cm^2. Tsai *et al.* [174] used an Au inter-layer to alloy with lithium metal upon cycling and provide uniform current distribution and lower interface resistance. R_{int} reduced from >1000 Ω cm^2 to ∼380 Ω cm^2 with stable cycling at 0.25 mA/cm^2 at 50 °C for 140 h. However, Au may be useful to alloy with Li metal and allow uniform current distribution but it is not electronically blocking.

Organic polymer layers have been reported, with polyethelene oxide (PEO) being the standard polymer to experiment with. Spencer *et al.* [175] studied the use of PEO:LiTFSI(salt) on Ta-doped LLZO. They observed that the interfacial resistance increased between the polymer and LLZO. They applied XPS and ToF-SIMS to study the chemistry of the interface but no signs of degradation were obvious. It was then suggested that the interfacial resistance may have been from the corrosion layers from sample preparation or during heat treatment in certain atmospheres. This study can also be compared with the work done by Otto *et al.* [160] who used ToF-SIMS to investigate if potential SEI layers formed between Li metal and LLZO. Otto conducted In-situ ToF-SIMS by applying an electrical potential on the LLZO surface using a flood gun in the SIMS chamber to plate lithium which was already placed on the bottom side of the LLZO. Depth profiling from the plated Li side into the LLZO had a sharp contrast in the secondary ions, hence

indicating no SEI formation. On the other hand, in a situation where a possible SEI is formed a SIMS depth profile may show more elemental mixing with depth and a more gradual change in SI counts in the depth profile upon sputtering.

In the recent work by the scientific community, exotic interlayers and composites have been explored to improve LLZO's surface adhesion to Li metal. However, this is out of the scope of this work and readers interested are directed to these reviews [15, 82].

As discussed, much work has been done on preventing dendrite formation at the surface. However, new evidence has come to light suggesting that dendrite nucleation is occurring uniformly throughout LLZO, and not only concentrated at the electrode/electrolyte interface, which was initially proposed. Possible reasons and findings behind this phenomenon are mentioned in the following section.

3.3.2 Electronic conductivity in LLZO

In 2018 Shen *et al.* [176] used X-ray computed tomography (XCT) to visually inspect the role of porosity on dendrite formation in Al-LLZO, with the major outcome being that sintering from 1050 to 1150 °C leads to less connected pores, but dendrites still persisted upon cycling. But what was more interesting was that the size of the supposed pores increased during cycling with the increase being uniformly throughout the material. Even with the disclaimer that Li metal is indistinguishable from void space, it was apparent that the microstructure was altered drastically after cycling. To confirm this finding of uniform dendrite formation work by Han *et al.* [177] using neutron depth profiling (NDP) showed uniform lithium metal formation to a depth of 12 μm in LLZO with further suggestions made by Yue *et al.* that the uniform lithium metal inside LLZO is due to electronic conductivity [178] stating that an electronic conductivity (σ_e) in LLZO as high as $\sim 10^{-8}$-10^{-7} S/cm is sufficient enough for uniform Li^+ reduction to metal in the solid electrolyte, σ_e of similar proportions are also reported by other groups [179, 180]. Interestingly work by Phillip *et al.* [151] showed approximately two orders of magnitude lower σ_e of 10^{-10} S/cm on a single crystal of Ga-LLZO, whereas the higher values have been reported on

polycrystalline LLZO.

Computational Efforts

Mathematical modelling has been done to predict the possible reasons for electronic conductivity or electronic defects. One of the first contributions made to this theory was in 2018 by Tian *et al.* [181]. DFT was used to model LLZO electron density and showed that excess electrons could be trapped on surfaces and defects such as pores. It was found that the excess electrons were primarily located on surface La^{3+} ions in c-LLZO, and it is thermodynamically favourable for these electrons to reduce Li^{+} to Li metal. On the other hand, t-LLZO showed a uniform distribution of excess electrons over the surface with no preferential atomic sites. A year later Tian showed that the increased electron density on the surface of c-LLZO would lead to smaller band gap energies, with a band gap of $\sim$5 eV for the bulk and a noticeable decrease to $\sim$2 eV for the surface [182]. In this work the excess electrons were added to demonstrate where the electrons would reside, the finding suggests a good correlation with the observation of uniform dendrite formation as possible excess electrons in the real system may be in internal pores.

Following on from this work, in 2020 Squires *et al.* [70] used hybrid DFT calculation to understand the most likely point defect to occur in LLZO. Equilibrium defect concentrations were calculated for different atmospheric processing conditions. A wide range of defects was investigated including Li and O vacancies, and interstitial and cation anti-site defects. It was found that in all conditions except for reducing atmosphere, lithium vacancy concentration dominates which corresponds to much earlier findings by Santosh *et al.* [183], with anti-site cation defects as second most likely. In oxygen-poor atmospheres, oxygen vacancies are prominent with the lowest defect formation energy. Oxygen vacancies were also said to behave as colour centres. After the work by Han *et al.* [177] on neutron depth profiling (NDP), suggesting electronic conductivity is the cause for dendrites in LLZO, Squires *et al.* [184] in 2021 published their results on simulating electronic conductivity in LLZO, using first principle methods to calculate intrinsic electronic conductivity in LLZO again from different processing conditions and typical battery

operating conditions. Squires showed that with negligible electronic charge carrier concentration (i.e. electronics and holes) and low electron mobility 0.2 cm^2 V^{-1} s^{-1} an electronic conductivity of 10^{-10} - 10^{-12} S/cm for LLZO is expected. This estimation matches well with the finding by Philip *et al.* on single crystal LLZO [151].

More computational work was done by Kuganathan *et al.* [84], who investigated the different types of point defects in t-LLZO and which were the most favourable defects to form. Kuganathan showed that the most favourable disorder is from Li and O vacancy (Schottky defect pair) with an enthalpy of formation of 0.87 eV. Considerations on whether these vacancies would result in oxygen self-diffusion in the structure were studied. The E_a for oxygen migration via vacancies was calculated to be 1.65 eV which is much greater than that for Li diffusion at 0.45 eV.

Computational models for understanding the defects in LLZO have been of interest, and have overall stated that there may be negligible electronic conductivity in LLZO. However, most of these studies are done on bulk LLZO and do not take into consideration of grain boundary chemistry and doping. Simulating these variables is computationally expensive and requires larger supercells to be programmed, to take into account the increasing disorder from doping and grain orientation for grain boundary studies.

Experimental Findings

Measuring the electronic conductivity of LLZO and other solid-state electrolytes (SSE) is now a common protocol along with ionic conductivity. One of the first publications to show interest in electronic conductivity was by Wolfenstine *et al.* in 2012 [185]. An σ_e of $\sim$7.1x10^{-8} S/cm for $Ga_{0.25}$-LLZO was reported but no further interest was shown as it was regarded as having no effect on the performance of Ga-LLZO. Similar values of σ_e (2.53x10^{-8} S/cm) were obtained for Ca and Nb co-doped LLZO by Song *et al.* [180]. Song proposed that the high electronic conductivity was from the grain boundary, and could lead to the recombination of Li ions with electrons under high voltage polarisation, from high current densities on the grain boundary. A possible solution to this was to

increase the ionic conductivity of the grain boundary and improve the interface contact, which will drive the voltage polarisation down. Doping and thin coatings on SSE particles were also suggested to increase the electron transfer barrier at the grain boundaries. The presence of free electrons was detected by Wolfenstine *et al.* in 2013 [186] in c-LLZO when the sample was exposed to a highly reducing environment. Molten lithium was used as the reducing atmosphere and LLZO pellets were submerged inside. After recovering the SE pellet a chemical colouration was observed from a white pellet to a dark colour. It was stated that the colour change was from the colour centre formation (from trapped electrons in oxygen vacancies). Electron paramagnetic resonance (EPR) spectroscopy was done to show unpaired electrons in the pellets from before and after treatment. The sample before produced no EPR signal, whereas the pellet after treatment showed a strong signal, indicating unpaired electrons. A g-factor of 1.9997 for the EPR signal was stated and said to be from free unpaired electrons; this value is exceptionally close to that of a free electron in a vacuum or lithium metal which has a paramagnetic electron in the 2s orbital [187,188].

A practical approach to understanding the point defect concentrations in LLZO with varying temperature and oxygen partial pressure (pO_2) was done by Zhan *et al.* (2018) [189]. Cubic undoped LLZO was used in this work which exhibited a lower electronic conductivity of 10^{-11} S/cm at 294 K. The activation energy for electron transfer was measured at pO_2 = 0.09 bar from 20-727 °C with lower temperatures showing an E_a = 0.33 eV and at higher temperature E_a = 0.66 eV. Based on certain charge neutrality conditions, the defect concentrations depending on pO_2 were calculated. Under a reducing atmosphere, both lithium and oxygen vacancies dominated and electron defects were high. On the other hand in oxidising conditions, the growing defect is electron holes. Cheng *et al.* [190] studied the impact of sintering under Ar and Air on Al-LLZO, and obtained σ_e of 2.1x10^{-9} S/cm and 1.0x10^{-10} S/cm respectively, indicating the increase is due to oxygen vacancy formation under Ar atmosphere sintering. Kubicek *et al.* [32], indirectly probed the presence of oxygen vacancies on single crystalline Ta-LLZO, and polycrystalline Ta-, Al-, and Ga-doped LLZO. Oxygen-18 isotopic exchange was done on all samples followed

by ToF-SIMS depth profiling to extract oxygen diffusion profiles which were said to be only possible from vacancies, as oxygen interstitials are unlikely in densely packed garnet lattice structures. Tracer diffusion coefficients (D^*) of 10^{-14} to 10^{-12} cm^2 s^{-1} was reported. High overall D^* reported was said to be an indication of significant oxygen vacancies.

Tsai *et al.* [174] proposed that grain boundaries are to blame for dendrite formation in the garnets. Tsai used Ta-LLZO sintered in an alumina crucible which is known to contaminate LLZO with from the lithia-alumina eutectic formation at high-temperature sintering [19]. It was stated that aluminium-rich grain boundaries are unstable with lithium metal as they may form lithium aluminates. An aluminium contamination-free Ta-LLZO approach was also done, with LLZO densified using hot pressing. However, dendrites in grain boundaries were also observed using TEM and EELS. Liu *et al.* [191] revealed that Li-ions could indeed combine with electrons in the grain boundaries of LLZO and nucleate dendrites. EELS was done on several grain boundaries and showed that band gaps of some boundaries were as low as 1.0 eV and as high as 5.8 eV which is typically observed for the bulk. These low band gaps of some grain boundaries could be the cause of uniform lithium metal nucleation along the garnet solid electrolyte. The samples were prepared using hot pressing it was stated that conductive carbon which may infiltrate the LLZO from the graphite sample holder may be the reason for low band gaps. On the other hand, Al-doped LLZO was used in this work and so elemental segregation to the grain boundaries may also be a factor to consider as reported by Brugge *et al.* [149].

The difficulty in understanding grain boundaries is apparent, with very little to no techniques yet available that can analyse the chemistry and electrochemical properties simultaneously with a high lateral resolution for imaging. Therefore it is crucial for *in operando* techniques to be developed that can measure these factors under typical battery operating conditions.

3.4 Summary and Objectives

As discussed, extensive research to prevent dendrites formation in garnets is currently being done. Two proposed reasons for dendrites formation in LLZO have been put forward which include inhomogeneous contact between lithium metal and LLZO causing localised Li ion current flow, and the second sufficiently high electronic conductivity and local chemistry disparity at grain boundaries. The first is being tackled from many directions including; heating LLZO to remove contamination, microstructure engineering, applying external pressure, and developing interlayers for better wetting between the metallic anode and electrolyte. The role of electronic conductivity and grain boundaries in LLZO on dendrite nucleation is still unsolved with research in this area now beginning to pick up traction and reporting σ_e for SSE becoming a norm. Recent findings have shown that uniform dendrites in the garnets are observed and it is linked to electronic conductivity, whereas some research groups suggest that grain boundary chemistry is responsible for the reduction of Li ions to metal and short-circuiting of the cell.

The objective of this work is to investigate and understand the role of the atmosphere and crucible on the performance of LLZO. Both Ga- and Ta-doped LLZO are used; this is because each dopant substitutes in different lattice sites of the electrolytes and may play a role in dendrite formation. The following chapter will explain the experimental techniques used in this work and the working principles of the instruments. The results and discussion chapters follow, with the first presenting the experimental findings at a macro-scale for Ga-LLZO using techniques such as SEM, XRD, EIS, EPR, ICP-OES etc. This is followed with the same but for Ta-LLZO. The seventh chapter looks at the surface chemistry of both Ga-LLZO and Ta-LLZO using XPS, ToF-SIMS and LEIS which are also processed under different atmospheres and crucibles. The final results and discussion chapter is on oxygen diffusion in LLZO and possible links to dendrites from oxygen vacancies in grain boundaries. Concluding remarks and a summary will follow with a section on constructive future work.

Chapter 4

Experimental and Instrumentation

The experimental chapter will describe the methods used to prepare the samples including heat treatments and battery assembly. Sample preparation for characterisation using instruments such as X-ray diffraction (XRD), Scanning Electron Microscopy (SEM) and Secondary Ion Mass Spectroscopy (SIMS) etc. and their respective data analysis methods will also be explained in this chapter.

4.1 Sample Processing Methods

The following sections will discuss the basic preparation methods for the samples, including heat treatments, polishing, relative density measurements etc. The doped LLZO were purchased as pure cubic phase powders from Toshima Japan [192]. Any other material will be stated otherwise. Prior to purchasing LLZO from Toshima gallium doped LLZO (Ga-LLZO) was synthesised using a citric acid and nitrate-based sol-gel route developed by Bernuy-Lopez *et al.* [134] which is a modified Pechini-type method [193]. However, this was no longer used as it was difficult to achieve impurity and secondary phase-free products 100% of the time and is a common issue in many other research groups when discussed during conferences. Therefore purchasing LLZO became a more reliable and time-saving method for the work done with LLZO. Before using LLZO supplied by Toshima, the powder is first analysed by XRD and is discussed in section 4.2.

4.1.1 Thermal Treatments

Once all tantalum (Ta-) or gallium (Ga-) doped LLZO was received from the supplier [192] they were immediately stored in an argon-filled glovebox with O_2 and H_2O concentrations <0.6 ppm as consistently as possible. In order to produce dense pellets of LLZO, approximately 0.5g of powder is placed in a 10mm die and pressed using a uniaxial press inside the glovebox. The powder is pressed under 1.5-2 tonnes for 1 minute to form compact green body pellets. The green body is then placed in a crucible either an alumina, magnesia or zirconia crucible depending on what is being studied. The pellet inside the crucible is embedded in the 'mother' powder, this is the powder before pressing in order to prevent

the pellet from melting onto the crucible at high sintering temperatures and to minimise lithium loss which is thought to occur due to high temperatures. The pellets are then sintered at 1150 °C for Ga-LLZO or 1250°C for Ta-LLZO. Two sintering atmospheres were studied; argon as the oxygen-poor (reducing) atmosphere and oxygen as the oxidising atmosphere. The furnace with the argon atmosphere is built into the glovebox so the samples do not leave the glovebox. Oxygen atmosphere sintering is done in a tube furnace outside the glove box as shown in figure 4.1(right). The tube furnace has steel flanges connected to a diaphragm pump on one end and a high-purity dry oxygen (99.9999 % 0.5 ppm H_2O) cylinder supplied by BOC on the other end, to prevent moisture from entering the atmosphere during densification.

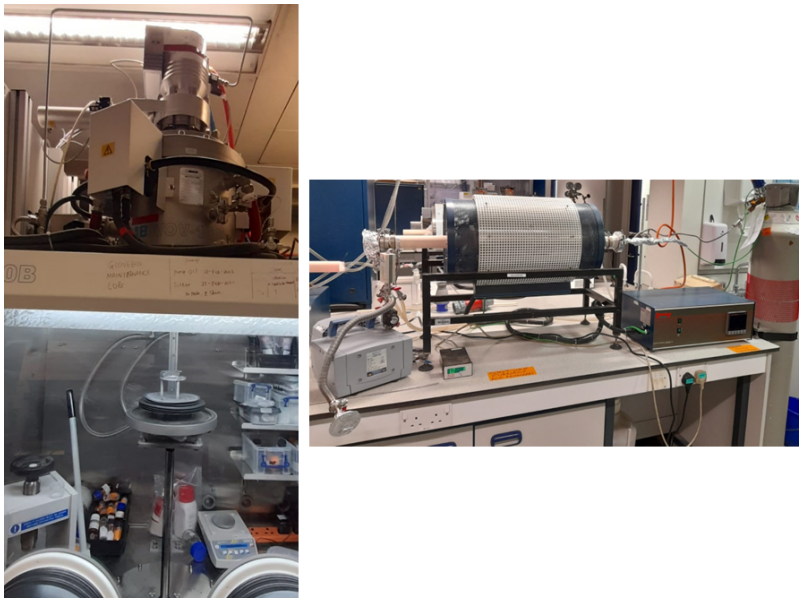


Figure 4.1: [Left] furnace inside glovebox for heat treatments under argon atmosphere. [Right] Tube furnace with a dry vacuum pump and high-purity oxygen cylinder.

For sintering in the glovebox furnace the argon pressure is kept at 5 mbar whereas, for the oxygen tube furnace, the oxygen is left to flow at 1 bar. 1150 and 1250 °C were used for Ga-doped and Ta-doped LLZO respectively with heating and cooling ramps of 5°C/min, and the dwell time was set to 6 hours. To minimise samples sintered in the tube furnace outside of the glove box coming in contact with moisture in the ambient atmosphere at the end of the sintering heat treatment, the samples were removed at

temperatures between 250-300 °C and taken straight into the glovebox antechamber and left to cool down to room temperature under argon.

Temperatures above 1100°C were applied to facilitate grain growth and pellet densification during the sintering treatment. The high temperature was also the case for the discovery of Al^{3+} insertion into the garnet network by Murgan *et al.* [77], when an alumina crucible was used. It was also shown by Murugan *et al.* that Al^{3+} resulted in the superior ionic conductivity of LLZO as it stabilised to room temperature cubic phase LLZO, made feasible due to the liquid phase sintering which forms a liquid eutectic at 1055°C of $Li_2O - Al_2O_3$ indicated by the phase diagram in figure 4.2 [19, 194].

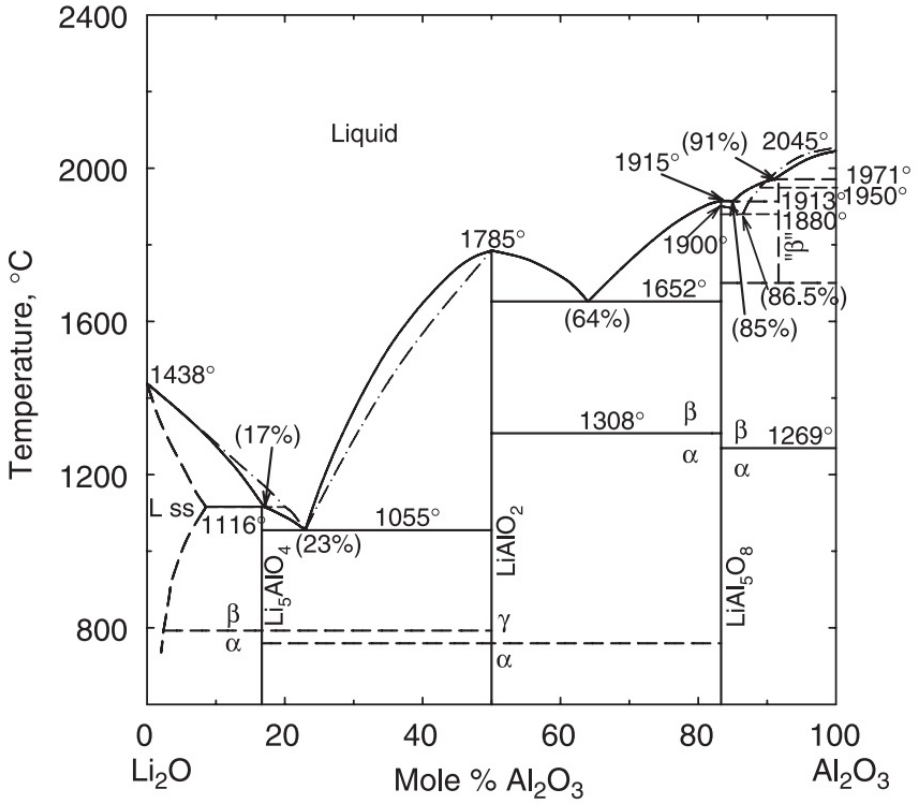


Figure 4.2: Lithia-Alumina phase diagram showing the liquid phase of lithia-alumina eutectic at 23% Al_2O_3 concentration at 1055°C. Modified Cook and Plante phase diagram of lithia-alumina taken with permission from Kulkarni *et al.* [19]

Once the LLZO pellet densification treatment is done, the pellet is ground to remove the excess powder on which the green pellet was placed. The grinding and polishing steps are discussed in section 4.1.2. After polishing the pellet goes through a thermal

grooving step.

The thermal grooving step occurs at 900° for 30 minutes with a heating and cooling rate of 10°C/min, while the sample is between platinum foil. This step will remove surface contaminants and reveal the surface grain boundaries for image analysis studies using SEM and SIMS. The thermal grooving procedure removes the amorphized damage done by the grinding and polishing by allowing the recrystallization of the grains which reveals the grain boundaries and causes a relief effect [195, 196]

4.1.2 Grinding and Polishing

In this section grinding and polishing steps will be discussed to finish the LLZO pellet samples. In the context of this work grinding will be used for the coarse finishing of the pellet surface and polishing will be used to define the fine polishing of the pellet surface.

Once the pellet has been removed from the furnace after the densification treatment it is brought outside of the glovebox and hand-ground on SiC paper with generous amounts of isopropanol to prevent excessive moisture exposure and to wash off the SiC particles from the grinding paper. To remove the hardened mother powder on the pellet, coarse paper is used which includes, and in the same order; 800, 1200, 2000, 2500, 4000-grit SiC grinding paper from Struers [197]. After the 4000 grit paper is used the pellet is viewed under an optical microscope to check for any remaining scratches caused by the previous grade SiC papers.

Pellet surfaces were ground down to 1200-grit paper for LLZO samples used for electrochemical measurements, whereas samples for micro-structure measurements were taken to 4000-grit paper equivalent to 5 μm roughness.

Samples to be analysed by ToF-SIMS require smoother surfaces, and in this case, diamond suspensions and polishing pads were used. Water-free diamond suspensions in isopropanol from Struers with particle sizes 3, 1 and 0.25 μm were used with separate polishing pads also by Struers. LLZO pellets were mounted onto a sample holder for an

automatic polishing machine (TegraSystem Remote by Struers). Crystal bond from Agar Scientific was used to mount samples onto the holder. Crystal bond is a clear organic polymer that hardens at room temperature. Samples were polished using MD-Dac, MD-Nap and MD-Chem pads from Struers with the 3, 1, and 0.25μm diamond suspensions respectively. Each polishing step was done for 10 minutes at 2Gpa of force and washed with n-Hexane sonication between each step change in diamond suspension size. A final check of the samples is done to ensure no major scratches remain on the pellet surface. Samples are sonicated with acetone to remove the crystal bond and finally sonicated with n-Hexane and left in the glovebox antechamber for 10 minutes under vacuum to dry, before further treatment.

4.1.3 Density Determination

The relative density as a percentage was determined using the Archimedes method in deionised water. Ethanol could not be used as it would evaporate causing the displayed balance to fluctuate. Therefore, the samples used were sacrificed as they will react with the water. Once the weight of the dry pellets and submerged pellets were recorded, the density was calculated using equation 4.1, where, $w(a)$ and $w(fl)$ are the mass measured in air and in the fluid respectively, $\rho(fl)$ is the density of the fluid used which depends on the temperature, and $rho(a)$ is the density of air. The theoretical density (ρ_{theory}) is calculated using equation 4.2. Where n is the formula units per unit cell which is 8 for LLZO, M_W is the molecular mass, V is the unit cell volume determined from X-ray diffraction measurements discussed in the structure refinement section 4.2.3, and N_A is Avogadro's number (6.02x10^{23} mol^{-1}).

$$\rho_{exp} = \rho(air) + \frac{w(a)\rho(fl)}{\rho(fl) \times (w(a) - w(fl)} \tag{4.1}$$

$$\rho_{theory} = \frac{nM_w}{N_A V} \tag{4.2}$$

The relative density ($\rho_{relative}$) as a percentage is derived using equation 4.3.

$$\rho_{relative}(\%) = \frac{\rho_{exp}}{\rho_{theory}} \times 100 \tag{4.3}$$

4.1.4 Vickers Hardness

Vickers Hardness tests were done on the doped LLZO samples. All the samples were stuck onto a sample polishing holder with crystal bond and ground down to 5 μm roughness using the 4000 grit SiC paper with isopropanol, in order to ensure that samples stay level when tested. The Wilson VH1102 Micro Hardness Tester was used to determine the hardness of the solid electrolytes, before indentation was carried out, the samples were placed in focus under the optical microscope. A load of either 50 g or 100 g was applied, with the lesser load used if 100 g resulted in a distorted indentation or cracks. The area of the indentation is then calculated and the Vickers Harness (HV) value is obtained using the equation below (equation 4.4). HV is converted to GPa (1 HV = 0.009807 GPa) for ease of comparison and understanding.

$$VickersHardness(HV) = \frac{TestLoad}{AreaofIndentation} \tag{4.4}$$

4.2 X-ray Diffraction

This section will cover the theory behind X-ray diffraction (XRD), sample preparation and the instrument settings used for diffraction analysis. The section following will cover the data analysis and the methods used for structure refinements.

4.2.1 X-ray Diffraction Theory

X-ray diffraction (XRD) is a non-destructive technique which is a relatively quick and easy measurement to conduct. XRD can provide information on the crystal structure, unit cell parameters, phase identification, and purity of materials. When incident X-rays are directed toward a sample whether crystalline (ordered) or amorphous (disordered) two processes can occur, either absorption or reflectance (scattering) of the radiation, the latter is what is used in XRD. XRD data are commonly displayed as the intensity of the scattered X-rays against the scattering angle (2θ). As X-rays have wave-particle duality properties they can reflect constructively to give a signal or destructively to cancel each other out. Bragg's Law shown in equation 4.5 is used to help understand the signals from constructive interference.

$$2dsin\theta = n\lambda \tag{4.5}$$

Where d is the inter-planar spacing indexed by hkl which are known as the Miller indices, λ is the wavelength of the incident X-rays, n is an integer number for reflected beams in phase, and θ is the angle of reflectance or incidence of the X-ray beam with the crystal planes. The schematic representation of Bragg's Law is shown in figure 4.3 [198].

The X-ray diffractometer's detector collects the scattered X-rays at each angle specified by the user and outputs a 2D diffraction pattern, which is then used to identify the purity and compounds present in the sample.

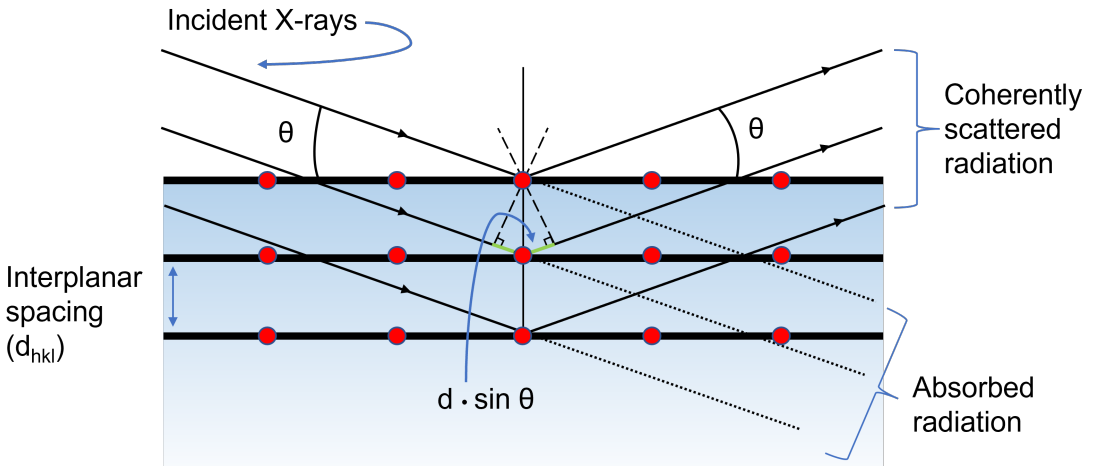


Figure 4.3: Schematic representation of Bragg's Law in a Bragg-Brentano geometry.

4.2.2 X-ray Diffraction Measurements

X-ray diffraction characterisation was done on both doped LLZO-purchased powder and heat-treated pellet samples and are indicated in their respective diffraction patterns. Powder samples and polycrystalline pellets were analysed using the MPD PANanalytical by X'Pert. All samples were measured from 10 to 60 2θ degrees with a step size of 0.016 2θ degrees and 70 seconds per step (scan time approximately 40 minutes). Measurements were done using a $Cu - K_\alpha$ source ($\lambda = 0.154$nm) at 40 keV. Powder samples are measured without rotating the sample, while polycrystalline pellets are rotated to allow x-ray beam interaction with multiple crystal orientations to generate an averaged diffraction pattern. Data are viewed on the HighScore Plus software and exported for analysis using OriginPro. Diffraction patterns are compared using reference patterns obtained from the ICSD [135, 199, 200].

4.2.3 Le Bail Refinement

The Le Bail refinement is a method developed to extract accurate unit cell parameters and peak intensities from powder diffraction data without determining the full structural model. In essence, the method iteratively adjusts a hypothetical structure's cell parameters to best match the observed diffraction pattern. By decomposing the observed diffraction pattern into individual Bragg peak profiles and then refining the peak positions, intensities,

and widths, the Le Bail method can generate a diffraction pattern that closely matches the experimental one. One of its significant advantages is that it can handle datasets where the crystal structure is not fully known or is too complex for direct methods. However, it's important to note that while the Le Bail refinement provides accurate unit cell parameters and peak intensities, it does not yield atomic positions within the unit cell

Refinement methods were used to determine the density which is then used to calculate the relative density; both the space group and unit cell volume were also obtained to understand how the sample preparation methods affect the crystal structure and lattice parameters. Le Bail method [201] was used to calculate the above-mentioned parameters which were done on GSAS-II software [202, 203]. The Le Bail method uses both experimental data and a reference XRD pattern of cubic LLZO to calculate a structural model. The input standard used for modelling provides the space groups and approximate cell parameters of the phases which are expected to be found in the sample. The program refines these cell parameters and the peak shapes to match the experimental data. The intensity is then matched between the standard and the experimental with iterative fitting and adjustment of parameters to achieve the best fit. The fit of the data was assessed visually and with the value from the goodness of fit parameter (χ) which provides an indication of the fit between the calculated model and experimental data with an output of a residual plot.

To conduct the Le Bail refinement using GSASII, both experimental and reference XRD patterns are requisite, in conjunction with specific instrument parameters. The x-ray source utilized is Cu K-alpha, with the Bragg-Brentano diffractometer setup. Prior to the refinement process, a background is delineated on the XRD pattern, where a minimum of nine points is set to achieve optimal fitting; it was observed that the inclusion of more than nine background points does not notably enhance the fitting accuracy. The refinement involves iterative steps where critical parameters like unit cell dimensions, phase fraction, peak shifts, and coefficients for Gaussian and Lorentzian functions are progressively adjusted. Typically, a maximum of ten refinement cycles are engaged prior

to extracting the output. To enhance the fit precision, sample displacement correction can be invoked. Throughout the refinement process, the Chi-squared value serves as an indicator of fit quality, complemented by visual inspection of the matched data. The final outcome is subsequently illustrated using OriginPro, which showcases the experimental and reference XRD pattern, the exact peak position markers, and a residual plot capturing the quality of the fit.

4.3 Microstructure Analysis

In this experimental section, all techniques used to analyse the microstructure will be explained. The application of optical microscopy to scanning electron microscopy will be outlined. Firstly optical microscope-based techniques will be discussed which includes the optical microscope-based white light interferometer by ZYGO. Electron microscopy methods will be discussed for both imaging and focused ion beam (FIB) milling.

4.3.1 Optical microscopy-based measurements

Reflective optical microscopy was used as an initial characterisation method for surface features on sintered and polished samples. The Nikon Eclipse LV150 brightfield microscope with digital capabilities [204] was used to take images of pellet samples after sintering to observe grain size. Pellets which undergo polishing steps are viewed under the optical microscope to estimate what polishing step is to be applied if any surface scratches remain or when to stop once all scratches have been removed from previous grinding papers.

Dimensional measurements of craters and structures milled using focused ion beam (FIB) methods are done using microscope-based white light interferometry. The instrument used was the NewView 7000 manufactured by the Zygo Corp. [20]. The measurement itself has many names however, the common names are coherence scanning interferometry (CSI) or white light scanning interferometry (WLSI) which are used in literature [205]. This section will discuss the operation and working principles of WLSI. WLSI is preferred over stylus profilometry due to the complex surface of the polycrystalline material used in this work.

Interferometry is based on white light waves and how the wave amplitudes interact with each other. If two waves are in phase the result will be an amplitude that is twice the size of the individual waves, assuming they have the same initial amplitude as shown in figure 4.4. If the waves are out of phase by 180° the summed result will be zero amplitude as shown in figure 4.5. The adding (constructive) and cancelling (destructive) wave behaviour is known as superposition which is the cause of dark and light strips known

as the interference fringes which are viewed on screen from the microscope and can be seen in figure 4.6.

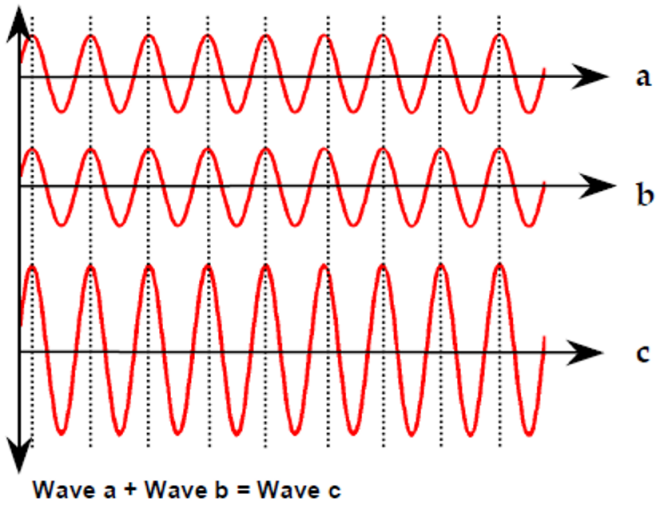


Figure 4.4: In phase light waves showing constructive interference. [20]

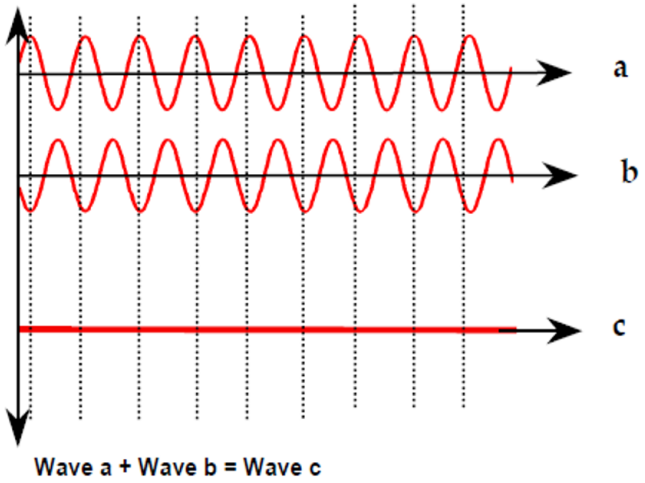


Figure 4.5: Out-of-phase light waves showing destructive interference. [20]

To obtain an interferogram, the superposition of the light waves is used. A beam splitter separates the waves which then travel different paths and are then converged to form the interference pattern. This can be seen in figure 4.7. The beam director plate directs the light from the source to the objective lens which has an internal beam splitter.

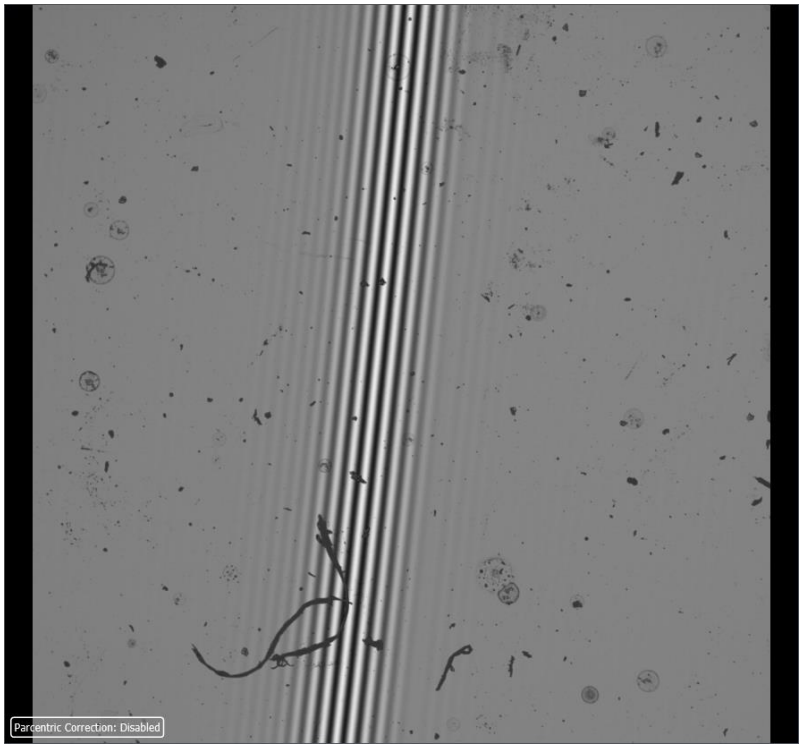


Figure 4.6: Interference fringes on Si wafer using NewView 7000.

The light is then split and one beam is directed towards the samples and from the other to the internal reference mirror. The microscope works in reflective mode where the beam is reflected back off the sample and the internal reference mirror. The two beams recombine and are directed towards the detector shown in figure 4.7 which is a schematic of the constituent parts of a WLSI. For the interference pattern to be obtained the optical path length between the internal reference mirror and the sample should be close to identical to get the bands shown in figure 4.6. To achieve a full topography map the NewView 7000 does an automated procedure which scans the total field of view with the interference fringes scanned over the full area; this process generates the topography map shown in figure 4.8.

4.3.2 Scanning Electron Microscopy

Electron microscopy instruments used in this work were either the LEO Gemini 1525 FEG SEM or the JEOL 6010LA, primarily used for imaging and EDX measurements and the

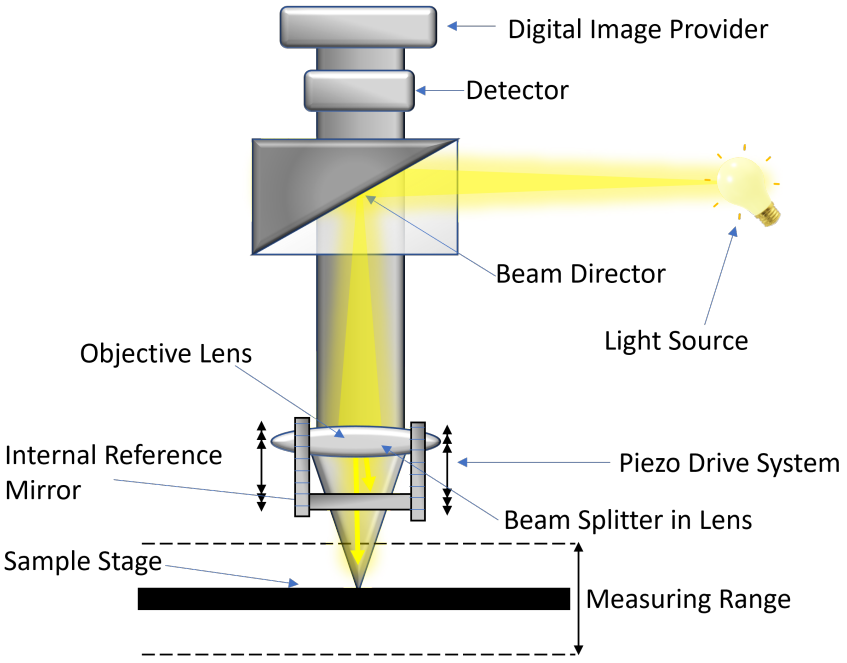


Figure 4.7: Schematic of White Light Interferometer

FEI-Thermofisher Scientific Hydra Dual-beam for imaging and focused ion beam (FIB) milling for the sample used in the Hi5 SIMS.

Electron microscopy uses an accelerated beam of electrons which are generated from a high-temperature resistant material such as tungsten filaments. Electrons are used for imaging as they can behave as both light (wave) and object (particles); this is known as the wave-particle duality and allows us to replace visible light used in optical microscopes. The benefit of using electrons over white light is that electrons have smaller wavelengths, around 12 picometers (pm) when the electrons are accelerated to energies around 20 keV [206], whereas visible light is between 400-700nm. The smaller wavelength is what provides the improved resolution for imaging over optical microscopes; this relation between wavelength and resolution is known as the Rayleigh criterion [207]. The Rayleigh criterion, states that in order to distinguish between two closely spaced objects, the central maxima intensity of one should fall on the first-order minima of the other object's intensity, as otherwise, the two closely spaced objects will be seen as one.

The electron microscopy method used herein is known as scanning electron mi-

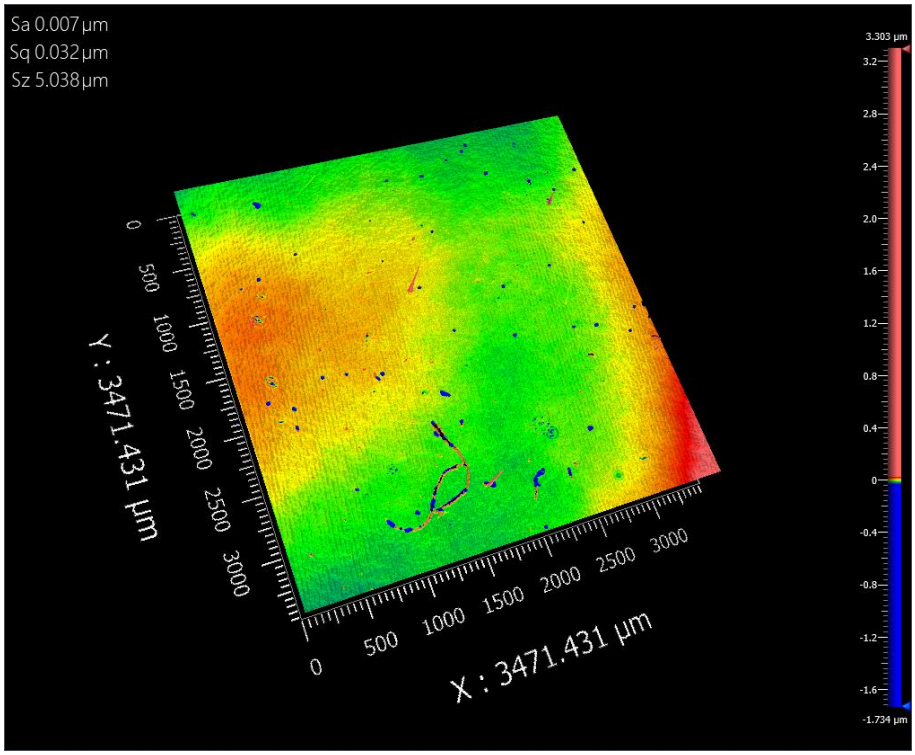


Figure 4.8: Full topography map of the silicon wafer displayed in 3D view.

croscopy (SEM) which generates images using electron-sample interactions, where the primary electron beam is scanned over a region of interest on the sample. To minimise noise and errors in data collection the analysis is done under a vacuum ($1x10^{-6}$ mbar) this also prevents electrons from colliding with particles in the atmosphere. Primary electrons are typically accelerated towards the sample between 5-20 keV, which will then generate three main signals shown in the schematic in figure 4.9 [21].

The first signal commonly used is the secondary electrons to generate images of the microstructure and topography. Secondary electrons are generated when the primary electrons collide with the weakly held electrons in the sample's conduction band and are ejected. These electrons are from the surface of the sample ($<$ 50nm) and will have energies no more than 50 eV [208]. Secondary electrons also help provide topographical information, which is a result of the angle of incidence of the primary electron beam on the sample's surface. Protruding features on the sample result in primary electrons travelling further into that region of the sample, causing more secondary electrons to be ejected

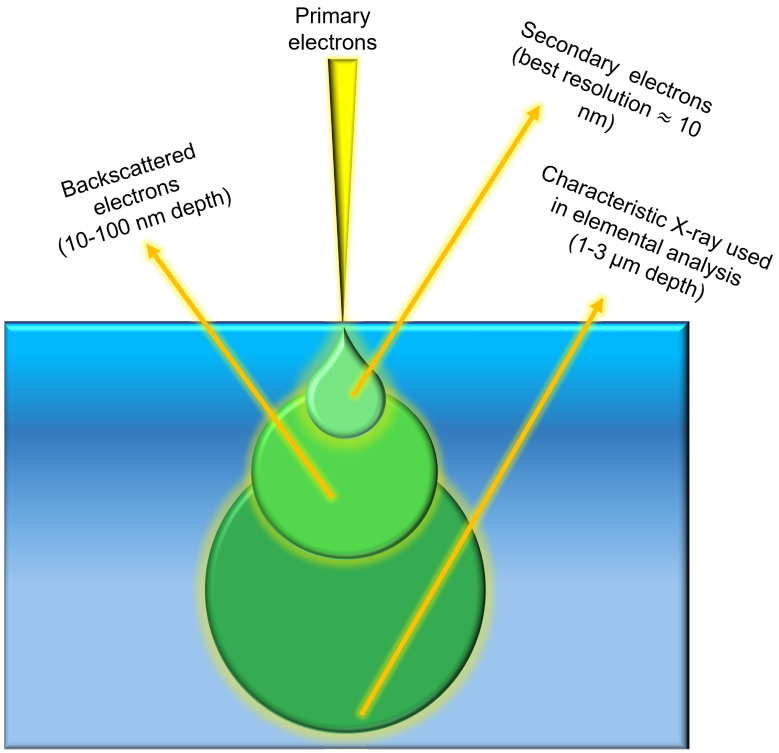


Figure 4.9: Schematic showing the interaction volume of primary electrons towards the samples which generates three main signals picked up by the detectors [21].

which makes those features (e.g. ridges and edges) appear brighter. The opposite occurs for pores and other depressions on the surface. Tilting the sample can also confirm the topography by comparing images at different angles.

The second signal typically analysed is the backscattered electrons. When the primary electrons interact with the sample and bounce back this is known as backscattering. The backscattered electrons are produced from a greater depth range and higher energy in comparison to the secondary electrons. The depth interaction is affected by the atomic number of the elements in the sample and can be altered by changing the accelerating voltage on the primary beam and spot size. Compositional information can be obtained from the backscattering effect because structures composed of mainly higher atomic number elements will appear as bright features, whereas low atomic number compositions appear darker. Therefore backscatter analysis can distinguish whether certain microstructures are pores or low atomic number composed features [207].

The third signal used to give chemical information is the characteristic X-rays of elements. The application of these X-rays is known as SEM energy dispersive X-ray spectroscopy (SEM-EDX or SEM-EDS). SEM-EDX works by the bombardment of a high-energy primary electron with an atom's core-shell electron. The unstable hole in the atom's core electron level results in an outer electron falling and filling this hole, in turn releasing energy in the form of X-rays which are characteristic of each element. Energy from the outer shell electron when it drops to a core level can result in other weakly interacted electrons in the outer level being ejected, which is known as Auger electrons; both effects can be seen in figure 4.10.

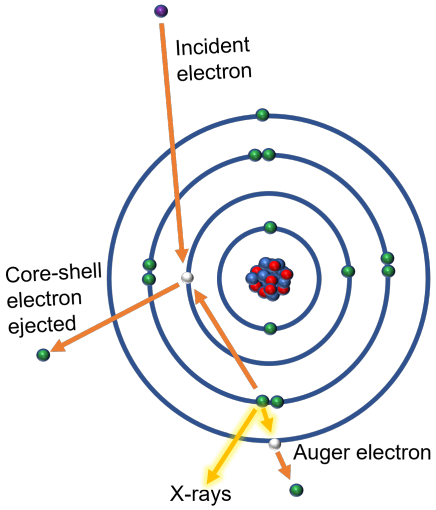


Figure 4.10: Schematic showing the interaction of primary electrons resulting in characteristic x-rays, which are using SEM-EDX and the generation of Auger electrons. [22]

4.4 Stoichiometry Determination using ICP-OES

Quantitative bulk composition analysis was done using inductively coupled plasma-optical emission spectroscopy (ICP-OES). The stoichiometry of each sample was obtained using ICP-OES, to provide an initial understanding of the concentration of the elements in the garnet samples and if they are affected by the final processing conditions. Both the as-purchased LLZO powder and the processed LLZO pellets were analysed. A Thermo-Scientific iCAP 6300 Duo ICP spectrometer was used to analyse the samples which were dissolved in 20wt% nitric acid (ICP grade from sigma), with sonication and heating to 40°C. Concentrations in the range between 1ppm-20ppm were made, which is within the range for the elemental standards. Calibration standards of Li, Ga, Ta, La, Zr, Al, and Mg were made using concentrations of 1 ppm, 5 ppm, 10 ppm and 20 ppm. All samples were measured gravimetrically in the volumetric flasks before dissolving in nitric acid solution. The oxygen nonstoichiometry is estimated using the equation 4.6. Where, Li, La, Zr, Ga, and Ta are the derived stoichiometry from ICP-OES analysis.

$$O = \frac{((3 \times Ga \ or \ (5 \times Ta)) + (1 \times Li) + (3 \times La) + (4 \times Zr))}{2} \tag{4.6}$$

ICP-OES is a highly sensitive technique measuring samples down to low parts per billion (ppb), under ideal conditions. The most commonly understood is ICP-MS which takes into account the elemental mass of the samples to determine the composition, whereas, in ICP-OES, a plasma torch in a quartz tube with flowing argon gas and surrounded by an induction coil is used. Ar plasma is formed by the ignition of flowing argon gas by the coil when a high-frequency current is applied. The samples are then drawn up by the instrument and injected into the plasma. The samples then undergo an electronic transition which produces electromagnetic radiation and various wavelengths respective to the elements. Concentrations were obtained by using the intensity of the emitted light from each element.

4.5 Electrochemical Characterisation

The methods used for electrochemical measurements done in this work are described in this section. Techniques used to obtain the ionic conductivity, electronic conductivity and critical current density for cell failure are mentioned here, which will also include sample preparation and cell assembly. Firstly sample preparation and measurement for electrochemical impedance will be described to determine the ionic properties, second constant DC voltage measurements are outlined for obtaining electronic conductivity, and finally, galvanostatic cycling to push lithium symmetric cells to their limit and determine the current at which failure occurs.

4.5.1 Cell Assembly

Two types of samples are used for conducting electrochemical impedance spectroscopy (EIS), lithium symmetric cells and gold symmetric cells with LLZO. The latter was used for understanding the grain and grain boundary ionic properties of LLZO and performing variable temperature EIS to calculate activation energies (E_a) for Li-ion migration. Au is considered ionically blocking which is why it is applied to prevent contribution from interface signals in the Nyquist plots. However, in some instances, it can alloy with Li when used as a current collector as reported by Krauskopf and Kim *et al.* [209, 210].

To prepare the Au symmetric cells (Au|LLZO|Au) the LLZO electrolyte is removed from the furnace and ground down to approximately 1 mm using 1200 grit SiC paper with isopropanol (IPA) and then sonicated in IPA for 15 minutes followed by another 15 minutes of sonication with n-hexane. The LLZO pellets are thermally etched to 900°C for 30 minutes with Pt foil coverage. Hole reinforcement stickers are placed on both sides of the pellet shown in figure 4.11.

The sticker acts as a mask for Au to be deposited in the centre of the pellet. The deposited gold has a diameter of 6mm. Au deposition was done using the Q150T magnetron sputter coater by Quorum Technologies Ltd, UK [211]. Au was sputtered using 20 mA of current for 2 minutes which results in an Au thickness of ∼50 nm.

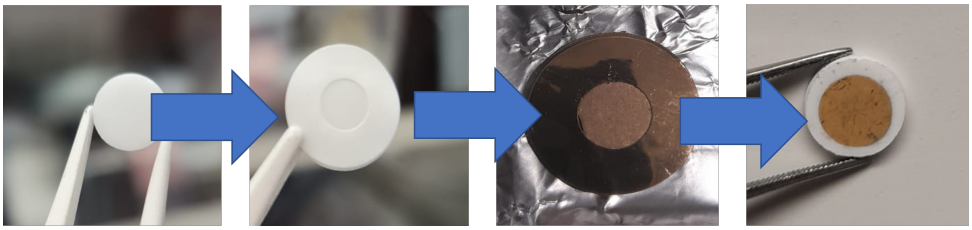


Figure 4.11: Steps showing the fabrication of LLZO with gold blocking electrodes in a symmetric configuration.

Lithium metal symmetric cells (Li|LLZO|Li) were made by preparing the doped LLZO sample in the same manner as above. To add the lithium metal electrodes, the lithium metal chips supplied by MSE supplies [212] is mechanically scraped to a mirror finish, inside the Ar-filled glovebox. Once the Lithium metal appears lustrous it is cut using a disc cutter to 6 mm diameters. The assembled Li|LLZO| Li cell is shown in figure 4.12a and was placed in a coin cell as shown in the schematic of figure 4.12b. The lithium metal is placed on the electrolyte and pressed down with the weight of a small steel block for 5 minutes. Once the Li metal has adhered to the electrolyte and is not sliding off, it is placed in a coin cell which will apply more pressure from the spring. The pressure in the coin cell will remain stable throughout the experiments and is more compact so the Li|LLZO interface will stabilise. This is why not much pressure is applied to the electrode on the LLZO before inserting into the coin cell, as it can start to relax with lower applied pressure in the coin cell if more pressure is applied beforehand. Coin cells by XIAMEN TOB New Energy Technology Co. LTD. [213] were used to make the cells. LLZO thickness of approximately 1 mm was used (1.10-0.9 mm range) as this ensures sufficient pressure is applied in the coin cell. Coin cells were made using one wave spring and two 0.5 mm spacers which provide an empty cavity of around 0.98 mm used for the electrolyte and electrodes. Pellets larger than 1.2mm result in improper sealing of the coin cell and electrolyte cracking. On the other hand, electrolytes less than 0.85 mm result in not enough pressure applied to the electrodes on the electrolyte and poor contact between the sample and the coin cell components.

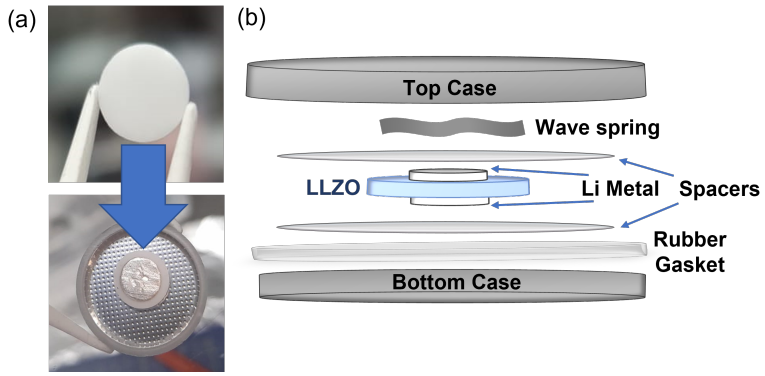


Figure 4.12: Assembly of lithium metal on LLZO, (a) image of an LLZO pellet before and after placing the lithium metal electrodes to make a Li|LLZO|Li symmetrical cell used for galvanostatic cycling in a coin cell and (b) schematic of coin cell components used to cycle the cell.

4.5.2 Electrochemical Impedance Spectroscopy (EIS)

EIS measurement theory

EIS is used in a variety of areas such as corrosion, biosensors, sensor development, fuel cells and battery characterisation [214]. EIS was used in this work to determine the ionic conductivity of the electrolyte. EIS applies a small alternating current (AC) electric potential (with fixed amplitude) and the current output is measured; this is known as potentiostatic mode and is commonly used in this field of research. The other possibility is the galvanostatic mode where the current amplitude is fixed and the voltage is measured. The instrument used to apply this electric field is known as the frequency response analyser (FRA). The FRA also measures the output signals to provide us with impedance information. When the cell is connected to the FRA the small AC sinusoidal potential is applied at varying frequencies, typically from high frequencies to low frequencies. A phase shift (ϕ) of the output current may occur at each frequency which is measured by the FRA, which in-turn generates the frequency dependant resistance also known as the impedance (Z_ω) of the material and is shown in the equation 4.3 where the subscript ω is for frequency dependency.

$$Z_\omega = \frac{V_\omega}{I_\omega} \tag{4.7}$$

The impedance equation is similar to Ohm's Law ($R = V/I$ where R is resistance, V is voltage and I is current which are all time-dependent). However, in the impedance equation, each term is frequency dependent, where V_ω and I_ω are the frequency-dependent potentials and current respectively. Impedance data can then be represented in two common ways, either in the vector form which is defined by the impedance magnitude and the phase angle (i.e. Bode plot) or the complex form which displays the complex impedance split into the imaginary (Z") and real (Z') impedance as shown in the schematic in figure 4.13.

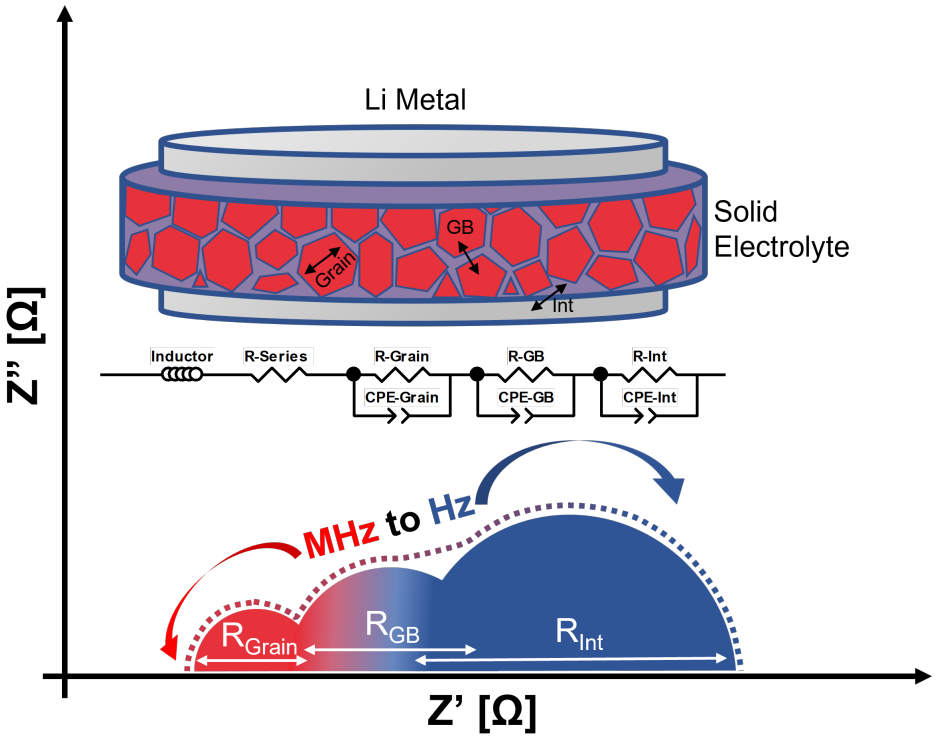


Figure 4.13: Schematic of Nyquist plot, representing where each impedance signal is generated from using the diagram of a symmetric cell, the Randles circuit shown represents each contribution to the Nyquist plot.

Different frequencies are applied to separate signals from processes in the material caused by the different component parts such as the grains (bulk), grain boundary and

interface contributions. This is why a small perturbation of AC potential is applied as each component will have distinct electrical relaxation times at each frequency range. Electrochemical cells can be modelled as a network of passive electrical circuit elements which are known as equivalent circuits or Randle circuits as shown in the centre of figure 4.13. The equivalent circuit elements (EC-elements) are used to fit and Nyquist plot and calculate impedance responses which are then compared to the actual sample's response from the FRA. The primary types of EC-elements used in this work are the resistor, constant phase element (CPE), and inductor.

To understand each of these components, their relation to impedance will be taken into account. The impedance of a resistor is equal to the resistor itself ($Z_\omega = R$), with a phase angle of 0°, which is why the resistance contribution of the EC-element is entirely on the real plane of the Nyquist plot. The relation of impedance with the capacitor and inductor are shown in equations 4.8 and 4.9, respectively,

$$Z_\omega = \frac{-j}{\omega C} \tag{4.8}$$

$$Z_\omega = j\omega L \tag{4.9}$$

Where j is the imaginary number $\sqrt{-1}$, $\omega = 2\pi f$ (f = frequency (Hz)). The inductor has a positive j which agrees with the impedance response observed on a Nyquist plot from inductance as it appears on the positive side of the imaginary axis (i.e. below the Z' axis). The opposite is true for the capacitance contribution.

Operating Parameters for EIS Measurements

EIS measurements were done in a Linkam HFS600E-P stage coupled to a Solartron 1260 frequency response analyzer. An AC perturbation potential with an amplitude of 20 mV was applied from a frequency range of 13 MHz-1 Hz with logarithmic data collection at

20 points per decade. Disclaimer: The FRA used can apply frequencies up to 32 MHz however this is not stable and is shown by the KK validity test discussed below in the EIS data analysis section. Frequency ranges were split into three ranges 13 MHz-500kHz, 500kHz-500 Hz and 500Hz-1 Hz with 2 s integration and ten cycles delay; 1 s integration and five cycles delay; 30 cycles integration and three cycles delay, respectively, to minimise noise. The Linkam stage is used to maintain the temperature during measurement, the temperature capabilities of the Linkam are from 600°C to -100° (negative temperatures are achieved with liquid nitrogen). A range of temperatures was used for Arrhenius plots to determine the activation energy. To minimise the possibility of a temperature gradient in the samples during measurements, the samples were allowed to equilibrate at the required temperatures for 1.5 hours before measurements. Practical temperature ranges used in the Linkam climate stage were between -10to100°C, lower than -10°C was avoided as ice would form in the stage as shown in figure 4.14. Results were fitted to the EC-elements using RelaxIS 3 by Rhd instruments and data validity was determined using the Lin_KK tool by Karlsruhe Institute of Technology.



Figure 4.14: Linkam climate stage used for variable temperature EIS measurements. Image shows the difficulty of conducting measurements below -10°C which results in ice formation.

EIS Data Analysis

Data analysis and fitting was done on the RelaxIS3 software, and data interpretation was done using the brick-layer model for EIS analysis defined by Irvine *et al.* [215]. Typical Nyquist plots obtained can either have well-defined semicircles or have overlapping signals as shown by the dotted line in figure 4.13 and is commonly observed with LLZO impedance spectra, shown by Pesci *et al.* [216]. The overlapping of signals is due to the features having similar relaxation times which is the reciprocal of the characteristic frequency ($\tau = \frac{2\pi}{\omega}$) where τ is the relaxation time. Before continuing with data interpretation and extracting any values the quality of the data is checked using the KK-test [217, 218]. The validity test checks the quality of the data obtained in terms of linearity, stability, and causality which is done by applying a mathematical connection between the real and imaginary constituents of the impedance data and outputs a residual plot. If the residual plots do not deviate more than 1% then sufficient data quality is considered and it can be analysed further. Figure 4.15 shows the KK test residual plots when EIS measurements are done from 32 MHz to 1 Hz (a) and 13 MHz to 1 Hz (b). The KK test shows that the data from 32 MHz to 13 MHz is not suitable for fitting.

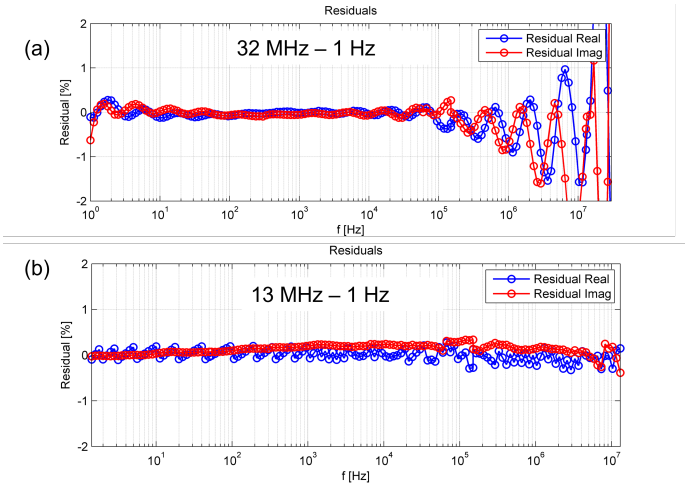


Figure 4.15: KK test comparison of residual plots (a) measurement from 32 MHz to 1 Hz, and (b) 13 MHz to 1 Hz.

To determine the ionic conductivity the resistivity is calculated from the impedance using the Nyquist plots by fitting it to parallel RC-elements as discussed above. It can

be seen from figure 4.12 that the semi-circles have been placed away from the Z" and Z' axis intercept. This is because the instrument itself and the wires used to connect the FRA to the samples have their own resistance known as the series resistance (R_{Series}) and inductance which are taken into account when fitting the data by using a single resistor and inductor element. However, if no response below the real axis is obtained the inductor element is not required to fit the data. To fit the semi-circles obtained from the sample, parallel R-CPE elements are used (CPE is the constant phase element). CPE is used because it is not constrained by any physical properties whereas, capacitors are. Hence CPE can be used to model the capacitance behaviour of imperfect semi-circle signals. "Depressed" semi-circles are common for solid electrolyte EIS measurements, due to disorder at the macroscopic scale, such as varying grain sizes and orientations. This is why a range of capacitance values are used to distinguish whether the impedance signal is attributed to the bulk, GB or interface components [215, 219]. CPE is modelled to the Nyquist plot and used to calculate the capacitance which can give an indication of what the semicircle can be attributed to. The Brug equation (e.q. 4.10) is used to convert the CPE to capacitance,

$$C = \frac{(CPE_Q \times R)^{\frac{1}{CPE_n}}}{R} \tag{4.10}$$

Where, CPE_Q and CPE_n are CPE parameters obtained from the fitting software and R is the resistance of each semicircle. Once the capacitance (C) is determined it is possible to calculate the characteristic frequency using equation 4.11

$$\omega = \frac{1}{R \times C} \tag{4.11}$$

The resistivity and hence conductivity (σ) (conductivity is the inverse of resistivity) is calculated from equations 4.12 for bulk and grain boundaries and interfacial resistivity from equation 4.13.

$$\sigma_{bulk(orGB)} = \frac{1}{R_{bulk(orGB)}} \times \frac{L}{A} \tag{4.12}$$

$$R_{Int} = \frac{R \times A}{2} \tag{4.13}$$

R is the resistance from the Nyquist plot, A and L are the electrode area (cm^2) and electrolyte thickness (cm) respectively. These are the methods used to provide the resistivity properties of the solid electrolytes used in this work.

The activation energy (E_a) is obtained by doing EIS measurements at various temperatures ranging from 0-100°C. An Arrhenius plot of lnσT vs 1000/T, and a slope of -E_a/R gives the E_a as seen from equation 4.14, where R is the gas constant and σ_o is the intercept and is the maximum possible conductivity if no energy barrier for migration existed.

$$ln\sigma = ln\sigma_o - \frac{E_a}{RT} \tag{4.14}$$

4.5.3 Electronic Conductivity

The electronic conductivity of the solid electrolyte was measured using the Biologic SP-240 FRA and Potentiostat by Biologic [220]. Time-resolved DC polarisation measurements were done using symmetric Au|LLZO|Au at RT (∼28 °C) as described by Zhan *et al.* and others [128, 189, 221, 222]. When applying the constant voltage of 200 mV for 1 hour the current will gradually decrease with time and eventually reach the plateau. Using the known voltage and equilibrated current the resistance can be determined and in turn the electronic conductivity.

4.5.4 Cell Cycling

To investigate cell failure, galvanostatic cycling was done using the 580 Battery Test System by Scribner [223]. The galvanostatic method is used on Li|LLZO|Li symmetric cells at RT (∼28 °C). A constant current density is applied on either side of the cell in an alternating pattern, in order to stimulate charge and discharge behaviours (commonly termed stripping and plating). The measurement of critical current densities (CCD) will be discussed further in Chapter 5. CCD measurements are used to evaluate the ability of metal|SE|metal symmetrical cells to withstand metal filament penetration during cycling. Gradually increasing the current density from 0.01 mA/cm^2 in steps of 0.01 mA/cm^2 until a sudden drop in the voltage of cells is detected indicating a short-circuited solid electrolyte. Depending on the publications, the galvanostatic dwell time at each current density is either (i) duration or (ii) capacity based. In this thesis, the latter mode of operation (i.e. constant capacity) is preferred as it guarantees that, at each current density, the same amount of Li metal is stripped and plated from each side. A constant areal capacity of 0.1 mAh/cm^2 was used on Li|LLZO|Li with the same cell dimensions as described above for EIS measurements. At each current density applied with a constant areal capacity of 0.1 mAh/cm^2, *approx.* 7.32 μg or 0.5 μm thick, are cycled.

4.6 Surface Analysis

Herein, the techniques used to examine the surface chemistry are explained as well as methods used to prepare their respective samples for analysis. There are three types of instrumentation used to study the surface chemistry which include X-ray photoelectron spectroscopy (XPS), which analyses depths between 0.5-10 nm, secondary ion mass spectroscopy (SIMS) which has depth resolutions down to around 1 nm in the best case, and low energy ion scattering (LEIS) with can be used to investigate the surface monoatomic layer. Figure 4.16 shows a schematic for relative depth analysis of the three techniques.

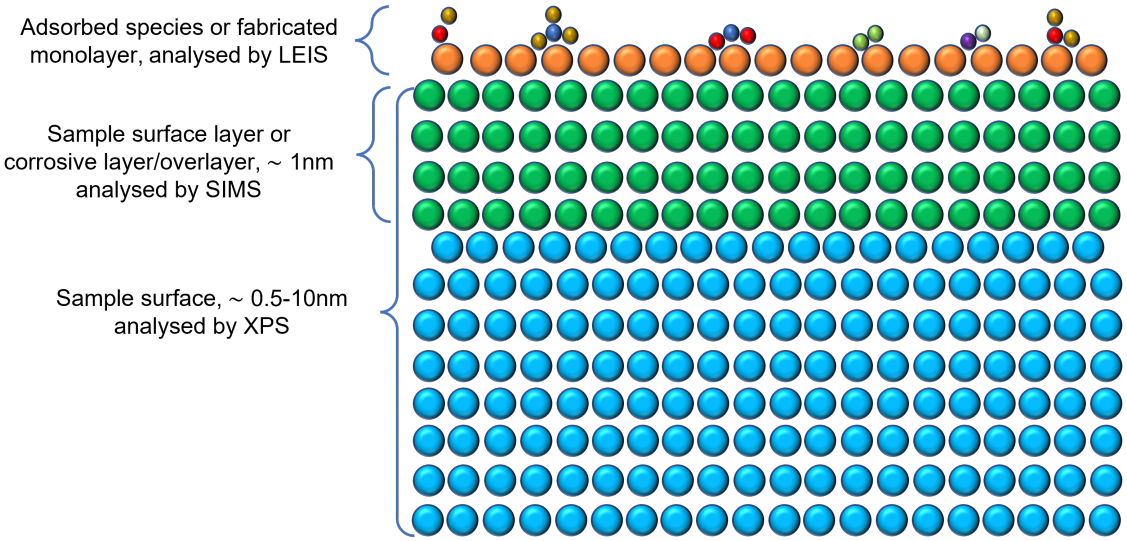


Figure 4.16: Diagram showing relative analysis depth of the different surface characterisation techniques used in this work, (not drawn to scale).

4.6.1 X-ray Photoelectron Spectroscopy

X-ray photoelectron spectroscopy (XPS) uses an X-ray source to provide chemical information of the surface, typically from 0.5-10 nm of depth analysis [224]. XPS is classed as a quantitative characterisation technique because it can give information on the chemical environment from which the signals appear and an indication of the number of elements present from the analysis depth.

Theory Behind XPS

XPS use X-rays of a monochromatic wavelength (aluminium Kα source in this case), that are directed towards the sample which results in the emission of electrons from various orbital levels (i.e. valence or core) from the elements; these are termed photoelectrons. The signals observed from the core electron's binding energy (E_B) are used to provide information on the chemical environment. The binding energy is determined by using equation 4.15 and assumes no energy is lost from further collisions of the photoelectron, which is why XPS is done under high vacuum levels ($\sim$x10^{-7} mbar).

$$E_K = h\nu - \Phi - E_B \tag{4.15}$$

Where Φ is the work function of the sample, which means the minimum work needed to extract electrons from the Fermi level into the vacuum level, and E_K is the kinetic energy of the photoelectron emitted by the X-rays. $h\nu$ is the photon energy of the incident X-rays. Figure 4.17 is used to visually understand how the terms in equation 4.15 are physically behaving and what they look like.

There are two sides to the schematic in fig.4.17. The micro view (left side) shows the different terms used in equation 4.15. It shows that E_B is the energy required to get the electron which is excited by the X-rays to the Fermi level which is defined as the highest energy level the electron can occupy at absolute zero. If the electron has sufficient energy it can leave the Fermi level and enter the vacuum level, and can then be analysed by the detector if it retains its kinetic energy (E_K). The macro view shows the photoelectrons pathway at a larger scale. Two possibilities are represented, (1) shows an excited electron that can collide with other particles in the sample surface thereby losing kinetic energy and possibly contributing to the spectra background, and (2) the photoelectron is on a collision-free path and keeps its kinetic energy which explains the necessity of a vacuum. Electrons deeper in the samples may not have enough energy to escape the sample due to collisions which reduces their kinetic energy. To give an estimation of the sampling

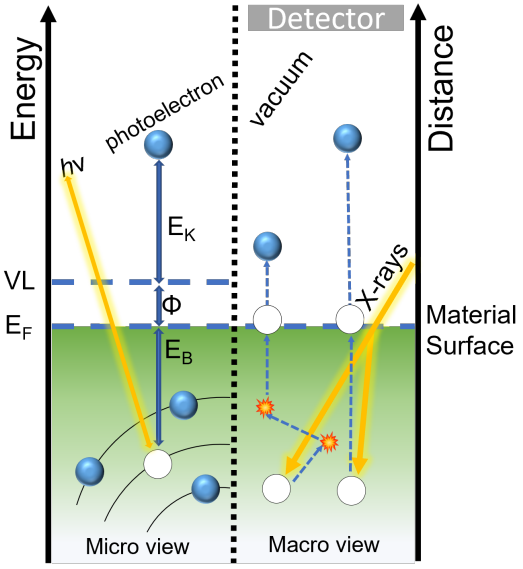


Figure 4.17: Schematic showing micro view (atomistic scale) on the left side and the macro scale on the right side of the interaction of X-ray radiation on core level electron to generate photoelectrons. VL is for the vacuum level and E_F is for Fermi Level. (not drawn to scale).

depth of the X-rays it is related to the radiation wavelength by three-fold (hence 3λ = the penetration depth). In the case of Al Kα which is between 1 - 3.5 nm would give a depth of around 3 - 10 nm [225].

Sample Preparation and Measurement

XPS was conducted to investigate any oxidation changes observed and possible contamination signals from the various processing conditions used to synthesise LLZO. The effect of the processing atmospheres on the oxidation state of the LLZO was studied and contamination from the different crucibles used during heat treatments.

Pellet samples that had been ground down to 1200 grit, and thermally etched in the same atmosphere as they were sintered, were used. To prevent the sample surface from being contaminated by ad-atoms or corrosion layers from moisture and CO_2 exposure a vacuum suitcase is used. Samples are packed in the glovebox under an argon atmosphere in an airtight vacuum suitcase. Samples that are thermally etched under oxygen outside the glove box are removed at 300°C and immediately placed into the glovebox to prevent

samples from cooling down and reacting with the ambient atmosphere. Once the samples are packed in the vacuum suitcase they are placed into the instrument as fast as possible. The instrument used was the Thermo Scientific K-Alpha + spectrometer with a chamber pressure of 2×10^{-7} mbar and an Al Kα X-ray source with $h\nu$ of 1486.6 eV, the survey spectra are collected using a pass energy of 200 eV, and 20 eV for core levels with varying scan and dwell times to increase the signal to noise ratio. The beam spot size is 200x200 μm with the addition of an electron flood gun to compensate for sample charging as the samples used are electronic insulators. A double focusing 180° hemispherical analyser and 2D detector are used to collect the photoelectrons.

Analysis and data interpretation was done with the help of Dr Gwilherm Kerherve. All the peak shift binding energies were normalised to the C 1s peak of advantageous carbon at 284.8 eV. The XPS data was analysed using Avantage software using a smart fitting feature, which uses Shirley-type background [226] for Zr 3d, Ga 2p, O 1s and C 1s and a linear background for Li 1s. To compare signal intensities all signals were normalised to La 3d.

4.6.2 Low Energy Ion Scattering

To analyse the topmost layer of the material low energy ion scattering (LEIS) is used which is a non-destructive technique if depth profiling mode is not applied. LEIS is a powerful technique that can provide the elemental composition of the sample surface by using scattered energies of the backscattered primary ions when they interact with the atoms on the material being studied. Figure 4.18 shows a diagram of the working principles of LEIS and the instrumentation setup [23].

LEIS uses noble gas ions such as (He^+, Ne^+ or Ar^+) as the primary ions with known masses and energies typically between 0.5-10 keV. The primary ions are directed normal to the sample surface which is then backscattered elastically by the surface atoms as shown in figure 4.18a. The atomic composition is obtained as the different elastic scattering results in the backscattered ions having varying energies depending on the mass of the

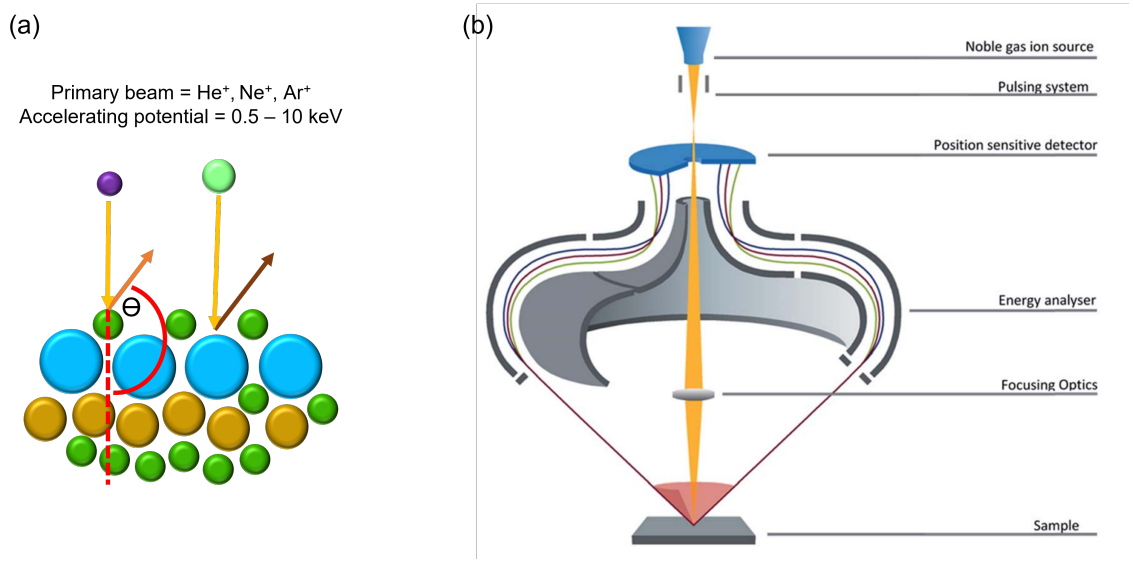


Figure 4.18: Schematic showing (a) Primary ion interaction with surface particles and (b) basic working principles of how backscattered ions are detected (image taken with permission from a publication by Cushman *et al.* [23].).

atoms it interacted with. LEIS can give an indication of the quantity of specific elements on the sample surface with respect to the other atoms present, the chemical environment does not influence the signals obtained in LEIS, therefore LEIS is said to be independent of matrix effects and provides the possibility of quantifying atomic composition of the material surface, however, standards are typically required [227].

The governing equation for LEIS is shown in equation 4.16 which is based on energy and momentum conservation to yield the final energy of the backscattered atom (E_f) [23, 227].

$$E_f = k \times E_p = \left(\frac{cos\theta \pm \sqrt{(\frac{M_s}{M_p})^2 - sin^2\theta}}{1 + \frac{M_s}{M_p}} \right)^2 \times E_p \tag{4.16}$$

Where k and E_p are the kinematic factor which describes the motion of the backscattered particles and the energy of the primary ion particle respectively. M_S and M_P are the mass of the primary ion particle used and the element it scatters off respectively (where $\frac{M_s}{M_p} \geq 1$, and θ is the angle through which scattering takes place ($\theta \geq 90°$)shown in

figure 4.18. Backscattered ions that are from the sample surface show the highest intensity however primary ions that travel further into the samples before scattering back also produce signals known as "in-depth" (E_{id}) signals which have lower intensity as they have less energy $E_{id} << E_f$. Based on equation 4.15 only ions in the sample that have a greater mass than the primary ion can be detected. With the option of using a $^4He^+$ primary ion beam, it is theoretically possible to detect all elements except hydrogen, however, this is not the case and is explained in chapter 7.

The working principals of LEIS are shown in figure 4.18b; it uses an ion source typically a noble element plasma source, electrostatic lenses to focus the beam, mass filters, toroid shaped energy analyser and a detector. The primary ions are first heated and ionised to a plasma from various gas sources either He, Ne or Ar or a mixture before it is focused onto the sample surface they passed through various lenses to get the right energy required and current for measurement. A mass filter is used to purify the beam if a single isotope to prevent multiple signals from different isotope interactions with the sample. After the primary ions scatter from the sample they are extracted and move through the toroid analyser if they meet the analysis angle of 145°, the energy of the backscattered ions are then detected as they move through the analyser at different speeds. The whole system is operated under ultra-high vacuum (10^{-8} mbar) to prevent collisions and energy loss from residual gas particles and contaminants.

LEIS Instrumentation

All LEIS measurements were conducted on the Qtac^{100} LEIS instrument developed by ION-TOF GmbH, Munster, Germany. The instrument used a double toroidal energy analyser which collects backscattered ions at 145°. The primary ion column by Oregon Physics was used and it positions normal to the sample surface. Analysis of gallium, aluminium and magnesium was done using a helium ion source (3keV, 5nA) which could also be used for the larger elements such as zirconium, lanthanum and tantalum. However, the energies corresponding to these elements would overlap and make it difficult to distinguish their respective energy onset signals. To improve the peak separation a neon primary ion

beam (5keV, 1nA) was used for analysing the heavier elements only. Analysis area would typically be either 1000 μm or 500 μm, and all analysis using either a He^+ or Ne^+ was done in static mode with the dose density of the primary ions kept below 10^{14} ions cm^{-2} in order to avoid any secondary ions from being ejected. Depth profile analysis was done using an Ar^+ (50 keV, 100nA) beam with the sputtering area larger than the analysis area typically 1000 μm^2 or 1500 μm^2 and the dose density above 10^{15} ions cm^{-2} to provide sputtering, this is called dynamic mode. To ensure both beams are coincident they are aligned using a 50 mesh grid on the LEIS sample holder and are shown in figure 4.19. All samples were pellets and transferred using the vacuum suitcase to minimise any corrosive layer and advantageous carbon being adsorbed onto the samples. All data analysis was done on the iontof 5 software and re-plotted on Origin Pro.

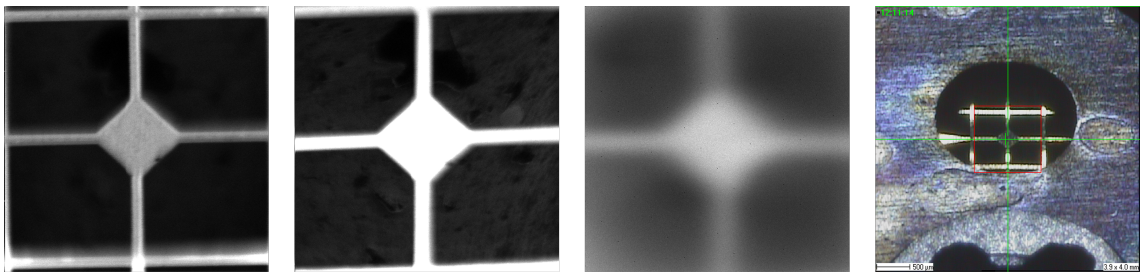


Figure 4.19: 500x500 μm secondary electron images showing the primary ion beams (a) He^+ and (b) Ne^+)alignment on the 50 mesh grid and (c) Ar^+ sputter beam alignment to avoid analysing crater edges, poor definition in the image from the Ar^+ is due to it having a larger spot size, (d) is the camera view of the 50 mesh grid on the sample holder.

4.6.3 Secondary Ion Mass Spectroscopy

Secondary Ion Mass Spectroscopy (SIMS) as the name suggests works by using the mass of ejected ions and therefore is inherently destructive to the sample. SIMS was used extensively in this work to obtain a better understanding of elemental segregation both in-depth and laterally in the form of ion maps. One of the main benefits of SIMS techniques is also their sensitivity down to parts per billion (ppb) and high mass resolution which can help distinguish between isotopes which is crucial to the study of oxygen diffusion experiments in LLZO described in section 4.7.

Studying surface chemistry of solid-state electrolytes was essential to this research which is why SIMS methods were employed as it can be done in-house with relative ease, especially for light elements such as H, Li, and O which are more difficult with X-ray-based methods.

Working Principal of SIMS

To generate secondary ions from the sample under investigation an energised beam of primary ions is directed towards the surface of the sample which then collides with the elements in the samples resulting in some of the energy being transferred into the sample and releasing the secondary particles which can include both charged and neutral species. The processes that take place following primary ion bombardment are shown in figure 4.20. The processes include recoil implantation, whereby the primary ion loses energy upon collision with target material and causes the target particle to move further into the material, the second known as cascade mixing is where the primary ion with sufficient enough energy can implant itself further into the material causing a reshuffle mechanism with other atoms. The third is where the primary ion is scattered back into the vacuum and the fourth is sputtering to generate secondary ions which will then migrate through the analyser before arriving at the detectors [24]. The analysis depth can vary from 2-3 nm to as much as 10 nm due to multiple collisions and cascade mixing from sputtering [228, 229].

To minimise the cascade mixing from the primary ions and ejection of secondary particles (i.e. neutrals, electrons, negative and positive ions) the primary ion gun can be used in static with current densities and ion dose densities less than 1 nA cm^{-2} and 10^{15} ions cm^{-2}, this should restrict the impact to the outermost layer of atoms shown in literature [24, 230]. The primary ion dose density (PIDD) can be calculated using 4.17, where I_p is the primary ion current, t is the time for analysis, e is the electronic charge (1.6×10^{-19} coulombs) and A is the analysis area. However, as SIMS is a destructive technique it is primarily used in dynamic mode achieved by increasing the primary ion current, which in turn allows depth profile to be obtained [24]. Depth profiles are shown as depth or time verse secondary ion counts. SIMS techniques can either use a single

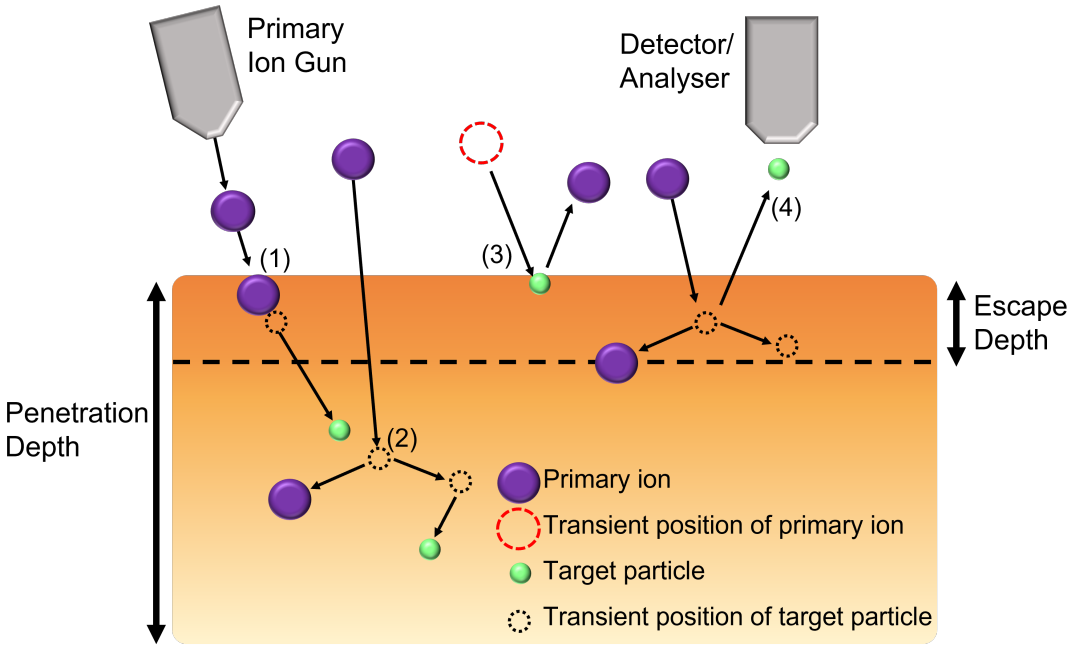


Figure 4.20: Diagram showing key processes that can occur during primary ion bombardment of target materials and these include; (1) recoil implantation, (2) cascade mixing, (3) primary ion reflection and (4) cascade mixing with sputtering. Image adapted from [24]

beam to do both sputter and analysis or use a dual beam system whereby a sputter beam of higher energy is employed to mill away some material before the primary ion beam at lower energy and current is used to generate the secondary ions for analysis.

$$PIDD = \frac{I_p t}{eA} \tag{4.17}$$

Contrary to LEIS, SIMS is a technique which is hindered by the matrix effect. The matrix effect is when the material surrounding the target species can alter its sputtering and ionisation properties, hence making quantitative analysis difficult as it can affect the ionisation yield. Equation 4.18 is used to explain the emission of secondary ions.

$$I_x = I_p C_x S \gamma F \tag{4.18}$$

Where I_x is the secondary ion yield of species x which is the measured ion counts, I_p is the primary ion beam current. C_x is the concentration of species x, S is the sputter yield of x and γ is the ionisation efficiency (i.e. the probability of the target species forming positive or negative ions), both S and γ depend on the selection of the ion beam and the target material, and F is the transmission of the analysis system. The SIMS equation suggests that quantification is easily achieved because it shows I_x is proportional to C_x. However, this is not as straightforward as the ionisation of target species (γ) is affected by the chemical environment (i.e. the matrix effect). A method for quantification using isotope exchange experiments is discussed in section 4.7.

After the sample has been sputtered, the secondary ions need to be separated with respect to their masses which is where the analyser comes into play and is discussed below.

4.6.4 Analysers in SIMS

SIMS techniques are normally divided into their method for analysing the secondary ions and these include Time of Flight (ToF), Quadrupole (Q), and Magnetic Sector (MS) - SIMS shown in 4.21. Herein the ToF and Quadrupole SIMS will be discussed in detail and the latter only briefly as it was not used in this work, for more detail on MS-SIMS please refer to literature [231–234].

Quadrupole Mass Filter

Quadrupole mass filters (QMS) were used extensively in both static and dynamic SIMS from the mid-1970s to the 1990s. however, their popularity slowly declined due to the improvements made to both the magnetic sector and time of flight mass filters, which could accommodate the requirements for high mass resolution ($M/\Delta M$). T

The advantages of QMS are that they are relatively inexpensive due to their relative simplicity shown in comparison to the other analysers and more compact, measurements when the elemental analysis is from a simple substrate where isobaric interference

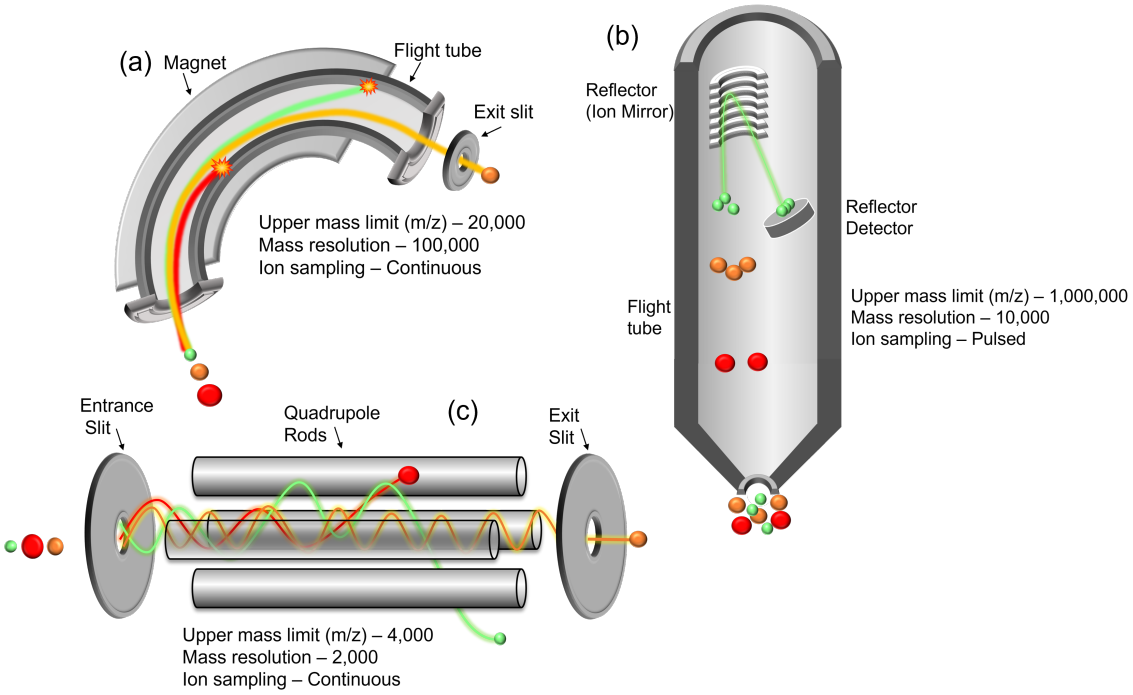


Figure 4.21: Three main SIMS analysers used (a) magnetic sector, (b) time of flight, and (c) quadrupole.

are minimal (i.e. high-purity samples with low isotope concentration differences). An example of this would be a doped silicon substrate used as chips in electrical devices. QMS also provide greater flexibility to the working distance (due to reduced extraction field) which allows for sample surface angles to be varied with ease.

Quadrupole-based SIMS instruments only allow the analysis of secondary ions of a particular mass at a time. Thus, if information on multiple secondary ions is required, the mass filter must be switched back and forth among the respective masses during analysis. All other secondary ions produced at the same time are filtered out. However, as the switching time of electrostatic units is much faster than that of electromagnetic units, quadrupole mass filters can switch to different masses at a much faster rate than magnetic sector analysers (discussed below). This can improve data acquisition times and can compensate, to some degree, for their low transmission.

A schematic of the components of a quadrupole mass filter is shown in figure 4.21c.

In essence, this consists of four rods whose axes lie parallel to the ion's initial entrance as can be seen from the entrance slit and all the rods are of equal radius, length and distance from each other. A DC potential is placed onto two of the opposing rods with the other rods receiving the opposite potential. An RF signal is then placed on all the rods which generates a time-varying field and allows only specific ions of known m/z ratio to pass through the exit slit and into the detector. The remaining ions that pass-through will not be able to pass through at their initial trajectory if the conditions are not set for their collection and they are subsequently lost.

Time of Flight Mass Filter

ToF mass filters were the last of the main mass filters to be introduced with SIMS instruments, however, their application and development in SIMS have been growing fast in the SIMS community. SIMS utilising ToF mass filters are most effective in static SIMS and shallow Dynamic SIMS (operated in pulsing mode with a sputter beam to achieve depth profiles) studies. The ultimate benefit of ToF analysers is their ability to detect all ejected secondary ions of the same polarity within a given m/z range for data analysis to be done of different species if not considered during the time of measurements. ToF also benefits from it having the highest upper mass limit and high mass resolution with minimal loss of sensitivity.

The main drawbacks of ToF analysers are three, (1) increased analysis time when operated in Dynamic mode relative to Magnetic Sector based SIMS, (2) relatively large data files as it collects all secondary ions of the same polarity which fill up large data drives, especially if long analysis is carried out and, (3) sample surface has to be smooth to improve the mass resolution as secondary ions with same m/z are ejected at similar times that can be hindered by the topography of the sample.

ToF analysers installed on SIMS are typically reflectron based as this helps to improve the mass resolution and by pass the requirement for increasing the length of the flight tube which can make the instrument more cumbersome. The purpose of a reflector

is shown in figure 4.21b, it is located close to the top of the flight tube where the ions are redirected downward towards the detector. The secondary ions arrive at the detector in order of increasing mass with lighter ions such as H^+ arriving first as they have a greater velocity in comparison to heavier ions such as U^+. To further increase the potential of the ToF mass filter is to use the primary ion beam in bunched mode. Using it in bunched mode will shorten the pulse time width on the sample surface, hence shortening the pulse duration. This in turn allows the mass filter to work closer to its full potential as the secondary ion collection time is increased and less time is spent in between pulsing the beam.

Magnetic Sector Mass Filter

Magnetic sector (MS) analysers like all the above-mentioned mass filters existed well before SIMS techniques were invented. MS analysers have the best mass resolution and used in cases where the optimum detection limits are needed. The analyser is used with dynamic SIMS analysis and is primarily suitable and used extensively for looking at short-lived and rare isotopes such as in radioactive and geological samples. The schematic in figure 4.21a is a basic representation of the working principle of the magnetic sector analyser. However, the current available MS-SIMS can parallel detect up to seven secondary ions [235, 236]. To detect multiple SI this will require the instrument to have multiple magnetic sector channels which can be it's biggest drawback, among others, such as a lower upper mass limit making it not suitable for biological samples that have large protein structures. MS analysers also have a slower rate at which the magnetic field can be switched which defines the m/z ratio of secondary ion reaching the detector and the cost of these instruments is much greater than Q-SIMS and ToF-SIMS owing to their size and complexity. The magnetic sector works by applying a magnetic field on the flight tube perpendicular to the ion's trajectory which will cause the ions to either deviate from their initial path and collide with the flight tube wall and miss the exit slit. Only ions chosen to be collected will pass through the exit slit and be detected.

More information on mass filters used in SIMS can be found in the book, Sec-

ondary Ion Mass Spectrometry - An Introduction to Principles and Practices by Paul van der Heide [234].

4.6.5 SIMS Instruments and Measurement

TOF-SIMS

ToF SIMS was used extensively in this PhD work, the instrument used was the dual-beam ToF-SIMS V by ION-TOF GmbH, Münster, Germany, equipped with a vacuum suitcase which was used to transport all samples in and out of the SIMS and LEIS instruments. A primary Bi^+ ion gun was used as the analysis beam in the form of a liquid metal ion gun (LMIG). The Bi^+ are formed using a field emission process with high extraction field to give an ion beam with high brightness, the beam will have a small relative energy spread and hence a good focus which will allow good lateral resolution, this will be elaborated on below in this section. As the name suggests the technique used two beams, the second is the sputter beam. The ToF-SIMS instrument has a selection of three sputter beams that can be used and they include O_2^+ and which is used during positive secondary ion collection, Ar_n^+ (argon cluster) primarily used when gentle sputtering is required (e.g. organic material), and Cs^+, the latter is used primarily in this work and will be discussed further. Cs^+ has a chemical effect during sputtering and is used to collect negative secondary ions. Caesium ions readily lose their single valence electron ($Cs[Xe]6s^1$) which is taken by the more electronegative secondary ion species such as oxygen. The sputter beam is always rastered over a larger area than the analysis area, in order to prevent crater edge effects that can distort the data. Figure 4.22 shows the beam alignment on the A-grid on the sample holder, this ensures the beams are coincident and ensures the analysis beam will be in the centre of the craters during measurements. The areas used for both primary and sputter beam rastering will be mentioned in the captions of the data figure in the following results chapters.

The primary ion beam can be used in two modes either in High Current Bunch Mode (HCBM) or Burst Alignment Mode (BAM) [237]. HCBM uses a short pulse of

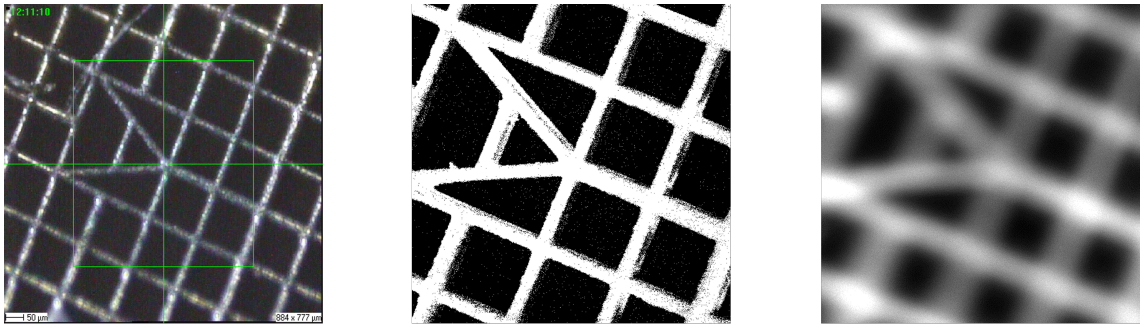


Figure 4.22: 500x500 μm images using 1024x1024 pixels, optical image of A-grid (left), SI image using a Bi^+ primary ion beam on the A grid (centre), and an SI image from the Cs^+ sputter beam on the A-grid (right). The alignment of the beams was done to avoid analysing crater edges, the poor definition in the image from the Cs^+ is due to it having a larger spot size.

$\sim$ 20ns of the primary ions which go through the condenser in order to form a smaller packet of ions of $\sim$ 0.6ns (i.e. bunched) this will allow more time for the secondary ions to go through the ToF analyser and improves the mass resolution in comparison to burst mode. BAM uses a much longer primary ion pulse of $\sim$ 100ns which is then split into shorter pulses $\sim$ 1 ns using a MHz signal (i.e. burst mode). The comparison between HCBM and BAM is made using a gallium liquid metal ion source (LMIS) by De Souza *et al.* [237]. However, this knowledge can still be applied to the ToF-SIMS instrument used in this work which uses a bismuth LMIS. Work done by Mazarov *et al.* [238] and Bischoff *et al.* [239] compare Bi^+ LMIS to Ga^+. Bismuth was chosen as it is the heaviest, non-radioactive element in the periodic table and exhibits a relatively low melting point of 271.4 ^{o}C to its neighbouring elements. Bismuth has many isotopes but only one has a high half-life which is 2.01×10^{19} years for ^{209}Bi making it 100 % abundant, therefore no requirement for a mass filter. When Bi LMIS was compared to Ga LMIS on a NiTi shape memory alloy substrate, Bi LMIS showed a five-fold higher sputter rate when operated on the same conditions [238]. Similar results were shown when applied to other substrates including Si, SiO_2 and Ge, Bi LMIS also showed a much lower penetration depth vs that of Ga LMIS with the same acceleration voltage, this is because Bi is heavier than Ga, hence slowing the impact on the substrate. A side advantage of using a Bi LMIS in this

work over Ga LMIS is that the samples studied herein contain gallium which would be difficult to analyse with a gallium analysis beam.

The ToF-SIMS instrument used in this work was always operated in burst mode, to prevent saturation of the detector. This mode will not hinder the collection of minor secondary ion isotopes which is used for the IEDP studies with ^{18}O. Higher lateral resolution in comparison to bunched mode is achieved with burst mode, which is vital when secondary ion map data are collected especially to distinguish between bulk, pores, and grain boundaries. This is made possible as the primary ion beam spot size for burst mode is between 350-400 nm whereas it is 4 μm in bunched mode. The ToF-SIMS instrument also allows the possibility to improve the lateral resolution to 150-200 nm using extreme imaging mode (i.e. the beam is collimated). However, this was not used, instead, a greater pixel density was applied if higher quality images were necessary, pixel density is different for each analysis area, this information is mentioned in the captions of the respective figures.

The primary ion gun was used in burst mode with an accelerating voltage of 25 keV (default setting by IONTOF) and a current of around 0.20 pA (measured using faraday cup) and pulsed to seven peaks for the mass spectrum, burst delay was altered to ensure all peak heights were similar in the mass spectrum. A caesium sputter beam was applied using a 2 keV accelerating voltage and around 150 nA current. A flood gun was also used as a charge compensation method because all samples herein are electrically insulating. The measurement was done in non-interlaced mode with one second for analysis, one second for sputtering and one second for collection.

Before continuing with measurements the mass spectrum which is obtained first with the primary ion beam rastering over the chosen analytical area is calibrated. To calibrate the mass spectrum species such as H^-, C^-, CH^-, C_2H^-, CH_2^-, Cl^- and, F^- are used as these are typically found as contaminants on sample surfaces. Species used for calibration are not the same secondary ions of interest during the analysis. This work focuses on collecting negative secondary ions such as LiO^-, GaO^-, LaO^-, ZrO^-,

etc. All data is analysed on IONTOF 5 measurement explorer software which allows the observation of all other secondary ions species of the same polarity at the time of analysis, which is an advantage of a ToF analyser as mentioned previously.

Quadrupole FIB-SIMS (Hi5)

In the latter stages of this PhD, the contribution was made to potential future work using a SIMS instrument in the development stages. The focused ion beam SIMS with dual quadrupole analysers nicknamed the "Hi5" is being used to assist with *in-operando* SIMS measurements. Only the technique development and initial measurements using the Hi5 will be shown in this thesis. The Hi5 was developed by Dr Richard Chater at Imperial College London, with engineers at Hiden Analytical and Oregon Physics. The instrument was constructed using the grant proposed by Dr Aguadero, Professor Skinner, and Professor Kilner of Imperial College [240].

The Hi5 uses a plasma ion source as both the analysis and sputtering beam (dynamic SIMS), the primary ion column was developed by Oregon Physics. There are three options for the plasma source which include xenon, oxygen, and hydrogen, with only the xenon currently in full operation at the time of this work. Operating conditions for the Xe^+ beam are accelerating voltages ranging from 1 to 30 keV and currents from 1 pA to 1 μA. Beam spot sizes down to 35 nm is possible with 30 keV and 10 nA with Xe^+ which is set using the Hyperion Software by Oregon Physics. The spot size was determined using the generated secondary electron image collected using the SED detector and line scan analysis on ImageJ software. secondary electron and ion images are viewed using Raith Nanofabrication software which is used to control the primary ion beam.

The Hi5 is equipped with dual quadrupole analysers for simultaneous positive and negative secondary ion collection, with mass spectra observed on the MASoft software by Hiden and depth profiles and SIMS Imaging on the Mapper software by Hiden. The Hi5 main chamber is also fitted with a caesium and electron flood gun. *In-operando* temperature studies are possible as the sample holder stage can be heated and cooled

with liquid nitrogen, electrochemical measurements can be done in the main chamber during SIMS analysis as there are kleindiek mico-manipulators that can be connected to a potentiostat or FRA. The inside of the main chamber of the Hi5 is shown in figure 4.23.



Figure 4.23: Image inside the Hi5 main chamber with all components labelled. The sample holder and stage were removed during the time of this picture. electron flood gun and caesium gun are not visible from this angle and are located on the opposite side.

There are two pre-chambers, one is for loading samples, which can be done using a vacuum suitcase by Ferrovac, this pre-chamber also allows for optical characterisation of the sample using a detachable white light interferometer. The second pre-chamber is for *in-situ* preparation where samples can be isotopically labelled using D_2O before transferring them into the main chamber for diffusion studies.

4.7 Isotopic Exchange Depth Profile (IEDP)

To understand the role of oxygen vacancies and grain boundary chemistry of the garnet material, isotopic exchange depth profile (IEDP) was done. IEDP works by enriching the samples with oxygen-18 isotope via gas diffusion in other words labelling the sample, before SIMS depth profiling. This, in turn, can provide self-diffusion coefficients (D^*) which give an indication of oxygen mobility in the material. IEDP is a widely used method of characterising fuel cell materials and has been successfully demonstrated in previous work by Kilner and Chater *et al.* [88, 90, 241].

4.7.1 Isotopic Exchange

Sample preparation for isotopic exchange is done as described above for SIMS analysis, where the LLZO pellets are polished to 0.25 μm roughness and thermally grooved to 900°C before entering the quartz exchange tube. ^{18}O is used for the isotope exchange as it is the second most abundant isotope of oxygen at 0.205% compared to the most abundant isotope which is 99.757% for ^{16}O. The least abundant isotope of oxygen is ^{17}O at 0.038% and it is not possible to distinguish its signals in the mass spectrum using the ToF-SIMS as it overlaps with that of OH^- which has a mass of 17.00276 amu during negative secondary ion collection, even though the mass resolution ($m/\Delta m$) for ToF analysers is *circa.* 10,000. $^{18}O_2$ is used as the tracer isotope for this technique as it is cheaper and in higher abundance than ^{17}O and can be easily detected and observed in the mass spectrum from ToF-SIMS.

Before the samples are exchanged, some criteria need to be followed and these include; (1) the shape - samples should be in the form of a pellet or half a pellet, small cubes should be avoided [242], (2) the thickness - the thickness of the samples used should be higher than $4\sqrt{D^*t}$ where D^* is the diffusion coefficient and t is the isotopic exchange time. sample thickness is important to prevent artificially increased diffusion tails which may occur if two diffusion paths meet from either side, (3) the density - the relative density of the samples should be greater than 95% in order to avoid short circuit diffusion through pores [243].

The isotopic exchange set-up is shown in the schematic in figure 4.24; the exchange rig is an in-house constructed apparatus. The apparatus is known as the dry exchange rig and provides a means of controlled diffusion experiments. The rig is comprised of a tube furnace which can be rolled on and off the quartz tube which is used to hold the sample in the necessary atmosphere, there are three gas reservoirs attached and these include nitrogen for venting the system before opening and disconnecting the quartz tube, O_2 for doing pre-annealing and remove any oxygen concentration gradients in the samples during preparation and the $^{18}O_2$ reservoir for the isotopic exchange, each cylinder can be opened independently and the gas pressure in the sample tube and temperature is recorded digitally on a dedicated computer. The rig has a residual gas analyser (RGA) (by Hiden Co.) attached to monitor the $^{18}O_2$ fraction before and after the exchange is done. The system has two pumps, the first is the roughing pump to initialise the vacuum from the ambient atmosphere before the turbo pump is switched on to achieve higher vacuum levels down to 2x10^{-}8 mbar.

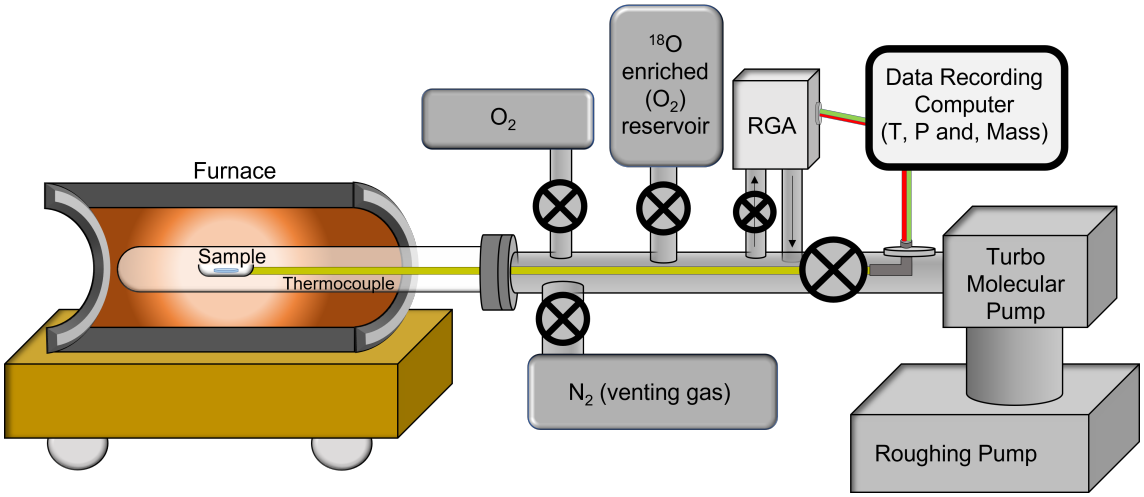


Figure 4.24: Schematic of dry exchange rig

For oxygen diffusion experiments samples are first placed into a clean and dry quartz tube and connected to the vacuum system, ensuring the thermocouple is touching the sample holder. The system is then pumped down with a roughing pump to achieve a vacuum level of approximately 0.05 mbar before turning on the turbo pump which provides a vacuum level of around 4x10^{-7} mbar before the quartz tube is closed to the vacuum.

200 mbar of oxygen is added to the quartz tube and the pre-heated furnace at 350°C is rolled onto the tube. A pre-annealing step with O_2 gas is done to eliminate any oxygen concentration gradients in the samples and is typically 10 times longer than the time used for the isotopic exchange with $^{18}O_2$ enriched gas. The time for the exchange is important as it affects the penetration depth of the tracer isotope. Once the pre-annealing with the unlabelled oxygen is done (typically overnight) the furnace is rolled away and the tube is left to cool to room temperature. The sample tube is then evacuated to $4x10^{-7}$ mbar and filled with 200 mbar of $^{18}O_2$ enriched oxygen gas. before rolling the furnace back on and ensuring the sample is in the hot zone of the furnace. The isotopic exchange is done for 45 minutes following the procedure described by Kubicek *et al.* [32], which will allow for results to be compared as the same conditions were implemented. The temperature and time for the exchange is recorded using the computer. Once the tracer isotope exchange is done the samples are removed and transported to the ToF-SIMS as quickly as possible to minimise the formation of a corrosion layer. To investigate the effect of processing conditions on the oxygen vacancies and to obtain SIMS images of labelled ^{18}O samples chemical exchanges were done. Chemical exchange is when the samples are isotopically labelled using $^{18}O_2$ directly without any pre-annealing with O_2, so the oxygen concentration gradients may be more visible due to the samples processing conditions.

Diffusion profiles are obtained using the depth profile mode of ToF-SIMS, which are fitted to the Crank's solution for a semi-infinite media using the TraceX application installed in Matlab developed by S. J. Cooper at Imperial College [244].

4.8 Electron Paramagnetic Resonance (EPR)

To detect the presence of free or unpaired electrons in LLZO, electron paramagnetic resonance (EPR) was employed. This section is split into two parts, the first providing a basic overview of the working principles of EPR and the second will be the sample analysis which was done by Dr. Irena Nevjestic, at Imperial College London.

4.8.1 Working Principles of EPR

As the technique name suggests, unpaired (paramagnetic) electrons are required for this method of analysis to be useful. EPR is based on the interaction of unpaired electrons with the applied magnetic field (B_0), which is produced by a magnet on the instrument. This interaction is known as the Zeeman Effect. When an external magnetic field is applied to the unpaired electrons, they begin to act like a compass i.e. they will align with or against the magnetic field. Because electrons have a spin quantum number (m_S) of 1/2, the electrons which align parallel to the magnetic field have a spin $m_S = -1/2$ and those antiparallel will be $m_S = +1/2$ as shown in the schematic below (fig.4.25).

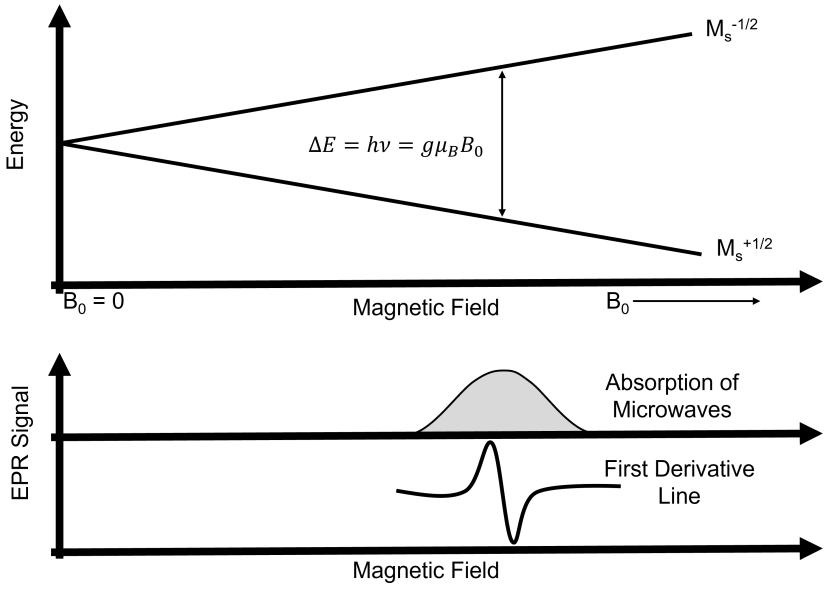


Figure 4.25: EPR operation basics.

The split in the energy between the two spin states is due to the interaction

involving the magnetic field and the electron spins and is given by equation4.19

$$\Delta E = g\mu_B B_0 \Delta m_S = g\mu_B B_0 = h\nu \tag{4.19}$$

Where g is the g-factor, μ_B is the Bohr magnetron, B_0 is the magnetic field, and Δm_S is the change in spin state. The energy difference is equal to $h\nu$ for the spectrometer. Hence at the magnetic field at which the energy difference between the two spins equals that of $h\nu$, absorption of the energy results and is termed the field of resonance as shown in the schematic above with the absorption peak. The first derivative of the absorption signal is used to deduce the EPR signal. Note that the field for resonance value is not used as a fingerprint for identifying the cause of the response. This is because different EPR instruments use different microwave frequencies to provide the same signal at various magnetic fields. Therefore the g-factor is used as it is independent of microwave frequency, this is shown in table 4.1 [35].

Table 4.1: Field of resonance for g = 2 sample at various microwave frequencies [35]

Microwave band	Microwave frequency (GHz)	B_0 (for g =2) gauss
L	1	390
S	3	1,070
X	9	3,380
K	24	8,560
Q	35	12,480
W	94	33,600

The g-factor can help to determine what is causing the signal, for example, a "free electron" will have a value of 2.0023. Whereas unpaired electrons (radicals) on elements in organic compounds e.g. benzosemiquinone have their spin density on the oxygen with g-factor $\sim$ 2.004 and the oxygen radicals in nitroxide g $\sim$ 2.006. The difference in g-factor is a bit more distinct for inorganic species for example Cu^{2+} will have a g-factor up to 2.3 whereas a vanadyl ion has g $\sim$ 1.96 [35].

In many cases, EPR is used with more complicated samples that will produce

multiple signals depending on their nuclear spin number and whether the unpaired electron is being influenced by neighbouring nuclei, this phenomenon is termed the hyperfine interactions and is important in deducing the environment the unpaired electron resides. The nuclei of an atom in a compound may often have their own magnetic moment, therefore behaving as a tiny magnet as it radiates its own local magnetic field upon the electron, which can result in peak splitting of the EPR signal. The number of splittings (hyperfine lines) of the EPR signal is determined using the nuclear spin number (I) in the equation $2nI + 1$ where n is the number of symmetry equivalent nuclei. The intensity of the signals is also indicative of the concentration of the unpaired electrons, providing suitable measurement conditions are applied. For more depth into the operation of EPR and the theory, refer to Quantitative EPR book by Gareth R. Eaton [35].

4.8.2 Sample Analysis with EPR

The Bruker X-band (9.5-9.9 GHz) continuous-wave (CW) ELEXSYS E500 system with MD-5 resonator was used for EPR measurements. The CW operation allows high sensitivity, down to 1x10^9 spins (i.e. detection limit). The spectrometer is fitted with a 1.45 T magnet. All measurements were conducted on powdered samples at room temperature with broad scans from 50-1000 mT magnetic field sweep with three scans each to observe possible signals. The magnetic field sweep range was narrowed if signals were observed and scanned five times to further improve the signal-to-noise ratio.

All measurements and data handling were done with the help of Dr Irena Nevjestic. Data analysis and fitting were done using the easy spin package installed on to Matlab. To fit the EPR data, estimated g-factor values of ∼2.001 for 6 observed peaks and a hyperfine value of 215 MHz was used. To fit the background response from the sample holder a g=2 was also used and no hyperfine constant, and a microwave frequency of 9.55 GHz.

Chapter 5

Sintering Atmosphere and Crucible Choice for Ga-LLZO Preparation

In this chapter the change in atmosphere and crucibles during heat treatments are investigated systematically on $Ga_{0.25}$-$Li_{6.25}La_3Zr_2O_{12}$ (Ga-LLZO) using bulk characterisation methods. Sintering Ga-LLZO under reducing (argon) and oxidising (oxygen) gases are done and the use of three different crucibles, namely alumina (Al_2O_3), magnesia (MgO), and zirconia (ZrO_2) are employed as they are commonly used in literature. Characterisation techniques used in this chapter include XRD, SEM, ICP-OES, micro indentation for hardness measurements, density, EIS, galvanostatic cycling, and EPR.

Some of the Ga-LLZO samples used in this chapter will be used in chapters 7 and 8, therefore this chapter will also provide results on the quality of the material. XRD is used to check for phase purity and microscopy for microstructure analysis. Electrochemical characterisation using impedance spectroscopy will give performance information on the ionic conductivity, time-resolved constant potential DC measurements are used to measure the total electronic conductivity, which is followed by galvanostatic cycling measurements on Li|Ga-LLZO|Li symmetric cells. Finally, a new attempt to understand possible "free" electrons is studied with EPR spectroscopy.

Samples used herein, are assigned abbreviations based on dopants, crucibles and atmospheres used. For example, if Ga-LLZO is sintered on an alumina crucible whilst, under an argon atmosphere, the nomenclature used will be "GAA". On the other hand, if the sample is processed with a zirconia crucible and under oxygen, it will be labelled as "GZO", this is summarised in the table below (table 5.1).

5.1 Phase Purity

$Ga_{0.25}$-doped $Li_{6.25}La_3Zr_2O_{12}$ used in this chapter was purchased from Toshima Ltd. The as-purchased sample was first checked for purity using powder XRD to inspect for the presence of impurities or secondary phases before investigating the different processing conditions. The XRD pattern was fit to a single phase standard with the same stoichiometry using Le Bail refinement as shown in figure 5.1.

Table 5.1: Sample name for Ga-LLZO SE after processing.

Abbreviation	Crucible	Atmosphere
GAA	Al_2O_3	Argon
GAO	Al_2O_3	Oxygen
GMA	MgO	Argon
GMO	MgO	Oxygen
GZA	ZrO_2	Argon
GZO	ZrO_2	Oxygen

The sharp reflections imply that the cubic structure is the majority phase, with negligible peak splitting, which is indicative of t-LLZO phases. Space group $I\bar{4}3d$ was determined which is in line with the literature for Ga-LLZO. No apparent impurity phases are present in this starting material. A poor $\chi^2 = 7.87$ is primarily due to the intensity of the peaks not matching with the reference, this is expected in Le Bail refinement as peak intensity is considered to be all the same. On the other hand, lattice parameters can be obtained and are used to determine the cell volume being, 219.05 nm^3, which is consistent with literature on similar Ga-LLZO compositions [135].

For each of the samples prepared under the various conditions, XRD analysis was done on the pellets. The XRD patterns for each are displayed in figure 5.2.

Crucible

The XRD pattern for GAA, GMA, and GZA pellets are shown in figure 5.2a. All diffraction patterns show a pure cubic crystal structure when compared with the reference of a powder Ga-LLZO giving an averaged peak intensity. Higher peak intensity can be seen at 52° vs those at 51° for all argon sintered samples in comparison to the reference. It is also apparent that reflections at *circa.* 26° and 27° exhibit a change in relative intensities as compared to the standard. The change in intensity may be due to crucibles altering grain orientation as the samples are in pellet form. To confirm whether grain orientations are influenced by crucible choice, SEM electron back-scatter diffraction (EBSD) would need to

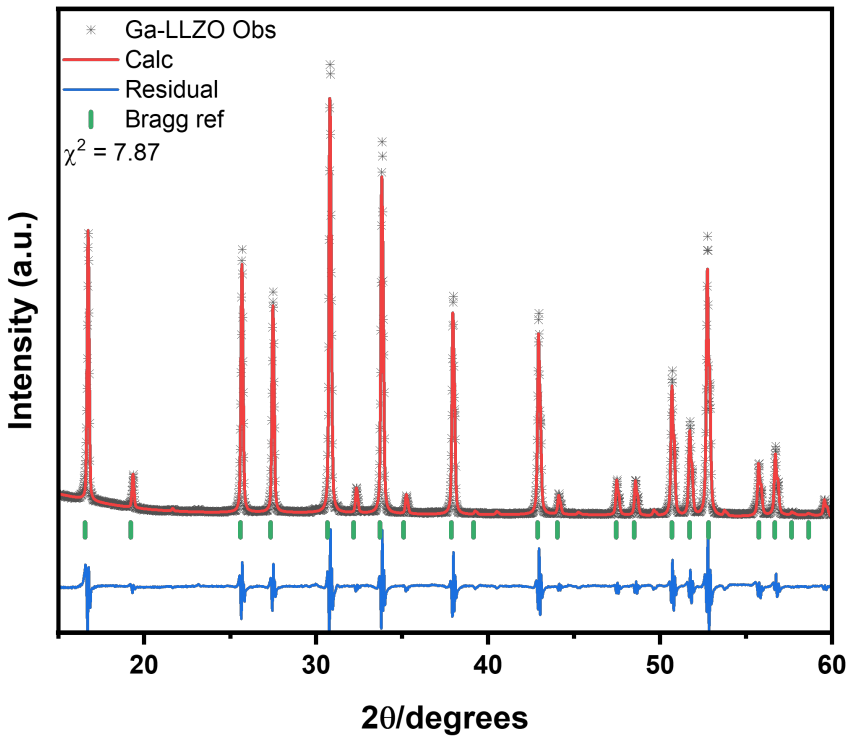


Figure 5.1: Le Bail refined XRD pattern for as purchased Ga-LLZO, showing no noticeable reflections from impurities or secondary phases. Reference of Ga-LLZO from ICSD ref. 136577

.

be employed to visualise grain orientation. There are little to no reflections from impurities between the different crucible preparations. The insets in figure 5.2 are of the pellets post-heat treatment. The use of different crucibles does not have a drastic effect on the pellets' optical appearance. However, for GZA samples, a slight blue tinge is apparent, which is more noticeably observed by eye. All samples sintered under argon were semi-transparent primarily due to large grain size as discussed later.

Le Bail refinement was done on all the XRD patterns to determine the cell volume, which is recorded in Table 5.2 and the refined XRD patterns shown in the appendix figure A.1. Again very little change in the cell volume is observed, with GMA samples having the largest cell volume of 219 nm^3. A possible explanation for the increased cell volume of

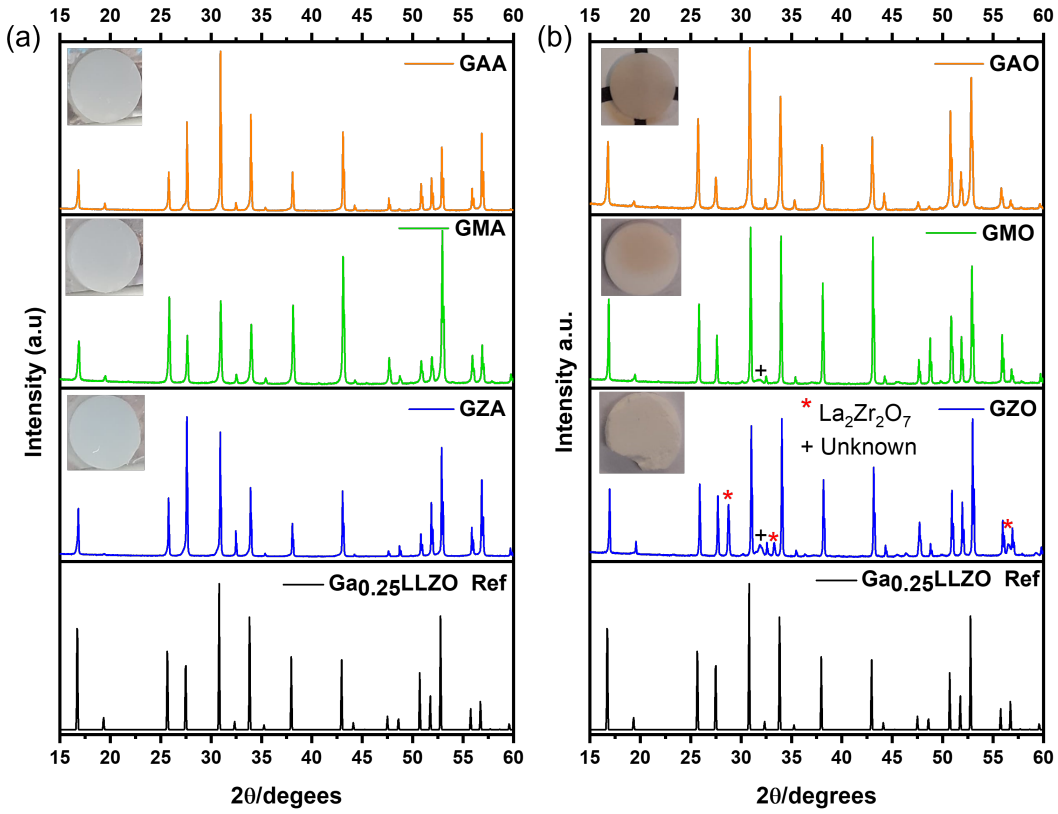


Figure 5.2: XRD pattern of all Ga-LLZO samples after processing, (a) all samples sintered under argon with different crucibles, (b) all samples sintered under oxygen with different crucibles. A red asterisk indicates the presence of pyrochlore secondary phase in GZO, and a black cross indicates reflection from an unknown material.

GMA in comparison to GAA and GZA may be due to the incorporation of Mg from the crucible at high temperatures of 1150°C. Mg^{+2} has a larger ionic radii than Al^{+3}, 79 pm vs. 57 pm respectively [245], this may increase the lattice volume when comparing GAA with GMA. However, no such mechanism is known of at this moment or has been reported for Mg incorporation, unlike the mechanism of a Li_2O-Al_2O_3 liquid eutectic phases forming at 1055°C [194], which is below the sintering temperatures used in this work. A report by Konar *et al.* [246] shows that a Li_2O-MgO liquid phase would be possible at greater temperatures (>1650°C), far above those used in this work. On the contrary, in this work, some Ga-LLZO pellets had melted on the MgO crucibles when sintered at 1150°C under argon, as shown in figure A.2.

Atmosphere

By changing the heat treatment atmosphere a significant change in the pellet's appearance was noted, when compared to those sintered under argon. Figure 5.2b shows the XRD patterns of all samples sintered under flowing oxygen. All pellets appeared with a beige tinge, which may be due to changes in microstructure, grain sizes, impurity phases or oxidation of the Ga-LLZO. Only the inset image of the GAO pellet in figure 5.2b shows a semi-transparent sample, as you can vaguely see the black cross through the pellet. Impurity signals are noticeable in GMO and GZO XRD patterns. Two signals are reported, that of pyrochlore ($La_2Zr_2O_7$) [135] which is a common impurity phase formed in LLZO, thought to be due to lithium loss during heat treatments. The other broad reflections observed for GMO and GZO XRD patterns could not be identified. All cell volumes of the samples sintered under oxygen were increased which may be from less oxygen lost which is highly likely when processing under reducing conditions as predicted by Squires *et al.* [70].

Table 5.2: Stoichiometery of samples after processing determined via ICP-OES and oxygen determined using equation 4.6, cell volume obtained from XRD refinement and relative densities.

Sample	Stoichiometry from ICP	Cell Volume (nm^3)	relative density (%)
Ga-LLZO	$Ga_{0.23}Li_{5.94}La_3Zr_{2.02}O_{11.86}$	219.05±0.05	-
GAA	$Ga_{0.20}Li_{5.76}La_3Zr_{1.66}O_{11}$	216.64±0.03	97±1
GAO	$Ga_{0.29}Li_{5.62}La_3Zr_{2.19}O_{12.12}$	219.92±0.08	95±2
GMA	$Ga_{0.24}Li_{5.50}La_3Zr_{2.01}O_{11.63}$	218.66±0.06	98.0±0.5
GMO	$Ga_{0.27}Li_{5.98}La_3Zr_{2.04}O_{11.98}$	218.96±0.03	95±1
GZA	$Ga_{0.27}Li_{6.28}La_3Zr_{2.25}O_{12.54}$	217.39±0.03	96.5±0.2
GZO	$Ga_{0.23}Li_{4.76}La_3Zr_{2.02}O_{11.28}$	218.70±0.05	81±2

5.1.1 Density and Hardness

Higher densities were achieved from sintering under argon with all crucibles at around 98%, and lower relative densities were obtained with their oxygen atmosphere-treated

counterparts. This may be due to moisture contamination as oxygen heat treatments are done outside of the Ar glovebox, or the change in furnace type. To mitigate moisture during sintering a constant flow of dry oxygen is passed through the tube furnace, with simultaneous vacuum on the opposite side and metal tubing. The lowest densities were from both GZA and GZO samples. Sintering using zirconia crucibles produces less dense LLZO pellets as it cannot provide a liquid phases sintering mechanism which is considered to improve the density as seen when using alumina crucibles. All relative density values are recorded in table 5.2.

Hardness measurements were done as it was noticed that samples from the oxygen atmosphere and zirconia crucible, especially GZO and GZA pellets were difficult to handle, brittle and delaminate post-sintering. Figure 5.3 shows the Vicker's Hardness values in comparison to lithium metal. Both samples from the zirconia crucible showed lower levels of hardness compared to the others. The highest levels are obtained by GAA and GMA which corresponds to higher densities.

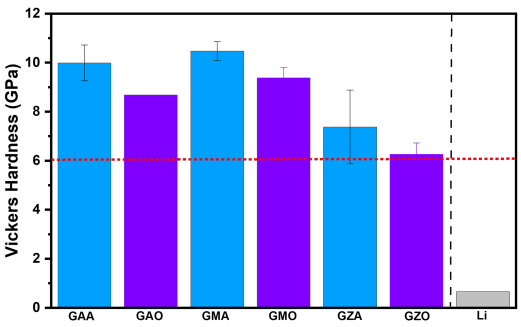


Figure 5.3: Vicker's Hardness values of all samples, compared with lithium metal. The red dashed line indicates average literature values obtained for LLZO [25, 26].

5.1.2 Elemental Analysis

ICP-OES was used to determine the stoichiometry of the SEs after each treatment. Lanthanum was used as the standard with all other elements calculated with respect to it. A significant decrease in the Li quantity for GZO is determined at 4.76 Li p.f.u., which may

have been from lithium-free pyrochlore being present in GZO. The Ga molar fraction does not have a large variation between the samples, this may be expected as the processing conditions may not affect the concentration.

To determine if Mg is in GMA samples from the crucibles, ICP-OES analysis was done. Using an 11 ppm solution of Ga-LLZO to determine the Ga stoichiometry, *ca.* 2 ppm of Mg was obtained, the same is observed for Al from alumina crucibles in GAA samples. This equates to 2ppm of Mg or Al for 100 mg of GMA and GAA respectively. However, this was only seen for GMA as for GAO and GMO a 0.1 ppm Al and Mg response was recorded respectively.

Under ideal conditions, the oxygen stoichiometry should be equal to 12. LLZO with O less than 12 moles p.f.u. is expected as with lithium loss, oxygen vacancies form to stabilise the charge imbalance, equation 4.6 is used to determine the oxygen nonstoichiometry. GAO with $O_{12.12}$ is reported which may be from an uptake in oxygen from the atmosphere at high processing conditions, which may lead to the increase in cell volume. The discrepancy may also be from sample preparation as not all the GAO may have dissolved, or undetectable secondary phases such as $La_2Zr_2O_7$ (pyrochlore), may have led to higher Zr concentration in the solution. A limitation of ICP analysis is its requirement for samples to be entirely in solution form to ensure accurate measurements. This might explain the discrepancies in the obtained stoichiometries, as Ga-LLZO does not fully dissolve in water and nitric acid. It may necessitate the use of hydrofluoric acid for complete dissolution

5.2 Microstructure

The microstructure was examined using optical and electron microscopy. Optical microscope images were taken after sintering and SEM images were taken after polishing and thermal grooving. The detection mode used for SEM was chosen on which provided better grain boundary definition. For all samples sintered using alumina crucible, grain sizes of $>$ 100 μm were the majority when sintered under argon, whereas under oxygen atmosphere

a near bimodal distribution of grain sizes was observed at $\sim 10\mu$m and > 100 μm, see figure5.4.

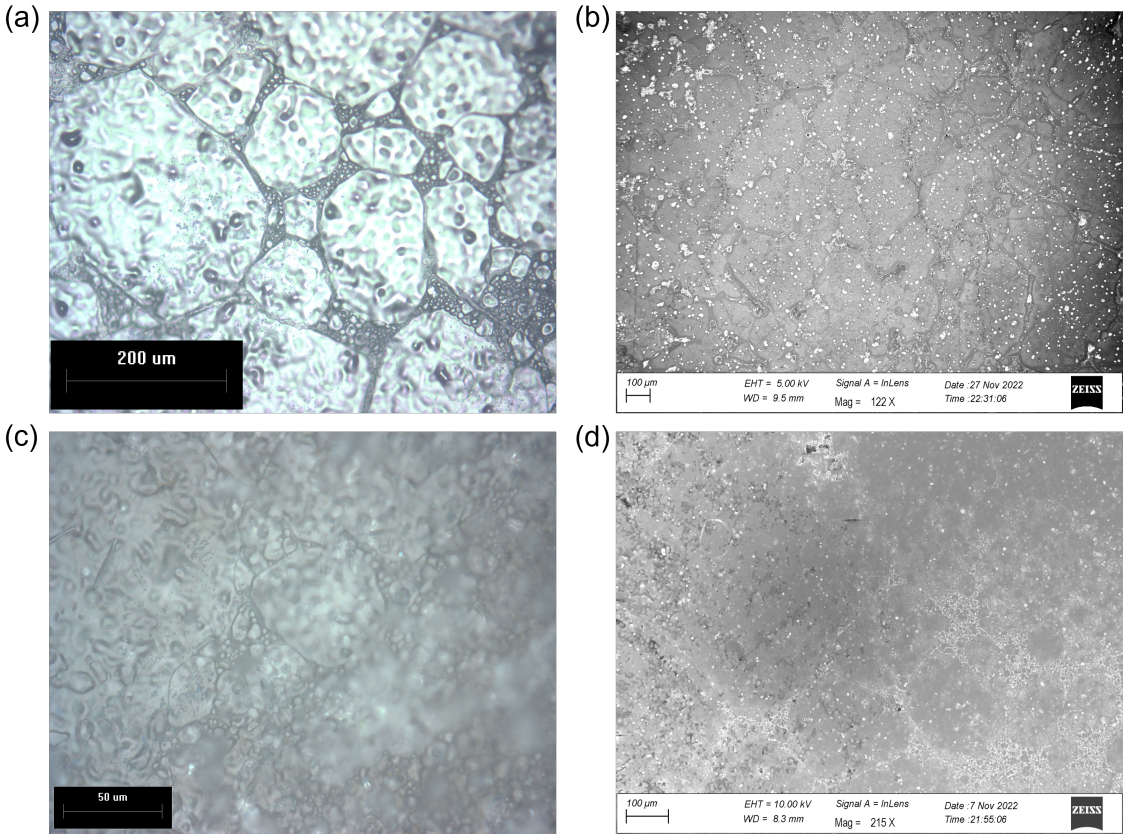


Figure 5.4: Microstructure images before and after polishing and thermal grooving from left to right (a) optical image of GAA, (b) SEM image of GAA, (c) optical image of GAO, and (d) SEM image of GAO

Similar observations are obtained for samples using MgO crucibles as shown in figure 5.5. However, the pellet surface after sintering shown in the optical images has a wave-like textured surface, which is removed from grinding/polishing, figure A.3 makes this more evident to see with the WLI image of a pre-polished pellet of GMA. Figure 5.5b shows the back-scattered image of a polished pellet of GMA; there are small white features which may be indicative of secondary phases composed of high atomic number elements. The secondary phase to give this signal is commonly associated with pyrochlore, although it may not be in a high enough concentration to be detected by XRD.

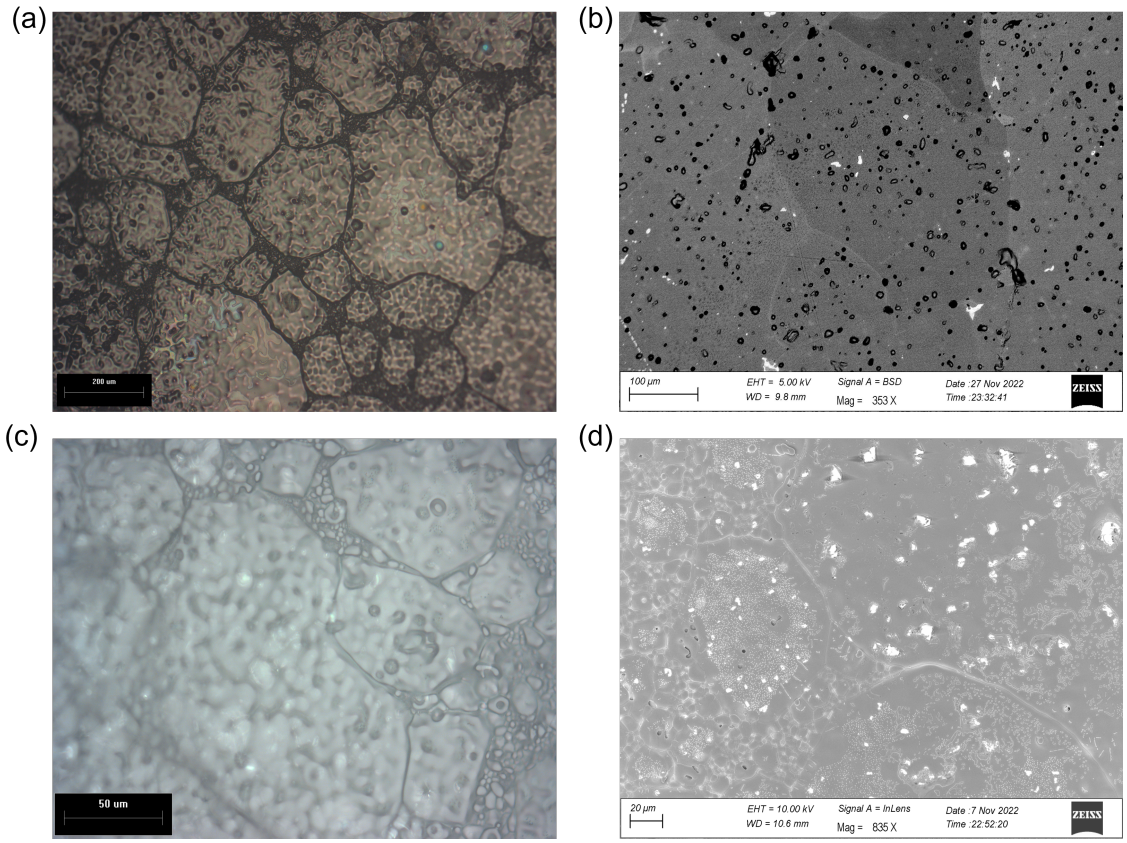


Figure 5.5: Microstructure images before and after polishing and thermal grooving from left to right (a) optical image of GMA, (b) SEM image of GMA, (c) optical image of GMO, and (d) SEM image of GMO.

Samples sintered using zirconia crucibles showed similar grain sizes when sintered under argon (GZA). On the other hand, noticeably smaller grains developed for GZO samples ranging from 5-20 μm as seen in figure 5.6, and no suitable optical micrographs

were achieved for GZO grains.

There is a difficulty in analysing LLZO samples with SEM to obtain highly defined images because the samples are known to reduce from long exposure to a focused electron beam. Upon contact of the sample with the electron beam, lithium ions can reduce to lithium metal and extrude which can be seen by the white features on the GZO sample in figure 5.6c. This has recently been shown by Zhu *et al.* [247], where an electron beam is focused around the LLZO grain boundary which results in lithium metal formation on the top surface, hence indicating that local chemistries at grain boundaries are prone to Li-ion reduction.

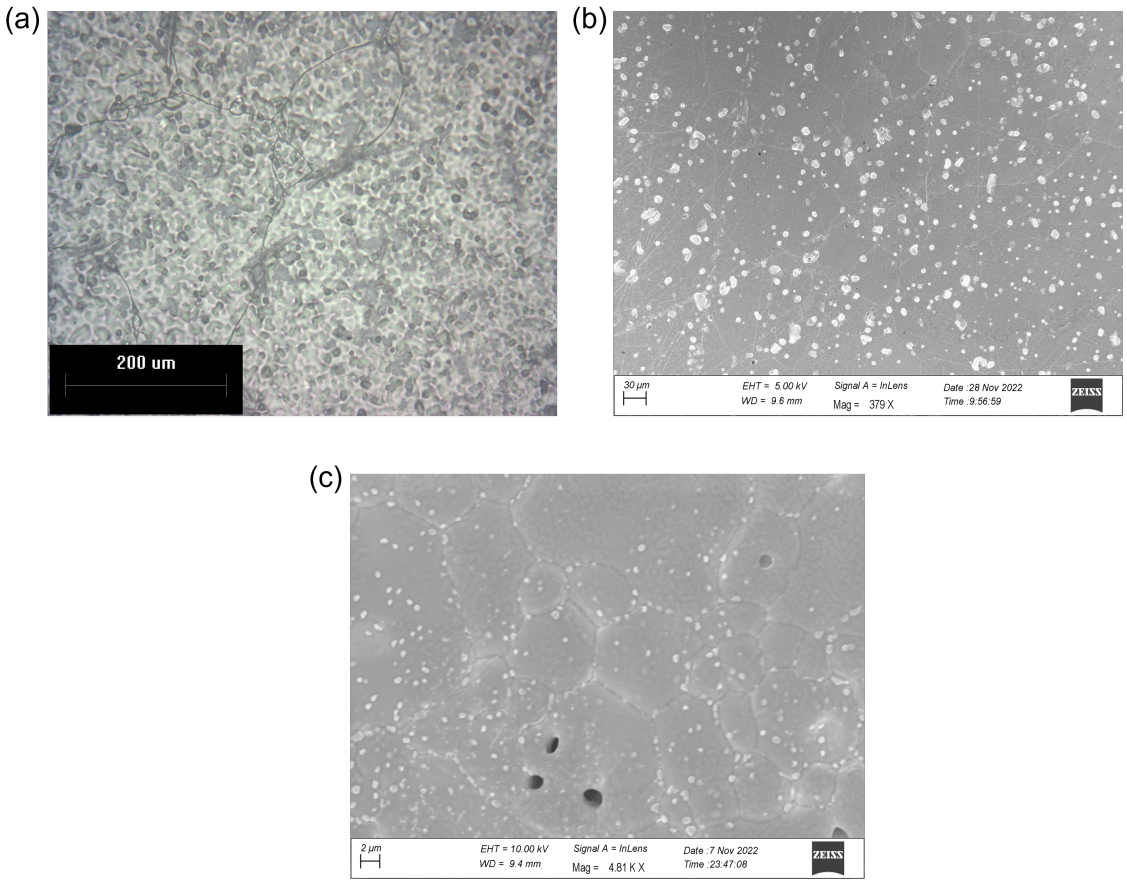


Figure 5.6: Microstructure images before and after polishing and thermal grooving from left to right (a) optical image of GZA, (b) SEM image of GZA, (c) SEM image of GZO. (no optical image of GZO is presented, owing to the difficulty of getting a suitable image showing grain size before polishing and thermal grooving)

5.3 Electrochemical Measurements

In this section, the results from EIS, time-resolved DC measurements and galvanostatic cycling will be presented. EIS measurements were used to measure the ionic conductivity and interfacial resistance of the solid electrolytes using both Au blocking and Li metal electrodes respectively. Electronic conductivity measurements were done using constant applied voltage on an Au|LLZO|Au configuration. Electronic conductivity data are becoming a popular parameter to determine in solid electrolytes, in order to understand whether the processing conditions have an influence on this property.

The cyclability and onset of dendrites are measured using galvanostatic cycling. This analysis technique provides the current density at which the SE fails, known as the critical current density (CCD) based on the initial voltage drops.

5.3.1 Ionic and Electronic Conductivity

The ionic conductivity values presented here are at 25°C. The bulk (grain interior) conductivities for all samples processed under argon gave similar conductivity values of approximately 0.5 mS/cm. This may be expected as grain sizes are of similar magnitude, as seen from the SEM images previously. The total ionic conductivity is around 0.25 mS/cm for argon-sintered samples (data from GAA and GZA samples). Regarding GMA no GB conductivity data could be determined, hence no σ_{total}. The total activation energy of 0.22 and 0.25 eV, for GAA and GZA respectively was determined. All EIS data are tabulated in table 5.3 and figures of Nyquist and Arrhenius plots are discussed below by comparing processing atmosphere.

The Nyquist plots for GAA and GAO are presented in figure 5.7a and c, which were measured at 25°C. Both Nyquist plots were obtained using Au|LLZO|Au symmetric cells and show contributions for bulk and grain boundary. The response was fitted using two RC parallel elements. In all cases, the Nyquist plots have been normalised to the electrolyte thickness for comparison of bulk and grain boundary contributions. There is a significant decrease in the ionic conductivity of GAO samples relative to GAA which are tabulated in 5.2. The higher ionic conductivity of GAA corresponds to literature for samples prepared in similar conditions [248]. The XRD analysis of GAA and GAO, shows no noticeable secondary phases that may affect the resistance of the material. However, possible contamination or secondary phase concentrations that are present may be in fewer quantities than the detection limit of XRD which is ∼1%. Higher resistance at the grain boundary may be due to impurities or secondary phases being present there. From the optical and SEM images of GAO in figure 5.4 it is clear there is more abundance of smaller grains which equate to more grain boundary regions per unit area, in comparison

to that of GAA with a larger grain size. The greater abundance of small grains in GAO may influence the GB conductivity. On the other hand, the significantly lower bulk ionic conductivity in GAO is unusual and unclear as to what may be the cause at this point and further work is required.

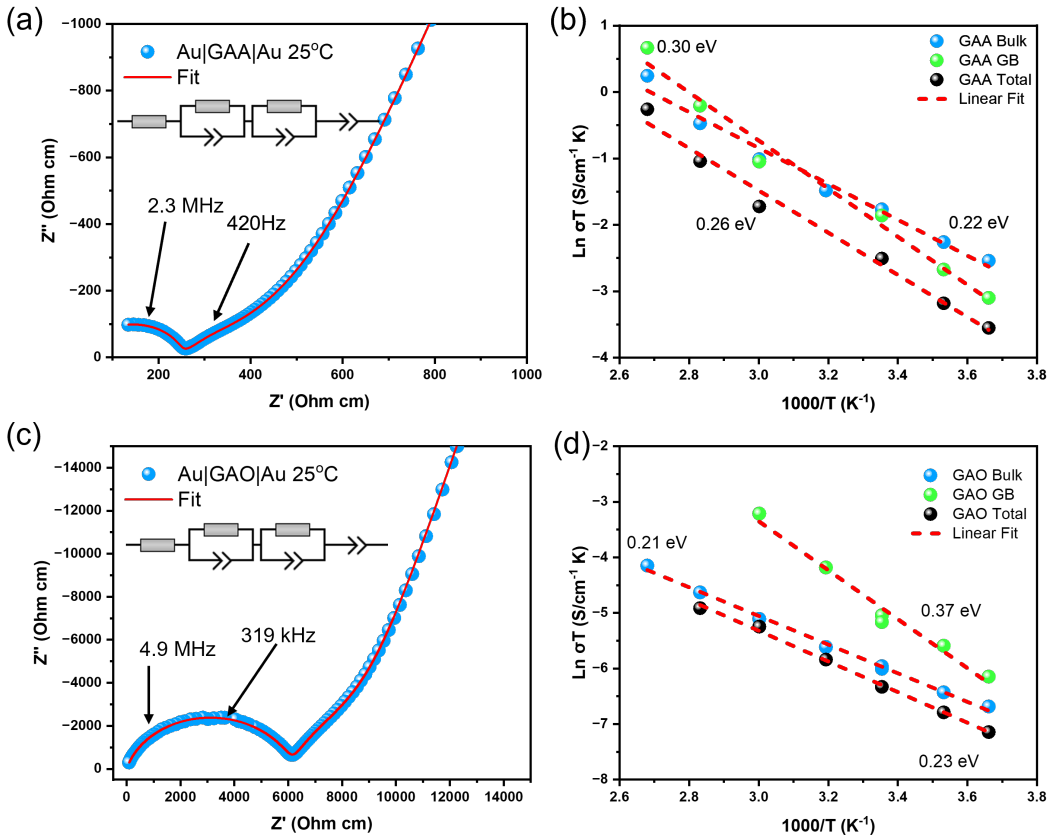


Figure 5.7: Au|LLZO|Au Nyquist and Arrhenius plots for GAA (a) and (b) respectively and for GAO (c) and (d). Inset on the Nyquist plot shows an equivalent circuit used to fit experimental data. Characteristic frequencies for bulk and grain boundaries are shown, calculated from 1/RC.

The reported interfacial resistance (R_{int}) is as expected based on work by Sharafi *et al.* [68], whereby, preparing the sample under an inert atmosphere and minimal exposure to moisture and CO_2 can lower the R_{int}. A benefit of sintering under argon is that it can be done inside a glove box, resulting in improved surface wettability, deduced from the lower interfacial resistance of 4.06 Ω/cm^2 for GAA. Furthermore, GAO had a higher value of 113.54 Ω/cm^2. The higher R_{int} of GAO is most likely to have come from the

surface corrosion layer (carbonates and hydroxides). Corrosion layers can reappear on GAO during the transfer from the tube furnace to the glove box. A possible method to confirm this observation may be to conduct the thermal etch in the glove box furnace after the densification of GAO pellets.

Despite the variation in bulk and GB conductivities, the total activation energies of GAA and GAO are similar at 0.22 and 0.23 eV respectively which is coherent with recent publications of samples with the same composition [133]. The capacitance value in table 5.2 is used in conjunction with literature by Irvine *et al.* [215] to determine the microstructure responsible for the signals. Constant DC potential measurements were done on Au|LLZO|Au cells to evaluate the electronic conductivity as Au can prevent contribution from Li ions although Li alloying with Au is still a factor to consider. Values of σ_{eon} are between 10^{-8} to 10^{-7} S/cm which again has been previously reported in literature [133,178]. Although Cu blocking electrodes were employed in literature by Han *et al.* [177] with similar conductivity values obtained.

Regarding samples prepared on MgO crucibles, only the bulk ionic conductivity of GMA samples could be derived. Nyquist plots for GMA could only be fitted sensibly using one parallel RC unit as shown in figure 5.8a and a single CPE element for the lower frequency tail. The bulk conductivity calculated (i.e. 0.52 mS/cm) was similar to that of GAA which may be due to similar microstructure and composition. The activation energy of the bulk (0.35 eV) shown in the Arrhenius plot in figure 5.8b is higher than the that reported for GAA, but is in the same region as expected for Ga-LLZO. The interfacial resistance of 20.49 Ω cm^2 is greater than that of GAA. The increase may possibly be due to crucible effects, such as the possible aluminium insertion into the sample surface of GAA which has been shown in literature [149]. Aluminium oxide on the surface has also been thought to improve the wettability of lithium metal to LLZO which was studied previously by Han *et al.* [173]. A capacitance value for the interface is reported to be 4x10^{-8} F, although it is also on the same order of magnitude as for GB responses [215]. The complex impedance plot for Li|GMA|Li (shown in figure A.3c) could not be fitted with

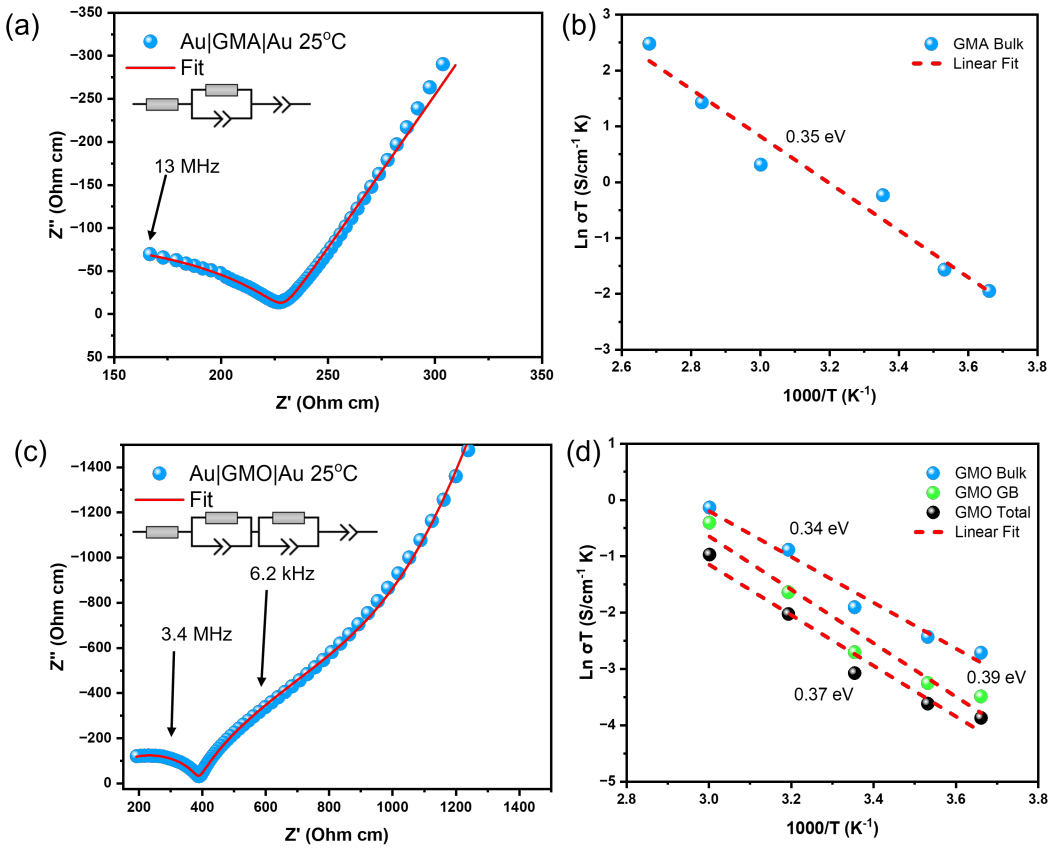


Figure 5.8: Au|LLZO|Au Nyquist and Arrhenius plots for GMA (a) and (b) respectively and for GMO (c) and (d). Inset on the Nyquist plot shows an equivalent circuit used to fit experimental data.

three parallel RC components to determine the bulk, GB and interface contributions. As a result only the R_{bulk} (grain interior resistance) and R_{Int} were obtained (see figure A3.c).

On the other hand grain boundary contribution could be measured via EIS for GMO samples, which is most likely from the difference in microstructure, with increased grain boundary density. GMO samples also presented possible impurity phases from the XRD pattern in figure 5.2b which corresponded to the pyrochlore phase and unknown impurity. As secondary phases have a tendency to form between grains it may result in the lower σ_{GB} which in turn has increased the GB activation energy to 0.39 eV.

The electronic conductivity of both magnesia crucible sintered samples were mea-

sured to be an order of magnitude lower than that of GAA and GAO at **ca.** 10^{-8} S/cm. Although the discrepancy is not a considerable amount, the difference may be associated with crucible choice. The investigation of possible Mg insertion spatially from the MgO crucible is discussed in Chapter 8 as it is already known that Mg is a contaminant using ICP methods.

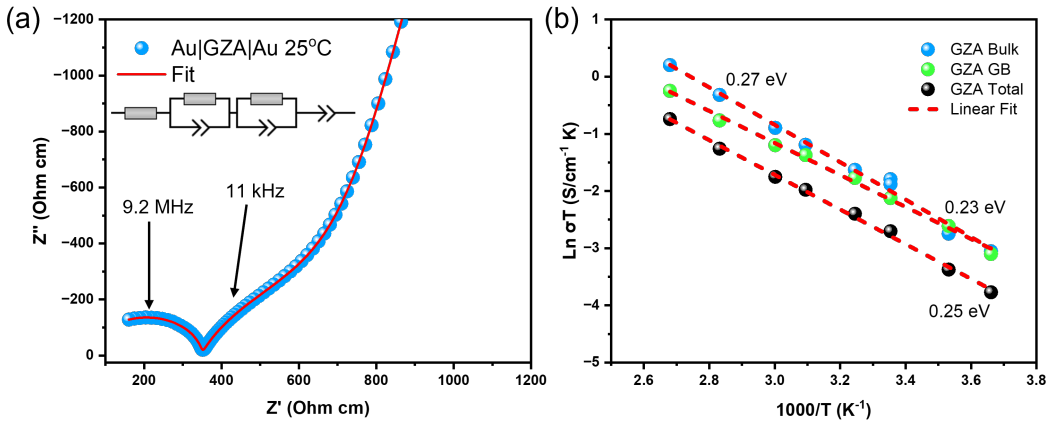


Figure 5.9: Au|LLZO|Au Nyquist and Arrhenius plots for GZA (a) and (b) respectively. Inset on the Nyquist plot shows an equivalent circuit used to fit experimental data. Characteristic frequencies for bulk and grain boundaries are shown.

Zirconia crucibles were used in this work as a control and as a possible inert crucible, in terms of no contamination, contrary to alumina crucibles. However, the use of zirconia crucibles leads to lower relative densities, described above. Therefore, only GZA could be characterised by EIS, because GZO samples would delaminate and fragment after sintering, aiding the difficulty to form a full pellet for electrode deposition. Figure 5.10 displays the Nyquist and Arrhenius plot using the Au|GZA|Au configuration. From the EIS data, both bulk and GB responses could be fitted, giving ionic conductivity of 0.51 and 0.40 mS/cm respectively. The ionic conductivity of both is lower than that of GAA but still in the range for reported Ga-LLZO values. Moreover, the total conductivity remains similar to that of GAA and with an interfacial resistance of *ca.* 20 Ωcm^2 which is similar to that of GMA. The total activation energy for GZA was measured to be 0.25 eV, again close to those of GAA and GAO.

In all cases, the electronic conductivity was measured to be in the range between 10^{-8} to 10^{-7} S/cm which is consistent with literature [178]. If we focus on lithium and electrons being the sole mobile charges a transport number of $\sim$0.99 is calculated for Li^+ in these materials. This is expected for LLZO and is required for it to be a successful solid electrolyte.

Table 5.3: Ionic conductivity, and capacitance values from EIS measurements at 25°C with Au|LLZO|Au cell, activation energy values from Au|LLZO|Au cell at a temperature range between 0-100°C, R_{int} from Li|LLZO|Li cell at 25°C. Electronic conductivity values form Au|LLZO|Au cell at 25°C

Sample	σ_{bulk} (mS/cm)	σ_{GB} (mS/cm)	σ_{total} (mS/cm)	R_{int} (Ω cm^2)	C_{bulk} (F)	C_{GB} (F)	C_{int} (F)	Total E_a (eV)	σ_e (S/cm)
GAA	0.57	0.52	0.27	4.06	$1.1\text{x}10^{-11}$	$1.0\text{x}10^{-7}$	$2.9\text{x}10^{-5}$	0.22±0.01	$2.63\text{x}10^{-7}$
GAO	$0.87\text{x}10^{-2}$	0.02	$0.60\text{x}10^{-2}$	113.54	$8\text{x}10^{-12}$	$1\text{x}10^{-7}$	$2\text{x}10^{-4}$	0.23±0.01	$1.27\text{x}10^{-7}$
GMA	0.52	-	-	20.49	$5\text{x}10^{-12}$	-	$4\text{x}10^{-8}$	-	$3.29\text{x}10^{-8}$
GMO	0.50	0.23	0.16	65.69	$1\text{x}10^{-11}$	$2\text{x}10^{-8}$	$3\text{x}10^{-5}$	0.37±0.04	$5.98\text{x}10^{-8}$
GZA	0.51	0.40	0.22	19.68	$1\text{x}10^{-11}$	$4\text{x}10^{-10}$	$7\text{x}10^{-8}$	0.25±0.01	$1.84\text{x}10^{-7}$

Cell Cycling

The durability of each LLZO sample post-processing is tested using galvanostatic cycling. This is whereby the sample is subjected to incremental increasing current density to initiate stripping and platting of lithium metal through the electrolyte. LLZO is considered "dead" when the output voltage drops drastically. On the other hand, when the voltage signal drops and with subsequent increase in the applied current density results in the voltage rising again, this is termed a "soft-short". In all cases, the voltage drop is primarily due to lithium metal dendrite formation but is still subject to speculation whether it is a consequence of poor interfacial resistance or inherent electronic conductivity in the electrolyte.

Figure 5.10 shows all the galvanostatic cycling profiles of each sample. In all cases, a constant areal capacity of 0.1 mAh/cm^2 was used with an initial current density of 0.01 mA/cm^2, which equates to 7.32 μg and a thickness of 485 nm of Li stripped/platted at each applied current density. The highest achieved CCD was from samples sintered under argon, with CCD reaching as high as 1.7 mA/cm^2 for GZA. Samples prepared under oxygen short-circuited much earlier at 0.45 and 0.5 mA/cm^2 for GAO and GMO respectively. The insets in figure 5.10 show the various Ga-LLZO post-cycling. All images show grey colouration which is a result of lithium metal dendrites. The common causes for the failure of LLZO during cycling, are poor surface wettability of LLZO to lithium metal and the electronic conductivity of LLZO resulting in Li-ion reduction to form metallic dendrites within the solid electrolyte.

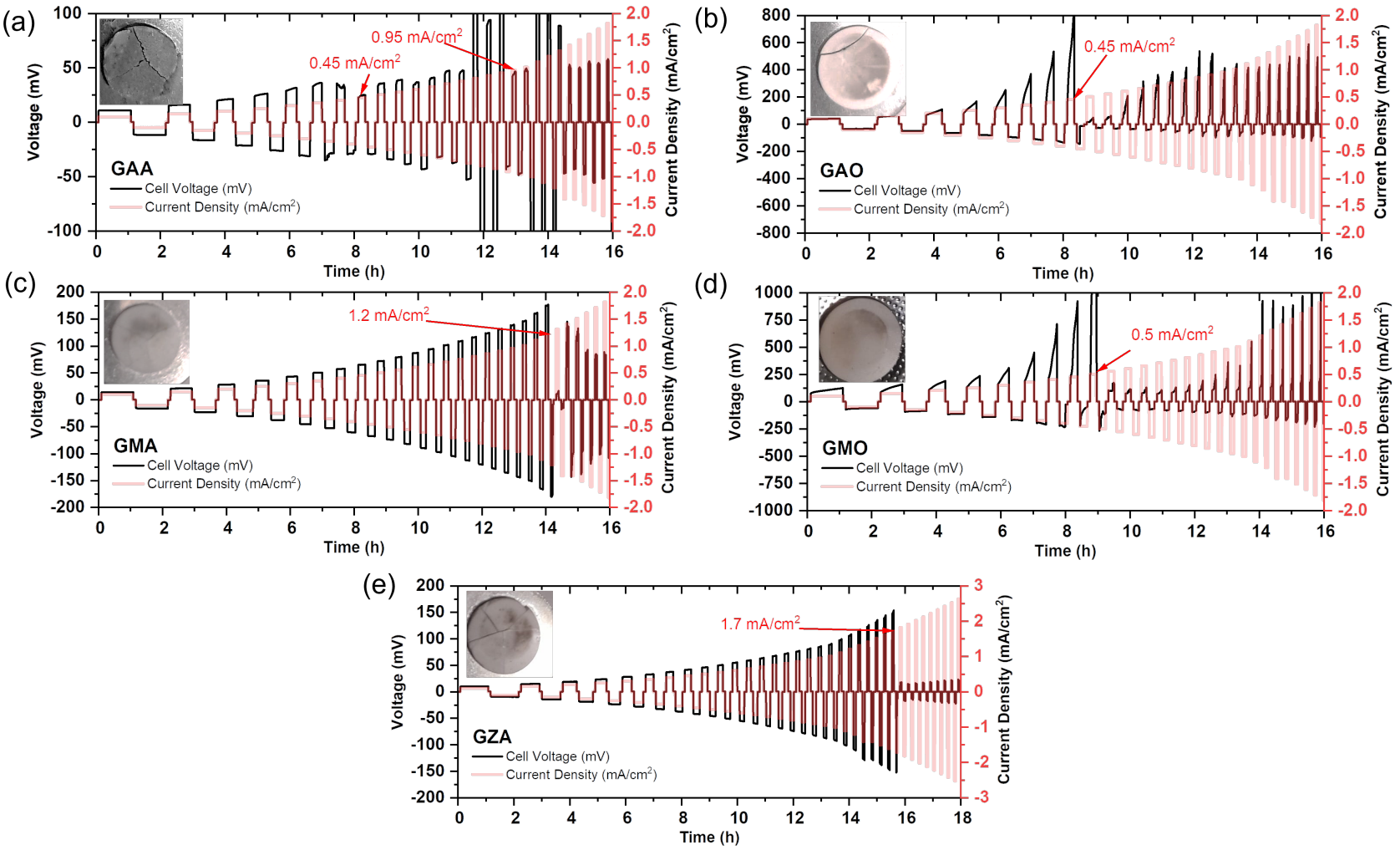


Figure 5.10: Galvanostatic cycling profiles of (a) GAA, (b) GAO, (c), GMA, (d) GMO, and (e) GZA. Cycling was done at room temperature (*approx.* 28°C). Measurement was done using a constant areal capacity of 0.1 mAh/cm^2 and an initial current density of 0.01 mA/cm^2. Inset on spectra show photos of LLZO after cycling

As discussed above concerning interfacial resistance, the sample prepared under oxygen exhibited greater R_{int} than those prepared under argon. This is primarily due to the difficulty in preventing corrosion layers from forming on the LLZO when transporting in an ambient atmosphere before Li electrodes can be placed onto the electrolyte. The samples processed under argon had noticeably lower R_{int} which may have assisted in reaching higher CCDs. Changes in garnet surface termination may be another possible explanation where the difference in elemental segregation occurs from the various processing conditions. The failure of GAA, GMA, and GZA is considered to be more to do with residual electronic conductivity as these samples are prepared under reducing atmospheres. Figure 5.11 shows a cross-sectional micrograph of a GAA pellet after failure from galvanostatic cycling. It is apparent that lithium metal features protrude from the sample which are shown as dark nodule-like features. The inset in figure 5.11 show the GAA pellet, the fractured pellet is likely due to the opening of the coin cell. This may be an indication of dendrite formation from possible electronic defects. Whereas, dendrite formation resulting from localised current distribution on the LLZO surface can cause a higher concentration of lithium filaments near the electrode/electrolyte interface. Both processes can still be possible as the lithium can migrate through micro-cracks from the interface making the appearance of dendrites uniform within the garnet.

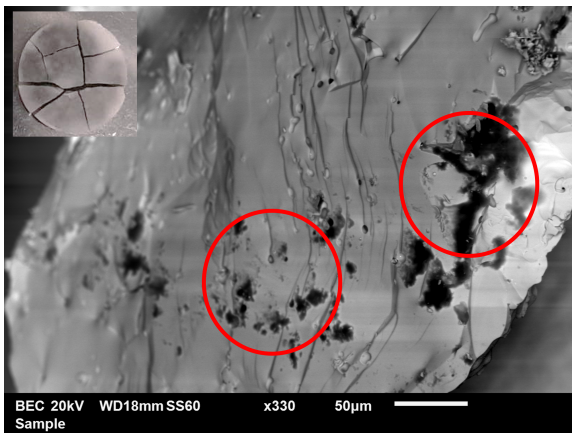


Figure 5.11: SEM back-scattered image of GAA cross-section post cycling, the red circle shows lithium metal traversing the electrolyte. Inset is an image of a GAA pellet after cycling

However poor Li|LLZO interface contact cannot be ruled out. Localised lithium distribution may begin to form as the interfacial contact begins to deteriorate during extended cycling. To understand whether there are residual unpaired electrons in these solid electrolytes EPR was conducted and discussed in the following section.

5.4 EPR Analysis

Electron paramagnetic resonance (EPR) analysis was employed to understand the possible existence of 'free' or unpaired electrons in the solid electrolytes. A comparison between all the processed Ga-LLZO samples is shown in figure 5.12 along with the as-purchased Ga-LLZO.

It is apparent that samples prepared under argon atmosphere (GAA, GMA, and GZA) produced EPR signals, ranging from 320-370 mT. On first inspection and comparison with GAO, GMO, and GZO spectra the peaks may be due to sintering under an oxygen-poor atmosphere resulting in oxygen vacancies dominating the possible defects formed, which was computationally proposed for c-LLZO by Squires *et al.* [70]. Oxygen vacancies can in turn trap free electrons, which would give a response. However, only a single EPR peak would be expected from unpaired electrons. Whereas, in this case, peak splitting, due to hyperfine coupling is observed. Hyperfine signals are due to the interaction of the unpaired electrons to local nuclear spins from neighbouring elements. These nuclear spins impose another magnetic moment on the lone electron, resulting in the splitting. The six-peak split is expected from the interaction of the electron with a nucleus with a spin number of 5/2 which would give six peaks. This is based on the splitting and multiplicity rule $(2nI + 1)$ where n is the number of symmetry equivalent nuclei (i.e. 1) and the nuclear spin number is I.

Although preparing Ga-LLZO under argon has shown to give the most promising results, it is evident that free electrons do evolve and can result in lithium-ion reduction and dendrite formation. At this moment it is unclear as to where the unpaired electron resides as the only elements with a nuclear spin of 5/2 are ^{91}Zr (abundance 11.22 %) and

^{17}Zr (abundance 0.038 %). Typically a six-peak split is observed from manganese which has 100% I = 5/2 [249–251]. However, if manganese contamination contributed to the signals, it should also be noticed for samples prepared under oxygen.

EPR is considered a quantitative technique, where a standard of known carbon radicals is used for quantification. However, in this case, the signals are weak making quantification not possible. A rough estimate for the free electrons would be to look at the instrument sensitivity limit, which is 1x10^9 electron spins. An attempt at fitting the GMA signal was done as it presented the most intense EPR response and is shown in figure 5.13.

The EPR signal of GMA was fit using EasySpin which is an open-source toolbox available using Matlab. The applied microwave frequency of 9.55 GHz was applied as a parameter for fitting the signals. The signal was first fit to the background with a g-factor of 2 and no hyperfine constant (H_A). The remaining six peaks were fit to a g-factor of 2.003 (free electron), but could also be fit to g = 2.001 which is the g-factor for Mn^{2+}, H_A of 215 MHz was used to fit the peak splitting. In this work, EPR could be used to identify possible free unpaired electrons, although it was not possible for quantification and environment identification as to where the electron resides. To further investigate the preferential location of free electrons computational efforts are encouraged.

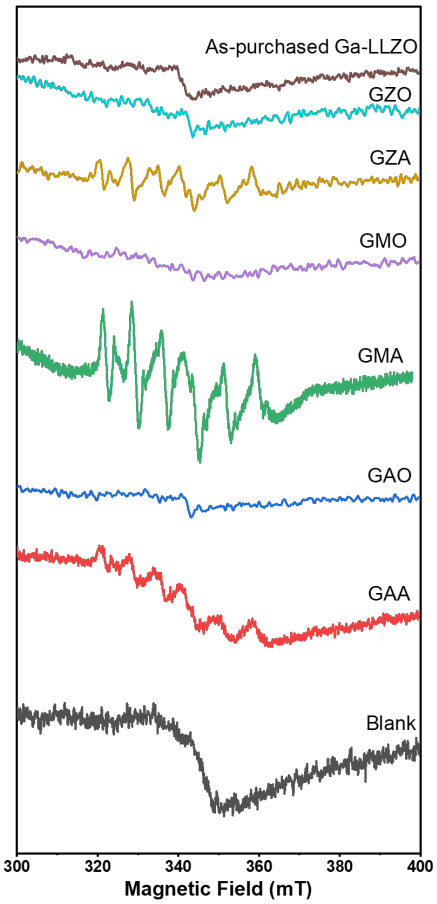


Figure 5.12: EPR response of powder, as-purchased Ga-LLZO (top) and the heat-treated material. Blank corresponds to an empty EPR sample tube, which has a background signal.

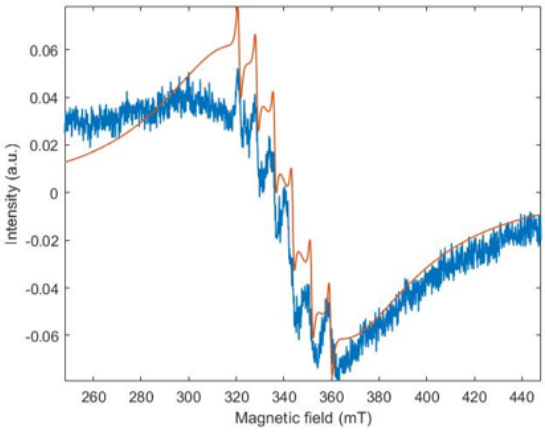


Figure 5.13: EPR response fitting of GMA powder, g = 2.001.

5.5 Summary

To summarise, the work done in this section was to compare the impact of both the sintering atmosphere and crucible choice on the properties of Ga-LLZO. Techniques used in this section were primarily used to understand the bulk properties i.e. the sample purity, microstructure, composition and electrochemical behaviour. It was found that samples prepared under argon performed better from an electrochemical perspective, giving a bulk ionic conductivity of ∼0.5 mS/cm and a total ionic conductivity of ∼0.2 mS/cm. Samples prepared under argon also outperformed their oxygen atmosphere-sintered counterparts during galvanostatic cycling, reaching CCD as high as 1.7 mA/cm^2. The improved performance of GAA, GMA, and GZA may be due to achieving material with high purity, high density and hardness and near uniform grain size distribution. In contrast, samples processed under oxygen resulted in secondary phases being present, large variations in grain size, poorer relative density and hardness. Sintering under oxygen also proved difficult to achieve pristine surfaces of the Ga-LLZO pellets as transport in the ambient atmosphere can result in corrosion layers forming which in turn can increase the interfacial resistance.

An interesting approach was used to understand whether trapped unpaired electrons are present in the solid electrolyte. To investigate this, EPR was employed and showed that indeed free electrons existed in the samples sintered under reducing conditions. However, no further information on the local environment and quantification could be extracted. An attempt to fit the EPR data was conducted and a g = 2.003 was determined which correlates to free electrons. Further work is necessary to understand the environment of the unpaired electron in which computational efforts may be required.

Chapter 6

Sintering Atmosphere and Crucible Choice for Ta-LLZO Preparation

In this chapter $Ta_{0.6}$-$Li_{6.4}La_3Zr_{1.4}O_{12}$ (Ta-LLZO) is studied. Ta-LLZO is studied as it utilises different doping sites and is another commonly studied garnet configuration. In Ta-LLZO the zirconium site is partially substituted, whereas the previously studied Ga-LLZO (Chapter 6) is doped onto lithium lattice sites. Herein, Ta-LLZO is processed using reducing (argon) or oxidising (oxygen) heat treatment atmosphere and with different crucibles, including Al_2O_3, MgO, and ZrO_2. Table 6.1 shows the nomenclature used to name the material after processing.

Table 6.1: Sample name for Ta-LLZO SE after processing.

Nomenclature	Crucible	Atmosphere
TAA	Al_2O_3	Argon
TAO	Al_2O_3	Oxygen
TMA	MgO	Argon
TMO	MgO	Oxygen
TZA	ZrO_2	Argon
TZO	ZrO_2	Oxygen

6.1 Phase Purity

Ta-LLZO was analysed by XRD to check for phase purity, the powder XRD pattern of the as-purchased Ta-LLZO is shown in figure 6.1. The XRD pattern shows a pure phase with no extra reflections from impurity or secondary phases. The XRD patterns were fit using Le Bail refinement method using a Ta-LLZO standard with the same nominal stoichiometry of $Ta_{0.6}$-$Li_{6.4}La_3Zr_{1.4}O_{12}$. A space group of $Ia\bar{3}d$ was determined, which is consistent for cubic phase Ta-LLZO. A lattice parameter of 12.92 $\mathring{A}$ and cell volume of 218.00 nm^3 was obtained, which is expected for LLZO garnets [252].

XRD analysis was done on Ta-LLZO pellets after processing with various conditions. The XRD patterns are shown in figure 6.2. In each case, pellets were used which are shown in the inset of their respective XRD pattern. No full pellet for TZO could be obtained as samples for TZO post-sintering would be fragmented. It is currently non-

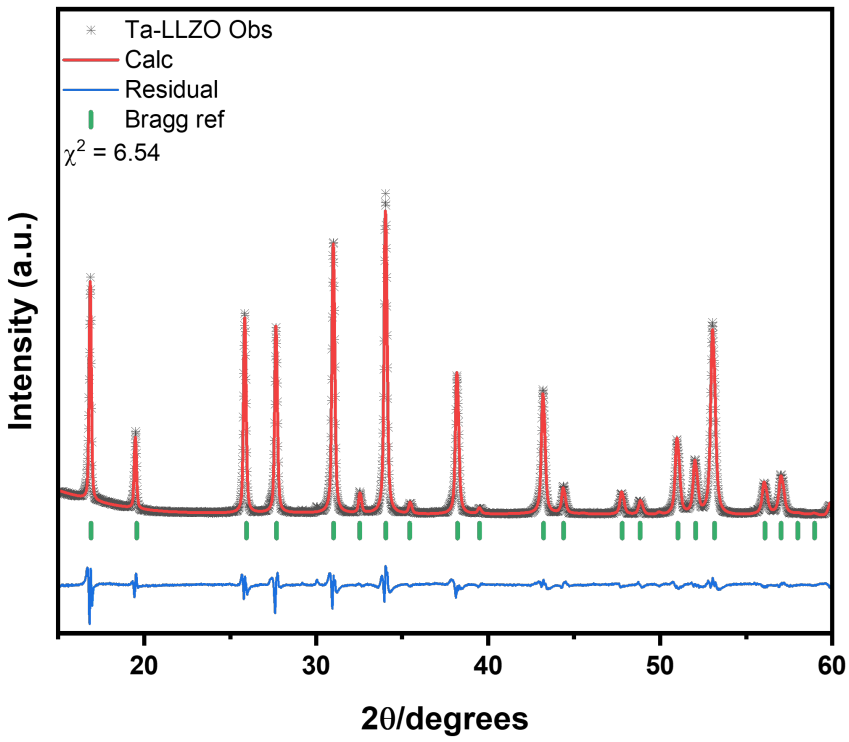


Figure 6.1: Le Bail refined XRD pattern for as-purchased Ta-LLZO. Reference of Ta-LLZO from ICSD ref. 22958.

conclusive as to the reason for TZO pellets to have shattered after the heat treatment.

Pure phases were obtained for both TAA and TMA, and the inset images also show partially transparent pellets, where the black cross can be visualised through the pellet. The semi-transparent pellets of TAA and TMA give an indication of large grain sizes, whereas pellets with small grains (i.e. lots of grain boundaries per unit area) appear opaque or no transparency. Grain boundaries refract light differently than the grain interior does which can give different optical properties, the microstructure is discussed in section 6.2. However, with all other samples pure phases could not be obtained as shown by the XRD pattern of TZA in figure 6.2a which shows reflections corresponding to pyrochlore and $La(OH)_3$. Moreover, TAO, TMO, and TZO all exhibited reflections from pyrochlore phases with the exception of TZO which consisted of lanthanum hydroxide and an unidentified

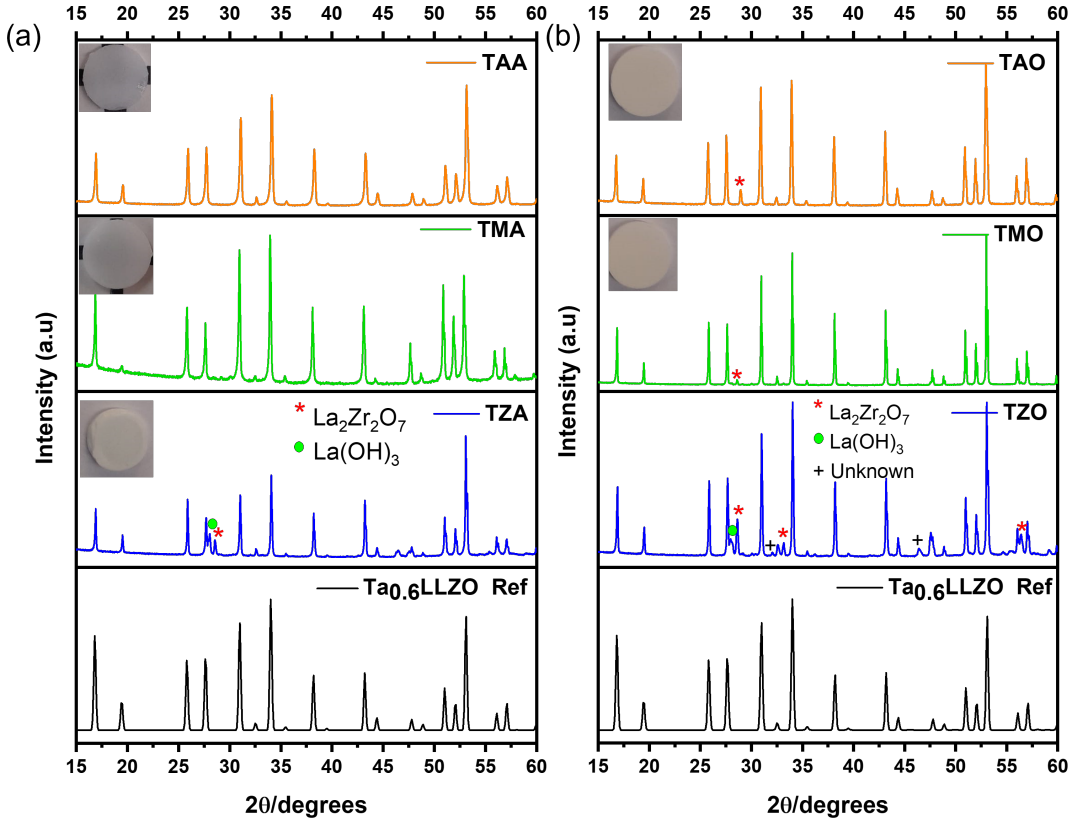


Figure 6.2: XRD pattern of all Ta-LLZO samples after processing, (a) all samples sintered under argon with different crucibles, (b) all samples sintered under oxygen with different crucibles. The red asterisk indicates the presence of pyrochlore secondary phase, the green circle labels reflection for $La(OH)_3$, and the black cross indicates reflection from an unknown material.

composition which had an XRD reflection at *ca.* 31.5° 2θ.

6.1.1 Density and Hardness

The relative density of each pellet was obtained using pellet fragments with the Archimedes method. Overall, samples sintered under argon displayed higher relative densities ranging between 90-98 %. On the other hand, samples prepared under oxygen had lower densities ranging from 87-96 %; all densities are tabulated in table 6.2. The highest relative densities achieved were obtained for Ta-LLZO sintered using alumina crucibles whether under argon or oxygen atmosphere. Sintering with alumina crucibles is expected to aid the densification

primarily from the *in-situ* liquid phase formed at high temperatures [194].

Table 6.2: Stoichiometery of samples after processing determined via ICP-OES and oxygen determined using equation 4.6, cell volume obtained from XRD refinement and relative densities.

Sample	Stoichiometry from ICP	Cell Volume (nm^3)	relative density (%)
Ta-LLZO	$Ta_{0.59}Li_{6.17}La_3Zr_{1.4}O_{11.86}$	216.05±0.04	-
TAA	$Ta_{0.56}Li_{6.16}La_3Zr_{1.4}O_{11.50}$	218.01±0.06	98.2±0.9
TAO	$Ta_{0.36}Li_{6.15}La_3Zr_{1.37}O_{11.04}$	216.52±0.04	96.0±1
TMA	$Ta_{0.41}Li_{5.92}La_3Zr_{1.41}O_{11.10}$	216.47±0.07	95±4
TMO	$Ta_{0.30}Li_{5.50}La_3Zr_{1.25}O_{10.35}$	217.64±0.03	91±2
TZA	$Ta_{0.35}Li_{6.29}La_3Zr_{1.46}O_{11.26}$	216.55±0.08	90±2
TZO	$Ta_{0.38}Li_{5.07}La_3Zr_{1.33}O_{10.46}$	215.71±0.09	87±4

Hardness measurements were done on pellets using Vicker's hardness methods with micro indentation. In all cases, samples with the highest density (i.e. sintered under argon), had the greatest hardness, as shown in figure 6.3. Hardness values as high as 10 GPa were measured for TAA which is consistent with work by Hu *et al.* [253]. However, hardness values do not represent the structural integrity of the pellets. This is because TZA has a greater hardness than TAO and TMO but full pellets of TZA were not obtained as TZA would delaminate. As TZA and TZO could not be prepared as complete symmetrical pellets this would make it difficult to conduct electrochemical studies as discussed further in section 7.3.

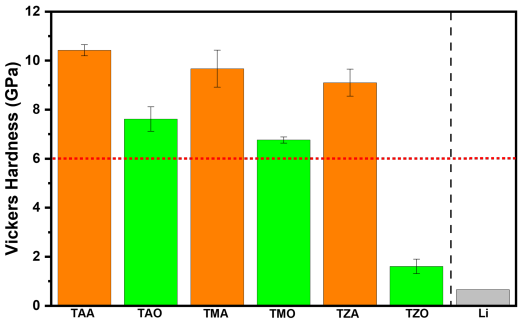


Figure 6.3: Histogram display the Vicker's Harness of Ta-LLZO pellets prepared under various conditions. The red dotted line is the average hardness of LLZO reported in literature [26]

6.1.2 Elemental Analysis

To investigate the resultant stoichiometry of Ta-LLZO after heat treatment, ICP-OES is used. In most cases in the literature, the stoichiometry stated is typically based on the synthesis and not a direct stoichiometry measurement. All determined stoichiometry are tabulated in table 6.2. There is a large variation in the stoichiometry from what is thought to be $Ta_{0.6}$-$Li_{6.4}La_3Zr_{1.4}O_{12}$. However, the as-purchased Ta-LLZO measured stoichiometery was $Ta_{0.59}Li_{6.17}La_3Zr_{1.4}O_{11.86}$. However, one of the main issues with ICP-OES analysis is that samples are required to be fully dissolved in the carrier solvent for accurate measurements. The main difficulty of handling Ta-LLZO for ICP-OES is that determining Ta concentration requires strong acids such as hydrofluoric acid, which was not possible at the time of this work.

In all samples, the calculated oxygen stoichiometry was lower than 12 moles p.f.u. The lower oxygen content may be due to lithium vacancies which are charge balanced via oxygen vacancies. However, the change in the oxygen moles is influenced by the stoichiometry of the remaining cations (Li, Zr, and Ta). The stoichiometry is also impacted by the secondary phases present as seen by the XRD patterns, these alternate phases are dispersed during sample preparation which interferes with the true stoichiometry of the garnet. A limitation of ICP analysis is its requirement for samples to be entirely in

solution form to ensure accurate measurements. This might explain the discrepancies in the obtained stoichiometries, as Ta-LLZO does not fully dissolve in water and nitric acid. It may necessitate the use of hydrofluoric acid for complete dissolution

6.2 Microstructure

The microstructure of the garnet was examined using both optical and electron microscopy. The grain dimensions were visualised using an optical microscope for pellets after sintering, whereas, SEM was used for pellets after polishing and thermal grooving steps. Figure 6.4 shows the microstructure of TAA and TAO for comparison between different sintering atmospheres. The grain size of both TAA and TAO is unambiguously observed using the optical microscope showing grain size of 50-100μm for TAA and between 10-50μm for TAO. The grain size for TAA could also be visualised using SEM as shown in 6.4b. However, TAO grain size was difficult to view with the SEM, as the surface appeared highly porous and would damage from long exposure to the electron beam.

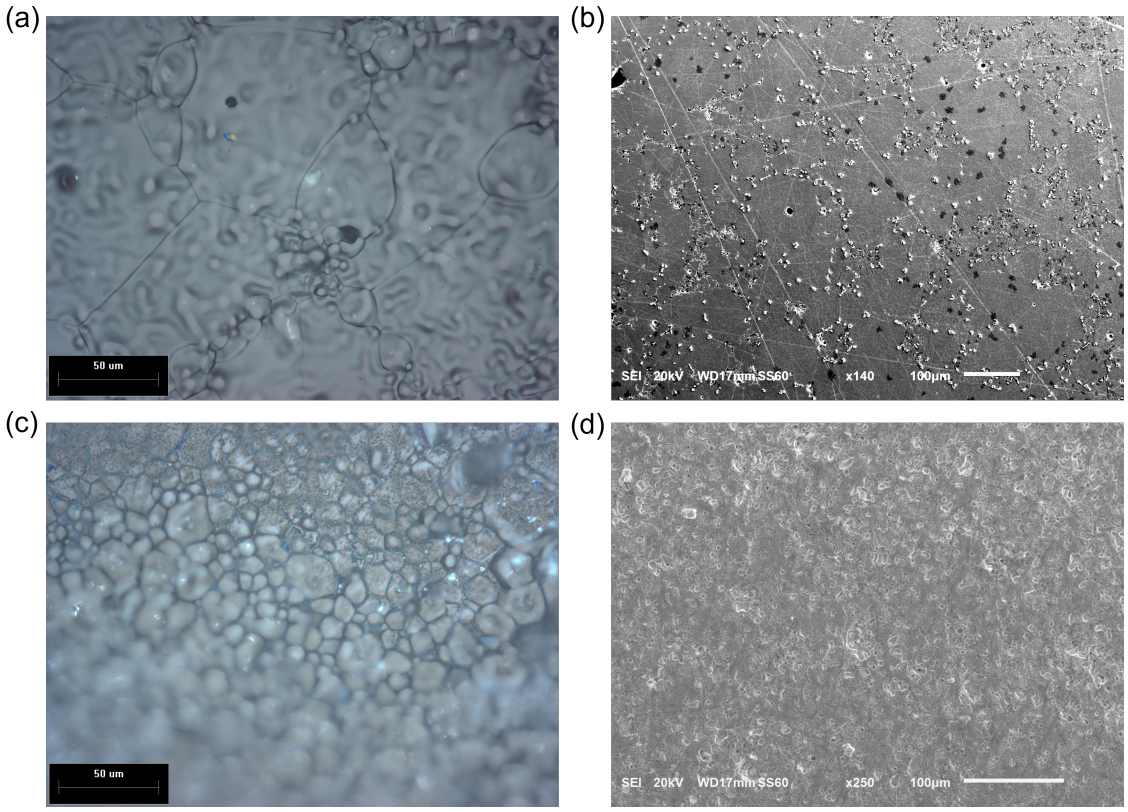


Figure 6.4: Microstructure of TAA and TAO pellet surface, (a) optical image of TAA after sintering, (b) SEM image of TAA pellet after polishing and thermal grooving, (c) optical image of TAO, and (d) SEM image of TAO pellet after polishing and thermal grooving.

The surface microstructure of the samples prepared using magnesia crucibles is shown in figure 6.7. A similar trend is followed, whereby sintering under argon achieved a majority larger grain size of ≥ 50 μm as shown in figure 6.5a. On the other hand, the TAO pellet is composed of significantly smaller grains of $\sim$5 μm which is noticeable from both the optical and scanning electron micrographs in figures 6.5c and d, respectively. TAO also appears to be more porous (see figure 6.5d) than TAA which has a lower density of pores as seen in figure 6.5b.

As discussed above, processing Ta-LLZO with zirconia crucibles produced pellets with poor density and hardness and the evolution of impure material. The microstructure of TZA resembles that of TAA and TMA as shown in figure 6.6a in the optical microscope, whereas, TZO has a much smaller grain and an extremely porous structure, which is the

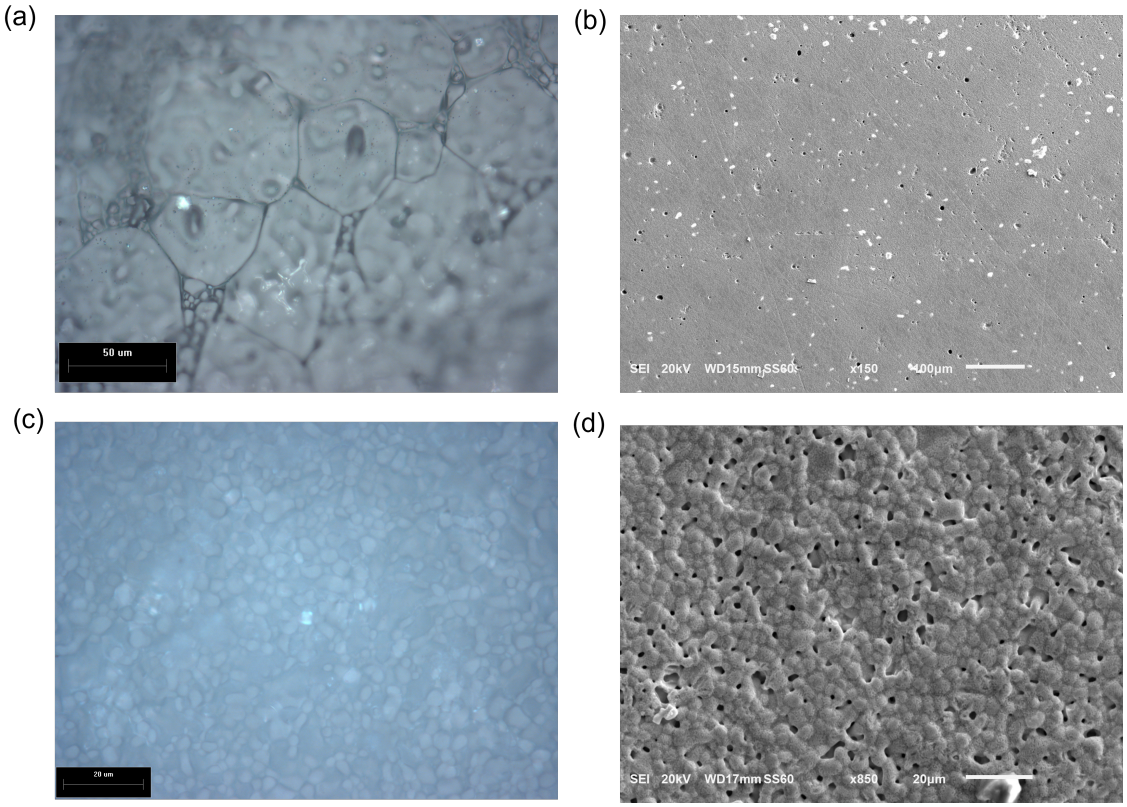


Figure 6.5: Microstructure of TMA and TMO pellet surface, (a) optical image of TMA after sintering, (b) SEM image of TMA pellet after polishing and thermal grooving, (c) optical image of TMO, and (d) SEM image of TMO pellet after polishing and thermal grooving.

cause for the low relative density and low hardness of the material. Although TZA has a high density and hardness, it would not form complete and symmetrical pellets and cracks would appear through the pellet after sintering using the zirconia crucible. With this in mind, both TZA and TZO could not be handled for electrochemical measurements because electrodes could not be deposited on non-uniform dimensions of the sample.

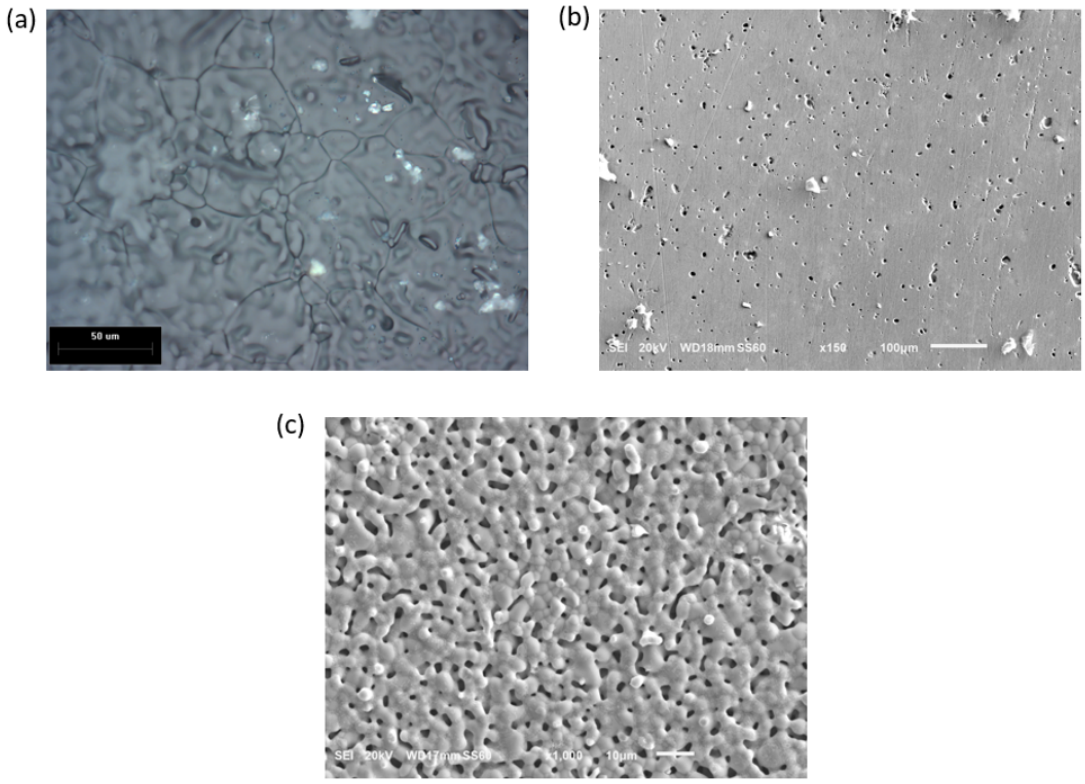


Figure 6.6: Microstructure of TZA and TZO pellet surface, (a) optical image of TZA after sintering, (b) SEM image of TZA pellet after polishing and thermal grooving, (c) SEM image of TZO pellet after polishing and thermal grooving (no suitable optical image of TZO could be obtained).

6.3 Electrochemical Analysis

To investigate the conductivity properties of the material used in this chapter, EIS was used for determining the ionic conductivity and time-resolved DC measurements were conducted for electronic conductivity using gold blocking electrodes with Au|Ta-LLZO|Au symmetric cell configuration. The activation energy for lithium ion migration was measured by variable temperature EIS. In order to determine the interfacial resistance a Li|Ta-LLZO|Li cell was used, for which the Nyquist plots are displayed in figure B.2 in the appendix section. All impedance and electronic conductivity data is tabulated in table 6.3.

The study of electrolyte failure due to dendrite formation was done using galvanostatic cycling on Li|TaLLZO|Li cell. This is whereby the current density is increased in incremental steps until the SE short circuits as shown by the sudden drop in the output

voltage. The short circuit is taken to from the formation of lithium metal dendrites which connect both electrodes through the electrolyte.

6.3.1 Conductivity measurements

EIS of Au|TAA|Au at 25°C achieved a bulk conductivity of 0.5 mS/cm which is in line with literature values as reported by Hu *et al.* [253]. The Nyquist plot for Li|TAA|Li is shown in figure 6.7a, and this Nyquist plot could only be suitably fit to one R-CPE element as shown by the inset, hence no contribution by the GB on the conductivity could be established. The activation energy for bulk ionic conductivity was measured to be 0.28 eV which is consistent with previously published work on Ta-LLZO. With regard to TAO, both bulk and GB contributions to the ionic conductivity were determined. TAO had a factor of two lower σ_{bulk} at 1.56x10^{-2} mS/cm, and a grain boundary conductivity of 1.4x10^{-3} mS/cm. from previous information on the sample purity and microstructure, this may have hindered the ionic conductivity of TAO. The bulk, GB, and total activation energy of TAO at ∼0.4 eV is also higher than that of TAA.

The Li|TAA interfacial resistance was measured to be 7.31 Ω cm^2, whereas, the Li|TAO had a R_{int} of 133.46 Ω cm^2. The higher interfacial resistance of TAO is most likely due to the formation of a corrosion layer on the pellet surface during transport from the furnace into the glovebox for cell assembly. Moreover, TAO had smaller grains which could increase the surface area for lithium metal contact, in turn increasing the interface resistance.

The bulk conductivity for TMA was measured to be 0.48 mS/cm which is in close proximity to that of TAA, meanwhile a significantly greater σ_{GB} of 9.27 mS/cm was measured. The high GB conductivity is unusual and may not resemble the true grain boundary property as the capacitance for the GB was *ca.* 10^{-7} F which overlaps the capacitance range for the interfacial contribution. The characteristic frequency for the GB also appears to be in the capacitance tail caused by the blocking electrodes as shown in figure 6.8a. A total activation energy of 0.36 eV is measured which is similar to literature

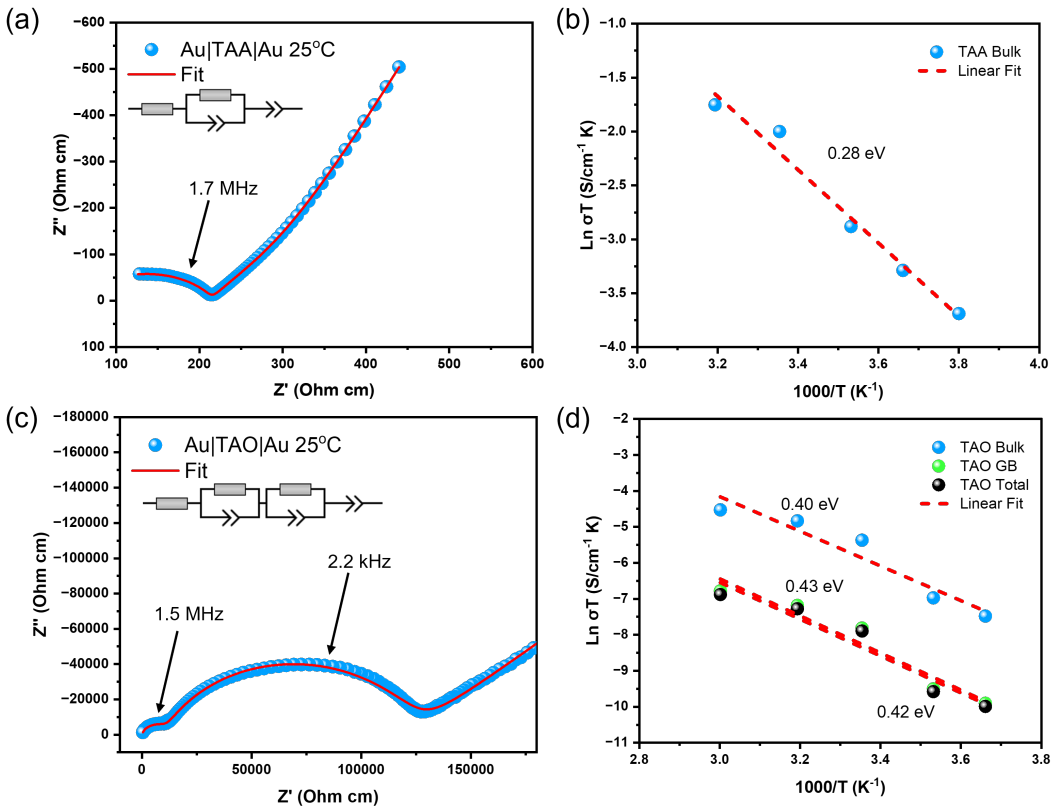


Figure 6.7: EIS data of TAA and TAO. (a) Nyquist plot of TAA, (b) Arrhenius plot of TAA, (c) Nyquist plot of TAO, and (d) Arrhenius plot of TAO. Inset on Nyquist plots show the equivalent circuits used for fitting

values by Li *et al.* [124]. TMO has much lower ionic conductivity values shown in table 6.3 which again may be due to changes in microstructure and impurity phases present. The total activation energy of TMO (0.46 eV) is also similar to that of TAO. The interfacial resistance of TMA is measured to be 12.75 Ω cm^2, whereas, TAA has a R_{int} of 7.31 Ω cm^2. This again can be due to the reasons explained previously for the samples sintered using alumina crucibles.

The electronic conductivity of all the samples was measured at RT using Au ionically blocking electrodes. Electronic conductivity values of *approx.* 10^{-7} mS/cm were measured for all samples with little variation. The low electronic conductivity and high ionic conductivity of TAA and TMA result in a transfer number of 0.99, which is ideal for a promising solid electrolyte, to minimise ionic resistance.

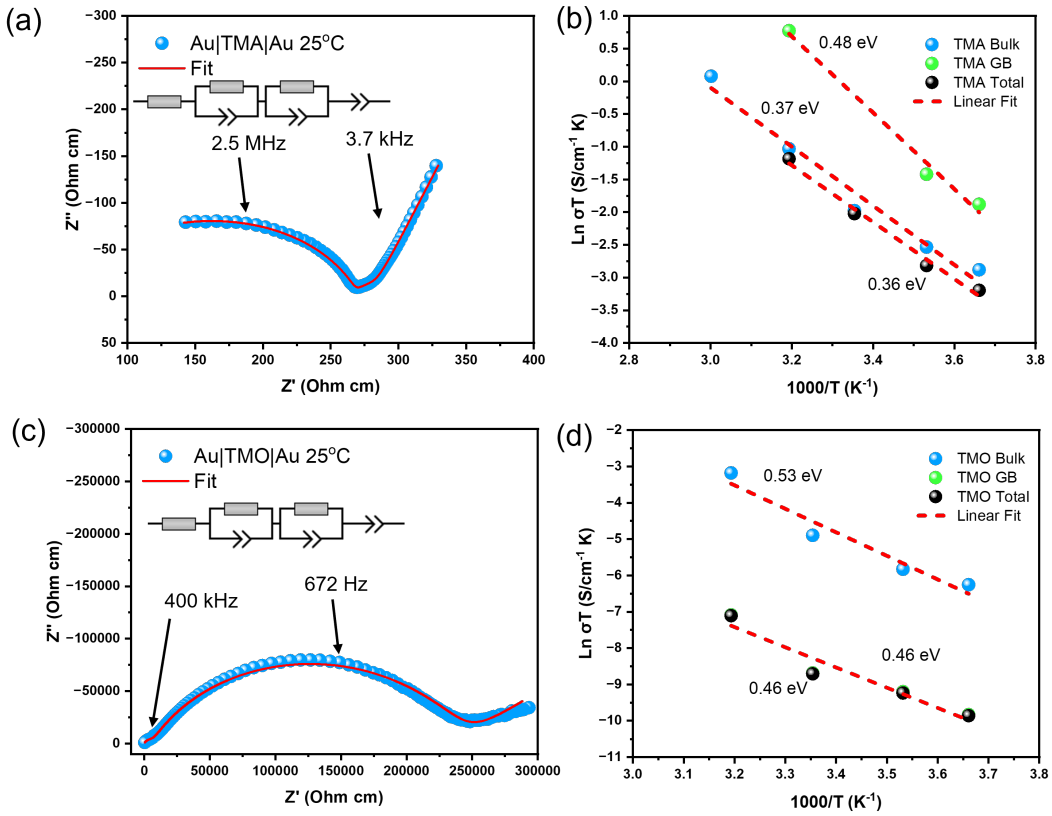


Figure 6.8: EIS data of TMA and TMO. (a) Nyquist plot of TMA, (b) Arrhenius plot of TMA, (c) Nyquist plot of TMO, and (d) Arrhenius plot of TMO. Inset on Nyquist plots show the equivalent circuits used for fitting

Table 6.3: Ionic conductivity, and capacitance values from EIS measurements at 25°C with Au|LLZO|Au cell, activation energy values from Au|LLZO|Au cell at a temperature range between 0-100°C, R_{int} from Li|LLZO|Li cell at 25°C. Electronic conductivity values for Au|LLZO|Au cell at 25°C

Sample	σ_{bulk} (mS/cm)	σ_{GB} (mS/cm)	σ_{total} (mS/cm)	R_{int} (Ω cm^2)	C_{bulk} (F)	C_{GB} (F)	C_{int} (F)	Total E_a (eV)	σ_e (mS/cm)
TAA	0.50	-	-	7.31	$1.4\text{x}10^{-11}$	-	$2.18\text{x}10^{-7}$	-	$1.09\text{x}10^{-7}$
TAO	$1.56\text{x}10^{-2}$	$0.14\text{x}10^{-2}$	$0.13\text{x}10^{-2}$	133.46	$2.83\text{x}10^{-12}$	$7.20\text{x}10^{-11}$	$1.28\text{x}10^{-6}$	0.42±0.01	$1.23\text{x}10^{-7}$
TMA	0.48	9.27	0.45	12.75	$1.31\text{x}10^{-11}$	$1.10\text{x}10^{-7}$	$9.88\text{x}10^{-5}$	0.36 ± 0.01	$1.28\text{x}10^{-7}$
TMO	$2.51\text{x}10^{-2}$	$5.68\text{x}10^{-4}$	$5.55\text{x}10^{-4}$	279.34	$5.24\text{x}10^{-12}$	$9.91\text{x}10^{-11}$	$8.94\text{x}10^{-6}$	0.46±0.01	$1.57\text{x}10^{-7}$

6.3.2 Cell Cycling

Galvanostatic cycling using Li metal electrodes was done to determine whether the various processing conditions would improve the cyclability of the solid electrolytes. It was expected that Ta-LLZO prepared under argon would cycle to higher current densities as seen in Chapter 5 for GAA and GMA. However, this was not the case whereby TAA and TMA shorted at 0.5 and 0.1 mA/cm^2 respectively. The cycling profiles are shown in figure 6.9 with the insets showing the electrolyte post-cycling. There are very few signs of discolouration from lithium dendrites for the argon atmosphere sintered samples. Interestingly the samples prepared under oxygen reached much higher CCD, and these experiments will need to be reproduced to understand if this is a reoccurring outcome. It is unclear as to what improved the cycling performance of TAO and TMO over TAA and TMA. A possible explanation me be the different microstructure of the solid electrolyte, where TAO and TMO have smaller grains which may have improved the wettability at the interface. From figures 6.9b and d the negative output voltages are shown to plateau which may hinder the full capacity of Li to be cycled which may have been an instrument safety feature as high voltages were being reached. The observed data for TAO and TMO is contrary to what is observed with Ga-LLZO and when is reported in the literature. Therefore, there may also be the possibility of Ta being partially reduced and forming an SEI layer, experiments such as in-situ XPS may help to understand if this is possible.

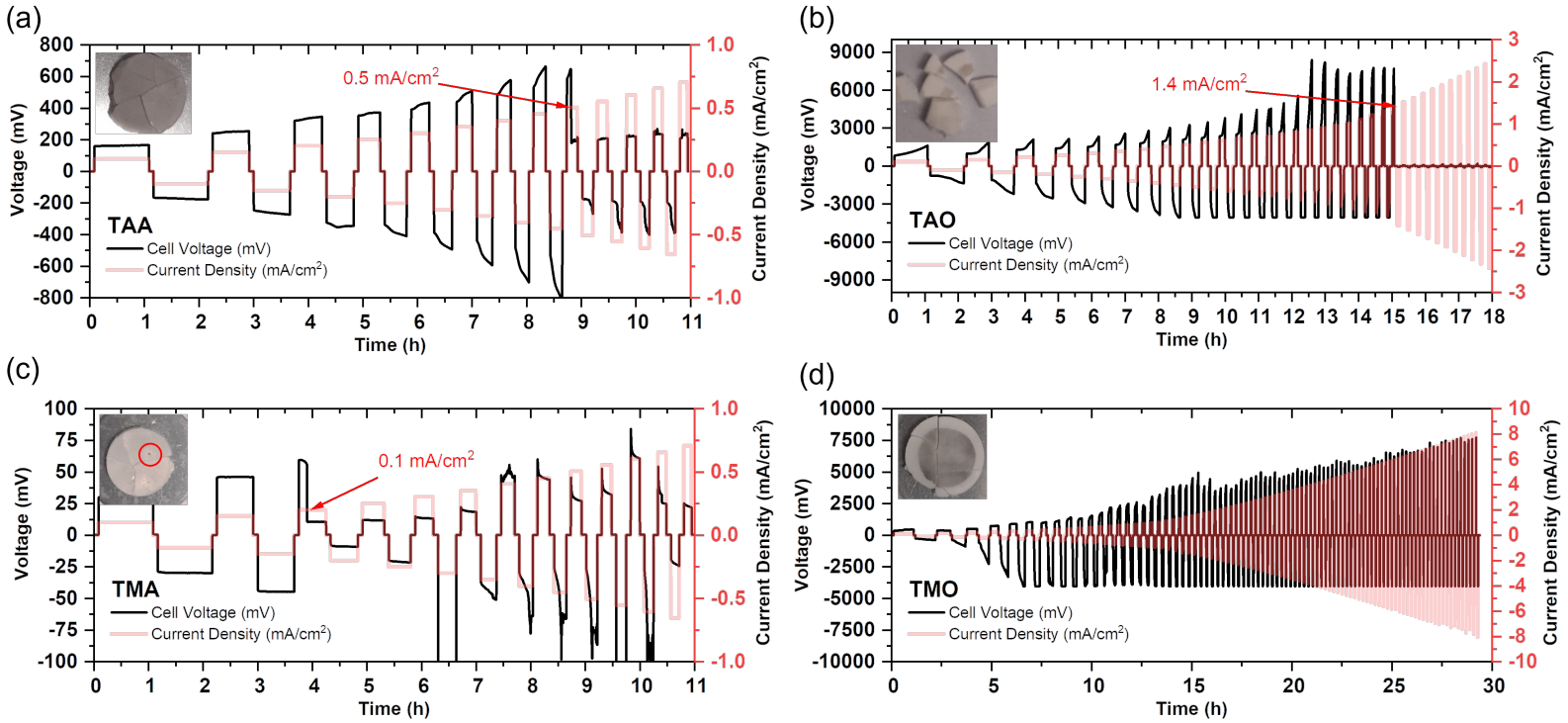


Figure 6.9: Galvanostatic cycling profiles of (a) TAA, (b) TAO, (c) TMA, and (d) TMO. Inset show the Ta-LLZO pellets after cycling. A constant areal capacity of 0.1 mAh/cm^2 and initial current density of 0.01 mA/cm^2 was used

6.4 EPR analysis

EPR analysis was done on Ta-LLZO to investigate the possible cause for the electronic conductivity and if unpaired electrons could be measured. Figure 6.10 shows the EPR response for all the Ta-LLZO samples in comparison to the as-purchased powder and a black EPR sample tube. It is clear that no noticeable signal is obtained for these samples which is in contrast to those measured for the Ga-LLZO material heat treated under argon. Therefore, the possible signals received using EPR may be due to Ga doping in LLZO, no further information could be extracted from the EPR of Ta-LLZO samples.

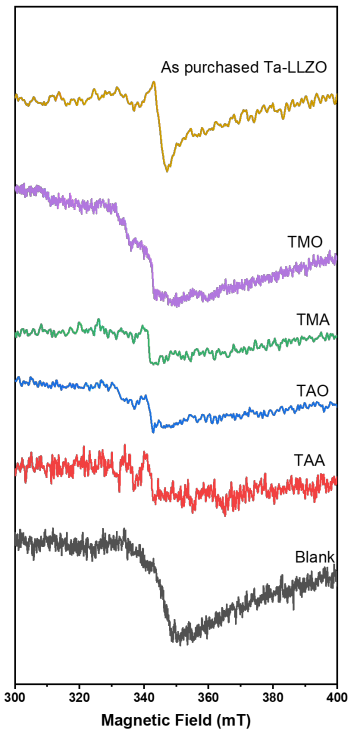


Figure 6.10: EPR of as-purchased Ta-LLZO and samples from various processing conditions

6.5 Summary

In this chapter, Ta-doped LLZO was investigated, and bulk characterisation techniques were used to understand the influence of processing atmosphere and crucibles on their properties. Under all processing conditions, a cubic phase with space group $Ia\bar{3}d$ was prepared. Heat treatment under argon would result in polycrystalline pellets with grain sizes typically exceeding 50 μm, whereas, sintering under oxygen resulted in grain sizes between 5-50 μm. Overall sintering under the reducing atmosphere would produce TAA, TMA, and TZA pellets with higher relative densities and hardness than sintering under oxygen, which may be due to the larger grain sizes. The higher density of TAA is commonly suggested to be from a liquid phase sintering process aided by the Al_2O_3 crucible, although it may contaminate the garnet with aluminium. However, ICP-OES of TMA showed Mg contamination of at least 2.5 ppm for 100 mg of garnet sintered using a MgO crucible which may aid Ta-LLZO densification. TAA and TMA showed the most promising characteristics with high bulk ionic conductivity of $\sim$0.5 mS/cm and activation energy of 0.28 eV and 0.37 eV for TAA and TMA, respectively. It was expected that TAA and TMA would achieve higher CCDs during cell cycling over their oxygen atmosphere-sintered counterparts. However, it was not the case, a possible reason for this may be the highly porous structure of TAO and TMO providing a more uniform stripping/plating process, even though with high interfacial resistance in comparison to TAA and TMA. Further work on obtaining pure phase TAO and TMO with similar microstructure to that of TAA and TMA is essential for there to be more certainty on the performance differences of these materials based on the conductivity and cyclability. Optimisation of oxygen sintering of Ta-LLZO to obtain pure compositions and similar microstructure to their argon sintered counterparts is required.

Chapter 7

Understanding the Effect of Atmosphere and Crucible on the Surface Chemistry of LLZO

Recent findings have shown that elemental segregation in garnets is present [132, 149]. The inhomogeneous distribution of the elements occurs both in-depth (i.e. from the surface into the bulk) and laterally, where in some cases segregation to the grain boundary is observed. Until now work has mainly been carried out on Al- and Ga-doped LLZO which are prepared using liquid phase sintering of LLZO pellets under argon on Al_2O_3 crucibles. Results by Brugge *et al.* [149] showed that Al and Ga dopants would segregate to grain boundaries which were shown by SIMS analysis. Contamination by Al from the crucible was also observed on Ga-LLZO samples, primarily intergranular, which may be used to explain the role of Al in densifying polycrystalline Ga-LLZO sintered in this way. Apart from dopants, Li is observed to segregate to the surface, whereas La and Zr increase towards the bulk.

Currently, no work has been done on understanding how processing conditions impact surface chemistry and elemental in-homogeneity in LLZO. In order to avoid crucible contamination and maintain density, MgO crucibles are being used [67, 254]. Little is known about whether MgO contaminates LLZO during high-temperature sintering. Work by Jiang *et al.* has shown using ICP-MS methods that Mg can contaminate LLZO from the crucible, and this was also confirmed in Chapter 5 of this work using ICP-OES. However, ICP methods cannot indicate the distribution of elements and results and distribution are taken to be uniform. In this work, we aim to study the surface chemistry of LLZO which is processed under argon vs. oxygen and with three different crucibles; alumina, magnesia and zirconia which is the control as no contamination should occur. Surface analysis techniques used include; XPS, ToF-SIMS, and LEIS. XPS is used to investigate possible changes in oxidation states and the chemical environment from the change in sample preparation conditions, and ToF-SIMS is used to investigate the lateral and depth distribution of the ions.

This chapter is divided into two sections based on dopants, the first section will be on Ga-doped LLZO whereby gallium substitutes onto the lithium lattice sites, while the second section will be on Ta-doped LLZO as tantalum substitutes onto zirconium lattice

sites.

7.1 Surface Chemistry of Ga-LLZO

7.1.1 XPS

As discussed in Chapter 5, there was an apparent colour change of the Ga-LLZO pellets when sintered under different atmospheres, where argon sintering produced white/blue semi-transparent pellets and oxygen sintered pellets appeared solid white/brown. This may have been from the change in microstructure having a different refractive index, colour centres (trapped electrons), or change in oxidation states. The latter was investigated using XPS. The XPS spectra of each sample are shown in figure 7.1 with the samples labelled using the same nomenclature as in chapter 5 (see table 5.1). Survey spectra of each sample are shown in the appendix in figure C.1 along with the fitting of each core level in figure C.4.

All binding energy where calibrated using the C 1s C=C of 284.8 eV and peak intensities normalised to that of La 3d for quantitative comparison. Samples were first wet polished and thermally etched to 900°C before transporting into the XPS instrument. Samples prepared under argon were transported in an XPS-compatible glovebox compatible vessel to minimise exposure to air, whereas, samples treated in a tube furnace with oxygen outside the glovebox were transported immediately to the glovebox and then into the glovebox-compatible sample holder. No *in-situ* surface sputter was done, as the electrolyte surface that is examined has to be under the same conditions when incorporated in electrochemical cells. Li 1s core levels did not have any change between the samples, with the largest peak corresponding to LiOH and $LiCO_3$ from the corrosion layer and lithium 1s from the lattice of the garnet. Two carbon peaks are observed, carbon from the corrosion layer at ∼289 eV and and graphitized carbon at 284.8 eV [149]. This matches well with the O 1s signal at ∼531.8 for OH, HCO_3, and CO_3. On the other hand, the O 1s corresponding to the metal-oxide around 529 eV with the signal from GAA and GMA at lower binding energy and those for GZA, GAO, and GMO at lower binding energy.

Peak shapes for O 1s core level spectra remain similar with minor shifts in binding energy. The same is noticed for Zr 3d core levels, which may be due to a slight change in oxidation state as Zr-oxides and sub-oxides may have formed at different atmospheres. Ga 2p signals could also be measured near the surface of GAA, GMA, and GZA, which may be due to gallium segregation to the surface under reducing atmosphere sintering as it is not observed for GAO or GMO. The gallium signals at ∼1117 eV and ∼ 1144 eV are from elemental/oxides which have similar binding energies. No change in energy is reported for La 3d with the signals obtained from La_2O_3 with the multiplet splitting of 4.6 eV [255].

Overall, XPS showed changes in Ga 2p signals with those samples sintered under argon producing signals which may be due to the surface segregation of Ga. Zirconium binding energy differed between the samples possibly indicating sub-oxide formation. No signals from crucible contaminants were detected, which could be because concentrations are below the detection limit or Mg and Al are located at the immediate surface. To detect crucible contaminants grazing angle XPS or highly sensitive SIMS technique can be employed.

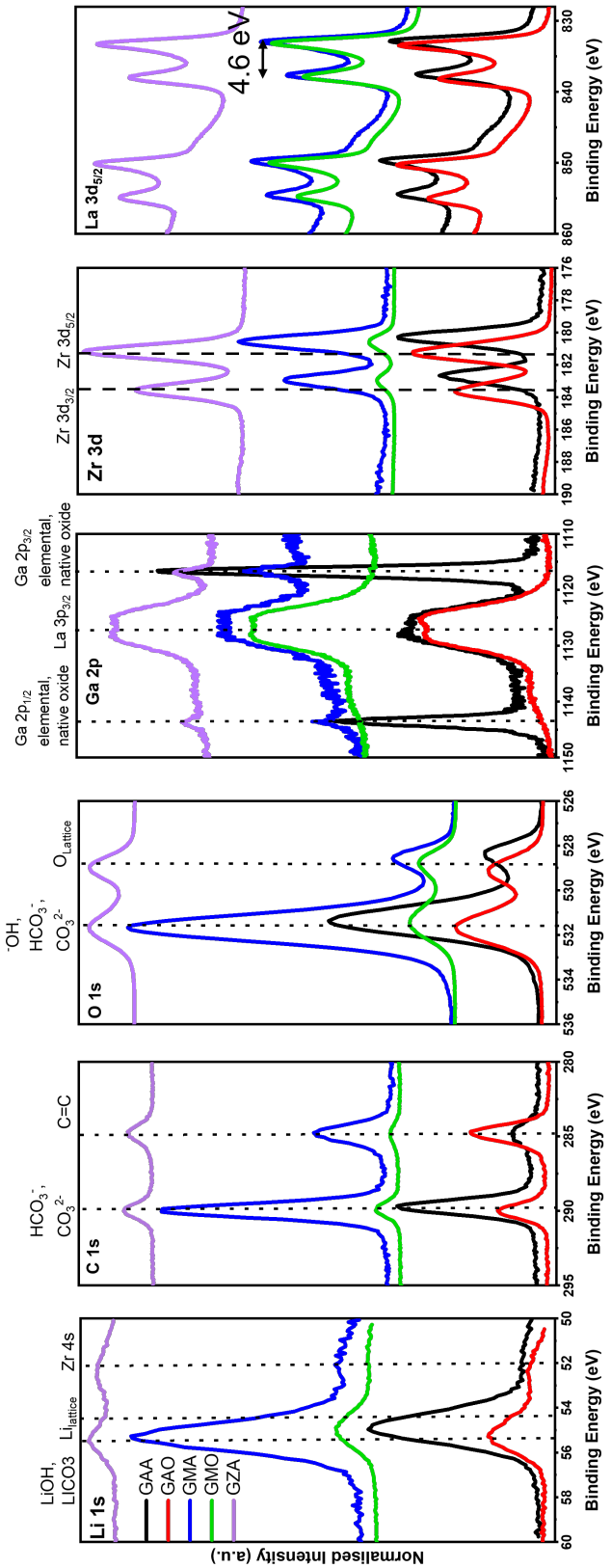


Figure 7.1: XPS spectra of key element core levels for Ga-LLZO pellets. The core levels are Li 1s. C 1s, O 1s, Ga 2p, Zr 3d, and La 3d, in order from left to right. The dashed line indicates the characteristic binding energy.

7.1.2 ToF-SIMS Depth Profile

A direct approach to studying the elemental distribution was done using ToF-SIMS. Depth profiles using Cs^+ sputter beam and Bi^+ analysis beam were done until the secondary ion counts plateaued. Choices of oxygen and argon sputtering are also possible on the instrument but during the time of this work, the Ar sputter beam was not operational and with time constraints could not be used. Oxygen sputtering can be used to detect cations because it preferentially enhances positive secondary ion (SI) yield. An oxygen sputter beam was employed briefly which is discussed later for GMA samples to look at cation distribution, but due to the fact that the oxygen beam was not working in good condition consistently, it could not be used as often. A comparison of cation DPs can still be made with the literature which uses the oxygen beam on the same instrument on Ga-LLZO which is prepared using a similar heat treatment to GAA [149]. Cs^+ on the other hand was best suited for this work as it produced good SI yields, and as the material of interest is an oxide, oxygen SI could be probed. Figure 7.2 shows the ToF-SIMS depth profiles of both GAA and GAO collected for negative secondary ions. During the time of this work, negative SI was measured using a caesium sputter beam as it enhances the negative ions, which is beneficial for analysing oxygen ions.

The SIMS depth profile of GAA (figure 7.2 left) shows three regions; (1) the surface corrosion layer which is high in carbon species, OH, and lithium SI, this layer is approximately 10 nm thick. Region (2) is the near-surface of LLZO which shows the decreasing concentration of the corrosion layer species. The remaining section is the bulk ($>$ 25nm), in which the concentration of the heavier SI rises such as LaO^- and ZrO^- this is similar to Al-LLZO SIMS DP by Otto *et al.* [160]. In the region between 10-25 nm in the DP there is an increase in GaO^- followed by a decrease, indicating the segregation of Ga at the surface along with lithium. Al contamination from the crucible is also prevalent as the concentration is initially masked by the corrosion layer, and when sputtered through, the AlO^- yield rises. The DP of AlO^- shows that it has penetrated into the bulk, which may be from the Li-Al-O eutectic phase that aids densification during sintering [194].

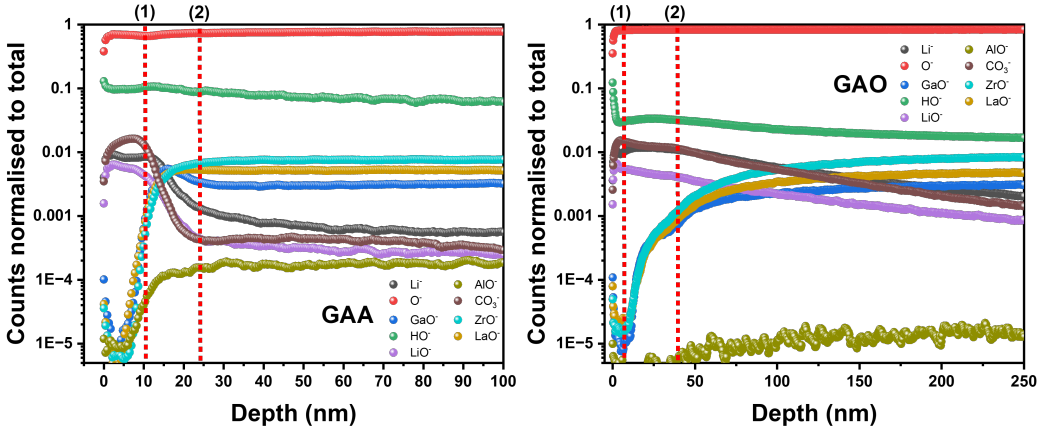


Figure 7.2: ToF-SIMS depth profile of GAA (left) and GAO (right). Depth profile of negative secondary ions using 2 keV, 150 nA Cs^+ sputter beam and 25 keV, 0.20 pA Bi^+ primary beam, analysis area is 150x150 μm, sputter area is 300x300 μm. The red dashed line indicates (1) the surface corrosion, (2) the LLZO surface, and the remaining is the bulk.

The right DP in figure 7.2 is of GAO. The DP can also be split into three regions, where (1) represents the surface corrosion of *approx.* 10nm which is composed of lithium hydroxides and carbonates, region (2) between 10-40 nm is the surface of GAO and from depth > 40 nm is the transition t bulk material. The biggest contrast between GAA and GAO is the Ga segregation which is shown as GaO^- (see figure 7.2 right) which is now away from the surface region and into the bulk, which is the same as Zr and La. AlO^- is also lower than that reported for GAA. The only difference between GAA and GAO is the atmosphere in which sintering was done, which may play a role in Ga dispersion. Different regions in LLZO may also impact the segregation observed as described by Brugge *et al.* [149] where she has shown changes in ion yield from different grains. However, her findings were mainly showing the Al segregation in different grains, caused by the contamination from alumina crucibles.

Recently, MgO crucibles have been used to provide dense garnet electrolytes and avoid crucible contamination as hypothesised. However, this is clearly not the case [254], GMA and GMO samples were sintered using MgO crucibles, and the ToF-SIMS DP are displayed in figure 7.3.

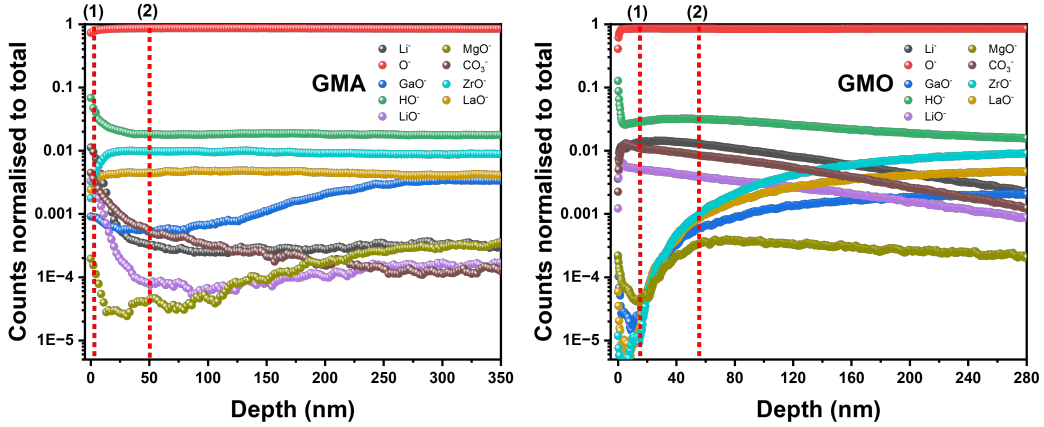


Figure 7.3: ToF-SIMS depth profile of GMA (left) and GMO (right). Depth profile of negative secondary ions using 2 keV, 150 nA Cs^+ sputter beam and 25 keV, 0.20 pA Bi^+ primary beam, analysis area is 150x150 μm, sputter area is 300x300 μm

The SIMS DP of GMA shows a similar elemental segregation behaviour to that of GAA. High SI yields are observed for Li and carbon-based species at the surface, which decrease instantly to ∼50 nm. Furthermore, the La and Zr oxide SI yields increase upon sputtering. Interestingly, the depth profile of MgO^-, GaO^-, and LiO^-, are similar, whereby there is an initial decrease from the surface to ∼ 50 nm, which is followed by a gradual increase to a depth of 250 nm until the counts plateau. Similar observations for Ga and Mg SI DP are shown in the SIMS DP of GMO. In comparison, LiO^- and CO_3 are segregated at the surface with a gradual decrease towards the bulk.

Finally, the DP of GZA is shown in figure 7.4 the elemental segregation is more vivid than those shown for GMA. Again, three regions are reported, the corrosion layer (0-15 nm), LLZO surface (15-35 nm), and the (bulk > 35 nm). The surface shows a distinct segregation of Ga, indicated by the GaO^- SI, which is followed by a decline towards the bulk and platue.

In all SIMS DP, it is noticeable that the OH^- yield is higher at the surface, primarily due to the formation of a LiOH corrosion layer. The OH counts drop towards the bulk but still has high counts, which can be from the high sputter yield from the Cs^+ sputter beam, whereas, the uniformity of the OH distribution in the bulk can also be from

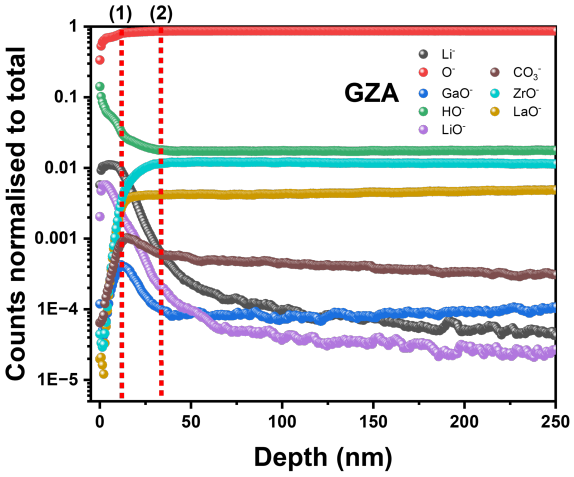


Figure 7.4: ToF-SIMS depth profile of GZA. Depth profile of negative secondary ions using 2 keV, 150 nA Cs^+ sputter beam and 25 keV, 0.20 pA Bi^+ primary beam, analysis area is 150x150 μm, sputter area is 300x300 μm

lithium-proton exchange, which can allow H^+ to diffuse into the material [145, 255].

ToF-SIMS has shown the variation in elemental concentration in Ga-LLZO from the surface into the bulk, by depth profiling. The confirmation of crucible contamination from alumina and magnesia was also reported. However, to confirm that the segregation is valid LEIS is employed. LEIS is necessary because ToF-SIMS SI yield can be influenced by the local environment of the ejected SI, known as the matrix effect. LEIS, on the other hand, is matrix independent analysis technique, as signals are from the scattering of the primary beam, with no sputtering. The following section will discuss LEIS data to confirm the results from ToF-SIMS depth profiles.

7.1.3 LEIS Depth Profile

LEIS was used to give another perspective on whether the distribution of elements in Ga-LLZO is true, in comparison to the findings with ToF-SIMS. LEIS spectra of GAA and GAO are shown in figure 7.5 using He^+ and Ne^+ primary beams. The He^+ beam is used to give a survey of all possible elements on the surface. With the He^+ beam O, Zr, and La can be detected as shown from the LEIS spectra of GAA. Whereas, for GAO

La and Zr are merged, with a slightly visible shoulder on the La peak corresponding to Zr. To separate the characteristic scattering energy for Zr and La, a Ne^+ primary beam is used, represented by the red plot. Lithium could not be detected as it was masked by the surface hydrocarbon signals, and sputtering during depth profiling which ejects lighter elements. However, attempts on detecting Li using LEIS with an ion-beam pulsing mode were done by Tellez *et al.* [256], although, this requires longer analysis time, and so with time constraints could not be set up. In some cases surface contaminants such as Na could be detected (shown in GAO LEIS spectra).

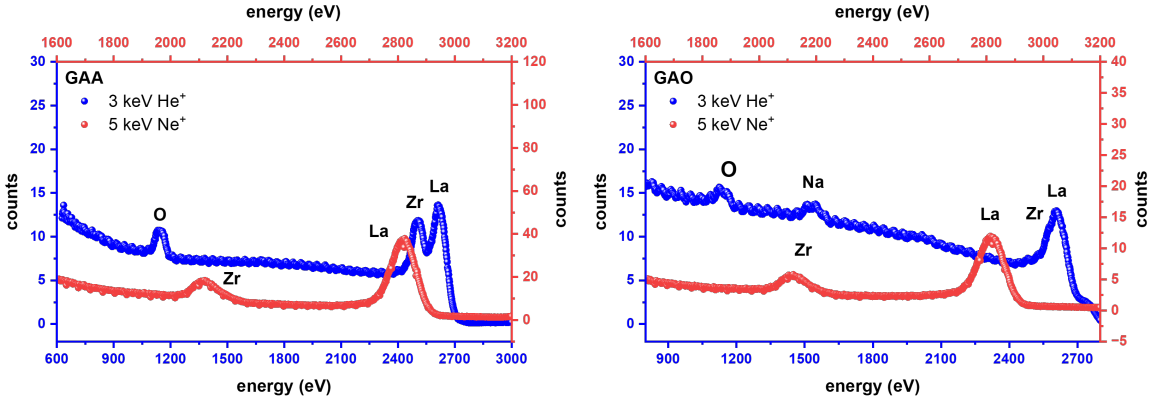


Figure 7.5: LEIS spectra of GAA (left) and GAO (right). Two primary ion beams are used to help distinguish between the Zr and La scattering energy using Ne^+ beam.

Depth profiling, using interlaced Ar sputtering with subsequent analysis was done to understand the elemental distribution of O, Zr and La as the only key species in the garnet to be detected by LEIS. LEIS depth profiles are shown in figure 7.6 from both primary ion beams. Depth profiles are displayed as dose (of the sputter beam) *vs.* counts, crater depths after analysis were too shallow to be measured using WLI, hence increasing dose density is an indication of sputtering. In all cases, there are low counts of La and Zr at the surface which increases into the bulk before plateauing. Oxygen distribution seems to gradually decline in the DP, which is not expected as the material studied is an oxide therefore oxygen should be distributed uniformly, as represented by ToF-SIMS DP. The gradual decline is a result of argon sputtering, which can reduce the surface, giving the

impression that oxygen concentration varies with depth. The onset of Zr and La profiles begins later when using the Ne^+ beam on GAA, GMA, and GZA, which is because at this time a fault emerged with the vacuum suitcase transfer, resulting in samples transported to the LEIS in ambient air, giving more time for a corrosion layer to form, which is sputtered through until Zr and La can be detected.

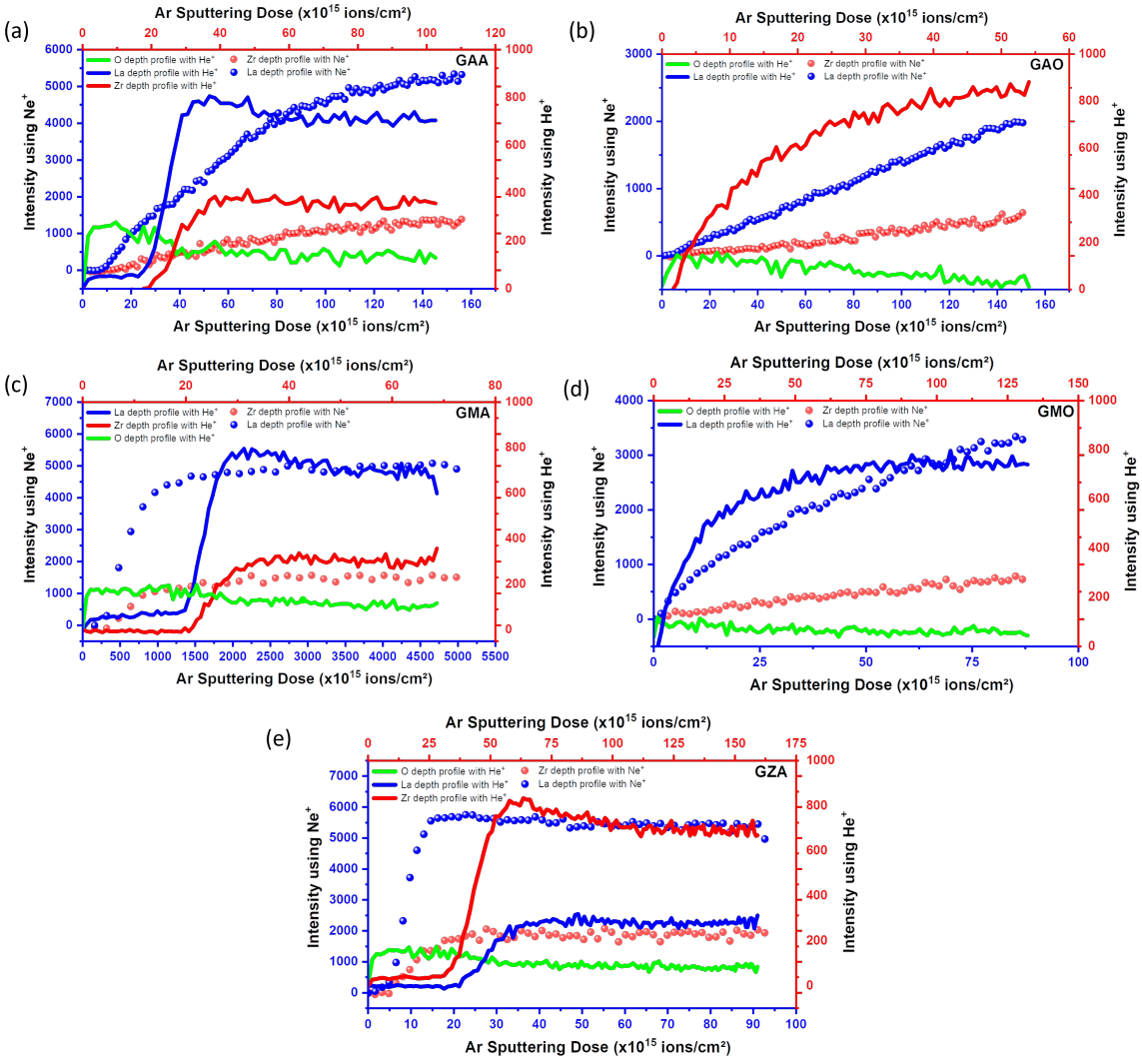


Figure 7.6: LEIS depth profile of (a) GAA, (b) GAO, (c) GMA, (d) GMO, and (e) GZA. Measurement using He^+ (solid line) and Ne^+ (scatter plot) primary beams, analysis area is 1x1 mm with a sputter area of 1.5x1.5 mm using Ar sputter beam.

7.1.4 ToF-SIMS Imaging

Elemental distribution was investigated laterally using SIMS mapping on Ga-LLZO sintered under argon while using different crucibles. Smooth surfaces had to be prepared by polishing down to 1/4 μm and thermal grooving to reveal grain boundaries, for SI images to be of high quality. Figure 7.7 shows the SI maps for GAA with an analysis area of 150x150 μm, to include multiple grain boundaries. All ion maps are normalised to the total to mitigate topography effects which can make SI yields appear greater than reality. From figure7.7a, long narrow regions are considered grain boundaries or inter-grain regions because the dimensions of the width are on the order of microns which is much larger than grain boundary thickness (i.e. 2-10 nm) [131, 257, 258]. Higher SI yields are observed for Li^+, GaO^-, and LaO^- along the intergranular regions, AlO^- is also segregated along this region which is from the crucible.

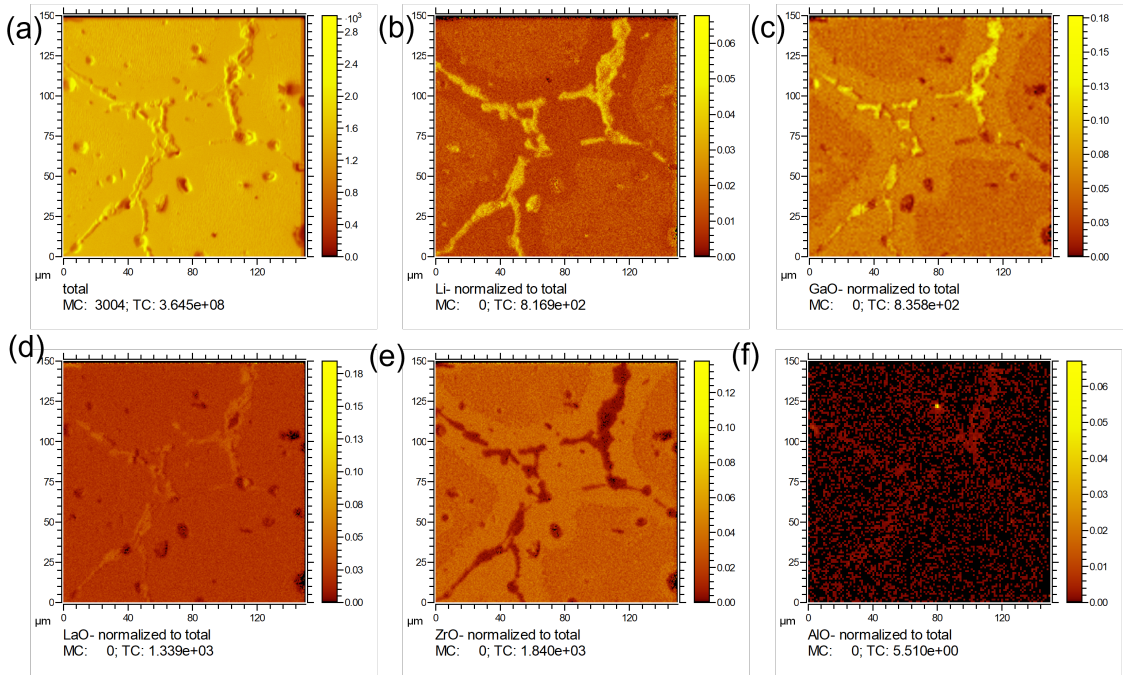


Figure 7.7: ToF-SIMS total SI maps of GAA showing (a) total SI, (b) Li^+ normalised to total, (c) GaO^- normalised to total, (d) LaO^- normalised to total, (e) ZrO^- normalised to total, and (f) AlO^- normalised to total. Measurement with Cs^+ sputter beam and 25 keV, 0.20 pA Bi^+ primary beam, analysis area is 150x150 μm, sputter area is 350x350 μm, and 512 pixels.

Pyrochlore is the common secondary phase to form upon lithium loss at high temperatures and is known to form between grains. However, the XRD pattern of GAA in figure 5.2 does not show reflections for pyrochlore. The SEM-EDX map was done in the same area as the SIMS map shown in figure C.4. It was confirmed that La was in the inter-grain regions, whereas Zr resided on the grains as shown in figure 7.7e and figure C.4. A third observation on elemental inhomogeneity is that between the bulk and grain boundary whereby SI yields of GaO^- and ZrO^- are shown in figure 7.7c and e respectively. On the contrary lithium counts in the same region is lower, a possible explanation for this may be the formation of a lithium-based corrosion layer. The corrosion layer may form more readily towards the centre of the grains, hence masking the surface SI yield of the other species. Ga and Al segregation at grain boundaries are observed more prominently when overlayed on ZrO^- SI map in figure 7.8, where the red corresponds to AlO^- and GaO^- in their respective ion maps, and green is from ZrO^-.

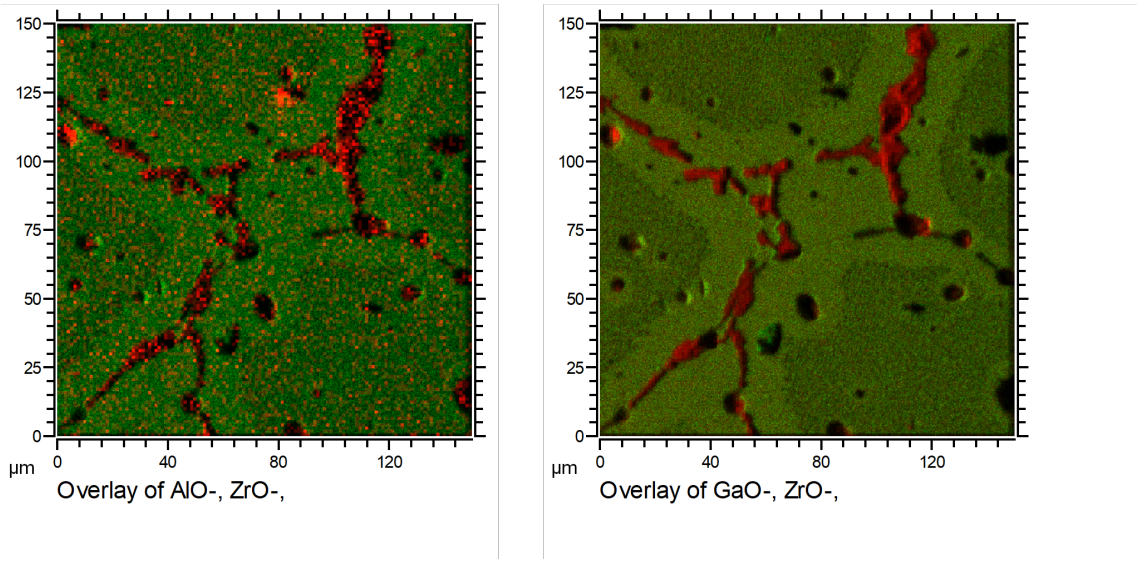


Figure 7.8: ToF-SIMS maps overlay of GAA showing, AlO^- in red, and ZrO^- in green (left), and GaO^- in red, and ZrO^- in green (right). Measurement with Cs^+ sputter beam and 25 keV, 0.20 pA Bi^+ primary beam, analysis area is 150x150 μm, sputter area is 350x350 μm, and 512 pixels.

Ion maps for GMA samples are shown in figure 7.9 using SI yields normalised to the total. With regards to GMA, both Li^+ and GaO^- are segregating at the grain boundaries, whereas in this case La and Zr species are located primarily on the grains.

The larger features of GaO^- in figure 7.9c may be due to a cluster of smaller grains that can produce more intense signals as GB density is higher in these regions. For comparison, another area of a GMA pellet was analysed and also showed GaO^- segregation at the GB shown in green in figure 7.10.

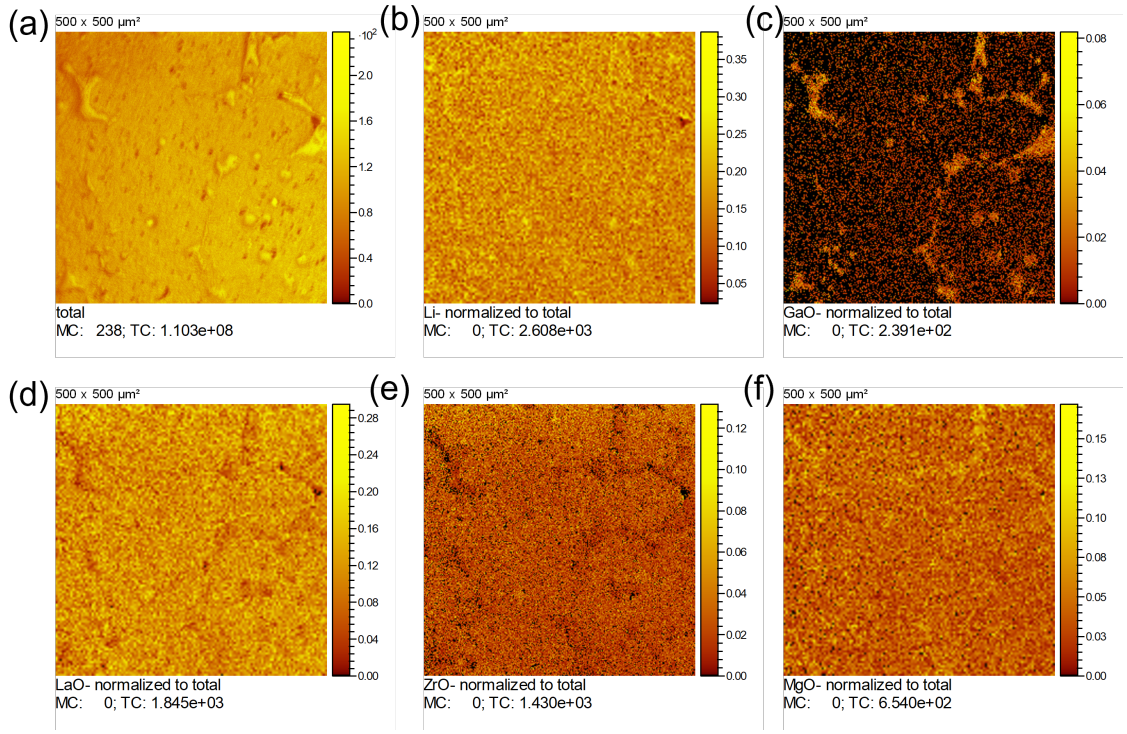


Figure 7.9: ToF-SIMS total SI maps of GMA showing (a) total SI, (b) Li^+ normalised to total, (c) GaO^- normalised to total, (d) LaO^- normalised to total, (e) ZrO^- normalised to total, and (f) MgO^- normalised to total. Measurement with Cs^+ sputter beam and 25 keV, 0.20 pA Bi^+ primary beam, analysis area is 500x500 μm, sputter area is 1000x1000 μm, and 1024 pixels.

Similar, to the findings observed for GAA with crucible contamination, the same is observed by SIMS mapping of GMA for MgO^- as shown in figure 7.9e. MgO seems to also segregate around GB of GaLLZO, which may be from a possible liquid phase formation during heat treatment. The segregation of MgO at GB may be more evident in figure 7.11(left) where the MgO signals are red and the ZrO which is part of the LLZO matrix is blue. MgO is also reported to be localised at the surface of GMA on the side facing the crucible during processing, this is seen in figure 7.11(right) using a 3D rendering overlay of MgO shown as green and ZrO as blue.

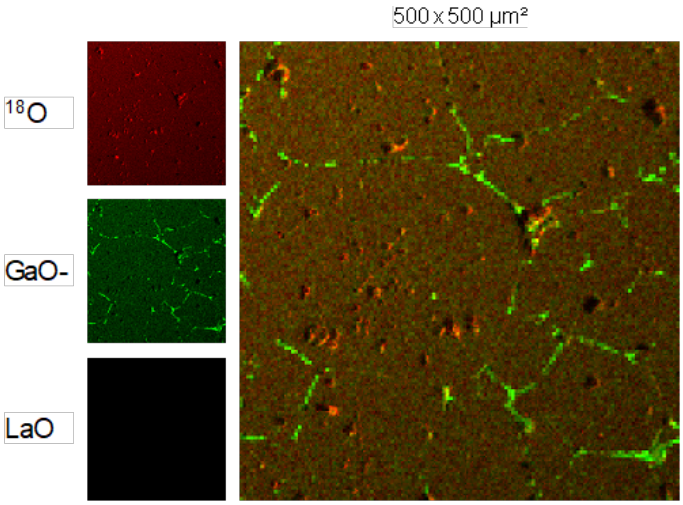


Figure 7.10: ToF-SIMS maps overlay of GMA showing, oxygen-18 in red, GaO^- in green, and LaO in blue. Measurement with Cs^+ sputter beam and 25 keV, 0.20 pA Bi^+ primary beam, analysis area is 500x500 μm, sputter area is 1000x1000 μm, and 1024 pixels.

Lastly figure 7.12 shows the SI maps for GZA, and figure 7.12a shows the total SI map which is the accumulation of the measured SI of interest. Features such as grain boundaries and pores are visible. Crucible contamination if any for GZA is not observed as the samples studied consist of Zr. Interestingly, in contrast to GAA and GMA, there is very little to no lithium segregation at the GB observed as shown in figure 7.12b. For GZA all nominal elements in the LLZO garnet show lateral homogeneity. However, gallium in the form of GaO^- in figure 7.12c and f remain segregated at the GB. Possible explanations for gallium segregation may be site competition with lithium or a possible entropy effect that occurs at high temperatures during sintering. Different crucibles were used to inhibit the segregation which was perceived to be linked to crucible contamination, a possible explanation for Ga may be to assist in forming dense polycrystalline pellets. Ga segregation at GB may also be linked to LLZO failure via dendrite formation, with Li forming an alloy with Ga, further work using *in-operando* SIMS is essential to investing this as a possibility.

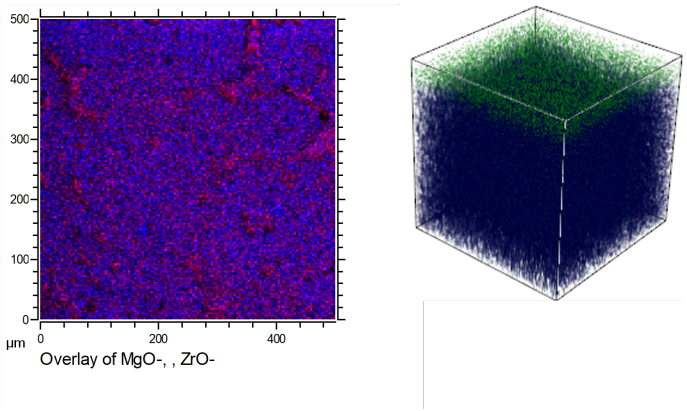


Figure 7.11: ToF-SIMS maps of GMA showing, (left) 2D overlay of GMA showing, MgO^- in red and ZrO^- in blue. (right) 3D overlay render of MgO^- in green and ZrO^- in blue (measurement by Dr Sarah Fearn). Measurement with Cs^+ sputter beam and 25 keV, 0.20 pA Bi^+ primary beam, analysis area is 500x500 μm, sputter area is 1000x1000 μm, and 1024 pixels.

7.2 Surface Chemistry of Ta-LLZO

7.2.1 XPS

A comparison of XPS data is shown for Ta-LLZO pellets prepared under the different conditions in figure 7.13. Analysis by XPS was done on pellets after thermally etching at 900°C in their respective atmospheres. This was done to understand the surface chemistry of the pellets which represents the same conditions used during cell assembly. The same approach for XPS measurement and data reconstruction was applied as discussed for Ga-LLZO. The survey spectra and core level fitting are shown in figures C.5 and C.6 respectively in the appendix.

Li 1s core level XPS spectra in figure 7.13 show a contribution from Li species which are part of the corrosion layer with binding energy ~56 eV and Li from the LLZO lattice at a lower binding energy of 55.35 eV. All pellet surfaces showed strong C 1s and O 1s signals corresponding to carbonates, hydroxides and residual hydrocarbons. Although TAA and TMA are prepared under argon atmospheres, the carbon 1s signal corresponding to corrosion layer compounds is stronger than their oxygen atmosphere counterparts. A possible explanation for this observation may be due to limited combustion of surface hy-

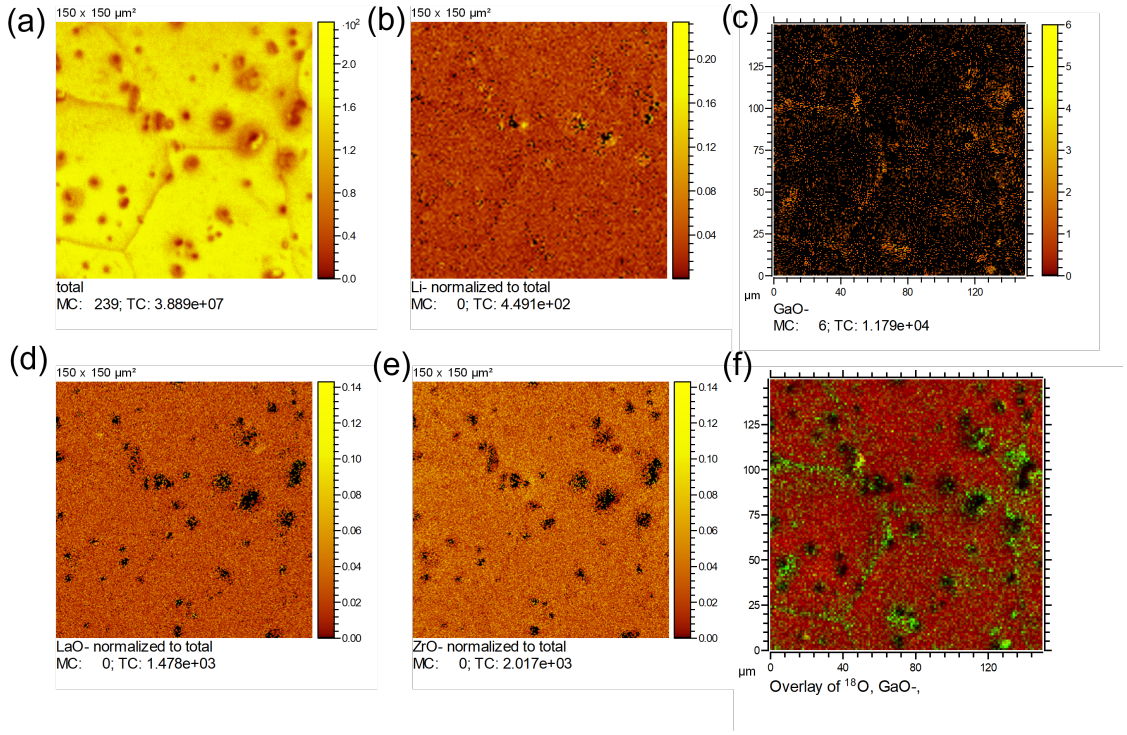


Figure 7.12: ToF-SIMS total SI maps of GZA showing (a) total SI, (b) Li^+ normalised to total, (c) GaO^- normalised to total, (d) LaO^- normalised to total, (e) ZrO^- normalised to total, and (f) GaO^- (green) overlay on $^{18}O^-$ (red). Measurement with Cs^+ sputter beam and 25 keV, 0.20 pA Bi^+ primary beam, analysis area is 150x150 μm, sputter area is 350x350 μm, and 512 pixels.

drocarbons (from the pre-washing step with n-Hexane) when heating under argon because oxygen is not available for complete combustion which may be possible for TAO and TMO sample preperation.

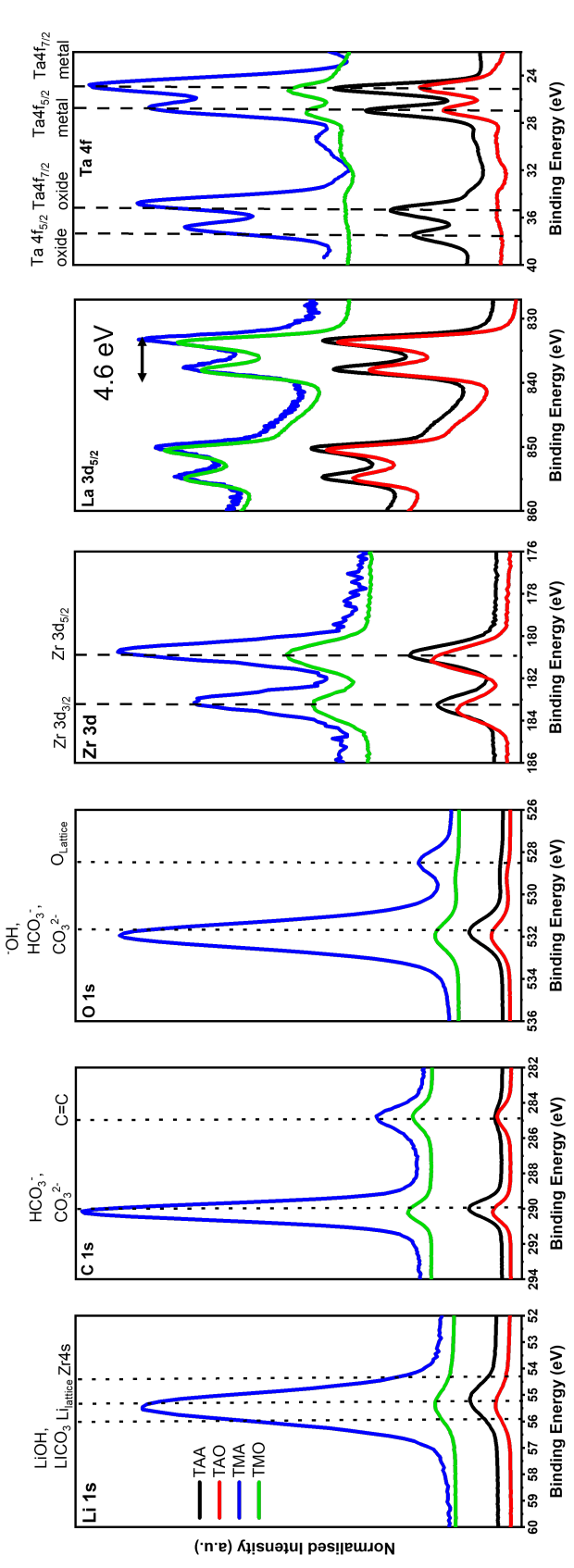


Figure 7.13: XPS spectra of key element core levels for Ta-LLZO pellets. The core levels are Li 1s. C 1s, O 1s, Zr 3d, La 3d, and Ta 4f, in order from left to right. The dashed line indicates the characteristic binding energy.

Matrix elements Zr and La show negligible change in their core level binding energy in figure 7.13. Zr 3d core level spectra were fit to zirconium oxide and sub-oxide from the LLZO and La 3d core level is a result of La-oxide from the matrix determined using the splitting multiplicity energy difference [149]. It is expected that after thermally etching that the C 1s, O 1s, and Li 1s signal corresponding to corrosion layers should be negligible, as shown in literature [68, 149]. However, a corrosion layer may have formed during transport to the XPS instrument, or the signals may in reality be lower with respect to surfaces prepared without thermal etching, which is not shown here. Ta 4f core level spectra are shown in the last spectra of figure 7.13 and correspond to Ta-O at binding energy around 25 eV for Ta $4f_{7/2}$, and the lower binding energy shoulder of TAO and TMO from O 2s [259]. The higher binding energy shoulder on the Ta-O peaks may be from surface Ta-Cl impurities with binding energy around 33 eV [259]. Additional signals around 36 eV are obtained on the Ta 4f spectra, and it is currently unclear as to what is contributing to this signal. The higher binding energy signals which may correspond to tungsten (W 4f) around 36 eV [260, 261] are only truly seen for TAA and TMA samples. Moreover, as TAA and TMA are prepared in the glove box furnace which may have tungsten components there may be the possibility of contamination. This raises further questions because during heat treatment samples are always covered with a crucible lid to prevent contamination.

7.2.2 ToF-SIMS Depth Profile

ToF-SIMS depth profiles of all Ta-LLZO samples were conducted using the same beam conditions as was done for Ga-LLZO with a bismuth primary and caesium sputter beam. The depth profiles are shown in figure 7.14 and 7.15 using depths of sputter craters measured via optical interferometry. The depth distribution of elements for TAA is shown in figure 7.14(left). Similarities with GAA are obvious with regards to high levels of Li, LiO^-, and CO_3 at the surface shown between regions (1) and (2) with a thickness of ∼10 nm, the same region also shows lower SI yields for the heavier oxide m/z such as TaO^-, LaO^-, and ZrO^-. It may seem that there is a surface segregation of Li-based species,

but as this region is extremely thin and may be a corrosion layer, the true surface may begin after the region (2). The signals before region (1) of around 5 nm, show unusual behaviours of low counts for proposed corrosion layer elements. The initial low counts may be SIMS artefacts caused by the interaction of the top surface with the beams before sputtering can equilibrate.

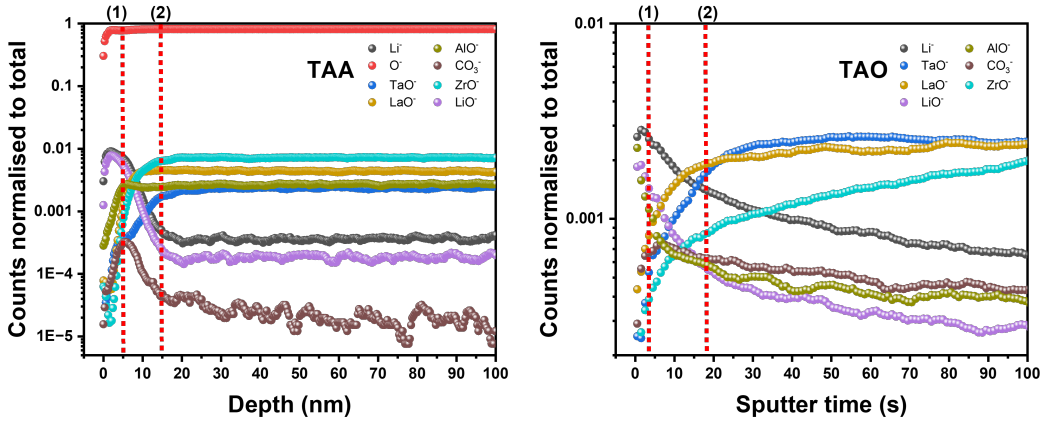


Figure 7.14: ToF-SIMS depth profile of TAA (left) and TAO (right). Depth profile of negative secondary ions using 2 keV, 150 nA Cs^+ sputter beam and 25 keV, 0.20 pA Bi^+ primary beam, analysis area is 150x150 μm, sputter area is 300x300 μm. The region left to the red dashed line indicates (1) the surface corrosion/ SIMS artefact, (2) the LLZO surface, and the remaining is the bulk.

The concentration of tantalum follows the same trend as Zr and La. This is in contrast to Ga doping where surface segregation is observed. This difference can be due to both the doping site and mass of Ta, where Ta is doped onto the Zr lattice sites. Figure 7.14(right) shows the DP for TAO, with similar transitions in elemental distribution into the bulk but not exactly the same as for TAA. The first difference is that ZrO^- SI yield increases much slower and a plateau is not reached in the first 100 nm. Both TAA and TAO depth profiles have been normalised to the total SI counts, with this in mind, and considering the CO_3^-, it is an order of magnitude higher than in TAA, which is due to the preparation of TAO outside of the glove box. The oxygen SI yield for TAO was close to unity and would limit the visibility of all the other SI, which is why it is omitted from the DP in figure 7.14(right).

Crucible contamination is prevalent in both TAA and TAO samples shown by the SIMS DP, from the AlO^- SI. Both samples show Al at the surface, TAA has Al distributed into the bulk, while on the other hand, TAO has Al at the surface which declines towards a depth of 100 nm. As previously discussed in Chapter 6, Ta-LLZO sintered under Ar atmosphere had higher relative density (98%) compared to TAO (96%) which may have been due to more Al incorporation aiding the density under reducing atmospheres.

Moving onto the analysis of Ta-LLZO prepared in MgO crucibles, the ToF-SIMS DP (figure 7.15)shows similar behaviour to their alumina crucible counterparts. Considering MgO^- SI show different depth profiles between TMA (figure 7.15left) and TMO (figure 7.15right), whereby MgO^- SI yields appear to increase and then become constant in the bulk for TMA, and the opposite is observed for TMO. An unusual observation is made in the change in TaO^- and ZrO^- SI counts for Ta-LLZO prepared under argon vs oxygen, seen from samples used in all crucibles. The change observed is the higher apparent counts of ZrO^- vs. TaO^- for TAA and TMA, which is contrary to the SI counts for the same species in TAO and TMO. At this moment, it is unclear as to what may be causing the changes in the relative yields, with the reason being more surface charging inhibiting SI extraction for samples prepared under oxygen as this is also affecting all the species of interest. The microstructure of TAO and TMO which is highly porous as discussed in Chapter 6 figure 6.4 and 6.5, the porosity can result in uneven sputtering with a fraction of SI arriving at the detector is lower and some SI can re-scatter within the pores. This finding further emphasises the importance of dense, highly polished surfaces for reliable ToF-SIMS measurements.

7.2.3 LEIS Depth Profile

LEIS DP was used to complement the finding obtained using ToF-SIMS and to show a matrix-independent analysis of La, Zr, and Ta distribution with respect to depth using interlaced analysis and sputtering. Two analysis beams were used independently on separate regions of interest. Figure 7.16 shows the total LEIS spectra after depth profiling using

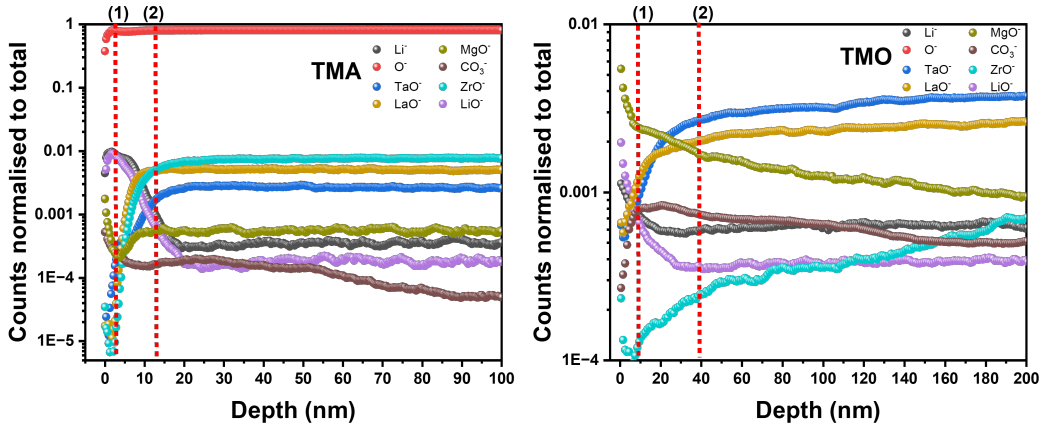


Figure 7.15: ToF-SIMS depth profile of TMA (left) and TMO (right). Depth profile of negative secondary ions using 2 keV, 150 nA Cs^+ sputter beam and 25 keV, 0.20 pA Bi^+ primary beam, analysis area is 150x150 μm, sputter area is 300x300 μm. The region left to the red dashed line indicates (1) the surface corrosion/ SIMS artefact, (2) the LLZO surface, and the remaining is the bulk.

the different analysis beams, namely He^+ and Ne^+ on TAA (left) and TAO (right). He^+ is required to achieve signals from all atoms as shown by the blue spectra on both TAA and TAO. However, in some situations, the scattering energy of He^+ which corresponds to the interaction with Zr and Ta cannot be distinguished from La as shown in figure 7.16(right). With this in mind, Ne^+ primary beam is used to better resolve the signals shown by the red plots, but this does not allow the measurement of oxygen because it is smaller than neon. Surface contamination can also be detected, such as Na as seen on TAO using a He^+ beam shown in figure 7.16(right). Corrosion layer elements such as carbon are observed at lower energies which give high backgrounds, however, this is not shown in the LEIS spectra as it has been sputtered through.

LEIS depth profiles for all Ta-LLZO samples are reported in figure 7.17. In all cases despite processing conditions, La has the highest intensity, which is due to La having large atomic radius and is the second most abundant cation in the garnet after Li. Overall, La, Ta, and Zr show low intensities at the surface which increase upon sputtering (i.e. removing corrosion layers) and intensities plateau towards the bulk which is indicated by higher sputtering dose densities.

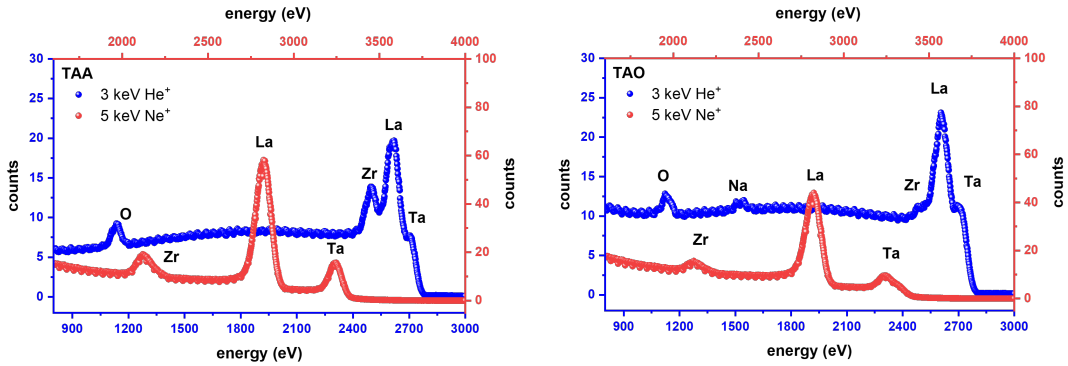


Figure 7.16: LEIS spectra of TAA (left) and TAO (right). Two primary ion beams are used to help distinguish between the Zr and La scattering energy using the Ne^+ beam.

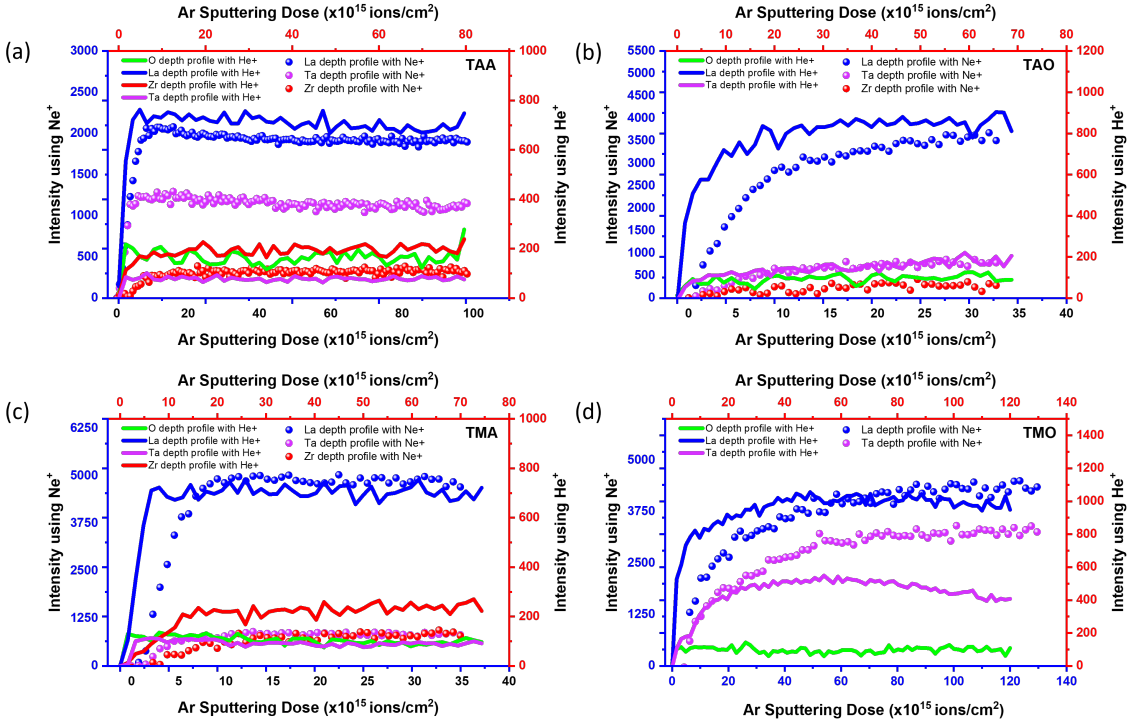


Figure 7.17: LEIS depth profile of (a) TAA, (b) TAO, (c) TMA, and (d) TMO. Measurement using 3 keV, 4.4 nA He^+ (solid line) or 3 keV, 1 nA Ne^+ (scatter plot) primary beams, analysis area is 1x1 mm with a sputter area of 1.5x1.5 mm using 50 eV, 100 nA Ar sputter beam.

7.3 Summary

To summarise, the work in this chapter employed advanced surface analysis techniques such as XPS, ToF-SIMS, and LEIS, to investigate the surface chemistry of the garnets. Samples prepared under different atmospheres and using different crucibles were examined, including LLZO with two different doping strategies; the same sample processing conditions were used for samples discussed in chapters 6 and 7.

First, Ga-doped LLZO was studied, to understand the possible changes in the chemical environment and oxidation state of Ga-LLZO after treatment XPS was used. Little change was shown with regard to the oxidation state of the garnet elements from the heat under oxygen or argon atmosphere. Ga 2p signals for samples prepared under argon were observed, and none for GAO and GMO. This indicated the possibility of Ga segregation towards the surface. ToF-SIMS DP would confirm this as a direct measurement of SI ion depth distribution in the garnet. Segregation also persisted between the nominal LLZO elements where Li showed higher SI yields towards the surface, on the contrary LaO^- and ZrO^- ion yields would appear lower at the surface and increase towards the bulk. To confirm the segregation pattern, LEIS which is a predominantly matrix-independent characterisation technique was utilised. LEIS verified that La and Zr would segregate away from the surface and would be dispersed uniformly throughout the bulk. Ample evidence shows variation in Ga-LLZO elements with respect to depth. Having said that, lateral elemental distribution was measured using a ToF-SIMS mapping approach. Due to time constraints, SIMS mapping could only be done for GAA, GMA, and GZA samples. Firstly, unusual segregation of LaO^- measured at the grain boundaries region was reported for GAA, this coincided with Li^+ and GaO^- segregation at the same region which has been discovered before [149]. Whether the elemental segregation is a result of secondary phase formation at the grain boundary or inherent to the LLZO, images showed changes in chemistry adjacent to the grain boundary.

Regarding crucible effects, GAA SIMS maps showed increased Al signals at grain boundaries, which is considered to be a result of the eutectic phase from the alumina

crucible to aid the sintering of the garnet. That said, MgO crucibles are being used as an alternative, and regarded as inert, similar to zirconia crucibles, but still produce dense electrolytes. However, MgO crucibles are not inert and have been shown to contaminate LLZO via ICP-based methods. In this chapter, SIMS mapping showed MgO^- at Ga-LLZO grain boundaries which may also be caused by the formation of a liquid eutectic phase, which is a possibility as Ga-LLZO were shown to melt onto MgO crucibles in some instances. The exact mechanism of how LLZO densifies with MgO is currently unclear which will need to be investigated in future work with a possible suggestion of liquid phase sintering from Li_2O-MgO eutectic phase as proposed by Konar *et al.* [246] from the phase analysis study. Overall, elemental segregation at grain boundaries is apparent and unavoidable with the different processing conditions. The segregation may change the local chemistry and electronic properties of grain boundaries which can result in failure from the formation of dendrites during cycling. The electronic properties of GB were investigated by another research group showing stark differences in electronic band gap but was not clear as to what may be the origin of this disparity a the time [191].

Ta-LLZO surface chemistry was studied in the second part of this chapter. As with Ga-LLZO similar elemental segregation was reported using ToF-SIMS depth profiling. In all samples, Li would be found to preferentially distribute to the surface. Difficulties still remain in distinguishing the Li contribution to the SIMS depth profile which may have also come from surface lithium carbonates and hydroxides. Interestingly, the Ta dopant would follow the same segregation profile as La and Zr, which was confirmed by LEIS DP. Using XPS negligible changes in chemical environment or oxidation state were observed between the different samples. However, when scanning the Ta 4f core level to observe the signals at binding energy ~25 eV corresponding to Ta-O, additional peaks were observed at higher binding energy around 34 eV. This was unfamiliar as none of the elements in the garnet correspond to this signal. The signals at 34 eV were present in both TAA and TMA Ta 4f core level XPS spectra, which are characteristic of tungsten-oxide. The only other key difference between samples prepared under argon and oxygen is the different

furnaces where TAO and TMO are prepared in tube furnaces with alumina tubes. On the other hand, TAA and TMA were prepared in a glove box furnace that may have tungsten components that possibly vaporise at low pressures and high temperatures. It is not known with certainty what is producing this response but this will be investigated in due course.

Chapter 8

The Role of Oxygen Vacancies on Dendrite Formation

Recent studies have been propping up on electronic conductivity in LLZO being a major player in dendrite formation during battery cycling with garnet electrolytes [70, 177, 178, 182, 189, 191]. LLZO failure by uniform dendrite nucleation has been attributed to point defects such as oxygen vacancies [184] trapping electrons [186], inherent residual electronic conductivity [178], and grain boundary/ surface chemistry [182, 191].

In this chapter, an indirect approach to locating oxygen vacancies was conducted via isotopic labelling of the garnet with oxygen-18 (^{18}O) and imaging via ToF-SIMS. This is then followed by understanding oxygen diffusion in LLZO via vacancies which were first reported by Kubicek *et al.* [32] using isotopic exchange depth profiling (IEDP). This chapter is divided into two sections, the first is on imaging of ^{18}O enriched Ga-LLZO and the second on oxygen diffusion in LLZO.

8.1 Isotopic Labelling and Imaging

In this section, Ga-LLZO samples prepared under argon (GAA, GMA, and GZA) were used as they achieved the desirable characteristics including; large grains, visible GB, high density, and purity. Samples were chemically exchanged with ^{18}O before imaging with ToF-SIMS. Figure 8.1 shows the ^{18}O SI maps of the respective samples, highly resolved images were obtained primarily by polishing and thermally grooving the samples to reveal grain boundaries. A high number of pixels was also used to ensure over-sampling and improve the lateral resolving power.

From figure 8.1 it is clear that GAA and GMA show enrichment of ^{18}O in grain boundaries. whereas GZA shows higher ^{18}O counts from the grain interior, the depth of the crater was not measured as it was too shallow to measure using the WLI. A trade-off between achieving a high-resolution image and obtaining a sufficiently deep crater had to be made for this data. Therefore, the images represent the chemistry of at least a few hundred nanometers depth, this implies that the GBs have lower diffusion coefficients to the bulk. The higher ^{18}O intensity at the GB may indicate higher oxygen vacancy density in the GB. GB chemistry was investigated in Chapter 8 and showed segregation

of Li and Ga and preferential Al and Mg contamination from the crucibles at the grain boundaries. Recently, work by Lui *et al.* [191] reported grain boundaries with lower band gaps, eluding to changes in local chemistry, trapped electrons, or carbon contamination as Lui uses spark plasma sintering with graphite sample mounts. In comparison GZA which is prepared using a zirconia crucible, does not show GB with ^{18}O enrichment. The only detectable segregation at the GB of GZA was that from GaO^- measured by ToF-SIMS, whereas, Li appeared to be uniformly distributed at the bulk.

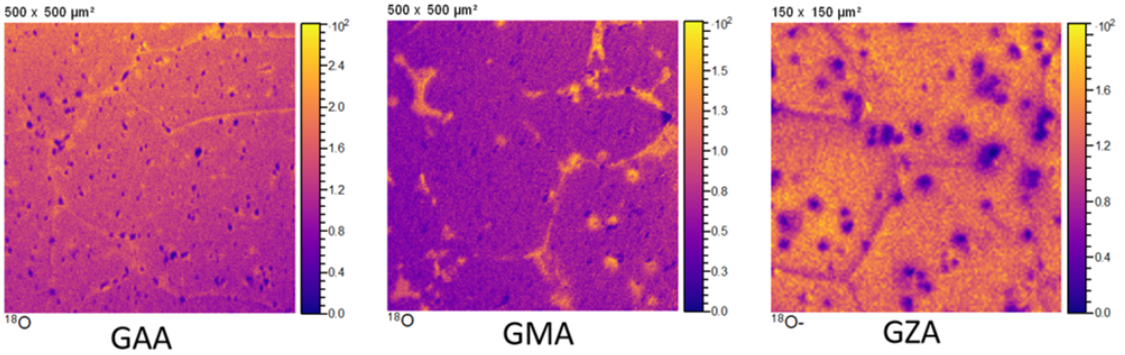


Figure 8.1: ^{18}O enriched ToF-SIMS maps of GAA (left), GMA (centre), and GZA (right). Beam conditions, Cs^+ sputter beam and 25 keV, 0.20 pA Bi^+ primary beam. Analysis area is 500x500 μm, sputter area is 1000x1000 μm, and 1024 pixels, for GAA and GMA. Analysis area is 150x150 μm, sputter area is 350x350 μm, and 512 pixels, for GZA.

The high uptake of ^{18}O in the GB of Ga-LLZO may be due to trapped electrons in oxygen vacancies. This may be a possible explanation when considering the EPR signals of Ga-LLZO shown in Chapter 6. However, due to time constraints, a comparison could not be made with Ga-LLZO sintered under oxygen. The proposed hypothesis when sintering under oxygen is less ^{18}O enrichment as less oxygen vacancy defect may exist as reported by Squires *et al.* [184].

8.2 Oxygen Diffusion

IEDP was employed as a direct observation for oxygen mobility in LLZO garnets via self-diffusion. Figure 8.2 shows the ToF-SIMS maps of ^{18}O and diffusion profiles for the Ga-LLZO material prepared under argon with various crucibles. Tracer diffusion (D^*)

coefficients ranging from 1-4x10^{-17} cm^2/s were measured overall. The ^{18}O fraction was measured on regions predominantly composed of bulk, with minimal contribution from the grain boundaries, shown in figure 8.2a, c, and e. Although it has been previously shown that fast grain boundary diffusion is possible, the measurement is mainly over bulk material, hence dominating the diffusion profile, with minimal long diffusion tails from fast GB diffusion.

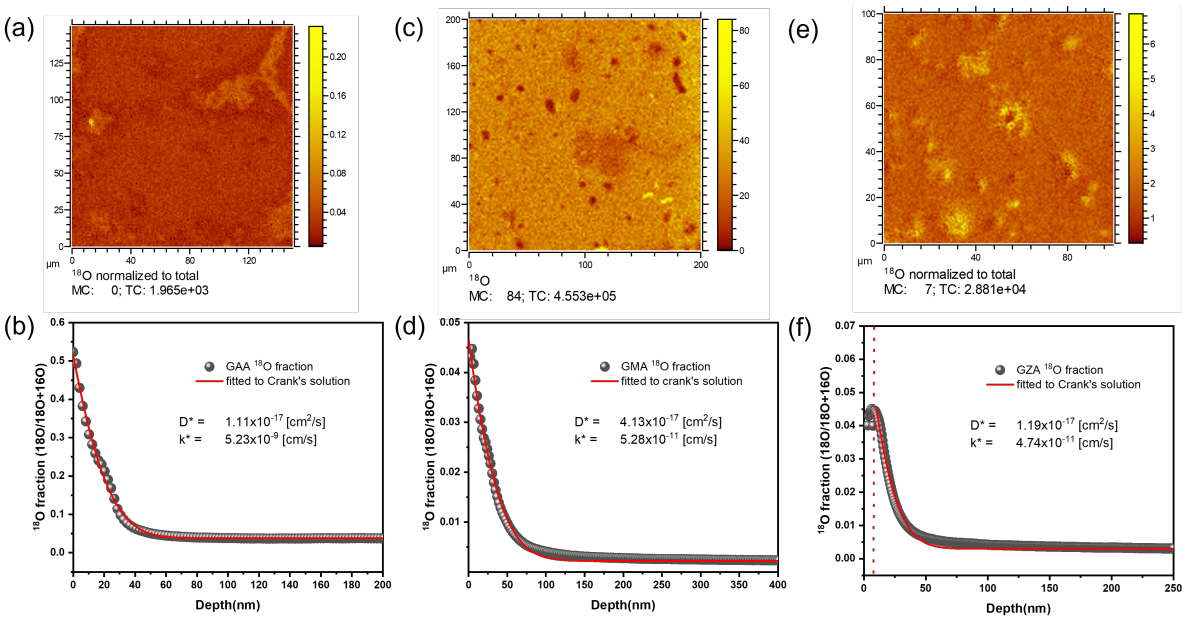


Figure 8.2: IEDP ^{18}O self-diffusion profiles and corresponding ^{18}O SI maps via ToF-SIMS for (a, b) GAA, (c,d) GMA, and (e, f) GZA (red dotted line showing the elimination of lower ^{18}O fraction at the surface from corrosion layer, when fitting). Beam conditions, Cs^+ sputter beam and 25 keV, 0.20 pA Bi^+ primary beam. Analysis area is 150x150 μm, sputter area is 350x350 μm, and 256 pixels, for GAA. Analysis area is 200x200 μm, sputter area is 400x400 μm, and 256 pixels, for GMA. Analysis area is 100x100 μm, sputter area is 300x300 μm, and 256 pixels, for GZA. Diffusion profiles are fit to Crank's solution for a semi-infinite media.

Initially, by comparison with literature data [32] of the similar material, the tracer diffusion coefficient (D^*) is *approx.* two orders of magnitude lower. The reason for the significant difference in D^* between literature values and the values reported here is possibly due to different densities. The samples used in this work have an average 95% relative density, whereas 92-93% density values were reported in the literature. The lower relative density can result in short-circuit diffusion through pores, hence increasing the diffusion

coefficient. The processing atmosphere used to prepare the garnet in literature was not mentioned making a comparison with respect to sintering gas not possible.

To determine whether oxygen mobility is linked to doping in LLZO a study between Ga and Ta-doped LLZO was made. It was shown in Chapter 8, that Ga segregation occurs at GB and surfaces, whereas Ta is segregated towards the bulk similar to the matrix composition of LLZO. Therefore, IEDP was done on Ta-LLZO samples with the ToF-SIMS maps of ^{18}O and self-diffusion profiles displayed in figure 8.2.

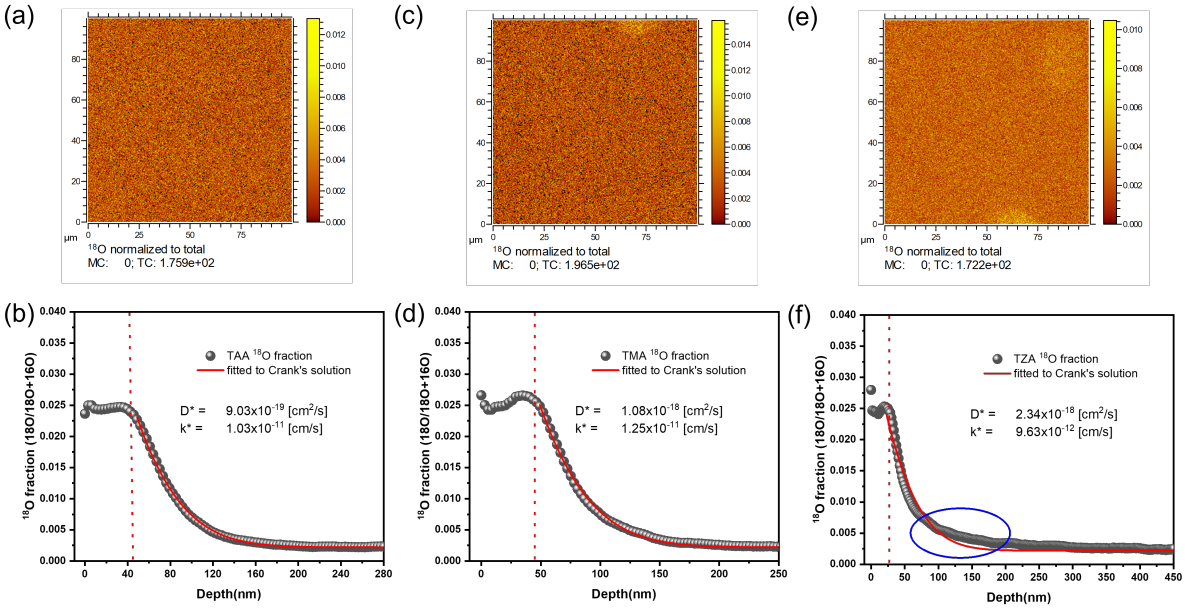


Figure 8.3: IEDP ^{18}O self-diffusion profiles and corresponding ^{18}O SI maps via ToF-SIMS for (a, b) TAA, (c,d) TMA, and (e, f) TZA. The red dotted line shows the elimination of the lower ^{18}O fraction at the surface from the corrosion layer when fitting. Beam conditions, Cs^+ sputter beam and 25 keV, 0.20 pA Bi^+ primary beam. Analysis area is 100x100 μm, sputter area is 300x300 μm, and 256 pixels, for TAA, TMA, and TZA was used. Diffusion profiles are fit to Crank's solution for a semi-infinite media.

Due to time constraints, smaller analysis areas were used (100x100 μm), as shown in figure 8.3a, c, and e, the ^{18}O is uniform in these regions. The diffusion profiles of ^{18}O fraction are shown in figure 8.3b, d, and f, for TAA, TMA, and TZA respectively. The diffusion profiles were fit to Crank's solution to the semi-infinite media. Fitting of the profiles was done after the red dashed line, which indicates the surface after the corrosion layer corresponds to the lower ^{18}O fraction.

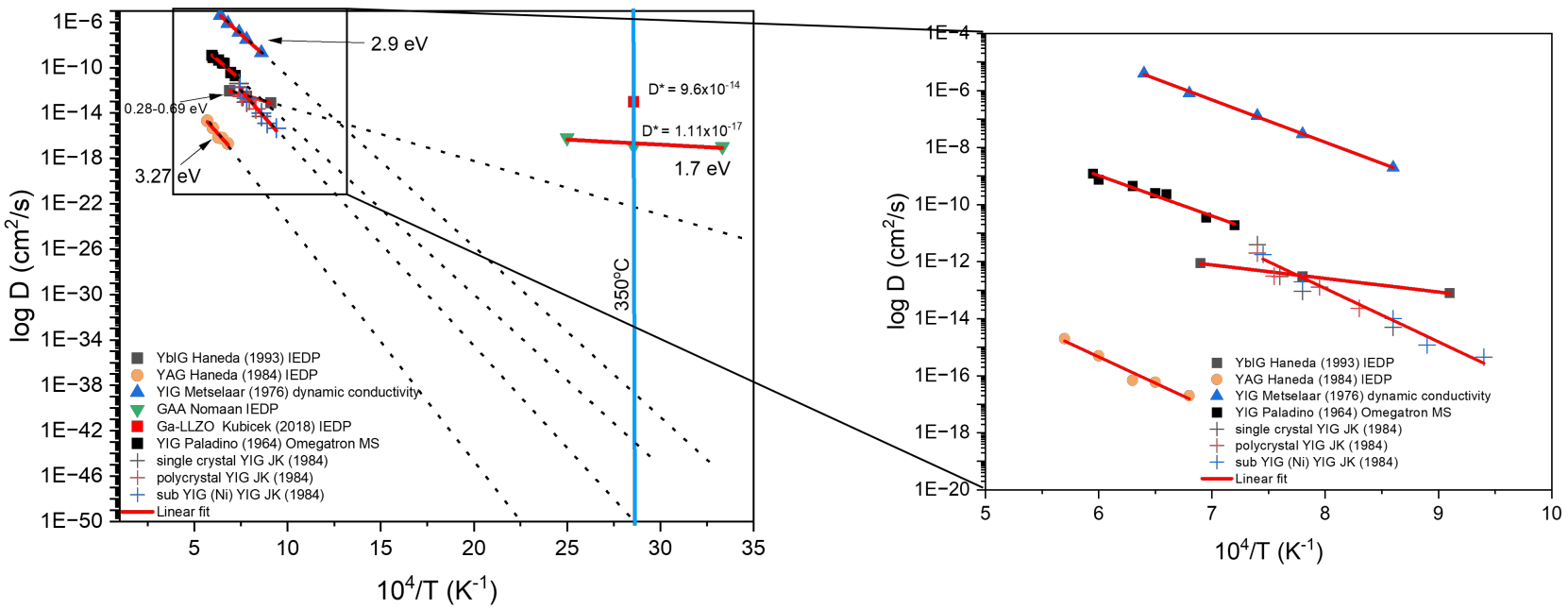


Figure 8.4: Arrhenius plot for oxygen diffusion in GAA, and comparison with other garnets including data for YAG [27], YIG [28–30], and YbIG [31]. The plot includes the self-diffusion coefficient for Ga-LLZO [32] with a similar composition to GAA. The magnified region shows a clearer representation of Arrhenius plots at higher temperatures.

An order of magnitude lower D^* was measured for Ta-LLZO at $\sim 10^{-18}$ cm^2/s, with respect to values obtained by Ga-LLZO, this may be due to Ga doping into Li sites which result in Li vacancies, counterbalanced by oxygen vacancies. With Ga known to segregate to the surface and GB, this may result in regions of higher oxygen vacancy density in LLZO. The reported D^* values in the literature for Ta-LLZO [32] showed to be several orders of magnitude higher than D^* for Ta-LLZO reported herein, again this may be due to a higher degree of porosity, acting as ^{18}O sinks. The surface exchange coefficient (k^*) determined between both doped LLZO compositions was approximately 4-6x10^{-11} cm/s with GAA having a k^* two orders of magnitude greater at 5.23x10^{-9} cm/s. The majority of the k^* values are coherent with those reported in the literature for similar LLZO compositions [32]. Possible explanations for higher k^* may be due to microstructure at the surface including porosity and grain boundaries, more oxygen vacancies at the surface may be a possibility with change in surface chemistry and partially oxygen-coordinated cations, such as La which can have a higher density of trapped electrons [174]. Differences in surface chemistry from thin corrosion layers can influence the extraction of k^*, although it was eliminated from the diffusion profile before fitting.

Garnets are known to be extremely well packed structures, hence diffusion of oxygen is considered to be primarily via vacancies. A comparison of D^* from oxygen diffusion/conductivity in other garnets is shown in figure 8.4. Comparison is made with $Y_3Al_5O_{12}$ (YAG) [27], $Y_3Fe_5O_{12}$ (YIG) [28–30], and $Yb_3Fe_5O_{12}$ (YbIG) [31]. Very little recent work has been done on oxygen diffusion in garnets, hence the limited literature. Nevertheless, what can be deduced is that previous work on oxygen diffusion was done at much higher temperatures, whereas isotopic exchange for LLZO is done at relatively lower temperatures to minimise further Li evaporation, which is obviously not of concern for YAG, YIG and YbIG. Similar diffusion coefficients for these materials were reported, but this is not to be mistaken as good agreement with LLZO diffusion coefficients, as the temperature differences are significant. However, upon extrapolation of the Arrhenius plots down to 350°, D^* for yttrium-based garnets are tens of orders of magnitude lower

than LLZO. This implies that LLZO may in fact have significantly higher oxygen vacancies.

Work on determining the activation energy for oxygen diffusion in Ga-LLZO is reported in the Arrhenius plot shown in figure 8.4(left) for GAA. Current values of 1.7 eV ±0.4 were measured, although one should bear in mind that more measurements are required to ensure the reliability of the data. However, upon first inspection, the activation energy is comparable with that by Kuganathan *et al.* [84], who computationally deduced an E_a of 1.65 eV for oxygen migration via vacancies in c-LLZO. A summary of E_a for oxygen diffusion in garnets is tabulated in table 8.1.

Table 8.1: Tabulated oxygen diffusion activation energies in garnets along with methods used to measure.

Garnet	Ea (eV)	Method	Ref
Ga-LLZO (GAA)	1.7 ± 0.4	SIMS IEDP	-
c-LLZO	1.65	Computational	[84]
YAG	3.27	SIMS IEDP	[27]
YIG	2.9	Dynamic Conductivity	[30]
YbIG	0.28-0.69	SIMS IEDP	[31]
YAG	2.6	Computational	[262]
YIG	2.84	Omegatron MS	[29]
YIG	3.7	SIMS IEDP	[28]

8.3 Summary

Results herein have built upon previous work by Kubicek *et al.* [32]. ^{18}O isotope exchanged Ga-LLZO showed preferential diffusion at the GB for GAA and GMA samples. The variation in local elemental inhomogeneity may be due to the higher density of oxygen vacancies around grain boundaries producing a chemical gradient for diffusion to occur. Oxygen vacancies in grain boundaries may harbour trapped electrons which can lower the electronic bandgap and induce dendrite formation upon Li^+ reduction, which may be seen as uniform. The local chemistry around grain boundaries such as Li, Ga, and crucible contaminant segregation, may also impact the defect chemistry, leading to higher density of oxygen vacancies. Grain boundaries span the length of polycrystalline Ga-LLZO SE which can act as regions for dendrite nucleation, giving the illusion that it is related to residual electronic conductivity. However, a more probable cause for uniform dendrite formation and propagation may be due to oxygen vacancies, trapping electrons, that do not necessarily have to be mobile.

IEDP measurements for determining the tracer diffusion coefficient (D*) of ^{18}O for Ga-LLZO and Ta-LLZO were done. D* around 10^{-17} and 10^{-18} cm^2/s for Ga-LLZO and Ta-LLZO samples respectively were determined. Upon comparison with oxygen diffusion coefficients in other garnets such as YIG and YAG, the D* for LLZO is significantly greater, indicating a higher concentration of oxygen vacancies. E_a related to oxygen diffusion via vacancies was measured to be 1.7 eV by variable temperature IEDP. The activation energy for oxygen diffusion was compared with YIG and YAG which predominantly showed higher E_a. However, the E_a for GAA was in similar proximity to literature data for c-LLZO using computational methods [84] which was linked to migration via oxygen vacancies.

Work is underway to produce D* for oxygen diffusion at extended ranges of temperatures to ensure a reliable determination of Ea for oxygen migration in LLZO. The effect of sintering under an oxygen atmosphere on D* will be investigated to understand whether changing from reducing to oxidising atmospheres will alter the oxygen vacancy concentration.

Chapter 9

Overall Summary and Future Work

9.1 Overall Summary

To summarise, this work has made comprehensive and practical efforts to study the bulk, surface and defect chemistry of LLZO garnet solid electrolytes. Two garnet electrolytes formed the base of the materials studied those being Ga- and Ta-doped LLZO as these are promising garnet compositions for solid electrolyte applications. The main structural difference is from the site of substitution by the dopants, that being partial Li substitution with Ga and partial Zr substitution with Ta. With growing concerns about the cause of dendrite formation in LLZO, two hypotheses were studied. The first hypothesis is that elemental segregation and crucible contamination may cause LLZO failure due to the difficulty in achieving elemental homogeneity in polycrystalline garnets. Therefore different atmospheres and crucibles were used to study their impacts on the LLZO properties, and building upon work by Brugge *et al.* [149]. The second hypothesis made was whether oxygen vacancies are located around grain boundaries, which is based on the findings by Lui *et al.* [191] in which some grain boundaries in LLZO have lower bandgaps. These oxygen vacancies can possibly act as colour centres and reduce Li^+ ions to metal within the electrolyte.

Both Ga-LLZO and Ta-LLZO were exposed to numerous sintering conditions using a combination of crucibles and heat treatment atmospheres. Crucibles used included alumina, magnesia, and zirconia which are relatively inexpensive and commercially readily available. The main focus of investigating different crucibles was to understand whether elemental segregation is influenced by crucible choice and if crucible contamination can be eliminated by using MgO or ZrO_2 crucibles which are not possible with Al_2O_3 crucibles. Al from alumina crucibles forms an *in-situ* Li-O-Al eutectic phase during liquid phase sintering which aids densification. Although this is a beneficial attribute of Al_2O_3 crucibles, it brings about further uncertainty on the composition of the LLZO being processed. ZrO_2 crucibles are an excellent choice to produce crucible contaminate-free garnets, but that is where the benefits end with its use. Zirconia crucibles have two main drawbacks for preparing LLZO, the first being that the crucible is unstable at high sintering tempera-

tures for garnets resulting in cracks in the crucible making the process expensive as the crucible is of short-term use. The second disadvantage of sintering with zirconia crucibles is the poor relative density of the garnets obtained. Keeping these in mind, the synthesis of garnets with MgO crucibles is a new alternative. MgO crucibles produce dense pellets and the crucibles are undamaged at high temperatures making them a cost-effective replacement in comparison to ZrO_2 crucibles. However, little is known about how MgO aids the densification of the garnet green body and if the process is clear of contamination. Sintering atmospheres of oxygen and argon were used to understand the role it plays in electronic conductivity which is portrayed to be the route cause for dendrite nucleation in LLZO during cell cycling. The idea is that sintering under argon induces excessive oxygen vacancy evolution that can harbour electrons. Whereas, in oxygen-rich conditions minimal oxygen vacancies should form, as a result, the electronic conductivity should become negligible.

Herein, the contamination of both Ga-LLZO and Ta-LLZO by Mg was studied and proven to exist using both ICP-OES and ToF-SIMS. ICP-OES provided the detection of 2 ppm of Mg in 100 mg of LLZO. However, information on distribution is not obtained as ICP-OES requires solution-based samples. This is where ToF-SIMS comes in useful as both depth and lateral analysis of Mg distribution is possible. It was found that Mg is primarily segregated at the surface of the pellet side that is in contact with the crucible as would be expected. Furthermore, Mg in the form of MgO^- was shown to appear at the grain boundaries of GMA from SIMS SI images. These observations may give insight into the mechanism of sintering of Ga-LLZO which may be similar to that of alumina crucibles, i.e. evidence for a liquid phase sintering process taking place.

Sintering LLZO under argon vs. oxygen yielded interesting information towards the generation of free electrons in the garnet. By using EPR it was found that free electrons do exist in Ga-LLZO when sintered under argon, whereas none were detected from the oxygen-sintered Ga-LLZO. However, this was not the case for Ta-LLZO which did not have any EPR signals despite the processing condition used. This begs the question of

whether doping also plays a role in electronic conductivity. ToF-SIMS DP of both dopants was conducted and it was deduced that GaO^- would segregate to the pellet surface and grain boundaries as seen with Li^+. In contrast, Ta would generally distribute towards the bulk similar to that of Zr and La. What is clear from this is that elemental inhomogeneity is prevalent in garnets, especially if in polycrystalline form and has not been mitigated.

To understand oxygen vacancies in the electrolyte, IEDP was done with ^{18}O, as it would label regions which have high oxygen mobility which can then be scanned with ToF-SIMS imaging and depth profiling. ToF-SIMS imaging of GAA and GMA showed enriched grain boundaries with^{18}O, giving an indirect perspective of higher oxygen vacancy concentrations at GB. GAA and GMA grain boundaries also showed segregation of Li^+, GaO^-, and crucible contaminants, whereas GZA also exhibited GaO^- segregation at the grain boundary and in turn no observable enrichment with ^{18}O. The mobility of oxygen via vacancies was investigated by tracer diffusion methods, followed by ToF-SIMS DP to obtain a diffusion profile. The ^{18}O fraction diffusion profile was fit to Crank's solution to extract D* of $\sim 10^{-17}$ and $\sim 10^{-18}$ cm^2/cm for Ga-LLZO and Ta-LLZO respectively. Upon comparison of D* with other non-lithium conducting garnets such as YIG and YAG, it was found to be tens of orders of magnitude greater, indicating a significant amount of oxygen vacancies may be present in LLZO. The generation of oxygen vacancies in doped-LLZO may be considered extrinsic, made possible by doping and high-temperature processing, whereas YIG and YAG oxygen vacancies may be more intrinsic in nature. The activation energy for oxygen migration in Ga-LLZO was studied by conducting IEDP at various temperatures. An E_a of 1.7 eV for oxygen diffusion was obtained which is significantly lower than for YIG and YAG which are around 3 eV, hence further insinuating relatively high oxygen mobility.

Based on the processing conditions, the conclusions for producing the best-performing doped-LLZO are as follows: Ga-LLZO prepared under argon using a MgO crucible (denoted as GMA) is the preferred method. GMA demonstrated a pure phase composition, as confirmed by XRD analysis, and large grain sizes exceeding $100\mu m$. This resulted in

a remarkable relative density of 98% and a hardness of approximately 10.5 GPa. Moreover, GMA was cycled to the highest CCD of 1.2 mA/cm^2 and exhibited a bulk ionic conductivity of 0.52 mS/cm, a value comparable to that of GAA and GZA. Notably, the electronic conductivity for GMA was an order of magnitude lower than GAA and GZA. Conversely, Ta-LLZO processed under argon with an alumina crucible (i.e., TAA) showcased superior properties, including a pure phase composition and substantial grain size. The relative density and hardness of TAA surpassed those of other Ta-LLZO variants processed under different conditions. During galvanostatic cycling, Ta-LLZO heat-treated under oxygen outperformed the rest of Ta-LLZO variants, a result contrary to expectations given the porous microstructure observed in TAO and TMO, which would typically precipitate rapid failure through dendrite formation. A direct comparison between Ta-LLZO sintered in argon and oxygen atmospheres proved elusive, leading to the conclusion that TAA is currently the superior material. Future studies are warranted to produce high-quality Ta-LLZO in both atmospheres, enabling a more definitive comparison.

9.2 Future Work

The next steps for solidifying the research in this PhD work would be to investigate if elemental segregation can be inhibited using shorter sintering times and lower temperatures, to prevent lithium loss and significant ion migration. The role of grain orientation on elemental homogeneity could be investigated by pairing ToF-SIMS with EBSD characterisation which is eluded in literature where segregation is shown to vary between grains in Ga-LLZO [149].

A key requirement for further development in the characterisation of battery materials is *in-operando* techniques. Work has been initiated on the development of *in-operando* SIMS analysis. The novel dual-quadruple plasma FIB-SIMS (nicknamed "Hi5") instrument has been developed at Imperial College Materials Department. The Hi5 allows for high lateral resolution SIMS imaging with simultaneous positive and negative secondary ion detection. Figure 9.1 shows the current capability of the Hi5. Small spot sizes using a Xe plasma beam are capable and can be tuned with adjusting beam current as shown in figure 9.1a. The beam current can be increased for quick milling and decreased for small spot sizes during SIMS measurements for high resolution. Beam spot sizes were measured by Dr Richard Chater using a TEM Cu grid and sharp contrast change from the edge over multiple beam currents, with figure 9.1b and c showing the process for 10 pA beam current from a 30 keV Xe beam.

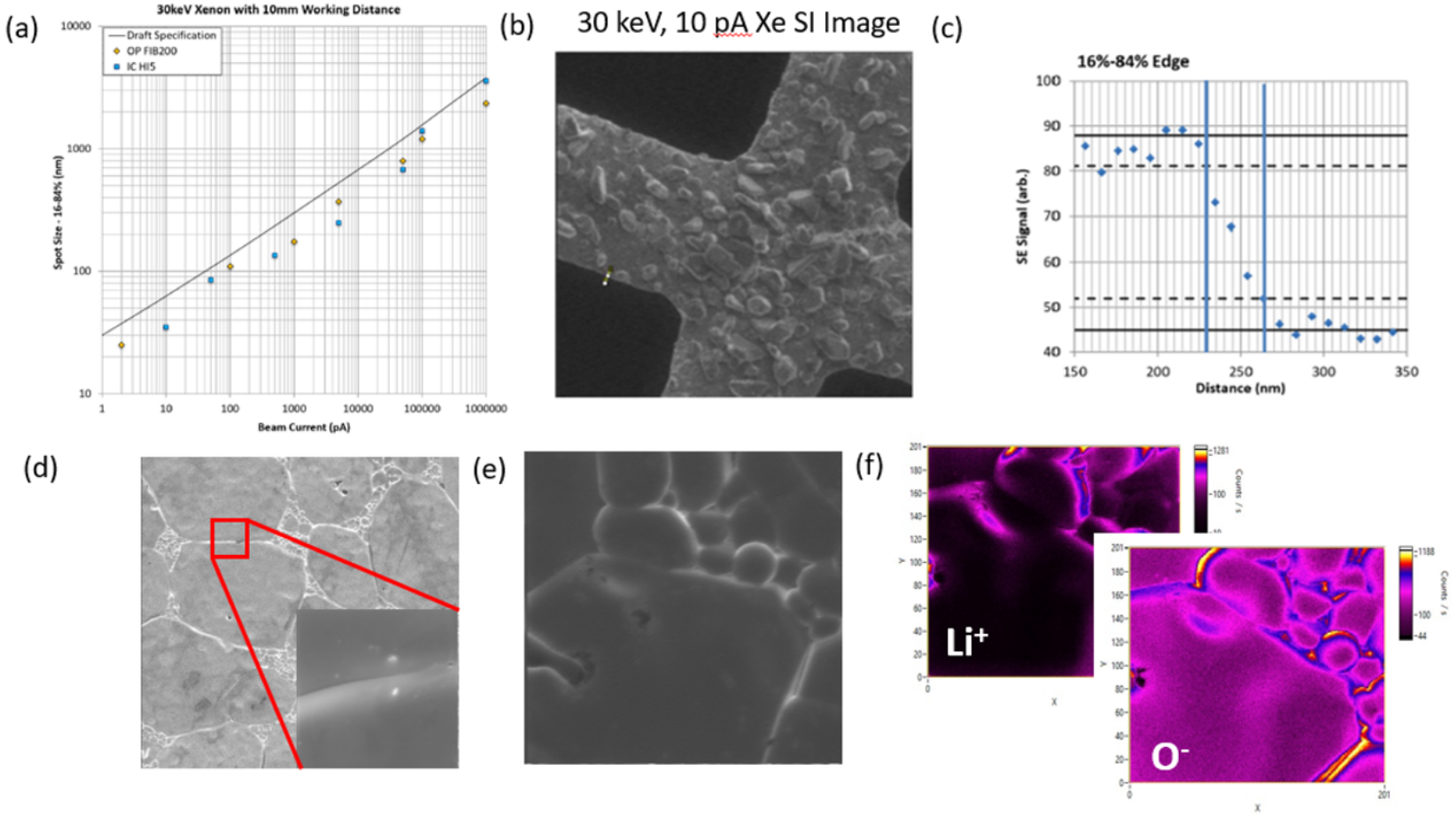


Figure 9.1: Current Hi5 capabilities using a Xe plasma primary ion beam. (a) show the correlation between beam current for a 30 keV Xe beam and sport size, (b) shows an SI image of a TEM grid achieved using Xe beam current at 10 pA. (c) Is the signal intensity from the edge of the TEM grid from Xe (30 keV, 10 pA) giving spot size down to 30 nm. (d) SE image of Ga-LLZO pellet surface viewed using 30 keV, 2 pA Xe beam, with inset showing magnification capability down to a grain boundary. (e) SI image of Ga-LLZO grain, with (f) as the corresponding SIMS images with simultaneous Li^+ and O^- collection

Figure 9.1d shows a secondary electron image of a Ga-LLZO pellet with a beam spot size of ∼25 nm, measured by Oregon Physics from a 30 keV, 2 pA Xe beam. The sample is also not polished as it is a direct observation of the surface after sintering; this is possible from the well-defined beam spot and a large working distance of 10 mm, which is not possible from ToF-SIMS instruments. Figure 9.1e shows the total SI image from the garnet which is used for initial SIMS analysis with the simultaneous positive and negative detection of the same region shown by Li^+ and O^-.

Hi5 also has the capability of selective milling and patterning which is shown in figure 9.2a, of a milled island to isolate a segment of a grain boundary. Electrical and electrochemical measurements can be done inside the Hi5 as it is equipped with UHV-compatible tungsten micro-probes to which potentiostats can be connected. An example of possible needle positions is shown in figure 9.2b on the isolated pillar. Larger electrochemical cells have been proposed as shown by the schematic in figure 9.2c for SIMS analysis of solid electrolytes during cell cycling.

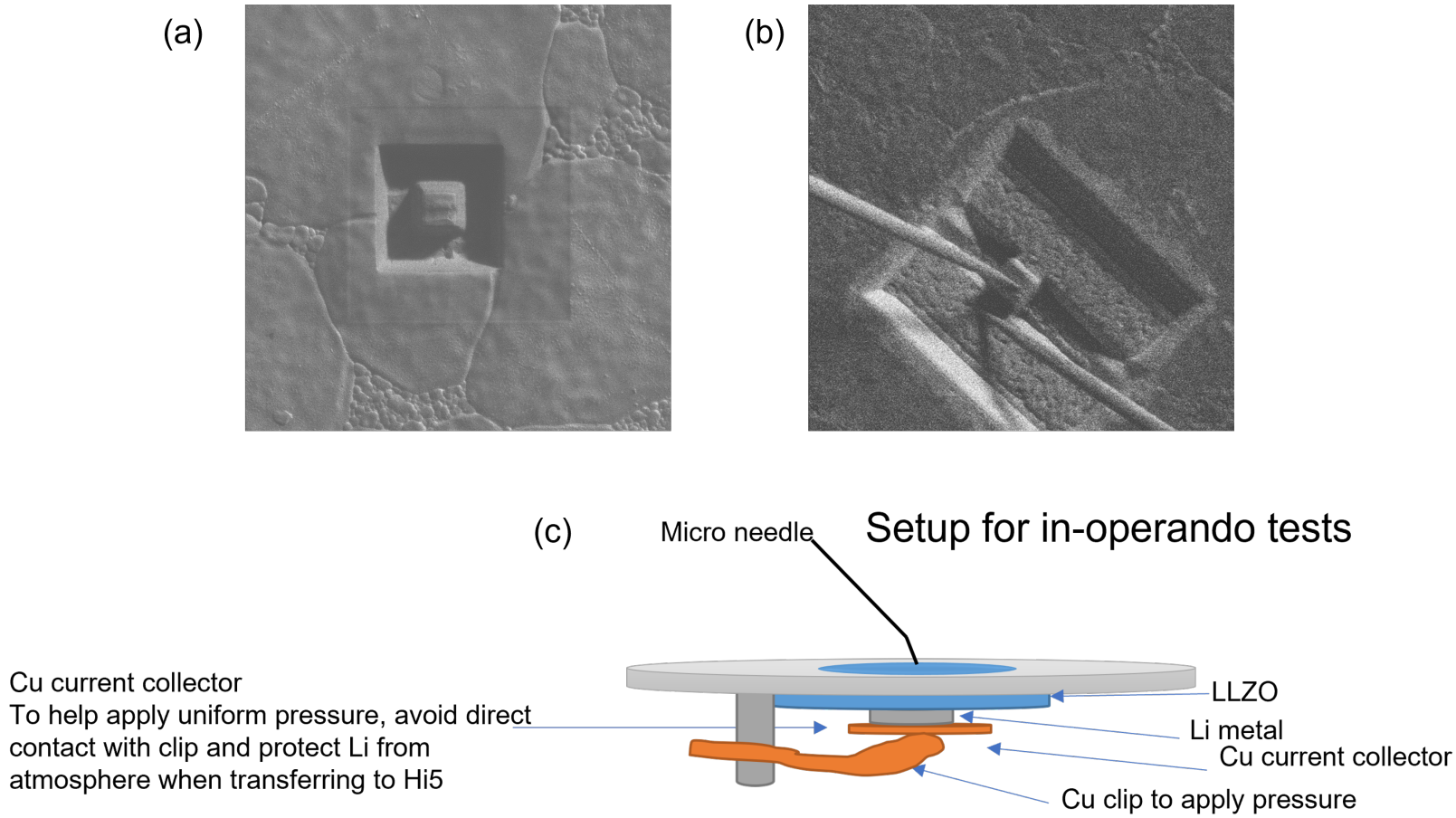


Figure 9.2: Proposed *in-operando* setups where, (a) shows SI image of grain boundaries island achieved with pattern milling, (b) micro-probes in position for possible electrochemical measurements, and (c) schematic of *in-operando* battery cycling.

Bibliography

[1] NASA/GISS. Global temperature [Available online]. https://climate.nasa.gov/vital-signs/global-temperature/, August 2022. Last accessed 03 August 2022.

[2] BloomberNEF. New energy outlook 2022 - primary energy consumption by fuel, net zero scenario[Available online]. https://about.bnef.com/new-energy-outlook/, August 2022. Last accessed 03 August 2022.

[3] Exxonmobil. Energy demand: Three drivers - global enrgy mix shifts to lower-carbon fuels [Available online]. https://corporate.exxonmobil.com/energy-and-innovation/outlook-for-energy/energy-demand#Transportation, August 2022. Last accessed 03 August 2022.

[4] Mckinsey & Company. Power spike: How battery makers can respond to surging demand from evs [Available online]. https://www.mckinsey.com/capabilities/operations/our-insights/power-spike-how-battery-makers-can-respond-to-surging-demand-from-evs, December 2022. Last accessed 03 December 2022.

[5] Bruce Dunn, Haresh Kamath, and Jean-Marie Tarascon. Electrical energy storage for the grid: a battery of choices. *Science*, 334(6058):928–935, 2011.

[6] John B Goodenough and Youngsik Kim. Challenges for rechargeable li batteries. *Chemistry of materials*, 22(3):587–603, 2010.

[7] John B Goodenough and Kyu-Sung Park. The li-ion rechargeable battery: a perspective. *Journal of the American Chemical Society*, 135(4):1167–1176, 2013.

[8] Chaofeng Liu, Zachary G Neale, and Guozhong Cao. Understanding electrochemical potentials of cathode materials in rechargeable batteries. *Materials Today*, 19(2):109–123, 2016.

[9] John Owen. 21 - ionic conductivity. In Geoffrey Allen and John C. Bevington, editors, *Comprehensive Polymer Science and Supplements*, pages 669–686. Pergamon, Amsterdam, 1989.

[10] Arumugam Manthiram, Xingwen Yu, and Shaofei Wang. Lithium battery chemistries enabled by solid-state electrolytes. *Nature Reviews Materials*, 2(4):1–16, 2017.

[11] Saisai Zhang, Hailei Zhao, Jingrong Guo, Zhihong Du, Jie Wang, and Konrad Świerczek. Characterization of sr-doped lithium lanthanum titanate with improved transport properties. *Solid State Ionics*, 336:39–46, 2019.

[12] Manuel Weiss, Dominik A Weber, Anatoliy Senyshyn, Jurgen Janek, and Wolfgang G Zeier. Correlating transport and structural properties in li1+ x al x ge2–x (po4) 3 (lagp) prepared from aqueous solution. *ACS applied materials & interfaces*, 10(13):10935–10944, 2018.

[13] Abin Kim, Seungjun Woo, Minseok Kang, Heetaek Park, and Byoungwoo Kang. Research progresses of garnet-type solid electrolytes for developing all-solid-state li batteries. *Frontiers in chemistry*, 8:468, 2020.

[14] Junji Awaka, Akira Takashima, Kunimitsu Kataoka, Norihito Kijima, Yasushi Idemoto, and Junji Akimoto. Crystal structure of fast lithium-ion-conducting cubic li7la3zr2o12. *Chemistry letters*, 40(1):60–62, 2011.

[15] Chengwei Wang, Kun Fu, Sanoop Palakkathodi Kammampata, Dennis W McOwen, Alfred Junio Samson, Lei Zhang, Gregory T Hitz, Adelaide M Nolan, Eric D Wachsman, Yifei Mo, et al. Garnet-type solid-state electrolytes: materials, interfaces, and batteries. *Chemical reviews*, 120(10):4257–4300, 2020.

[16] Lincoln J Miara, William Davidson Richards, Yan E Wang, and Gerbrand Ceder. First-principles studies on cation dopants and electrolyte— cathode interphases for lithium garnets. *Chemistry of Materials*, 27(11):4040–4047, 2015.

[17] Xingfeng He, Yizhou Zhu, and Yifei Mo. Origin of fast ion diffusion in super-ionic conductors. *Nature communications*, 8(1):15893, 2017.

[18] Frederic Aguesse, William Manalastas, Lucienne Buannic, Juan Miguel Lopez del Amo, Gurpreet Singh, Anna Llordés, and John Kilner. Investigating the dendritic growth during full cell cycling of garnet electrolyte in direct contact with li metal. *ACS applied materials & interfaces*, 9(4):3808–3816, 2017.

[19] Nagraj S Kulkarni, Theodore M Besmann, and Karl E Spear. Thermodynamic optimization of lithia–alumina. *Journal of the American Ceramic Society*, 91(12):4074–4083, 2008.

[20] Lambda. Zygo newview™ 7100]. https://www.lambdaphoto.co.uk/newview-7100.html, September 2022. Last accessed 30 September 2022.

[21] Ray F Egerton et al. *Physical principles of electron microscopy*, volume 56. Springer, 2005.

[22] John C Russ. *Fundamentals of energy dispersive X-ray analysis: Butterworths monographs in materials*. Butterworth-Heinemann, 2013.

[23] Cody V. Cushman, Philipp Brüner, Julia Zakel, George H. Major, Barry M. Lunt, Nicholas J. Smith, Thomas Grehl, and Matthew R. Linford. Low energy ion scatter-

ing (leis). a practical introduction to its theory, instrumentation, and applications. *Anal. Methods*, 8:3419–3439, 2016.

[24] Sarah Fearn. *An Introduction to Time-of-Flight Secondary Ion Mass Spectrometry (ToF-SIMS) and its Application to Materials Science*. 2053-2571. Morgan Claypool Publishers, 2015.

[25] William Manalastas Jr, Jokin Rikarte, Richard J Chater, Rowena Brugge, Ainara Aguadero, Lucienne Buannic, Anna Llordés, Frederic Aguesse, and John Kilner. Mechanical failure of garnet electrolytes during li electrodeposition observed by in-operando microscopy. *Journal of Power Sources*, 412:287–293, 2019.

[26] Jennifer E Ni, Eldon D Case, Jeffrey S Sakamoto, Ezhiyl Rangasamy, and Jeffrey B Wolfenstine. Room temperature elastic moduli and vickers hardness of hot-pressed llzo cubic garnet. *Journal of Materials Science*, 47:7978–7985, 2012.

[27] H Haneda, Y Miyazawa, and S Shirasaki. Oxygen diffusion in single crystal yttrium aluminum garnet. *Journal of crystal growth*, 68(2):581–588, 1984.

[28] JA Kilner, BCH Steele, and L Ilkov. Oxygen self-diffusion studies using negative-ion secondary ion mass spectrometry (sims). *Solid State Ionics*, 12:89–97, 1984.

[29] AE Paladino, EA Maguire Jr, and LG Rubin. Oxygen ion diffusion in single-crystal and poiycrystaiiine yttrium iron garnet. *Journal of the American Ceramic Society*, 47(6):280–282, 1964.

[30] R Metselaar and PK Larsen. Diffusion of oxygen vacancies in yttrium iron garnet investigated by dynamic conductivity measurements. *Journal of Physics and Chemistry of Solids*, 37(6):599–605, 1976.

[31] Hajime Haneda, Atsuo Watanabe, Y Kitami, and S Shirasaki. Oxygen self-diffusion in single and polycrystalline ytterbium iron garnet. In *Defect and Diffusion Forum*, volume 95, pages 1065–1070. Trans Tech Publ, 1993.

[32] Markus Kubicek, Andreas Wachter-Welzl, Daniel Rettenwander, Reinhard Wagner, Stefan Berendts, Reinhard Uecker, Georg Amthauer, Herbert Hutter, and Jürgen Fleig. Oxygen vacancies in fast lithium-ion conducting garnets. *Chemistry of Materials*, 29(17):7189–7196, 2017.

[33] Khalil Amine, Ryoji Kanno, and Yonhua Tzeng. Rechargeable lithium batteries and beyond: Progress, challenges, and future directions. *Mrs Bulletin*, 39(5):395–401, 2014.

[34] Ulrich Guth. *Kröger-Vinks Notation of Point Defects*, pages 1159–1160. Springer New York, New York, NY, 2014.

[35] Gareth R Eaton, Sandra S Eaton, David P Barr, and Ralph T Weber. *Quantitative EPR by Gareth R. Eaton, Sandra S. Eaton, David P. Barr, Ralph T. Weber.* Springer Vienna : Imprint: Springer, Vienna, 1st ed. 2010. edition, 2010.

[36] UnitedNations. United nations, global issues population [Available online]. https://www.un.org/en/global-issues/population#:~:text=The%20world%20in%202100,surrounding%20these%20latest%20population%20projections., August 2022. Last accessed 03 August 2022.

[37] BJ Csik and Kurt Schenk. Nuclear power in developing countries: Requirements and constraints. *IAEA Bulletin*, 29(2):39–42, 1987.

[38] William J Skirving, Scott F Heron, BL Marsh, Gang Liu, JL De La Cour, EF Geiger, and C Mark Eakin. The relentless march of mass coral bleaching: a global perspective of changing heat stress. *Coral reefs*, 38(4):547–557, 2019.

[39] Andreas Krause, Silvia Kloster, Stiig Wilkenskjeld, and Heiko Paeth. The sensitivity of global wildfires to simulated past, present, and future lightning frequency. *Journal of Geophysical Research: Biogeosciences*, 119(3):312–322, 2014.

[40] Juli G Pausas and Jon E Keeley. Wildfires and global change. *Frontiers in Ecology and the Environment*, 19(7):387–395, 2021.

[41] Abraham Alem Kebede, Theodoros Kalogiannis, Joeri Van Mierlo, and Maitane Berecibar. A comprehensive review of stationary energy storage devices for large scale renewable energy sources grid integration. *Renewable and Sustainable Energy Reviews*, 159:112213, 2022.

[42] Zhuang Zhang, Zhenya Duan, Dongming Chen, Yushen Xie, Xing Cao, and Jingtao Wang. Sodium acetate trihydrate-based composite phase change material with enhanced thermal performance for energy storage. *Journal of Energy Storage*, 34:102186, 2021.

[43] Peter Beaumont. Agricultural and environmental changes in the upper euphrates catchment of turkey and syria and their political and economic implications. *Applied Geography*, 16(2):137–157, 1996.

[44] Campbell Robertson. Iraq suffers as the euphrates river dwindles. *The New York Times*, 13, 2009.

[45] Kevin G Wheeler, Marc Jeuland, Jim W Hall, Edith Zagona, and Dale Whittington. Understanding and managing new risks on the nile with the grand ethiopian renaissance dam. *Nature communications*, 11(1):5222, 2020.

[46] George E Blomgren. The development and future of lithium ion batteries. *Journal of The Electrochemical Society*, 164(1):A5019, 2016.

[47] BloombergNEF. Lithium-ion battery pack prices rise for first time to an average of $151/kwh[Available online]. https://about.bnef.com/blog/lithium-ion-battery-pack-prices-rise-for-first-time-to-an-average-of-151-kwh/, December 2022. Last accessed 29 December 2022.

[48] Panasonic Energy. History of batteries [Available online]. https://www.panasonic.com/global/energy/study/academy/history.html, December 2022. Last accessed 30

December 2022.

[49] Bruno Scrosati. History of lithium batteries. *Journal of solid state electrochemistry*, 15(7-8):1623–1630, 2011.

[50] M Stanley Whittingham. Chemistry of intercalation compounds: Metal guests in chalcogenide hosts. *Progress in Solid State Chemistry*, 12(1):41–99, 1978.

[51] KJPC Mizushima, PC Jones, PJ Wiseman, and John B Goodenough. Lixcoo2 (0¡ x¡- 1): A new cathode material for batteries of high energy density. *Materials Research Bulletin*, 15(6):783–789, 1980.

[52] Alexandra K Stephan. The age of li-ion batteries. *Joule*, 3(11):2583–2584, 2019.

[53] Robert R Schaller. Moore's law: past, present and future. *IEEE spectrum*, 34(6):52–59, 1997.

[54] Ben Rowden and Nuria Garcia-Araez. A review of gas evolution in lithium ion batteries. *Energy Reports*, 6:10–18, 2020.

[55] M Stanley Whittingham. Lithium batteries and cathode materials. *Chemical reviews*, 104(10):4271–4302, 2004.

[56] Qi Liu, Xin Su, Dan Lei, Yan Qin, Jianguo Wen, Fangmin Guo, Yimin A Wu, Yangchun Rong, Ronghui Kou, Xianghui Xiao, et al. Approaching the capacity limit of lithium cobalt oxide in lithium ion batteries via lanthanum and aluminium doping. *Nature Energy*, 3(11):936–943, 2018.

[57] J-M Tarascon and Michel Armand. Issues and challenges facing rechargeable lithium batteries. *Nature*, 414(6861):359–367, 2001.

[58] Peter G Bruce, Stefan A Freunberger, Laurence J Hardwick, and Jean-Marie Tarascon. Li–o2 and li–s batteries with high energy storage. *Nature materials*, 11(1):19–29, 2012.

[59] Jihyun Jang, Yu-Ting Chen, Grayson Deysher, Diyi Cheng, So-Yeon Ham, Ashley Cronk, Phillip Ridley, Hedi Yang, Baharak Sayahpour, Bing Han, et al. Enabling a co-free, high-voltage lini0. 5mn1. 5o4 cathode in all-solid-state batteries with a halide electrolyte. *ACS Energy Letters*, 7(8):2531–2539, 2022.

[60] Donal P Finegan, Eric Darcy, Matthew Keyser, Bernhard Tjaden, Thomas MM Heenan, Rhodri Jervis, Josh J Bailey, Nghia T Vo, Oxana V Magdysyuk, Michael Drakopoulos, et al. Identifying the cause of rupture of li-ion batteries during thermal runaway. *Advanced Science*, 5(1):1700369, 2018.

[61] Arthur L Robinson and Jürgen Janek. Solid-state batteries enter ev fray, 2014.

[62] Moran Balaish, Alexander Kraytsberg, and Yair Ein-Eli. A critical review on lithium–air battery electrolytes. *Physical Chemistry Chemical Physics*, 16(7):2801–2822, 2014.

[63] Chen Liao. *Batteries: Materials principles and characterization methods*. IOP Publishing, 2021.

[64] Heinz Gerischer and Walter Ekardt. Fermi levels in electrolytes and the absolute scale of redox potentials. *Applied physics letters*, 43(4):393–395, 1983.

[65] Qing Zhao, Sanjuna Stalin, Chen-Zi Zhao, and Lynden A Archer. Designing solid-state electrolytes for safe, energy-dense batteries. *Nature Reviews Materials*, 5(3):229–252, 2020.

[66] Wei Luo, Yunhui Gong, Yizhou Zhu, Yiju Li, Yonggang Yao, Ying Zhang, Kun Fu, Glenn Pastel, Chuan-Fu Lin, Yifei Mo, et al. Reducing interfacial resistance between garnet-structured solid-state electrolyte and li-metal anode by a germanium layer. *Advanced Materials*, 29(22):1606042, 2017.

[67] Thorben Krauskopf, Hannah Hartmann, Wolfgang G Zeier, and Jurgen Janek. Toward a fundamental understanding of the lithium metal anode in solid-state batteries—an electrochemo-mechanical study on the garnet-type solid electrolyte li6. 25al0. 25la3zr2o12. *ACS applied materials & interfaces*, 11(15):14463–14477, 2019.

[68] Asma Sharafi, Eric Kazyak, Andrew L Davis, Seungho Yu, Travis Thompson, Donald J Siegel, Neil P Dasgupta, and Jeff Sakamoto. Surface chemistry mechanism of ultra-low interfacial resistance in the solid-state electrolyte li7la3zr2o12. *Chemistry of Materials*, 29(18):7961–7968, 2017.

[69] Joachim Maier. Thermodynamics of electrochemical lithium storage. *Angewandte Chemie International Edition*, 52(19):4998–5026, 2013.

[70] Alexander G. Squires, David O. Scanlon, and Benjamin J. Morgan. Native defects and their doping response in the lithium solid electrolyte li7la3zr2o12. *Chemistry of Materials*, 32(5):1876–1886, 2020.

[71] Guowei Li, Graeme R. Blake, and Thomas T. M. Palstra. Vacancies in functional materials for clean energy storage and harvesting: the perfect imperfection. *Chem. Soc. Rev.*, 46:1693–1706, 2017.

[72] Rainev Waser. Electroceramics. materials, properties, applications. by a moulson and j. m. herbert, chapman hall, london 1990, 464 pp., hardcover, e 49, isbn 0-412-29490-7. *Advanced Materials*, 4(10):698–699, 1992.

[73] F.A. Kröger and H.J. Vink. Relations between the concentrations of imperfections in solids. *Journal of Physics and Chemistry of Solids*, 5(3):208–223, 1958.

[74] Charles A Geiger. Garnet: A key phase in nature, the laboratory, and technology. *Elements*, 9(6):447–452, 2013.

[75] Junji Awaka, Norihito Kijima, Hiroshi Hayakawa, and Junji Akimoto. Synthesis and structure analysis of tetragonal li7la3zr2o12 with the garnet-related type structure. *Journal of solid state chemistry*, 182(8):2046–2052, 2009.

[76] Venkataraman Thangadurai, Heiko Kaack, and Werner JF Weppner. Novel fast lithium ion conduction in garnet-type li5la3m2o12 (m= nb, ta). *Journal of the American Ceramic Society*, 86(3):437–440, 2003.

[77] Ramaswamy Murugan, Venkataraman Thangadurai, and Werner Weppner. Fast lithium ion conduction in garnet-type li7la3zr2o12. *Angewandte Chemie International Edition*, 46(41):7778–7781, 2007.

[78] Yong Jiang, James B Adams, Mark Van Schilfgaarde, Renu Sharma, and Peter A Crozier. Theoretical study of environmental dependence of oxygen vacancy formation in ceo 2. *Applied Physics Letters*, 87(14):141917, 2005.

[79] Antonio Feteira, Kumaravinothan Sarma, Neil McN Alford, Ian M Reaney, and Derek C Sinclair. Microwave dielectric properties of gallium-doped hexagonal barium titanate ceramics. *Journal of the American Ceramic Society*, 86(3):511–513, 2003.

[80] Dong Ok Shin, Kyungbae Oh, Kwang Man Kim, Kyu-Young Park, Byungju Lee, Young-Gi Lee, and Kisuk Kang. Synergistic multi-doping effects on the li7la3zr2o12 solid electrolyte for fast lithium ion conduction. *Scientific reports*, 5(1):18053, 2015.

[81] Randy Jalem, MJD Rushton, William Manalastas Jr, Masanobu Nakayama, Toshihiro Kasuga, John A Kilner, and Robin W Grimes. Effects of gallium doping in garnet-type li7la3zr2o12 solid electrolytes. *Chemistry of Materials*, 27(8):2821–2831, 2015.

[82] Hongchao Sun, Shifei Kang, and Lifeng Cui. Prospects of llzo type solid electrolyte: from material design to battery application. *Chemical Engineering Journal*, page 140375, 2022.

[83] Anthony J Moulson and John M Herbert. *Electroceramics: materials, properties, applications*. John Wiley & Sons, 2003.

[84] Navaratnarajah Kuganathan, Michael JD Rushton, Robin W Grimes, John A Kilner, Evangelos I Gkanas, and Alexander Chroneos. Self-diffusion in garnet-type li 7 la3zr2o12 solid electrolytes. *Scientific Reports*, 11(1):451, 2021.

[85] Stefan Adams and Rayavarapu Prasada Rao. Ion transport and phase transition in li sub (7-x) la sub (3)(zr sub (2-x) m sub (x)) o sub (12)(m= ta super (5+), nb super (5+), x= 0, 0. 25). *Journal of Materials Chemistry*, 22(4):1426–1434, 2011.

[86] Adolf Fick. Ueber diffusion. *Annalen der Physik*, 170(1):59–86, 1855.

[87] J Crank. The mathematics of diffusion, 21–24 oxford university press, 1975.

[88] R.J. Chater, S. Carter, J.A. Kilner, and B.C.H. Steele. Development of a novel sims technique for oxygen self-diffusion and surface exchange coefficient measurements in oxides of high diffusivity. *Solid State Ionics*, 53-56:859–867, 1992.

[89] V Thoréton, M Niania, J Druce, H Tellez, and JA Kilner. Oxygen diffusion in ceramic mixed conducting la0. 6sr0. 4co0. 2fe0. 8o3- δ: The role of grain and twin

boundaries. *Journal of The Electrochemical Society*, 169(4):044513, 2022.

[90] J.A. Kilner, B.C.H. Steele, and L. Ilkov. Oxygen self-diffusion studies using negative-ion secondary ion mass spectrometry (sims). *Solid State Ionics*, 12:89–97, 1984.

[91] Audrey Esquirol, John Kilner, and Nigel Brandon. Oxygen transport in la0. 6sr0. 4co0. 2fe0. 8o3- δ/ce0. 8ge0. 2o2- x composite cathode for it-sofcs. *Solid State Ionics*, 175(1-4):63–67, 2004.

[92] BCH Steele. Oxygen transport and exchange in oxide ceramics. *Journal of Power Sources*, 49(1-3):1–14, 1994.

[93] Jason B Quinn, Thomas Waldmann, Karsten Richter, Michael Kasper, and Margret Wohlfahrt-Mehrens. Energy density of cylindrical li-ion cells: a comparison of commercial 18650 to the 21700 cells. *Journal of The Electrochemical Society*, 165(14):A3284–A3291, 2018.

[94] Jürgen Janek and Wolfgang G Zeier. A solid future for battery development. *Nature Energy*, 1(9):1–4, 2016.

[95] Zhangfeng Zheng, Shidong Song, and Yan Wang. Sol-gel-processed amorphous lithium ion electrolyte thin films: structural evolution, theoretical considerations, and ion transport processes. *Solid State Ionics*, 287:60–70, 2016.

[96] Yubin Zhang, Zhangfeng Zheng, Xiaoming Liu, Miaofang Chi, and Yan Wang. Fundamental relationship of microstructure and ionic conductivity of amorphous llto as solid electrolyte material. *Journal of the Electrochemical Society*, 166(4):A515, 2019.

[97] Yuki Kato, Satoshi Hori, Toshiya Saito, Kota Suzuki, Masaaki Hirayama, Akio Mitsui, Masao Yonemura, Hideki Iba, and Ryoji Kanno. High-power all-solid-state batteries using sulfide superionic conductors. *Nature Energy*, 1(4):1–7, 2016.

[98] Xianhui Nie, Jiulin Hu, and Chilin Li. Halide-based solid electrolytes: The history, progress, and challenges. *Interdisciplinary Materials*, 2(3):365–389, 2023.

[99] Xiaona Li, Jianwen Liang, Xiaofei Yang, Keegan R Adair, Changhong Wang, Feipeng Zhao, and Xueliang Sun. Progress and perspectives on halide lithium conductors for all-solid-state lithium batteries. *Energy & Environmental Science*, 13(5):1429–1461, 2020.

[100] PG Bruce and AR West. Ionic conductivity of lisicon solid solutions, li2+ 2xzn1-xgeo4. *Journal of Solid State Chemistry*, 44(3):354–365, 1982.

[101] EI Burmakin, VI Voronin, and G Sh Shekhtman. Crystalline structure and electroconductivity of solid electrolytes li 3.75 ge 0.75 v 0.25 o 4 and li 3.70 ge 0.85 w 0.15 o 4. *Russian journal of electrochemistry*, 39:1124–1129, 2003.

[102] Yuki Sakurai, Atsushi Sakuda, Akitoshi Hayashi, and Masahiro Tatsumisago. Preparation of amorphous li4sio4–li3po4 thin films by pulsed laser deposition for all-solid-state lithium secondary batteries. *Solid State Ionics*, 182(1):59–63, 2011.

[103] Longwei Liang, Xuan Sun, Jinyang Zhang, Jinfeng Sun, Linrui Hou, Yang Liu, and Changzhou Yuan. Sur-/interfacial regulation in all-solid-state rechargeable li-ion batteries based on inorganic solid-state electrolytes: advances and perspectives. *Materials Horizons*, 6(5):871–910, 2019.

[104] AS Bhalla, Ruyan Guo, and Rustum Roy. The perovskite structure—a review of its role in ceramic science and technology. *Materials research innovations*, 4(1):3–26, 2000.

[105] Yoshiyuki Inaguma, Chen Liquan, Mitsuru Itoh, Tetsurō Nakamura, Takashi Uchida, Hiromasa Ikuta, and Masataka Wakihara. High ionic conductivity in lithium lanthanum titanate. *Solid State Communications*, 86(10):689–693, 1993.

[106] Yoshiyuki Inaguma and Mitsuru Itoh. Influences of carrier concentration and site percolation on lithium ion conductivity in perovskite-type oxides. *Solid State Ionics*, 86:257–260, 1996.

[107] Antranik Jonderian and Eric McCalla. The role of metal substitutions in the development of li batteries, part ii: solid electrolytes. *Materials Advances*, 2(9):2846–2875, 2021.

[108] Litty Sebastian and J Gopalakrishnan. Lithium ion mobility in metal oxides: a materials chemistry perspective. *Journal of Materials Chemistry*, 13(3):433–441, 2003.

[109] Yaqi Zhu, Tian Wu, Jianguo Sun, and Masashi Kotobuki. Highly conductive lithium aluminum germanium phosphate solid electrolyte prepared by sol-gel method and hot-pressing. *Solid State Ionics*, 350:115320, 2020.

[110] Anastasia Vyalikh, Marc Schikora, Kaspar P Seipel, Max Weigler, Matthias Zschornak, Falk Meutzner, Wolfram Münchgesang, Tina Nestler, Viktor Vizgalov, Daniil Itkis, et al. Nmr studies of li mobility in nasicon-type glass-ceramic ionic conductors with optimized microstructure. *Journal of Materials Chemistry A*, 7(23):13968–13977, 2019.

[111] Xiaoge Hao, Qiang Zhao, Shiming Su, Shiqi Zhang, Jiabin Ma, Lu Shen, Qipeng Yu, Liang Zhao, Yong Liu, Feiyu Kang, et al. Constructing multifunctional interphase between li1. 4al0. 4ti1. 6 (po4) 3 and li metal by magnetron sputtering for highly stable solid-state lithium metal batteries. *Advanced Energy Materials*, 9(34):1901604, 2019.

[112] Pascal Hartmann, Thomas Leichtweiss, Martin R Busche, Meike Schneider, Marisa Reich, Joachim Sann, Philipp Adelhelm, and Jurgen Janek. Degradation of nasicon-type materials in contact with lithium metal: formation of mixed conducting interphases (mci) on solid electrolytes. *The Journal of Physical Chemistry C*, 117(41):21064–21074, 2013.

[113] Alfred Junio Samson, Kyle Hofstetter, Sourav Bag, and Venkataraman Thangadurai. A bird's-eye view of li-stuffed garnet-type li 7 la 3 zr 2 o 12 ceramic electrolytes for

advanced all-solid-state li batteries. *Energy & Environmental Science*, 12(10):2957–2975, 2019.

[114] Ning Zhao, Waquar Khokhar, Zhijie Bi, Chuan Shi, Xiangxin Guo, Li-Zhen Fan, and Ce-Wen Nan. Solid garnet batteries. *Joule*, 3(5):1190–1199, 2019.

[115] Mengyang Jia, Ning Zhao, Hanyu Huo, and Xiangxin Guo. Comprehensive investigation into garnet electrolytes toward application-oriented solid lithium batteries. *Electrochemical Energy Reviews*, 3:656–689, 2020.

[116] Sara Abouali, Chae-Ho Yim, Ali Merati, Yaser Abu-Lebdeh, and Venkataraman Thangadurai. Garnet-based solid-state li batteries: from materials design to battery architecture. *ACS Energy Letters*, 6(5):1920–1941, 2021.

[117] Venkataraman Thangadurai, Sumaletha Narayanan, and Dana Pinzaru. Garnet-type solid-state fast li ion conductors for li batteries: critical review. *Chemical Society Reviews*, 43(13):4714–4727, 2014.

[118] Michael P O'Callaghan, Danny R Lynham, Edmund J Cussen, and George Z Chen. Structure and ionic-transport properties of lithium-containing garnets li3ln3te2o12 (ln= y, pr, nd, sm- lu). *Chemistry of materials*, 18(19):4681–4689, 2006.

[119] Laiqiang Xu, Jiayang Li, Wentao Deng, Honglei Shuai, Shuo Li, Zhifeng Xu, Jinhui Li, Hongshuai Hou, Hongjian Peng, Guoqiang Zou, et al. Garnet solid electrolyte for advanced all-solid-state li batteries. *Advanced Energy Materials*, 11(2):2000648, 2021.

[120] Michael P O'Callaghan, Andrew S Powell, Jeremy J Titman, George Z Chen, and Edmund J Cussen. Switching on fast lithium ion conductivity in garnets: the structure and transport properties of li3+ x nd3te2- x sb x o12. *Chemistry of Materials*, 20(6):2360–2369, 2008.

[121] G Larraz, Alodia Orera, J Sanz, Isabel Sobrados, Virginia Diez-Gómez, and ML Sanjuán. Nmr study of li distribution in li 7- x h x la 3 zr 2 o 12 garnets. *Journal of Materials Chemistry A*, 3(10):5683–5691, 2015.

[122] Edmund J Cussen. Structure and ionic conductivity in lithium garnets. *Journal of Materials Chemistry*, 20(25):5167–5173, 2010.

[123] Hui Xie, Jose A Alonso, Yutao Li, Maria T Fernandez-Diaz, and John B Goodenough. Lithium distribution in aluminum-free cubic li7la3zr2o12. *Chemistry of Materials*, 23(16):3587–3589, 2011.

[124] Yutao Li, Jian-Tao Han, Chang-An Wang, Hui Xie, and John B Goodenough. Optimizing li+ conductivity in a garnet framework. *Journal of Materials Chemistry*, 22(30):15357–15361, 2012.

[125] Randy Jalem, Yoshihiro Yamamoto, Hiromasa Shiiba, Masanobu Nakayama, Hirokazu Munakata, Toshihiro Kasuga, and Kiyoshi Kanamura. Concerted migration

mechanism in the li ion dynamics of garnet-type li7la3zr2o12. *Chemistry of Materials*, 25(3):425–430, 2013.

[126] Jeff Wolfenstine, Hyungyung Jo, Yong-Hun Cho, Isabel N David, Per Askeland, Eldon D Case, Hyunjoong Kim, Heeman Choe, and Jeff Sakamoto. A preliminary investigation of fracture toughness of li7la3zr2o12 and its comparison to other solid li-ionconductors. *Materials letters*, 96:117–120, 2013.

[127] RH Brugge, JA Kilner, and A Aguadero. Germanium as a donor dopant in garnet electrolytes. *Solid State Ionics*, 337:154–160, 2019.

[128] Henrik Buschmann, Janis Dölle, Stefan Berendts, Alexander Kuhn, Patrick Bottke, Martin Wilkening, Paul Heitjans, Anatoliy Senyshyn, Helmut Ehrenberg, Andriy Lotnyk, Viola Duppel, Lorenz Kienle, and Jürgen Janek. Structure and dynamics of the fast lithium ion conductor "li7la3zr2o12". *Phys. Chem. Chem. Phys.*, 13:19378–19392, 2011.

[129] Yutao Li, Jian-Tao Han, Chang-An Wang, Sven C Vogel, Hui Xie, Maowen Xu, and John B Goodenough. Ionic distribution and conductivity in lithium garnet li7la3zr2o12. *Journal of Power Sources*, 209:278–281, 2012.

[130] Aude A Hubaud, David J Schroeder, Baris Key, Brian J Ingram, Fulya Dogan, and John T Vaughey. Low temperature stabilization of cubic (li 7- x al x/3) la 3 zr 2 o 12: role of aluminum during formation. *Journal of Materials Chemistry A*, 1(31):8813–8818, 2013.

[131] Ezhiyl Rangasamy, Jeff Wolfenstine, and Jeffrey Sakamoto. The role of al and li concentration on the formation of cubic garnet solid electrolyte of nominal composition li7la3zr2o12. *Solid State Ionics*, 206:28–32, 2012.

[132] Federico M Pesci, Rowena H Brugge, AK Ola Hekselman, Andrea Cavallaro, Richard J Chater, and Ainara Aguadero. Elucidating the role of dopants in the critical current density for dendrite formation in garnet electrolytes. *Journal of Materials Chemistry A*, 6(40):19817–19827, 2018.

[133] Jian-Fang Wu, En-Yi Chen, Yao Yu, Lin Liu, Yue Wu, Wei Kong Pang, Vanessa K Peterson, and Xin Guo. Gallium-doped li7la3zr2o12 garnet-type electrolytes with high lithium-ion conductivity. *ACS applied materials & interfaces*, 9(2):1542–1552, 2017.

[134] Carlos Bernuy-Lopez, William Manalastas Jr, Juan Miguel Lopez del Amo, Ainara Aguadero, Frederic Aguesse, and John A Kilner. Atmosphere controlled processing of ga-substituted garnets for high li-ion conductivity ceramics. *Chemistry of materials*, 26(12):3610–3617, 2014.

[135] Reinhard Wagner, Gunther J Redhammer, Daniel Rettenwander, Anatoliy Senyshyn, Walter Schmidt, Martin Wilkening, and Georg Amthauer. Crystal structure of garnet-related li-ion conductor li7–3 x ga x la3zr2o12: fast li-ion conduction

caused by a different cubic modification? *Chemistry of materials*, 28(6):1861–1871, 2016.

[136] Reinhard Wagner, Gunther J Redhammer, Daniel Rettenwander, Gerold Tippelt, Andreas Welzl, Stefanie Taibl, Jurgen Fleig, Alexandra Franz, Werner Lottermoser, and Georg Amthauer. Fast li-ion-conducting garnet-related li7–3 x fe x la3zr2o12 with uncommon i 43 d structure. *Chemistry of Materials*, 28(16):5943–5951, 2016.

[137] Mohamad M Ahmad. Estimation of the concentration and mobility of mobile li+ in the cubic garnet-type li 7 la 3 zr 2 o 12. *RSC Advances*, 5(33):25824–25829, 2015.

[138] C Deviannapoorani, L Dhivya, S Ramakumar, and Ramaswamy Murugan. Lithium ion transport properties of high conductive tellurium substituted li7la3zr2o12 cubic lithium garnets. *Journal of Power Sources*, 240:18–25, 2013.

[139] Bo Dong, Stephen R Yeandel, Pooja Goddard, and Peter R Slater. Combined experimental and computational study of ce-doped la3zr2li7o12 garnet solid-state electrolyte. *Chemistry of Materials*, 32(1):215–223, 2019.

[140] L Dhivya and Ramaswamy Murugan. Effect of simultaneous substitution of y and ta on the stabilization of cubic phase, microstructure, and li+ conductivity of li7la3zr2o12 lithium garnet. *ACS applied materials & interfaces*, 6(20):17606–17615, 2014.

[141] Dawei Wang, Guiming Zhong, Oleksandr Dolotko, Yixiao Li, Matthew J McDonald, Jinxiao Mi, Riqiang Fu, and Yong Yang. The synergistic effects of al and te on the structure and li+-mobility of garnet-type solid electrolytes. *Journal of Materials Chemistry A*, 2(47):20271–20279, 2014.

[142] Lucienne Buannic, Brahim Orayech, Juan-Miguel Lopez Del Amo, Javier Carrasco, Nebil A Katcho, Frederic Aguesse, William Manalastas, Wei Zhang, John Kilner, and Anna Llordes. Dual substitution strategy to enhance li+ ionic conductivity in li7la3zr2o12 solid electrolyte. *Chemistry of materials*, 29(4):1769–1778, 2017.

[143] Dawei Wang, Guiming Zhong, Wei Kong Pang, Zaiping Guo, Yixiao Li, Matthew J McDonald, Riqiang Fu, Jin-Xiao Mi, and Yong Yang. Toward understanding the lithium transport mechanism in garnet-type solid electrolytes: Li+ ion exchanges and their mobility at octahedral/tetrahedral sites. *Chemistry of Materials*, 27(19):6650–6659, 2015.

[144] Alodia Orera, Guillermo Larraz, José Alberto Rodríguez-Velamazán, Javier Campo, and María Luisa Sanjuán. Influence of li+ and h+ distribution on the crystal structure of li7–x h x la3zr2o12 (0 x 5) garnets. *Inorganic chemistry*, 55(3):1324–1332, 2016.

[145] Rowena H Brugge, AK Ola Hekselman, Andrea Cavallaro, Federico M Pesci, Richard J Chater, John A Kilner, and Ainara Aguadero. Garnet electrolytes for solid state batteries: visualization of moisture-induced chemical degradation and re-

vealing its impact on the li-ion dynamics. *Chemistry of Materials*, 30(11):3704–3713, 2018.

[146] May Nyman, Todd M Alam, Sarah K McIntyre, Grant C Bleier, and David Ingersoll. Alternative approach to increasing li mobility in li-la-nb/ta garnet electrolytes. *Chemistry of Materials*, 22(19):5401–5410, 2010.

[147] Asma Sharafi, Seungho Yu, Michael Naguib, Marcus Lee, Cheng Ma, Harry M Meyer, Jagjit Nanda, Maiofang Chi, Donald J Siegel, and Jeff Sakamoto. Impact of air exposure and surface chemistry on li–li 7 la 3 zr 2 o 12 interfacial resistance. *Journal of Materials Chemistry A*, 5(26):13475–13487, 2017.

[148] Lei Cheng, Cheng Hao Wu, Angelique Jarry, Wei Chen, Yifan Ye, Junfa Zhu, Robert Kostecki, Kristin Persson, Jinghua Guo, Miquel Salmeron, et al. Interrelationships among grain size, surface composition, air stability, and interfacial resistance of al-substituted li7la3zr2o12 solid electrolytes. *ACS applied materials & interfaces*, 7(32):17649–17655, 2015.

[149] Rowena H Brugge, Federico M Pesci, Andrea Cavallaro, Christopher Sole, Mark A Isaacs, Gwilherm Kerherve, Robert S Weatherup, and Ainara Aguadero. The origin of chemical inhomogeneity in garnet electrolytes and its impact on the electrochemical performance. *Journal of Materials Chemistry A*, 8(28):14265–14276, 2020.

[150] C Deviannapoorani, S Ramakumar, N Janani, and Ramaswamy Murugan. Synthesis of lithium garnets from la2zr2o7 pyrochlore. *Solid State Ionics*, 283:123–130, 2015.

[151] Martin Philipp, Bernhard Gadermaier, Patrick Posch, Ilie Hanzu, Steffen Ganschow, Martin Meven, Daniel Rettenwander, Günther J Redhammer, and H Martin R Wilkening. The electronic conductivity of single crystalline ga-stabilized cubic li7la3zr2o12: A technologically relevant parameter for all-solid-state batteries. *Advanced materials interfaces*, 7(16):2000450, 2020.

[152] Daniel Rettenwander, Reinhard Wagner, Andreas Reyer, Maximilian Bonta, Lei Cheng, Marca M Doeff, Andreas Limbeck, Martin Wilkening, and Georg Amthauer. Interface instability of fe-stabilized li7la3zr2o12 versus li metal. *The Journal of Physical Chemistry C*, 122(7):3780–3785, 2018.

[153] Yuxing Wang and Wei Lai. High ionic conductivity lithium garnet oxides of li7- xla3zr2- xtaxo12 compositions. *Electrochemical and Solid-State Letters*, 15(5):A68, 2012.

[154] Travis Thompson, Asma Sharafi, Michelle D Johannes, Ashfia Huq, Jan L Allen, Jeff Wolfenstine, and Jeff Sakamoto. A tale of two sites: on defining the carrier concentration in garnet-based ionic conductors for advanced li batteries. *Advanced Energy Materials*, 5(11):1500096, 2015.

[155] Shingo Ohta, Tetsuro Kobayashi, and Takahiko Asaoka. High lithium ionic conductivity in the garnet-type oxide li7- x la3 (zr2- x, nbx) o12 (x= 0–2). *Journal of Power Sources*, 196(6):3342–3345, 2011.

[156] Yiqiu Li, Zheng Wang, Yang Cao, Fuming Du, Cheng Chen, Zhonghui Cui, and Xiangxin Guo. W-doped li7la3zr2o12 ceramic electrolytes for solid state li-ion batteries. *Electrochimica Acta*, 180:37–42, 2015.

[157] Shufeng Song, Denis Sheptyakov, Alexander M Korsunsky, Hai M Duong, and Li Lu. High li ion conductivity in a garnet-type solid electrolyte via unusual site occupation of the doping ca ions. *Materials & Design*, 93:232–237, 2016.

[158] C Deviannapoorani, Lakshmi S Shankar, S Ramakumar, and Ramaswamy Murugan. Investigation on lithium ion conductivity and structural stability of yttrium-substituted li 7 la 3 zr 2 o 12. *Ionics*, 22:1281–1289, 2016.

[159] Ezhiylmurugan Rangasamy, Jeff Wolfenstine, Jan Allen, and Jeff Sakamoto. The effect of 24c-site (a) cation substitution on the tetragonal–cubic phase transition in li7- xla3- xaxzr2o12 garnet-based ceramic electrolyte. *Journal of Power Sources*, 230:261–266, 2013.

[160] Svenja-K Otto, Luise M Riegger, Till Fuchs, Sven Kayser, Pascal Schweitzer, Simon Burkhardt, Anja Henss, and Jürgen Janek. In situ investigation of lithium metal–solid electrolyte anode interfaces with tof-sims. *Advanced Materials Interfaces*, 9(13):2102387, 2022.

[161] Masashi Kotobuki, Hirokazu Munakata, Kiyoshi Kanamura, Yosuke Sato, and Toshihiro Yoshida. Compatibility of li7la3zr2o12 solid electrolyte to all-solid-state battery using li metal anode. *Journal of the Electrochemical Society*, 157(10):A1076, 2010.

[162] Charles Monroe and John Newman. Dendrite growth in lithium/polymer systems: A propagation model for liquid electrolytes under galvanostatic conditions. *Journal of The Electrochemical Society*, 150(10):A1377, 2003.

[163] Aniruddha Jana and R Edwin García. Lithium dendrite growth mechanisms in liquid electrolytes. *Nano Energy*, 41:552–565, 2017.

[164] Krzysztof Jan Siczek. Next-generation batteries with sulfur cathodes. 2019.

[165] Lukas Porz, Tushar Swamy, Brian W Sheldon, Daniel Rettenwander, Till Frömling, Henry L Thaman, Stefan Berendts, Reinhard Uecker, W Craig Carter, and Yet-Ming Chiang. Mechanism of lithium metal penetration through inorganic solid electrolytes. *Advanced Energy Materials*, 7(20):1701003, 2017.

[166] Eric Kazyak, Regina Garcia-Mendez, William S LePage, Asma Sharafi, Andrew L Davis, Adrian J Sanchez, Kuan-Hung Chen, Catherine Haslam, Jeff Sakamoto, and Neil P Dasgupta. Li penetration in ceramic solid electrolytes: operando microscopy analysis of morphology, propagation, and reversibility. *Matter*, 2(4):1025–1048, 2020.

[167] Bryan Kinzer, Andrew L Davis, Thorben Krauskopf, Hannah Hartmann, William S LePage, Eric Kazyak, Jürgen Janek, Neil P Dasgupta, and Jeff Sakamoto. Operando analysis of the molten li— llzo interface: understanding how the physical properties of li affect the critical current density. *Matter*, 4(6):1947–1961, 2021.

[168] Lei Cheng, Ethan J Crumlin, Wei Chen, Ruimin Qiao, Huaming Hou, Simon Franz Lux, Vassilia Zorba, Richard Russo, Robert Kostecki, Zhi Liu, et al. The origin of high electrolyte–electrode interfacial resistances in lithium cells containing garnet type solid electrolytes. *Physical Chemistry Chemical Physics*, 16(34):18294–18300, 2014.

[169] Lei Cheng, Wei Chen, Martin Kunz, Kristin Persson, Nobumichi Tamura, Guoying Chen, and Marca Doeff. Effect of surface microstructure on electrochemical performance of garnet solid electrolytes. *ACS applied materials & interfaces*, 7(3):2073–2081, 2015.

[170] Kun Kelvin Fu, Yunhui Gong, Gregory T Hitz, Dennis W McOwen, Yiju Li, Shaomao Xu, Yang Wen, Lei Zhang, Chengwei Wang, Glenn Pastel, et al. Three-dimensional bilayer garnet solid electrolyte based high energy density lithium metal–sulfur batteries. *Energy & Environmental Science*, 10(7):1568–1575, 2017.

[171] Huanyu Zhang, Faruk Okur, Claudia Cancellieri, Lars PH Jeurgens, Annapaola Parrilli, Dogan Tarik Karabay, Martin Nesvadba, Sunhyun Hwang, Antonia Neels, Maksym V Kovalenko, et al. Bilayer dense-porous li7la3zr2o12 membranes for high-performance li-garnet solid-state batteries. *Advanced Science*, page 2205821.

[172] Jordi Sastre, Moritz H Futscher, Lea Pompizi, Abdessalem Aribia, Agnieszka Priebe, Jan Overbeck, Michael Stiefel, Ayodhya N Tiwari, and Yaroslav E Romanyuk. Blocking lithium dendrite growth in solid-state batteries with an ultrathin amorphous li-la-zr-o solid electrolyte. *Communications Materials*, 2(1):76, 2021.

[173] Xiaogang Han, Yunhui Gong, Kun Fu, Xingfeng He, Gregory T Hitz, Jiaqi Dai, Alex Pearse, Boyang Liu, Howard Wang, Gary Rubloff, et al. Negating interfacial impedance in garnet-based solid-state li metal batteries. *Nature materials*, 16(5):572–579, 2017.

[174] Chih-Long Tsai, Vladimir Roddatis, C Vinod Chandran, Qianli Ma, Sven Uhlenbruck, Martin Bram, Paul Heitjans, and Olivier Guillon. Li7la3zr2o12 interface modification for li dendrite prevention. *ACS applied materials & interfaces*, 8(16):10617–10626, 2016.

[175] Dominic Spencer Jolly, Dominic LR Melvin, Isabella DR Stephens, Rowena H Brugge, Shengda D Pu, Junfu Bu, Ziyang Ning, Gareth O Hartley, Paul Adamson, Patrick S Grant, et al. Interfaces between ceramic and polymer electrolytes: a comparison of oxide and sulfide solid electrolytes for hybrid solid-state batteries. *Inorganics*, 10(5):60, 2022.

[176] Fengyu Shen, Marm B Dixit, Xianghui Xiao, and Kelsey B Hatzell. Effect of pore connectivity on li dendrite propagation within llzo electrolytes observed with synchrotron x-ray tomography. *ACS Energy Letters*, 3(4):1056–1061, 2018.

[177] Fudong Han, Andrew S Westover, Jie Yue, Xiulin Fan, Fei Wang, Miaofang Chi, Donovan N Leonard, Nancy J Dudney, Howard Wang, and Chunsheng Wang. High

electronic conductivity as the origin of lithium dendrite formation within solid electrolytes. *Nature Energy*, 4(3):187–196, 2019.

[178] Junpei Yue and Yu-Guo Guo. The devil is in the electrons. *Nature Energy*, 4(3):174–175, 2019.

[179] Jordi Sastre, Agnieszka Priebe, Max Döbeli, Johann Michler, Ayodhya N Tiwari, and Yaroslav E Romanyuk. Lithium garnet li7la3zr2o12 electrolyte for all-solid-state batteries: closing the gap between bulk and thin film li-ion conductivities. *Advanced Materials Interfaces*, 7(17):2000425, 2020.

[180] Yongli Song, Luyi Yang, Lei Tao, Qinghe Zhao, Zijian Wang, Yanhui Cui, Hao Liu, Yuan Lin, and Feng Pan. Probing into the origin of an electronic conductivity surge in a garnet solid-state electrolyte. *Journal of Materials Chemistry A*, 7(40):22898–22902, 2019.

[181] Hong-Kang Tian, Bo Xu, and Yue Qi. Computational study of lithium nucleation tendency in li7la3zr2o12 (llzo) and rational design of interlayer materials to prevent lithium dendrites. *Journal of Power Sources*, 392:79–86, 2018.

[182] Hong-Kang Tian, Zhe Liu, Yanzhou Ji, Long-Qing Chen, and Yue Qi. Interfacial electronic properties dictate li dendrite growth in solid electrolytes. *Chemistry of Materials*, 31(18):7351–7359, 2019.

[183] KC Santosh, Roberto C Longo, Ka Xiong, and Kyeongjae Cho. Point defects in garnet-type solid electrolyte (c-li7la3zr2o12) for li-ion batteries. *Solid State Ionics*, 261:100–105, 2014.

[184] Alex Squires, Daniel Davies, Sunghyun Kim, David Scanlon, Aron Walsh, and Benjamin Morgan. Low electronic conductivity of li7la3zr2o12 (llzo) solid electrolytes from first principles. *Chemrxiv.org*, This content is a preprint and has not been peer-reviewed., 2021.

[185] Jeff Wolfenstine, Joshua Ratchford, Ezhiyl Rangasamy, Jeffrey Sakamoto, and Jan L Allen. Synthesis and high li-ion conductivity of ga-stabilized cubic li7la3zr2o12. *Materials Chemistry and Physics*, 134(2-3):571–575, 2012.

[186] J Wolfenstine, JL Allen, J Read, and J Sakamoto. Chemical stability of cubic li 7 la 3 zr 2 o 12 with molten lithium at elevated temperature. *Journal of materials science*, 48:5846–5851, 2013.

[187] Charles-Emmanuel Dutoit, Mingxue Tang, Didier Gourier, Jean-Marie Tarascon, Hervé Vezin, and Elodie Salager. Monitoring metallic sub-micrometric lithium structures in li-ion batteries by in situ electron paramagnetic resonance correlated spectroscopy and imaging. *Nature Communications*, 12(1):1410, 2021.

[188] Y Yafet. g factors and spin-lattice relaxation of conduction electrons. In *Solid state physics*, volume 14, pages 1–98. Elsevier, 1963.

[189] Xiaowen Zhan, Shen Lai, Mallory P Gobet, Steven G Greenbaum, and Mona Shirpour. Defect chemistry and electrical properties of garnet-type li 7 la 3 zr 2 o 12. *Physical Chemistry Chemical Physics*, 20(3):1447–1459, 2018.

[190] Lei Cheng, Huaming Hou, Simon Lux, Robert Kostecki, Ryan Davis, Vassilia Zorba, Apurva Mehta, and Marca Doeff. Enhanced lithium ion transport in garnet-type solid state electrolytes. *Journal of Electroceramics*, 38:168–175, 2017.

[191] Xiaoming Liu, Regina Garcia-Mendez, Andrew R Lupini, Yongqiang Cheng, Zachary D Hood, Fudong Han, Asma Sharafi, Juan Carlos Idrobo, Nancy J Dudney, Chunsheng Wang, et al. Local electronic structure variation resulting in li 'filament'formation within solid electrolytes. *Nature Materials*, 20(11):1485–1490, 2021.

[192] Sakai Kenji. Materials system division of toshima manufacturing co., ltd. [Available online]. http://http://www.material-sys.com/service/llz/, August 2022. Last accessed 03 August 2022.

[193] Maggio P Pechini. Method of preparing lead and alkaline earth titanates and niobates and coating method using the same to form a capacitor, July 11 1967. US Patent 3,330,697.

[194] Lawrence P Cook. Phase equilibria of alumina. *Alumina chemicals: science and technology handbook*, pages 49–71, 1990.

[195] Masumi Sato, Regina Garcia-Mendez, and Jeff Sakamoto. Mapping hot-pressed li6. 25al0. 25la3zr2o12 (llzo) grains and grain boundaries through a simple thermal grooving technique. *Journal of Asian Ceramic Societies*, 8(3):793–803, 2020.

[196] Israel O Owate and Robert Freer. Thermochemical etching method for ceramics. *Journal of the American Ceramic Society*, 75(5):1266–1268, 1992.

[197] Struers. Grinding and polishing equipment and consumables [Available online]. https://www.struers.com/en/Products/Grinding-and-Polishing, August 2022. Last accessed 15 August 2022.

[198] William Clegg. *X-ray crystallography*. Oxford chemistry primers. Oxford University Press, Oxford, second edition. edition, 2015 - 2015.

[199] ICSD. Crystallographic database [Available online]. https://icsd.psds.ac.uk/search/basic.xhtml;jsessionid=DE2C372EA325EE2B5934EF3FDEBE59A2, August 2022. Last accessed 17 August 2022.

[200] Daniel Rettenwander, Gunther Redhammer, Florian Preishuber-Pflugl, Lei Cheng, Lincoln Miara, Reinhard Wagner, Andreas Welzl, Emmanuelle Suard, Marca M Doeff, Martin Wilkening, et al. Structural and electrochemical consequences of al and ga cosubstitution in li7la3zr2o12 solid electrolytes. *Chemistry of materials*, 28(7):2384–2392, 2016.

[201] Armel Le Bail, Huguette Duroy, and Jean Louis Fourquet. Ab-initio structure determination of lisbwo6 by x-ray powder diffraction. *Materials Research Bulletin*, 23(3):447–452, 1988.

[202] GSAS-2. Gsas-ii - crystallography data analysis software[Available online]. https://subversion.xray.aps.anl.gov/trac/pyGSAS, January 2023. Last accessed January 7, 2023.

[203] Brian H. Toby and Robert B. Von Dreele. *GSAS-II*: the genesis of a modern open-source all purpose crystallography software package. *Journal of Applied Crystallography*, 46(2):544–549, Apr 2013.

[204] Nikon. Eclipse LV150N/LV150NA. https://www.nikon.com/products/industrial-metrology/lineup/microscope/industrial-microscopes/lv150nl_lv150na/, September 2022. Last accessed 30 September 2022.

[205] RK Leach, L Brown, X Jiang, R Blunt, M Conroy, and D Mauger. Guide to the measurement of smooth surface topography using coherence scanning interferometry. 2008.

[206] LEOL. wavelength of electron [Available online]. https://www.jeol.com/words/emterms/20121023.071258.php#:~:text=wavelength, December 2022. Last accessed 13 December 2022.

[207] Joseph I Goldstein, Dale E Newbury, Joseph R Michael, Nicholas WM Ritchie, John Henry J Scott, and David C Joy. *Scanning electron microscopy and X-ray microanalysis*. springer, 2017.

[208] Bob Hafner. Scanning electron microscopy primer. *Characterization Facility, University of Minnesota-Twin Cities*, pages 1–29, 2007.

[209] Thorben Krauskopf, Rabea Dippel, Hannah Hartmann, Klaus Peppler, Boris Mogwitz, Felix H Richter, Wolfgang G Zeier, and Jürgen Janek. Lithium-metal growth kinetics on llzo garnet-type solid electrolytes. *Joule*, 3(8):2030–2049, 2019.

[210] Sewon Kim, Changhoon Jung, Hyunseok Kim, Karen E Thomas-Alyea, Gabin Yoon, Byunghoon Kim, Michael E Badding, Zhen Song, JaeMyung Chang, Jusik Kim, et al. The role of interlayer chemistry in li-metal growth through a garnet-type solid electrolyte. *Advanced Energy Materials*, 10(12):1903993, 2020.

[211] Quorum. Q150t plus - turbomolecular pumped coater [Available online]. https://www.quorumtech.com/q150t-turbo-pumped-sputter-coatercarbon-coater/, October 2022. Last accessed 31st October 2022.

[212] MSESupplies. 100g battery grade lithium chips 16mm diameter and 0.6mm thick for battery research [Available online]. https://www.msesupplies.com/en-gb/products/100g-battery-grade-lithium-chips-d-16mm-x-t-0-6mm-for-battery-research?variant=31705755811898, October 2022. Last accessed 31st October 2022.

[213] XIAMEN TOB NEW ENERGY TECHNOLOGY CO. LTD. Cr1632 coin cell case with gasket by 304ss [Available online]. https://www.tobmachine.com/cr1632-coin-cell-case-with-gasket-by-304ss$_p$909.*html*, *October*2022. *Lastaccessed*31*stOctober*2022.

[214] Andrzej Lasia. *Electrochemical impedance spectroscopy and its applications*. Springer, New York, 2014.

[215] John T. S. Irvine, Derek C. Sinclair, and Anthony R. West. Electroceramics: Characterization by impedance spectroscopy. *Advanced Materials*, 2(3):132–138, 1990.

[216] Federico M Pesci, Antonio Bertei, Rowena H Brugge, Steffen P Emge, AK Ola Hekselman, Lauren E Marbella, Clare P Grey, and Ainara Aguadero. Establishing ultralow activation energies for lithium transport in garnet electrolytes. *ACS applied materials & interfaces*, 12(29):32806–32816, 2020.

[217] Karlsruhe Institute of Technology (KIT). Kramers-kronig validity test lin-kk for impedance spectra [Available online]. https://www.iam.kit.edu/et/english/Lin-KK.php, October 2022. Last accessed 31st October 2022.

[218] M. Schönleber, D. Klotz, and E. Ivers-Tiffée. A method for improving the robustness of linear kramers-kronig validity tests. *Electrochimica Acta*, 131:20–27, 2014. Electrochemical Impedance Spectroscopy.

[219] J. Ross Macdonald. Impedance spectroscopy. *Annals of Biomedical Engineering*, 20(3):289–305, 1992.

[220] Biologic. Sp-240 potentiostat [Available online]. https://www.biologic.net/products/sp-240/, October 2022. Last accessed 31st October 2022.

[221] Martin Philipp, Bernhard Gadermaier, Patrick Posch, Ilie Hanzu, Steffen Ganschow, Martin Meven, Daniel Rettenwander, Günther J. Redhammer, and H. Martin R. Wilkening. The electronic conductivity of single crystalline ga-stabilized cubic li7la3zr2o12: A technologically relevant parameter for all-solid-state batteries. *Advanced Materials Interfaces*, 7(16):2000450, 2020.

[222] Oliver Gerbig, Rotraut Merkle, and Joachim Maier. Electron and ion transport in li2o2. *Advanced Materials*, 25(22):3129–3133, 2013.

[223] Scribner. 580 battery test system [Available online]. https://www.scribner.com/products/battery-test-systems/580-battery-test-system/, October 2022. Last accessed 31st October 2022.

[224] Sharmila M Mukhopadhyay. Sample preparation for microscopic and spectroscopic characterization of solid surfaces and films. *CHEMICAL ANALYSIS NEW YORK INTERSCIENCE THEN JOHN WILEY*, pages 377–412, 2003.

[225] Roger Smart, Stewart McIntyre, Mike Bancroft, and Igor Bello. X-ray photoelectron spectroscopy [Available online]. *https* :

//mmrc.caltech.edu/$SS_XPS/XPS_PPT/XPS_Sslides.pdf$, October 2022. Last accessed 31st October 2022.

[226] D. A. Shirley. High-resolution x-ray photoemission spectrum of the valence bands of gold. *Phys. Rev. B*, 5:4709–4714, Jun 1972.

[227] H.H. Brongersma, M. Draxler, M. de Ridder, and P. Bauer. Surface composition analysis by low-energy ion scattering. *Surface Science Reports*, 62(3):63–109, 2007.

[228] G. Bolbach, A. Viari, R. Galera, A Brunot, and J.C. Blais. Organic film thickness effect in secondary ion mass spectrometry and plasma desorption mass spectrometry. *International Journal of Mass Spectrometry and Ion Processes*, 112(1):93–100, 1992.

[229] Harold F. Winters and J. W. Coburn. Influence of the altered layer on depth profiling measurements. *Applied Physics Letters*, 28(4):176–179, 1976.

[230] *Surface analysis : the principal techniques.* Wiley, Chichester, 1997.

[231] A Benninghoven. Surface analysis by secondary ion mass spectrometry (sims). *Surface Science*, 299-300:246–260, 1994.

[232] Jean-Luc Guerquin-Kern, Ting-Di Wu, Carmen Quintana, and Alain Croisy. Progress in analytical imaging of the cell by dynamic secondary ion mass spectrometry (sims microscopy). *Biochimica et Biophysica Acta (BBA) - General Subjects*, 1724(3):228–238, 2005. Some Insights into the Biophysics of Complex Systems.

[233] Roger A. De Souza and Manfred Martin. Secondary ion mass spectrometry (sims) – a powerful tool for studying mass transport over various length scales. *physica status solidi c*, 4(6):1785–1801, 2007.

[234] Paul Van der Heide. *Secondary ion mass spectrometry : an introduction to principles and practices.* Wiley, Hoboken, New Jersey, 2014 - 2014.

[235] University of Oxford. Nanosims department of materials - the instrument[Available online]. http://nanosims.materials.ox.ac.uk/nanosimshome/instrument.html, January 2023. Last accessed January 7, 2023.

[236] CAMECA. Nanosims 50l[Available online]. https://www.cameca.com/products/sims/nanosims, January 2023. Last accessed January 7, 2023.

[237] R.A. De Souza, J. Zehnpfenning, M. Martin, and J. Maier. Determining oxygen isotope profiles in oxides with time-of-flight sims. *Solid State Ionics*, 176(15):1465–1471, 2005.

[238] P. Mazarov, A. Melnikov, R. Wernhardt, and A.D. Wieck. Long-life bismuth liquid metal ion source for focussed ion beam micromachining application. *Applied Surface Science*, 254(22):7401–7404, 2008.

[239] L. Bischoff, W. Pilz, P. Mazarov, and A. D. Wieck. Comparison of bismuth emitting liquid metal ion sources. *Applied Physics A: Materials Science & Processing*,

99(1):145–150, April 2010.

[240] Ainara Aguadero and Stephen John Skinner. High five: Resolution, sensitivity, in operando control, ultra high vacuum and ion sectioning in a single instrument (project reference ep/p029914/1) [Available online]. https://gtr.ukri.org, May 2023. Last accessed 25 May 2023.

[241] John A. Kilner, Stephen J. Skinner, and Hidde H. Brongersma. The isotope exchange depth profiling (iedp) technique using sims and leis. *Journal of Solid State Electrochemistry*, 15(5):861–876, May 2011. Copyright: Copyright 2012 Elsevier B.V., All rights reserved.

[242] R.A. De Souza and R.J. Chater. Oxygen exchange and diffusion measurements: The importance of extracting the correct initial and boundary conditions. *Solid State Ionics*, 176(23):1915–1920, 2005.

[243] William David. Kingery. *Introduction to ceramics*. Wiley series on the science and technology of materials. Wiley-Interscience, New York ;, 2nd ed. edition, 1976.

[244] S. J. Cooper. *Quantifying the Transport Properties of Solid Oxide Fuel Cell Electrodes*. PhD thesis, Imperial College London, 2015.

[245] Robert D Shannon. Revised effective ionic radii and systematic studies of interatomic distances in halides and chalcogenides. *Acta crystallographica section A: crystal physics, diffraction, theoretical and general crystallography*, 32(5):751–767, 1976.

[246] Bikram Konar, Dong-Geun Kim, and In-Ho Jung. Coupled phase diagram experiments and thermodynamic optimization of the binary li2o-mgo and li2o-cao systems and ternary li2o-mgo-cao system. *Ceramics International*, 43(16):13055–13062, 2017.

[247] Chao Zhu, Till Fuchs, Stefan AL Weber, Felix H Richter, Gunnar Glasser, Franjo Weber, Hans-Jürgen Butt, Jürgen Janek, and Rüdiger Berger. Understanding the evolution of lithium dendrites at li6. 25al0. 25la3zr2o12 grain boundaries via operando microscopy techniques. *Nature Communications*, 14(1):1300, 2023.

[248] Qi Liu, Zhen Geng, Cuiping Han, Yongzhu Fu, Song Li, Yan-bing He, Feiyu Kang, and Baohua Li. Challenges and perspectives of garnet solid electrolytes for all solid-state lithium batteries. *Journal of Power Sources*, 389:120–134, 2018.

[249] F Murzakhanov, G Mamin, A Voloshin, E Klimashina, V Putlyaev, V Doronin, S Bakhteev, R Yusupov, M Gafurov, and S Orlinskii. Conventional electron paramagnetic resonance of mn2+ in synthetic hydroxyapatite at different concentrations of the doped manganese. In *IOP Conference Series: Earth and Environmental Science*, volume 155, page 012006. IOP Publishing, 2018.

[250] Douglas F Franco, Danilo Manzani, Eduar E Carvajal, Gabriela Augusta Prando, José Pedro Donoso, Claudio J Magon, Selma G Antonio, Yara Galvao Gobato, and Marcelo Nalin. Optical and epr studies of zinc phosphate glasses containing mn 2+ ions. *Journal of Materials Science*, 55:9948–9961, 2020.

[251] PF Rapheal, E Manoj, and MR Prathapachandra Kurup. Syntheses and epr spectral studies of manganese (ii) complexes derived from pyridine-2-carbaldehyde based n (4)-substituted thiosemicarbazones: Crystal structure of one complex. *Polyhedron*, 26(17):5088–5094, 2007.

[252] Kunimitsu Kataoka and Junji Akimoto. Lithium-ion conductivity and crystal structure of garnet-type solid electrolyte li7- xla3zr2- xtaxo12 using single-crystal. *Journal of the Ceramic Society of Japan*, 127(8):521–526, 2019.

[253] Shan Hu, Pengyu Xu, Luize Scalco de Vasconcelos, Lia Stanciu, Hongwei Ni, and Kejie Zhao. Elastic modulus, hardness, and fracture toughness of li6. 4la3zr1. 4ta0. 6o12 solid electrolyte. *Chinese Physics Letters*, 38(9):098401, 2021.

[254] Yue Jiang, Yuxi Zhou, Zhiwei Hu, Yi Huang, and Xiaohong Zhu. Mgo or al2o3 crucible: Which is better for the preparation of llz-based solid electrolytes? *Ceramics International*, 46(3):3367–3373, 2020.

[255] Rowena Brugge. *Garnet ceramic electrolytes for next-generation lithium batteries*. PhD thesis, University of London, 2018.

[256] Helena Téllez, Ainara Aguadero, John Druce, Mónica Burriel, Sarah Fearn, Tatsumi Ishihara, David S McPhail, and John A Kilner. New perspectives in the surface analysis of energy materials by combined time-of-flight secondary ion mass spectrometry (tof-sims) and high sensitivity low-energy ion scattering (hs-leis). *Journal of Analytical Atomic Spectrometry*, 29(8):1361–1370, 2014.

[257] Wyatt E Tenhaeff, Ezhiyl Rangasamy, Yangyang Wang, Alexei P Sokolov, Jeff Wolfenstine, Jeffrey Sakamoto, and Nancy J Dudney. Resolving the grain boundary and lattice impedance of hot-pressed li7la3zr2o12 garnet electrolytes. *ChemElectroChem*, 1(2):375–378, 2014.

[258] O Cojocaru-Mirédin, J Schmieg, M Müller, A Weber, E Ivers-Tiffée, and D Gerthsen. Quantifying lithium enrichment at grain boundaries in li7la3zr2o12 solid electrolyte by correlative microscopy. *Journal of Power Sources*, 539:231417, 2022.

[259] Xinming Zhang, Xinxin Guan, Ya Zhang, Wei Zhang, and Qiang Shen. On the interfacial properties of the garnet-type electrolyte ceramic pellets of cubic li6. 4la3zr1. 4ta0. 6o12: A comprehensive improvement of the sintering additive of li-ion conducting licl. *Journal of Power Sources*, 556:232459, 2023.

[260] Ran Ji, Ding Zheng, Chang Zhou, Jiang Cheng, Junsheng Yu, and Lu Li. Low-temperature preparation of tungsten oxide anode buffer layer via ultrasonic spray pyrolysis method for large-area organic solar cells. *Materials*, 10(7):820, 2017.

[261] Michał Mazur, Damian Wojcieszak, Artur Wiatrowski, Danuta Kaczmarek, Aneta Lubańska, Jarosław Domaradzki, Piotr Mazur, and Małgorzata Kalisz. Analysis of amorphous tungsten oxide thin films deposited by magnetron sputtering for application in transparent electronics. *Applied Surface Science*, 570:151151, 2021.

[262] Zhen Li, Bin Liu, Jiemin Wang, Luchao Sun, Jingyang Wang, and Yanchun Zhou. Mechanism of intrinsic point defects and oxygen diffusion in yttrium aluminum garnet: first-principles investigation. *Journal of the American Ceramic Society*, 95(11):3628–3633, 2012.

Appendix A

Supplementary Information for Chapter 6

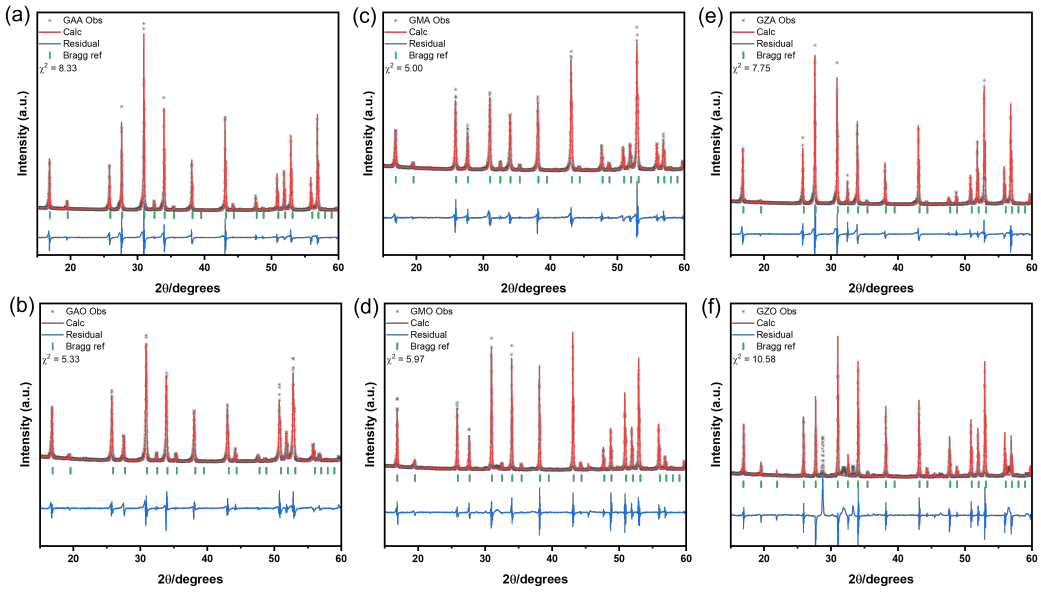


Figure A.1: Le Bail refined XRD pattern for all samples in chapter 5, used to determine lattice parameters, volume, space group and density.



Figure A.2: Ga-LLZO green pellet after sintering process melted into MgO crucible.

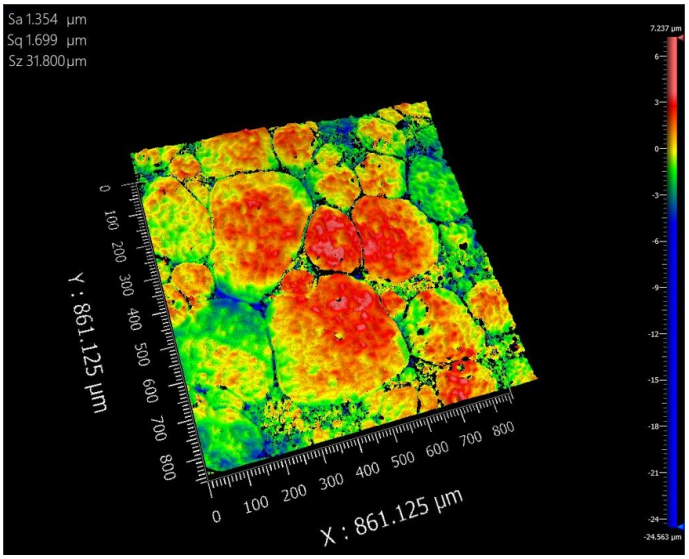


Figure A.3: Grain roughness post sintering of GMA, image from the white light interferometer.

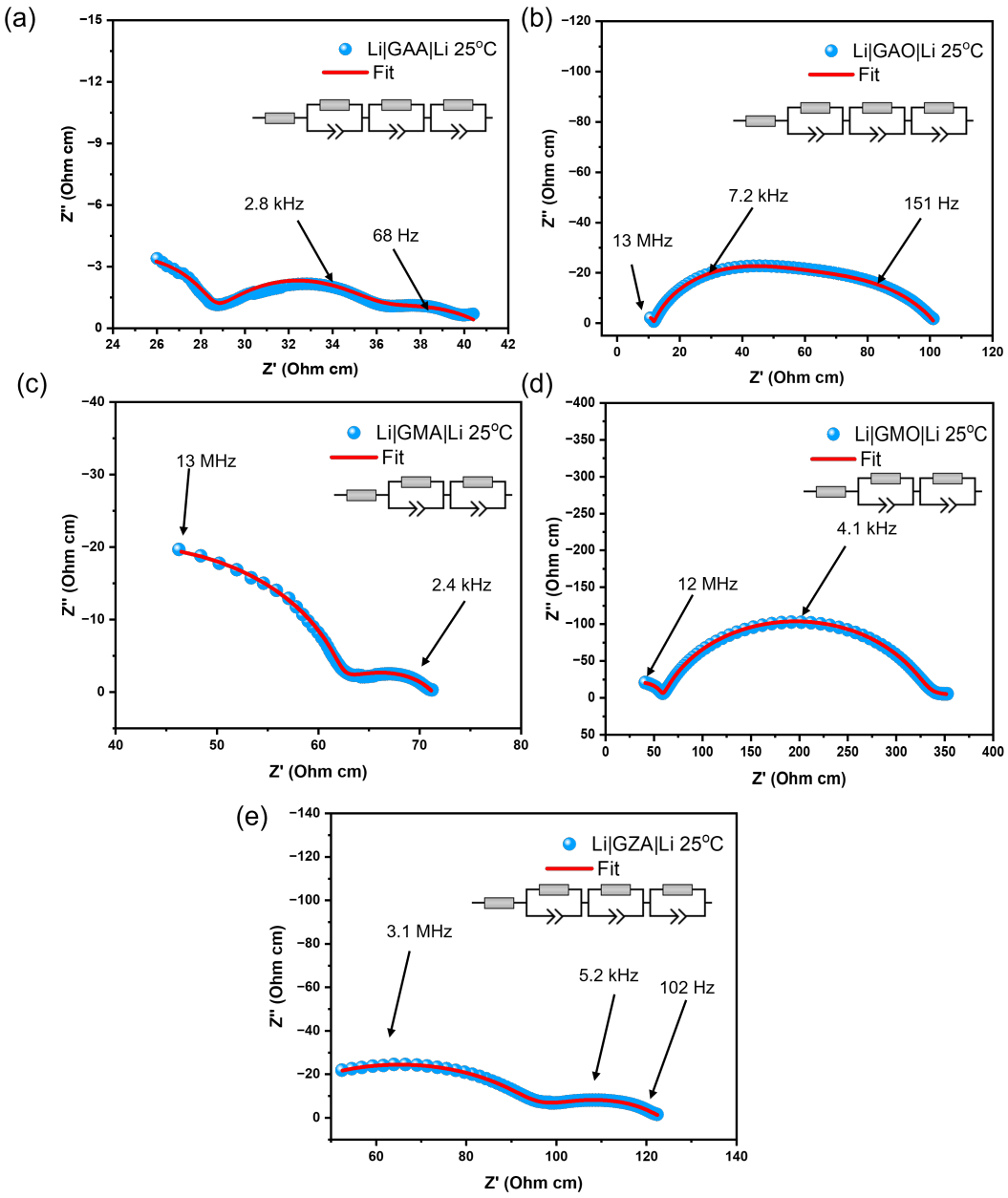


Figure A.4: Nyquist plots for Ga-LLZO prepared under various conditions. EIS obtained using Li|Ga-LLZO|Li at 25°C. Nyquist plot of (a) GAA, (b) GAO, (c) GMA, (d) GMO, and (e) GZA. Inset on the Nyquist plot shows the respective R-CPE equivalent circuit used to fit the data.

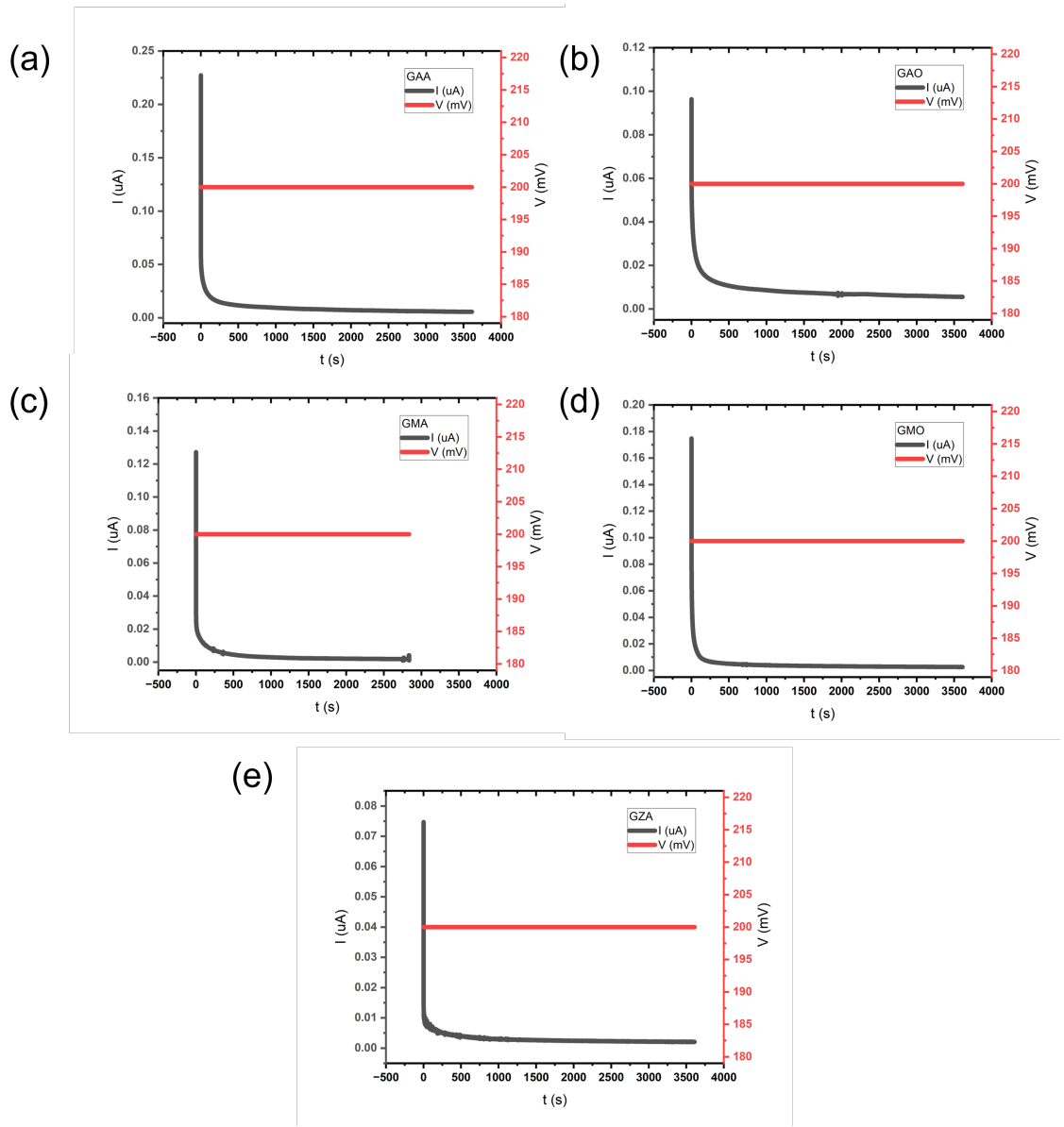


Figure A.5: All time-resolved DC voltage data for electronic conductivity measurements. Au|Ga-LLZO|Au used at RT with a measurement time up to 1 hour.

Appendix B

Supplementary Information for Chapter 7

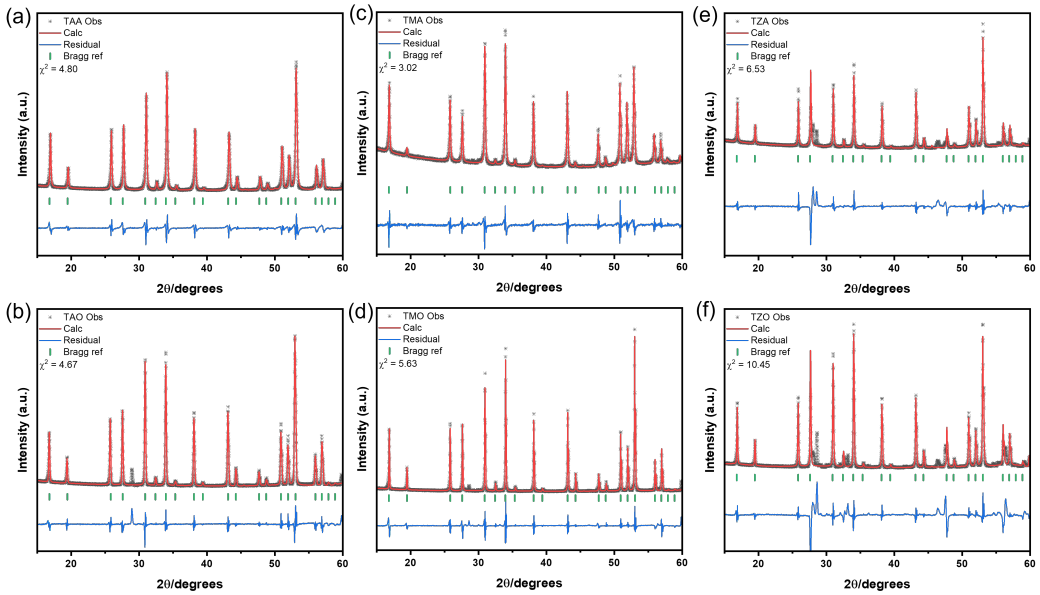


Figure B.1: Le Bail refined XRD pattern for all samples in chapter 5, used to determine lattice parameters, volume, space group and density.

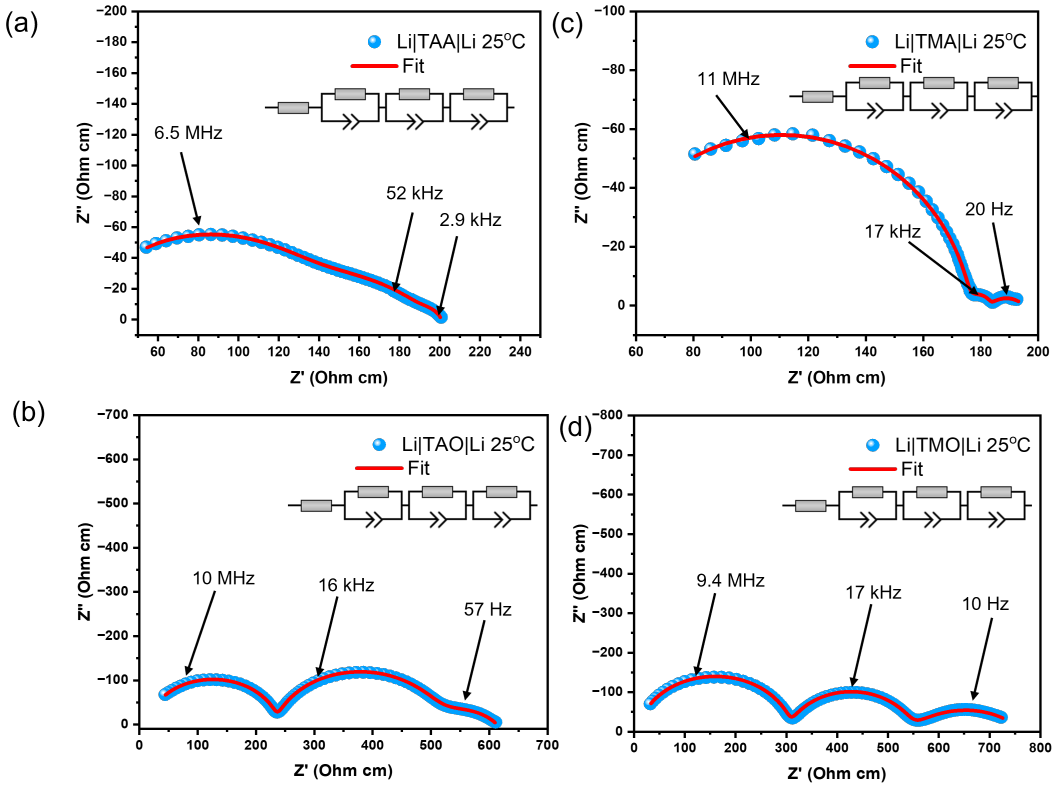


Figure B.2: Nyquist plots for Ta-LLZO prepared under various conditions. EIS obtained using Li|Ta-LLZO|Li at 25°C. Nyquist plot of (a) TAA, (b) TAO, (c) TMA, and (d) TMO. Inset on the Nyquist plot show the respective R-CPE equivalent circuit used to fit the data.

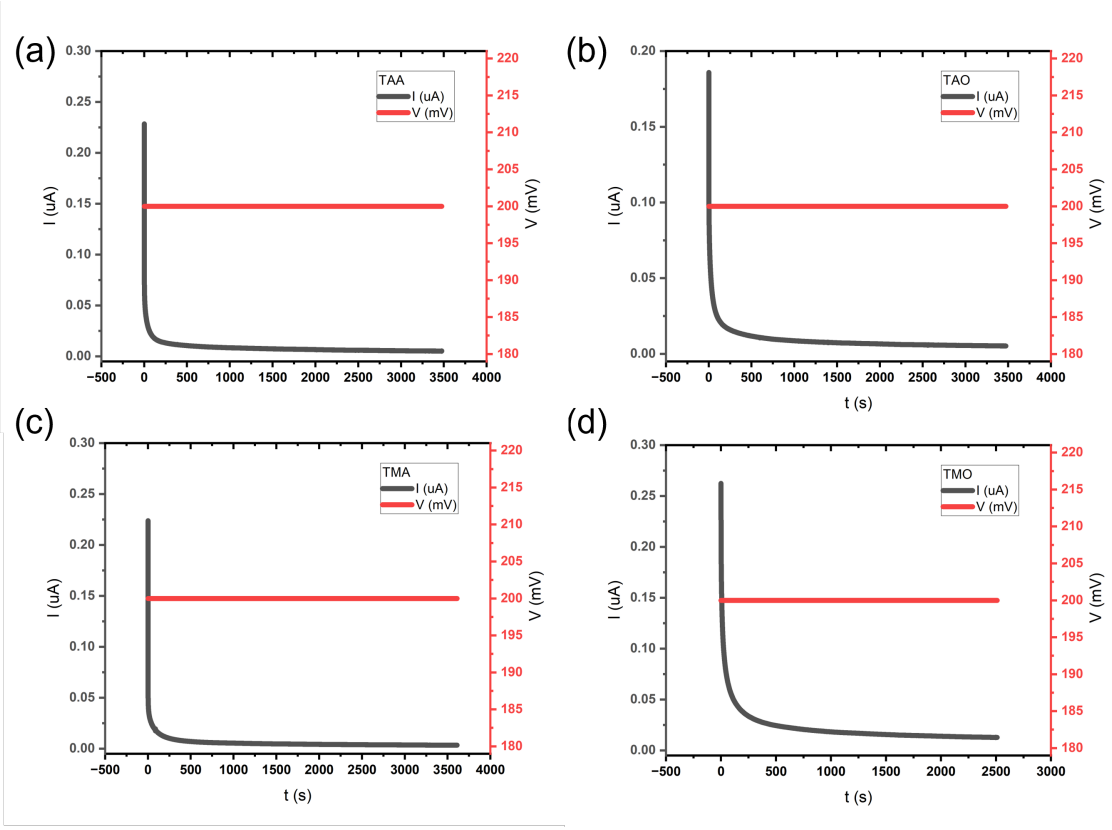


Figure B.3: All time resolved DC voltage data for electronic conductivity measurements. Au|Ta-LLZO|Au used at RT with a measurement time up to 1 hour..

Appendix C

Supplementary Information for Chapter 8

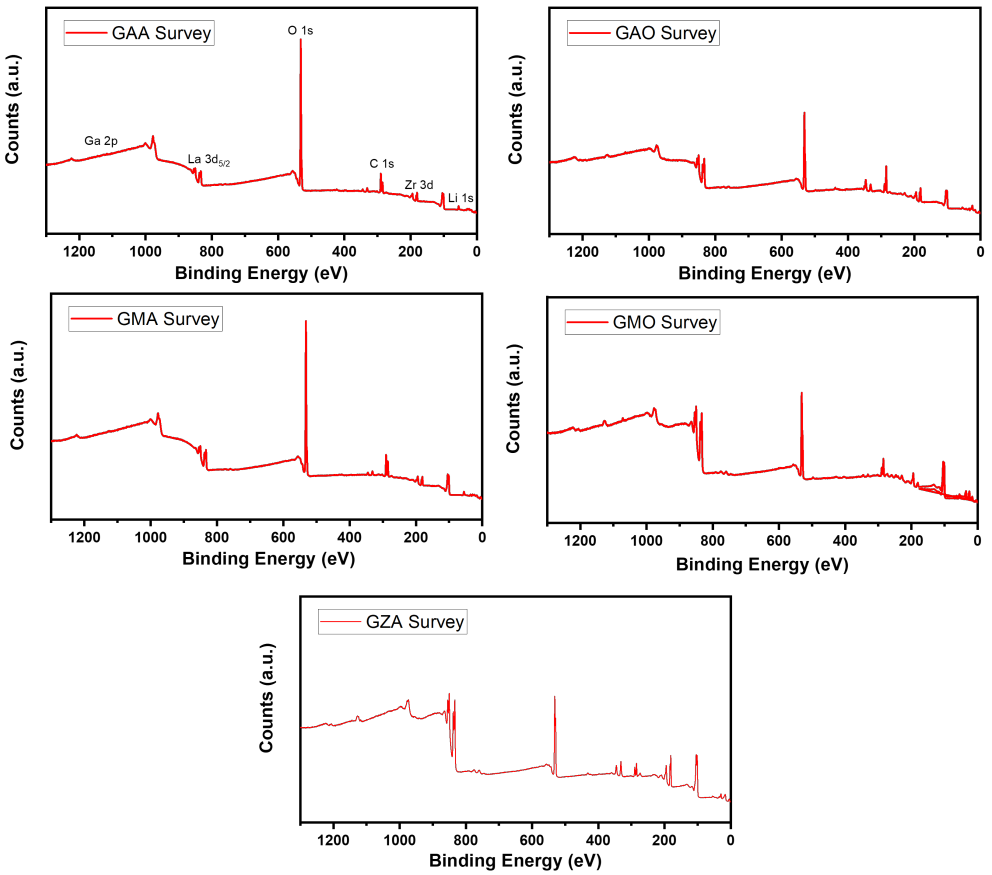


Figure C.1: XPS survey spectra for each Ga-LLZO composed pellet, with labelled core level peaks of interest

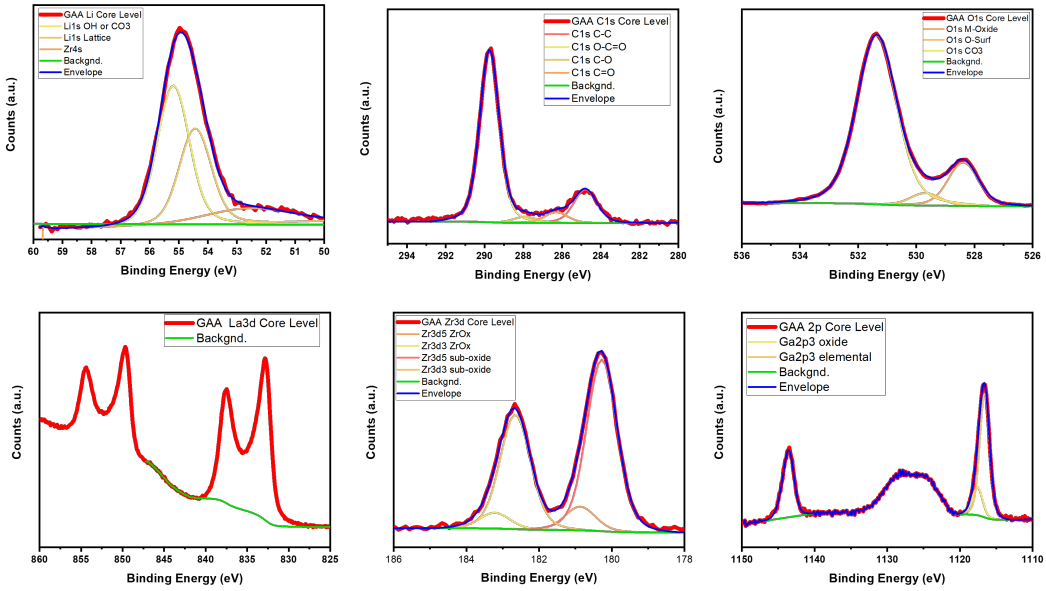


Figure C.2: Fitting of XPS core level spectra of key elements in Ga-LLZO.

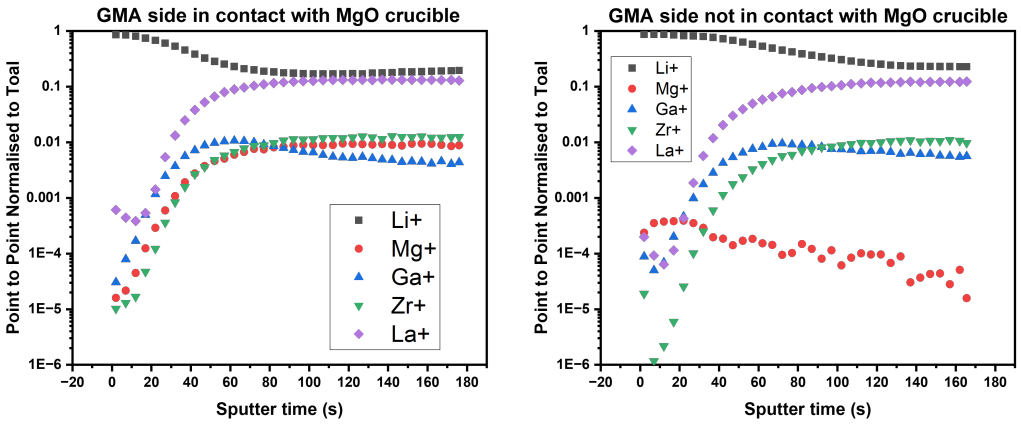


Figure C.3: ToF-SIMS DP of (right) GMA surface not in contact with MgO crucible during sintering and (left) GMA in the surface in contact with MgO crucible. Measurement is done with 25 keV, 0.20pA Bi^+ primary beam and 1 keV, 200 nA O_2^+ sputter beam. The analysis area is 500x500μm analysis area, 1000x1000μm crater area, and 512 pixels.

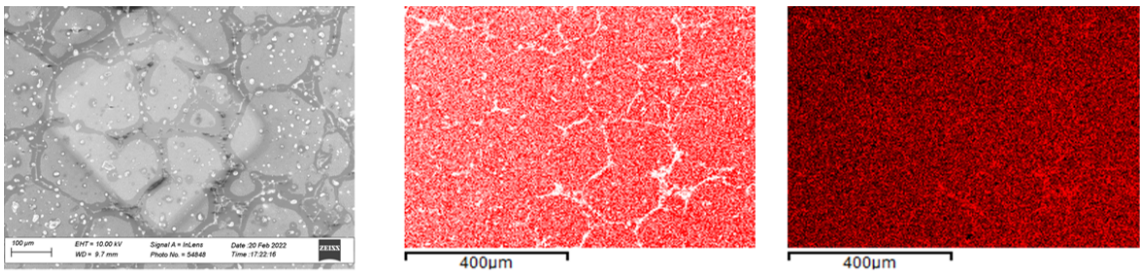


Figure C.4: SEM and EDX map of SIMS crater on GAA, SE image (left), Zr EDX map (middle), and La EDX map (right).

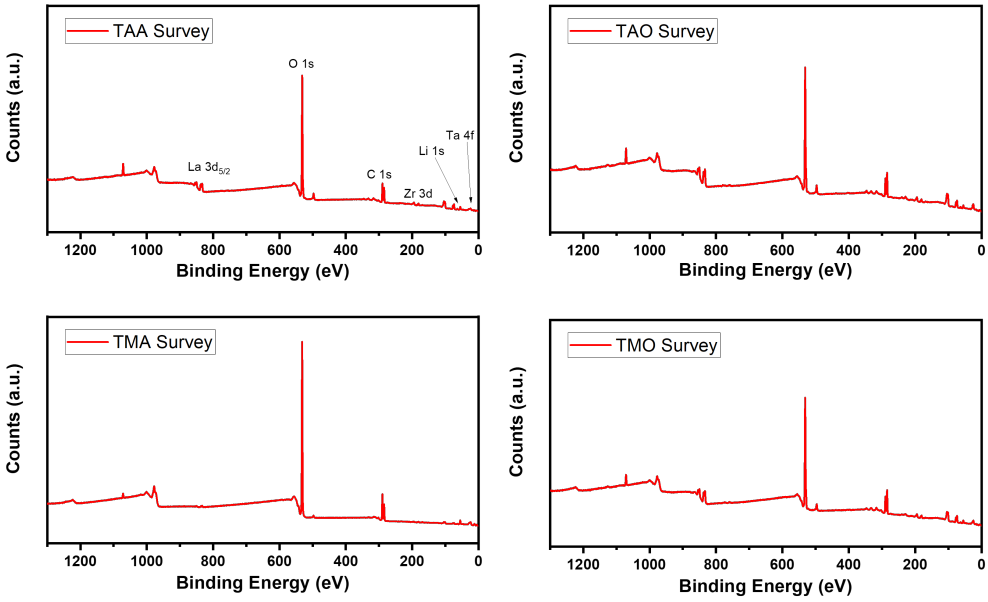


Figure C.5: XPS survey spectra for each Ta-LLZO composed pellet, with labelled core level peaks of interest

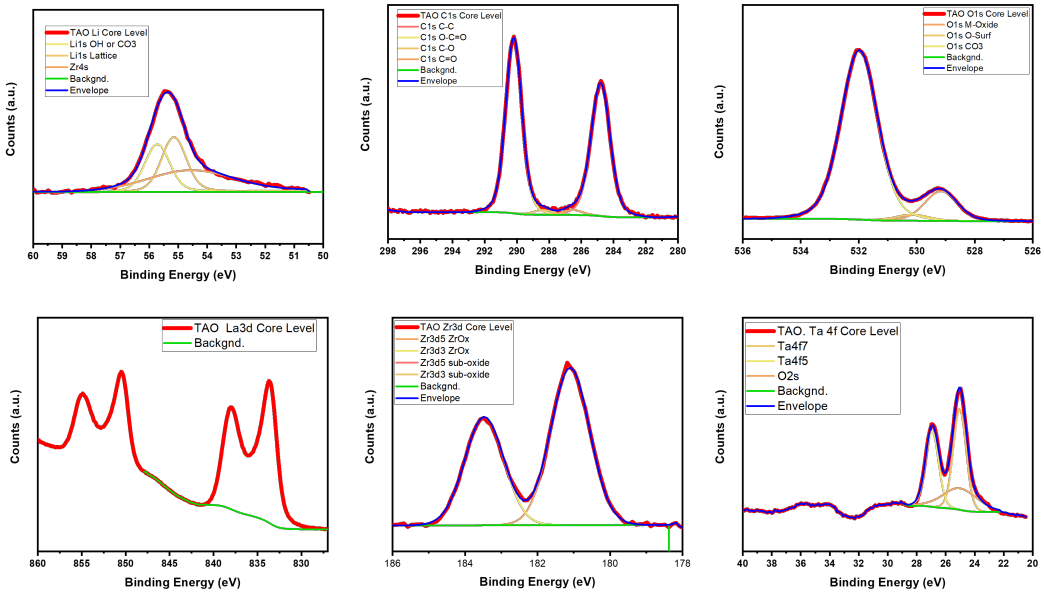


Figure C.6: Fitting of XPS core level spectra of key elements in Ta-LLZO.

Appendix D

Supplementary Information for Chapter 9

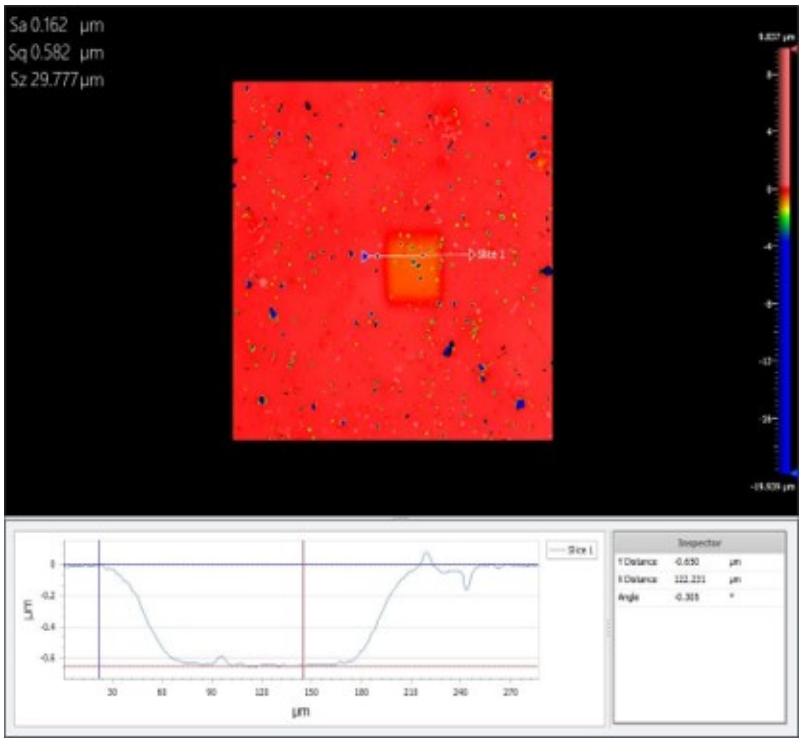


Figure D.1: Crater depth measurement using Zygo WLI, showing crater on GZA as an example. Depth is used for the diffusion profile.